UNIVERSIDAD DE ANTIOQUIA

INTEGRATED SYSTEM FOR THE PRODUCTION OF FUEL-CELL GRADE H_2 FROM BIOETHANOL

Autor

Bernay Cifuentes Vanegas

Universidad de Antioquia

Facultad de ingeniería, Departamento de Ingeniería Química

Medellín, Colombia

2021

Integrated system for the production of fuel-cell grade H_2 from bioethanol

Bernay Cifuentes Vanegas

Tesis presentada como requisito parcial para optar al título de:

Doctor en ingeniería Química

Asesores (a):

Felipe Bustamante Londoño, PhD en Ingeniería Química.

Martha Isabel Cobo Angel, PhD en Ingeniería.

Línea de Investigación:

Estrategias de mejoramiento energético y ambiental de procesos

Grupo de Investigación:

Grupo de Investigación en Catálisis Ambiental

Universidad de Antioquia

Facultad de ingeniería, Departamento de Ingeniería Química

Medellín, Colombia

2021

UNIVERSIDAD DE ANTIOQUIA

1 8 0 3

School of Engineering
Chemical Engineering Department

INTEGRATED SYSTEM FOR THE PRODUCTION OF FUEL-CELL GRADE H_2 FROM BIOETHANOL

BERNAY CIFUENTES VANEGAS

Advisor:
FELIPE BUSTAMANTE LONDOÑO
Co-advisor:
MARTHA ISABEL COBO ANGEL

Acknowledgements

I am grateful to professors Felipe Bustamante and Martha Cobo for their advice, support, and knowledge. I am fortunate you have been my advisors.

I thank my co-authors, prof. Juan A. Conesa, prof. Luis F. Córdoba, prof. Gabriela Diaz, prof. Jordi Llorca, prof. Lluis Soler, prof. Ruth Ruiz, MSc. Daniel G. Araiza, MSc. Nestor Sanchez, MSc. Laura Proaño, MSc. Alejandro Cifuentes, and BSc. July Gomez for their contribution to my doctoral research.

I also acknowledge the members of GCA (Grupo de investigación en Catalisis Ambiental) from Universidad de Antioquia, GEMA (Grupo de investigación en Energías, Materiales y Ambiente) from Universidad de La Sabana, IF (Instituto de Física) from Universidad Nacional Autónoma de México and INTE (Institut de Tècniques Energètiques) from Universitat Politècnica de Catalunya for their help and camaraderie.

Contents

1 Overview **13**
- 1.1 Introduction . . . 13
- 1.2 Objectives . . . 19
  - 1.2.1 General . . . 19
  - 1.2.2 Specific . . . 19
- 1.3 Document structure . . . 19
- 1.4 Academic products . . . 20
- 1.5 References . . . 22

2 Catalytic system based on powder catalysts **24**
- 2.1 Catalytic system to produce and purify syngas . . . 24
  - 2.1.1 Abstract . . . 26
  - 2.1.2 Introduction . . . 26
  - 2.1.3 Experimental . . . 29
  - 2.1.4 Results and discussion . . . 32
  - 2.1.5 Conclusions . . . 43
  - 2.1.6 Acknowledgments . . . 45
  - 2.1.7 References . . . 45
- 2.2 Selection of support for CO removal . . . 48
  - 2.2.1 Abstract . . . 50
  - 2.2.2 Introduction . . . 50
  - 2.2.3 Experimental . . . 52
  - 2.2.4 Results and discussion . . . 55
  - 2.2.5 Conclusions . . . 70
  - 2.2.6 Acknowledgments . . . 70
  - 2.2.7 References . . . 70
- 2.3 Modification of CeO_2 morphology . . . 74
  - 2.3.1 Abstract . . . 76
  - 2.3.2 Introduction . . . 76
  - 2.3.3 Experimental . . . 78
  - 2.3.4 Results and discussion . . . 80
  - 2.3.5 Conclusions . . . 94
  - 2.3.6 Acknowledgments . . . 94
  - 2.3.7 References . . . 96

3 Catalytic system based on monolith reactors **99**
- 3.1 Monolithic reactor for syngas production . . . 99
  - 3.1.1 Abstract . . . 101
  - 3.1.2 Introduction . . . 101
  - 3.1.3 Experimental . . . 103
  - 3.1.4 Results and discussion . . . 106
  - 3.1.5 Conclusions . . . 117

3.1.6 Acknowledgments . . . 117
3.1.7 References . . . 117
3.2 Monolithic reactor for CO removal . . . 120
3.2.1 Abstract . . . 122
3.2.2 Introduction . . . 122
3.2.3 Experimental . . . 125
3.2.4 Results and discussion . . . 129
3.2.5 Conclusions . . . 140
3.2.6 Acknowledgments . . . 141
3.2.7 References . . . 141

4 Technology description **145**
4.1 Introduction . . . 146
4.2 FPU prototype . . . 147
4.2.1 General description . . . 147
4.2.2 Syngas production . . . 149
4.2.3 CO removal from the syngas . . . 149
4.2.4 Cost of the prototype . . . 151
4.3 Non-centrifugal sugar industry in Colombia . . . 152
4.4 References . . . 154

5 Conclusions and Future Work **156**
5.1 Conclusions . . . 156
5.2 Future Work . . . 157

6 Supplementary Material **159**
6.1 Figures . . . 159
6.1.1 Figures for Chapter 2 - Section 1 . . . 159
6.1.2 Figures for Chapter 2 - Section 2 . . . 165
6.1.3 Figures for Chapter 2 - Section 3 . . . 168
6.1.4 Figures for Chapter 3 - Section 1 . . . 171
6.1.5 Figures for Chapter 3 - Section 2 . . . 173
6.1.6 Figures for Chapter 4 . . . 178
6.2 Tables . . . 180
6.2.1 Tables for Chapter 2 - Section 1 . . . 180
6.2.2 Tables for Chapter 2 - Section 2 . . . 183
6.2.3 Tables for Chapter 2 - Section 3 . . . 189
6.2.4 Tables for Chapter 3 - Section 2 . . . 191

List of Figures

1.1.1 Cooperation network in the framework project for the power and heat production from residual biomass that involves a H_2-based technology. 18

2.1.1 Overall process for energy production from biomass. Solid lines indicate continuous processes, while dotted lines indicate batch processes. The processes of interest in this paper are highlighted in blue. 27

2.1.2 (a) CO conversion, (b) CO_2 yield, (c) H_2 loss, and (d) CH_4 yield for CO-removal of a post-reforming stream on $AuCu/CeO_2$ catalysts. Inlet stream: 7.8% H_2, 2.0% CO, 0.5% CO_2, 0.3% CH_4, 1.4% H_2O, 1.8% O_2, 6.8% N_2, and 79.4% Ar. Total metal loading (Au+Cu) = 2 wt% in all catalysts. Response surface: Quartic model, $R^2 > 0.82$, Adjusted $R^2 > 0.8$, Prop. F<<0.1 (significant), and Lack of Fit>>3 (nonsignificant). The regression analysis for the response surfaces is available in Supplementary Material, Table SM.3 33

2.1.3 Individual contribution of the main CO-removal reactions on (a) CO conversion, (b) CO_2 yield, (c) H_2 lost, and (d) CH_4 yield on $Au_{1.0}Cu_{1.0}/Ce$ catalyst. Lines identified as CO-PROX, WGS, H_2 oxidation, and CO and CO_2 methanation correspond to independent evaluation using synthetic feeds. Post-reforming corresponds to actual post-reforming stream cleaning. SV was fixed in 6.5 ± 0.2 $L*g_{cat}^{-1}*min^{-1}$. 35

2.1.4 XPS spectra of Au 4f (a and b), Ce 3d (c and d), and O 1s (e and f) for reduced-oxidized (R-O) and used (U) samples of $AuCu/CeO_2$ catalysts. . . . 38

2.1.5 *Operando* DRIFTS spectra for CO-removal of a post-reforming stream on $Au_{1.0}Cu_{1.0}/Ce$ catalyst. Each spectrum was taken every 5 h t a total of 95 h. 40

2.1.6 (a) CO and H_2 conversion, and (b) CO_2 and CH_4 yield during the CO- removal of a post-reforming stream of a post-reforming stream over $Au_{1.0}Cu_{1.0}/Ce$ catalysts. Inlet stream: 7.8% H_2, 2.0% CO, 0.5% CO_2, 0.3% CH_4, 1.4% H_2O, 1.8% O_2, 6.8% N_2, and 79.4% Ar. Reaction conditions: SV=6.5 ± 2 $L*g_{cat}^{-1}*min^{-1}$; 50 mg of catalyst and 250 mg of inert quartz; 210 °C. Vertical lines show reactivation treatments every 24 h with an *in-situ* reduction with 8 mol% H_2/Ar (300 mL/min) at 300 °C for 1 h followed by degassing in Ar at 300 °C for 30 min. 42

2.2.1 Supports used in CO removal from syngas streams using CO-PROX, WGSR or CO-SMET reactions. 52

2.2.2 CO conversion obtained in the Cleanup reactor with supports (a,b) and supported 1 wt% Au–1 wt% Cu catalysts (c,d). Syngas feed: 7.8% H_2, 2.0% CO, 0.5% CO_2, 0.3% CH_4, 1.4% H_2O, 1.8% O_2, 6.8% N_2, and 79.4% Ar. Reaction conditions: The space velocity (SV) = 6.5 ± 0.2 $L/g_{cat}*min$ and 0.3 g of the catalytic bed. 57

2.2.3 H_2 yield obtained from a system that integrate the ethanol steam reforming (ESR) reactor and the cleanup reactor, where the CO removal is performed with bare supports (a,b) and supported 1 wt% Au–1 wt% Cu catalysts (c,d). Reaction conditions: SV = 6.5 ± 0.2 $L/g_{cat}*min$ and 0.3 g of the catalytic bed in both reactors. 58

2.2.4 Contribution of methanation in (**a**) the H_2 consumption and (**b**) CO conversion during the CO removal from an actual syngas. The shaded area conveys the trend of the experimental data. 61
2.2.5 Products distribution obtained from a system that integrate the ESR reactor and the cleanup reactor, where the CO removal is performed with (a) AuCu/CeO_2 and (b) AuCu/CeO_2-SiO_2 catalysts. Syngas feed: 7.8% H_2, 2.0% CO, 0.5% CO_2, 0.3% CH_4, 1.4% H_2O, 1.8% O_2, 6.8% N_2, and 79.4% Ar. Reaction conditions: The space velocity (SV) = 6.5 ± 0.2 L/g_{cat}*min and 0.3 g of the catalytic bed. Note: TOS = Time-on-stream. 62
2.2.6 H_2-temperature programmed reduction (TPR) profiles for Au–Cu catalysts supported on (a) single and (b) dual metal oxides. 63
2.2.7 CO conversion rate normalized by the surface area of the Au–Cu catalysts supported in (a) single and (b) dual metal oxides. 65
2.2.8 *In-situ* diffuse reflectance infrared Fourier transform spectroscopy (DRIFTS) of CO adsorption of (a, b) bare supports and (c, d) supported Au–Cu catalysts. 69
2.3.1 (a) CO conversion, (b) CO_2 yield, (c) H_2 loss and (d) CH_4 yield during the CO removal of a syngas stream over 1wt%Au-1wt%Cu/CeO_2 catalysts with different nano-shaped CeO_2: polyhedra (P), rods (R), cubes (C), and a blank (B) included for comparison. Syngas composition: 8.5% H_2, 2.2% CO, 0.5% CO_2, 0.3% CH_4, 1.5% H_2O and Ar balance. $\lambda = 1.8$. 82
2.3.2 XPS spectra of (a) Au $4f_{5/2}$ and $4f_{7/2}$, (b) Cu $2p_{3/2}$, (c) Ce $3d_{3/2}$ and $3d_{5/2}$, and (d) O 1s for AC samples of the 1wt%Au-1wt%Cu/CeO_2 catalysts with different nano-shaped CeO_2 (polyhedra (P), rods (R), cubes (C), and a blank (B)). 84
2.3.3 TEM images of 1wt%Au-1wt%Cu catalysts supported over CeO_2 with different morphologies: (a) polyhedra, (b) rods, (c) cubes and (d) blank. 86
2.3.4 Normalization of (a) CO conversion rate and (b) CO_2-formation rate with respect to the surface area on the CO removal from an actual syngas streams over 1wt%Au-1wt%Cu/CeO_2 catalysts with several nano-shapes: polyhedra (P), rods (R) and cubes (C); blank (B) is included as comparison. 88
2.3.5 DRIFTS spectra for CO adsorption on (a) supports and (b) 1wt%Au-1wt%Cu catalysts supported on several CeO_2 nanoshapes: polyhedra (P), rods (R), cubes (C) and blank (B). 90
2.3.6 X-ray diffraction patterns of (a) CeO_2 supports, (b) AC samples of AuCu/CeO_2 catalysts, (c) spent AuCu/CeO_2 catalysts after the activity tests and (d) spent AuCu/CeO_2 catalysts after the stability tests. Suffix indicate the kind of nano-shaped CeO_2: polyhedra (P), rods (R), cubes (C) and blank (B). . . . 91
2.3.7 Normalized Raman spectra of 1wt%Au-1wt%Cu supported over CeO_2 with different morphologies: polyhedra (P), rods (R), cubes (C) and blank (B). AC catalysts (AC), spent samples after the activity tests (U) and used after the stability tests (S). 92

2.3.8 Stability of 1 wt%Au-1wt%Cu/CeO_2 catalyst supported on different nano-shaped CeO_2 (polyhedra (P), rods (R) and cubes (C); blank (B) is included for comparison) for CO removal of a syngas stream: (a) CO conversion, (b) CO_2 yield, (c) H_2 loss and (d) CH_4 yield. Inlet stream: 7.8% H_2, 2.0% CO, 0.5% CO_2, 0.3% CH_4, 1.4% H_2O, 1.8% O_2, 6.8% N_2 and 79.4% Ar. Reaction conditions: 210 °C, SV=6.5 ± 0.2 L/g_{cat} min; 0.050 g of catalyst and 0.250 g of inert quartz. 95
3.1.1 (a) Ethanol conversion, (b) H_2 yield, (c) CH_4/H_2 molar ratio and (d) H_2/CO molar ratio obtained in the ESR over washcoated monoliths (solid lines) and powder catalysts (dashed lines) of RhPt/CeO_2-SiO_2, using synthetic-bioethanol. Reaction conditions: 5.0 L Ar/mL bioethanol inlet and S/E=3. CP: fresh powder catalyst, DS: dried slurry of catalyst, M-X: Monolith, where X is the washcoat loading in g_{cat}/cm^3. 107
3.1.2 (a) Ethanol conversion, (b) H_2 yield, (c) CH_4/H_2 molar ratio and (d) H_2/CO molar ratio obtained in the ESR over monolith washcoated with RhPt/CeO_2-SiO_2 catalysts, using synthetic-bioethanol and several carrier gas/bioethanol ratios. Reaction conditions: 0.12 g_{cat}/cm^3 of washcoat loading and S/E=3. . 110
3.1.3 Syngas composition obtained in the ESR over a monolith washcoated with RhPt/CeO_2-SiO_2, using (a) synthetic bioethanol and (b) actual bioethanol obtaining from glucose patrons. Reaction conditions: 1.6 L Ar/mL bioethanol inlet, 0.12 g_{cat}/cm^3 of washcoat loading and S/E=3. 112
3.1.4 DRIFTS spectra of spent samples of monoliths washcoated with RhPt/CeO_2-SiO_2 catalysts evaluated in stability tests. Spectra of removed washcoating from reduced monolith was used as background. 113
3.1.5 Syngas composition obtained in the ESR over a monolith washcoated with RhPt/CeO_2-SiO_2, using actual bioethanol obtaining from sugarcane press-mud (SPM-bioethanol). Reaction conditions: 1.6 L Ar/mL bioethanol inlet, 0.12 g_{cat}/cm^3 of washcoat loading and S/E=3. 114
3.1.6 Levelized costs of H_2 production from several technologies. Values were obtained from several references and updated to present value at January 2020. 116
3.2.1 Strategies to remove CO in a bioethanol fuel processor unit according to the type of fuel cell used. HT-WGS: high temperature water gas shift, LH-WGS: low temperature water gas shift, CO-SMET: CO selective methanation, CO-PROX: CO preferential oxidation, PSA: pressure swing adsorption. 123
3.2.2 Cost of (a) metal oxides and (b) AuCu based catalysts commonly used for CO removal in a B-FPU. Values obtained from Sigma Aldrich (www.sigmaaldrich.com), Merck (www.merckmillipore.com), Fisher Scientific (www.fishersci.com) and Alfa Aesar (www.alfa.com) in February 2020 for presentations between 50-1000 g and purity > 99 %. 125
3.2.3 CO conversion obtained over (a) bare supports and (b) supported AuCu catalysts. CeO_2-SiO_2 supports were labeled as CeSi-X, where X indicates the SiO_2 percent content (X = 25, 50 and 75 mol% SiO_2). Syngas feed: H_2 (19.9±0.3 mol%), CO (6.3±0.1 mol%), CO_2 (5.2±0.5 mol%), O_2 (5.6±0.3 mol%), H_2O (7.8±0.2 mol%), and N_2 (55.2±0.6 mol%). Reaction conditions: SV of 5.6 ± 0.3 L/g_{cat}*min and 0.35 g of the catalytic bed. 130

3.2.4 (a) UV-vis spectra for activated samples of Au-Cu catalysts. (b) Correlation of the lattice parameter and the average crystallite size of CeO_2 obtained by a Rietveld refinement of XRD patterns of Au-Cu catalysts. CeO_2-SiO_2 supports were labeled as CeSi-X, where X indicates the SiO_2 percent content (X = 25, 50 and 75 mol% SiO_2). 131
3.2.5 XPS spectra for (a) Au 4f, (b) Cu $2p_{3/2}$ and (c) Ce 3d in activated samples of AuCu catalysts supported on CeO_2-SiO_2 with several SiO_2 loadings. CeO_2-SiO_2 supports were labeled as CeSi-X, where X indicates the SiO_2 percent content (X = 25, 50 and 75 mol% SiO_2). 132
3.2.6 Raman spectra for (a) activated and (b) used samples of supported AuCu catalysts. CeO_2-SiO_2 supports were labeled as CeSi-X, where X indicates the SiO_2 percent content (X = 25, 50 and 75 mol% SiO_2). 134
3.2.7 Conversion of (a) CO and (b) H_2 obtained in the CO removal from a syngas over powder catalysts and monoliths washcoated with AuCu/Ce and AuCu/CeSi-75 samples. Suffixes P: powder and M: monolith. Syngas feed: H_2 (19.9±0.3 mol%), CO (6.3±0.1 mol%), CO_2 (5.2±0.5 mol%), O_2 (5.6±0.3 mol%), H_2O (7.8±0.2 mol%), and N_2 (55.2±0.6 mol%). Reaction conditions: SV = 5.6 ± 0.3 L/g_{cat}*min. 137
3.2.8 Temperature profiles for cross section of (a) a monolith washcoated with AuCu/Ce catalysts operating at 200 °C, (b) a monolith washcoated with AuCu/CeSi-75 catalysts operating at 200 °C, (c) a monolith washcoated with AuCu/Ce catalysts operating at 300 °C and (d) a monolith washcoated with AuCu/CeSi-75 catalysts operating at 300 °C. 138
3.2.9 Molar concentration of CO at several temperatures vs. channel length of monoliths washcoated with (a) AuCu/Ce and (b) AuCu/CeSi-75 catalysts. . 139
3.2.10 (a and b) Conversion of CO and H_2 and their corresponding product distribution (c and d) obtained in the CO removal over monoliths washcoated with AuCu/Ce and AuCu/CeSi-75 catalysts. Syngas feed: H_2 (19.9±0.3 mol%), CO (6.3±0.1 mol%), CO_2 (5.2±0.5 mol%), O_2 (5.6±0.3 mol%), H_2O (7.8±0.2 mol%), and N_2 (55.2±0.6 mol%). Reaction conditions: 220 °C, 3.3 g_{cat}/cm^2. 140
4.2.1 Diagram of the B-FPU developed in the project to H_2 production from actual bioethanol. 149
4.2.2 Cost distribution for (a) equipment and (b) modules of the B-FPU developed 153
SM.1 Stability during the steam reforming of ethanol over Rh-Pt/CeO_2-SiO_2 catalyst: product distribution of H_2, CO, CO_2, and CH_4 as a function of time-on-stream (TOS) on RhPt/CeO_2-SiO_2. Reaction conditions: 6.4 ± 0.2 L*g_{cat}-1*min^{-1} of SV, 50 mg of catalyst and 250 mg of inert quartz, feed was ethanol, water, and Ar with 1.8, 5.4, and 92.8 % molar, respectively. 159
SM.2 Evaluation of the effect of the inlet O_2/CO molar ratio on the CO removal: (a) CO conversion, (b) CO_2 yield, (c) H_2 conversion, and (d) CH_4 yield in the CO removal of a post-reforming stream on 1.0%Au-1.0%Cu/CeO_2 catalyst with different O_2/CO molar ratios (0.7, 0.9, 1.0, and 1.1). Reaction conditions: 8.5% H_2, 2.2% CO, 0.6% CO_2, 0.3% CH_4, 1.5% H_2O, and 86.9% Ar. A SV of 6.5 ± 0.2 L*g_{cat}^{-1}*min^{-1}, 50 mg of catalyst and 250 mg of inert quartz. . . . 160

SM.3 Effect of water presence on (a) CO and H_2 conversion, (b) CO_2 and CH_4 yield in the CO removal of a post-reforming stream on $Au_{1.0}Cu_{1.0}/Ce$ catalyst. Reaction conditions: A SV of 6.5 ± 0.2 $L*g_{cat}^{-1}*min^{-1}$, 50 mg of catalyst and 250 mg of inert quartz. 161
SM.4 Thermodynamic equilibrium calculations for the main CO-removal reactions on (a) CO conversion, (b) CO_2 yield, (c) H_2 lost, and (d) CH_4 yield. Data were obtained using a Gibbs reactor in Aspen Plus V9.0 (Aspen Tech, Burlington, MA, USA, 2016). The inlet of reactor was the feed composition describe in Table SM.1. Thermodynamic method = NRTL-SK. 162
SM.5 TEM images of reduced-oxidized (a) $Au_{0.5}Cu_{1.5}/Ce$, (b) $Au_{1.0}Cu_{1.0}/Ce$, (c) $Au_{1.5}Cu_{0.5}/Ce$ and (d) $Au_{2.0}/Ce$ catalysts, and (e-h) particle size distribution histograms for reduced-oxidized and used $AuCu/CeO_2$ catalysts. 163
SM.6 Reactivation treatments for Au-Cu/CeO_2 catalysts during the CO-removal of a post-reforming stream: (a) CO and H_2 conversion, (b) CO_2 and CH_4 yield as a function of time-of-stream, with several reactivation treatments, in the CO removal of a post-reforming stream on 1.0%Au-1.0%Cu/CeO_2 catalyst. Reaction conditions: 8.1% H_2, 2.1% CO, 0.6% CO_2, 0.3% CH_4, 1.4% H_2O, 83.1% Ar, 1.3% O_2, and 3.1% N_2. A SV of 6.5 ± 2 $L*g_{cat}^{-1}*min^{-1}$, 50 mg of catalyst and 250 mg of inert quartz. Vertical lines show reactivation treatments described in Table SM.1. 164
SM.7 (a and b) CO_2 and CH_4 (c and d) production in the CO-Cleanup reactor with simple and dual supports. Syngas composition: 8.4% H_2, 2.2% CO, 0.6% CO_2, 0.3% CH_4, 1.6% H_2O and Ar. λ=1.8. Reaction conditions: SV=6.5 ± 0.2 Lg_{cat}-$1min^{-1}$; 0.050 g of catalyst and 0.250 g of inert quartz. 165
SM.8 (a and b) CO_2 and CH_4 (c and d) production in the CO-Cleanup reactor with Au-Cu catalysts supported on simple and dual supports. Syngas composition: 8.4% H_2, 2.2% CO, 0.6% CO_2, 0.3% CH_4, 1.6% H_2O and Ar. λ=1.8. Reaction conditions: SV=6.5 ± 0.2 $Lg_{cat}^{-1}min^{-1}$; 0.050 g of catalyst and 0.250 g of inert quartz. 166
SM.9 H_2-TPR profiles of bare supports evaluated in the CO-removal from an actual syngas. 167
SM.10 TEM micrographs of CeO_2 supports with different morphology. Suffix corresponds to the type of nano-shaped CeO_2: polyhedra (P), rods (R), cubes (C) and blank (B). 168
SM.11 TEM micrographs of activated 1wt%Au-1wt%Cu/CeO_2 catalysts with different CeO_2 morphology. Suffix corresponds to the type of nano-shaped CeO_2: polyhedra (P), rods (R), cubes (C) and blank (B). 169
SM.12 EDS spectra of activated 1wt%Au-1wt%Cu/CeO_2 catalysts with different CeO_2 morphology. Suffix corresponds to the type of nano-shaped CeO_2: polyhedra (P), rods (R), cubes (C) and blank (B). 170
SM.13 Stability of RhPt/CeO_2-SiO_2 coating on a monolith with a 0.12 g_{cat}/cm^3 washcoated loading evaluated by (a) ultrasonic (pulses of 10 s with amplitude of 40 %) and (b) controlled atmospheres of water (1.3 L/min) and N_2 (2 L/min). 171

SM.18 SEM micrographs for monolith with a 0.12 g_{cat}/cm^3 washcoated loading: (a) fresh monolith channels, (b) fresh monolith walls, (c) fresh wash-coating thickness and (d) spent monolith walls in stability test with synthetic bioethanol. Images were obtained in a JSM 6490LV microscope (Jeol Geo Solutions, USA). Previously, samples were coated with gold using a sputter coating machine. . 172
SM.19 HRTEM micrographs and particle size distribution histograms for CeO_2 bare support before (a and b) and after (c and d) calcination at 500 °C for 2 h. 173
SM.20 Conversion of (a) CO and (b) H_2 in the CO removal from a syngas over several catalysts of AuCu/CeO_2-SiO_2 (SiO_2 percent content of 50 mol% was fixed in all samples) prepared by methods described in Table S-1. Syngas feed: H_2 (19.9±0.3 mol%), CO (6.3±0.1 mol%), CO_2 (5.2±0.5 mol%), O_2 (5.6±0.3 mol%), H_2O (7.8±0.2 mol%) and N_2 (55.2±0.6 mol%). Reaction conditions: SV of 5.6 ± 0.3 L/g_{cat}*min and 0.35 g of the catalytic bed. 174
SM.21 XRD profiles of CeO_2 for activated samples of AuCu catalysts. CeO_2-SiO_2 supports were labeled as CeSi-X, where X indicates the SiO2 percent content (X = 0, 25, 50 and 75 mol% of SiO_2). 175
SM.22 Percentage of catalyst weight loss in the stability tests of the monolith coating by (a) ultrasound and (b) thermal shock. 175
SM.23 CFD-predicted and experimental values for the molar flow of CO, H_2, CO_2 and O_2 in the outlet stream of reactor monoliths washcoated with (a and b) AuCu/Ce and (c and d) AuCu/CeSi-75 catalysts. CFD model was carried out in COMSOL Multiphysics software (5.5 version). 176
SM.24 Parity plots for the reactor monoliths washcoated with (a) AuCu/Ce and (b) AuCu/CeSi-75 catalysts. CFD model was carried out in COMSOL Multiphysics software (5.5 version). Two types of experimental data are included: data used to perform the non-linear regression of the CFD model ("experimental value") and data used to confirm the effectiveness of the model to predict fluxes ("validation point"). 177
SM.25 (a) Changes in enthalpy during the ESR and (b) net power production of the system presented in Figure SM.22. Response surface: Cubic model, R^2 >0.85, Adjusted R^2 >0.85 and Lack of Fit >>3 (non-significant). RhPt/CeO_2-SiO_2 catalysts were evaluated with actual bioethanol (i.e., obtained from fermentation of glucose patrons) with different S/E ratios (i.e., 3, 4, and 5). The results of catalytic tests were used to carry out an energy analysis of a B-FPU, using the methodology described in. The energy balances obtained from the simulated B-FPU were used to make response surfaces in the Design Expert ® software (11 version, USA). 178
SM.26 Bioethanol fuel processor unit simulated in Aspen Plus (11 version, USA). IC: heat exchanger, BR: bioethanol reformer, M: mixer, CO-RV: unit to CO removal, S: separator to remove H_2O or CO_2, HT-FC: high temperature fuel cell unit. 179

List of Tables

1.1 Recent news related to H_2 technology. . . . 13
1.2 Incentives, Law & Policy, and programs associated with H_2 technology. . . . 15
2.1.1 Chemical reactions involved in the CO-removal of post-reforming streams . . 28
2.1.2 Textural and morphological characteristics of AuCu/Ce catalysts 37
2.1.3 Comparison of various catalytic systems for CO removal 44
2.2.1 Minimum concentration of CO obtained in syngas, the apparent active metal dispersion (H/M ratio), surface area, OSC, and OSCC of Au–Cu catalysts supported on single and dual supports. . . . 59
2.2.2 Comparison of various catalytic systems for the CO removal using Au–Cu catalysts. . . . 59
2.2.3 Weight loss of Au–Cu catalysts supported on single and dual supports evaluated in CO removal from an actual syngas. . . . 67
2.3.1 Reaction network for the CO removal from syngas streams 77
2.3.2 Element abundance on catalyst surface, particle size and surface area of the 1wt%Au-1wt%Cu/CeO_2 catalysts with different nano-shaped CeO_2 (polyhedra (P), rods (R), cubes (C), and a blank (B)). . . . 85
2.3.3 TGA, XRD and Raman characterization of 1wt%Au-1wt%Cu/CeO_2 catalysts with different nano-shaped CeO_2 (polyhedra (P), rods (R), cubes (C), and a blank (B)). . . . 89
3.1.1 Composition of actual bioethanol samples 104
3.1.2 Comparison of various structured catalysts for ESR 115
3.2.1 Governing equations, kinetic model and reaction network involved in CFD simulations. . . . 128
3.2.2 Price of catalysts and the minimum CO concentration obtained in the outlet stream of the reactor. . . . 129
3.2.3 Atomic surface content, Auger parameter, Ce^{3+}/Ce^{4+} ratio, TO/F_{2g} index and BET surface area of AuCu/CeO_2-SiO_2 catalysts 132
3.2.4 Comparison of several structured catalysts for CO removal. 136
4.2.1 Description of the main streams of the prototype shown in Figure 4.2.1. . . . 148
4.2.2 Specifications for syngas production in the ethanol reformer 150
4.2.3 Kinetic parameters for syngas production from ethanol steam reforming over RhPt/CeO_2-SiO_2 catalyst. . . . 150
4.2.4 Specifications for CO removal from an actual syngas 151
4.2.5 Kinetic parameters for CO removal from syngas over AuCu/CeO_2 and AuCu/CeO_2-SiO_2 (Si/Ce=3) catalysts. . . . 152
SM.1 Reaction conditions to evaluate the contribution of the main reactions involved in CO removal 180
SM.2 Reactivation treatment for $Au_{1.0}Cu_{1.0}/CeO_2$ catalyst. . . . 181
SM.3 Results of regression analysis and ANOVA for model of the experimental data for activity and yield of AuCu/CeO_2 catalysts in CO-removal of post-reforming stream. . . . 182
SM.4 Revised papers for the selection of supports evaluated in the CO-removal. . . . 183

SM.5 Surface area, OSC, OSCC and weight loss of Au–Cu catalysts supported on single and dual supports. 188
SM.6 Carbon balance for activity tests. 189
SM.7 Actual loading and surface abundance of Au and Cu on AuCu/CeO_2 catalysts. 189
SM.8 Carbon deposition and crystal size of AuCu/CeO_2 catalysts. 190
SM.9 Methods evaluated for the synthesis of AuCu catalysts supported on a dual metal oxide of CeO_2-SiO_2. 191
SM.10 Assumptions for the CFD model in COMSOL Multiphysics software . . . 193
SM.11 Cost of precursors and yield for the synthesis of AuCu catalysts. 194
SM.12 Kinetic parameters for CO removal from syngas over AuCu/Ce and AuCu/CeSi-75 catalysts obtained in COMSOL Multiphysics software. 194

Abstract

A lab-scale prototype of a bioethanol fuel processor unit to produce H_2 suitable for high CO-tolerant fuel cells was developed in this Thesis. To this end, a system that couples bioethanol reforming to produce syngas and the CO removal from the syngas produced in the reformer was designed. Initially, the system was evaluated using powder catalysts in both modules of the fuel processor unit (i.e., the bioethanol reformer and the reactor for CO removal), focusing on selecting an appropriate AuCu-based catalyst to carry out CO removal from an actual syngas in a single catalytic unit. The effect of the Au/Cu ratio and the support on the catalytic performance in CO removal was studied. It was found that an AuCu catalyst with a weight ratio of Au/Cu = 1 supported on polyhedral nanoparticles of CeO_2 favors a balance between activity, selectivity and stability, ensuring a CO conversion $> 96\%$. Afterwards, catalysts structured on monoliths were evaluated for each module of the fuel processor unit. So, syngas was produced over monoliths washcoated with $RhPt/CeO_2$-SiO_2, which were evaluated with actual bioethanol (i.e., obtained from sugarcane press). The bioethanol reformer ensured a continuous production for 120 h of a syngas with an H_2 content $> 60\%$. Similarly, monoliths washcoated with AuCu catalysts were used for the CO removal, seeking to develop a compact and economical system to connect to the bioethanol reformer. It was identified that a monolith coated with an AuCu catalyst supported on a mixed oxide of CeO_2-SiO_2 (with molar ratio Si/Ce = 3) favors the production of a suitable gas (i.e., with a concentration of CO $< 5\%$) to be fed to a high temperature proton exchange membrane fuel cell. Finally, the results of the catalytic evaluations were used as a starting point to build a scaled prototype to produce H_2 from bioethanol obtained from residual biomass. The prototype had a cost of US$53,000, where 24% corresponds to the bioethanol reformer, 31% correspond to the unit to remove the CO, and the rest was ascribed to auxiliary equipment. The results of This thesis seek to contribute to the implementation of unconventional technologies associated with H_2 in the Colombian agroindustry sector.

1 Overview

1.1 Introduction

Energy availability is a key pillar to ensure economic development and human wellbeing in modern societies. However, negative effects on the environment and public health associated with the use of fossil fuels demand a rapid substitution of current energy resources. Thus, the concept of sustainability has gained relevance in the energy sector, becoming the starting point for designing new energy models. Indeed, according to Our World Data (https://ourworldindata.org), worldwide investment in renewable energies technologies exceeds US$ 280 billion. However, sustainability involves several areas of knowledge, including technical, environmental, economic and social considerations [1], and its application in emerging technologies requires a complex interdisciplinary collaboration. Hence, sustainable energy production is considered a manifestation of "collective intelligence" in human societies [2].

Power and heat production in fuel cells (FC) powered with hydrogen (H_2) has the potential to become a sustainable energy model due to the environmental and commercial benefits of its implementation [3]. H_2 has a high energy density (142 kJ/g) and can be obtained from residual biomass from agroindustry [4]. Furthermore, FC fed with H_2 do not generate pollution because water is the only chemical product [5], and they can be integrated into a variety of applications, including homes, commercial buildings, vehicles and electronic devices [6]. Consequently, the H_2-based technologies have gained ground in the last years, attracting the attention of several media, as shown in Table 1.1. In addition, tax incentives, Law & Policy changes in policies to promote clean energy, development of macro programs, and creation of specialized institutions are common strategies of governments to support H_2-based technologies, as shown in Table 1.2. Likewise, according to Cleantech group (www.cleantech.com), in 2019 investments in H_2 technologies exceeded US$ 580 million, being USA and China the main shareholders. Thus, the outlook of H_2 demand for new applications is promising. Nonetheless, there are still challenges that need to be addressed to establish sustainable H_2-based energy models [7].

Table 1.1. Recent news related to H_2 technology.

News	Description	Country	Organizations involved	Newspaper/ Resource	Autor
First came the hydrogen cars. Now, the refilling stations	Shows the increasing in H_2 electric cars market and the refilling stations in California	USA	Honda and Toyota	The New York Times	Neal E. Boudette; May 18th, 2017

A hydrogen-powered bus goes to Washington	Description of a bus fueled with H_2 that started operation in Washington D.C.	USA	Toyota and Stark Area Regional Transit Authority (SARTA)	The Washington Post	Fredrick Kunkle; April 12th, 2019
Why the future will be powered by hydrogen: Five key facts	Five key facts are presented to show why H_2 technology as a promising energy solution.	Japan	Several	The Wall Street Journal	Henry Bewicke; September 16th, 2019
Next stop, hydrogen-powered trains	A discussion about Hydroflex, which is a prototype of H_2 train at Long Marston with an autonomy of 75 miles.	UK	University of Birmingham and British rail company Porterbrook	BBC	Allison Hirschlag; February 27th, 2020
Powered by hydrogen, Hyundai's trucks aim to conquer the Swiss Alps	H_2-powered 18-tonne trucks are being tested in Switzerland	Switzerland	Hyundai Motor Company	Reuters	Vera Eckert, John Revill; February 28th, 2020
Dutch test hydrogen train as EU alliance set to launch	An overview of H_2 train technology in the Netherlands. In 2018, a similar technology was tested in Germany managing to the first commercial train fueled with H_2.	Netherlands and Germany	Alstom corporation	Euractiv	Sam Morgan; March 9th, 2020
Japan's MHPS wins US order for hydrogen-fired thermal power system	A report of a thermal power facility that uses a fuel mix of natural gas and H_2 to electricity production.	Japan	Mitsubishi Heavy Industries and Hitachi.	Asian Review	Naoki Watanabe; Nikkei, March 15th, 2020
Graforce develops technology to produce hydrogen from manure	An explanation of the use of an unconventional method called plasmalysis to H_2 production from animal and human excrements.	Germany	Graforce company	H_2 view	Joanna Sampson; March 17th, 2020

Is hydrogen the solution to net-zero home heating?	A proposal to replace natural gas by H_2 to heating homes.	UK	Worcester Bosch	The Guardian	Stuart Clark; March 21st, 2020
Toyota plans to develop fuel cell truck with Hino unit	A new electrical motor based on heavy-duty fuel-cell fueled with H_2 for trucks.	Japan	Toyota	US news	Naomi Tajitsu; March 23rd, 2020

Table 1.2. Incentives, Law & Policy, and programs associated with H_2 technology.

Country/ region	Incentives, Law & Policy	Programs and institutions	Resource
United States of America	Up to 50% of the cost to acquire zero emission vehicles	Clean cities coalition network	https://afdc.energy.gov
	US$ 0.50 of tax credit per gallon of liquefied H_2	Clean construction and agriculture program	
	Alternative fuel tax exemption, including H_2	Congestion mitigation and air quality (CMAQ) Improvement program	www.energy.gov
	A tax credit of up to US$ 8,000 for purchase fuel cell motor vehicles	State Energy Program (SEP) funding	cleancities.energy.gov
	Inclusion of H_2 as alternative fuel (Reference 42 code 13211 and Reference 26 code 6426).	Department of Energy (DOE) Hydrogen Program	www.hydrogen.energy.gov
	National corridors for alternative fuels (Public law 114-94)		
	Acquisition of alternative fuels Fleets (Reference 42, codes 13257, 13251, 13263 and 13212)		

Europe	France and the Netherlands have tax exemptions for the use of H_2 Most european countries have tax incentives for purchase fuel cell electric car Spain, Germany, Italy, Belgium, France and England have incentives for use of H_2 in gas grid	Hydrogen Strategy for a climate neutral Europe HyLAW: Identification of legal rules and administrative processes Hydrogen mobility Europe (H2ME1 and 2) programs Fuel cells and hydrogen joint undertaking (FCH JU) programs Hycarus: H_2 for aircraft FC powered RBS program: Fuel cells systems for communications CLEARgen DEMO program: system based on blue H_2	https://hydrogeneurope.eu www.fchea.org/intransition/2019/6/24/european - union http://hycarus.eu http://fcpoweredrbs.eu www.cleargen.eu
Asia	Japan is to offer 10% in tax reduction for companies that develop HH_2 fuel cell technologies. Also, there are subsidies ($\sim$ 25%) for purchase fuel cell electric car China has subsidies and tax exemptions for purchase fuel cell electric car costing less than US$ 42,000. Arab Emirates provides benefits in tax and fees for the use of green energy, including HH_2. South Korea has a subvention of US$ 3,400 on each purchase of fuel cell electric cars	Fukushima hydrogen energy research field (FH2R, Japan) National Center of Hydrogen Innovation (China) King Salman Park (Saudi Arabia) World's largest liquid hydrogen factory (Korea)	www.japan.go.jp/tomodachi/2019/autumn2019/fukushima. html https://omrania.com/project/king-salman-park/ https://pulsenews.co.kr

Latin America	Chile, Argentina, Mexico and Colombia (ley 1964 de 2019) offer tax exemptions for electric car, fuel cell electric motor and hybrid cars	Programa nacional de hidrógeno verde (Chile)	https://energia.gob.cl
		Instituto de tecnologías del hidrógeno y energías sostenibles (ITHES, Argentina)	https://ithes-uba.conicet.gov.ar
		Plan nacional de hidrógeno (PNH, México)	https://petroquimex.com/plan-nacional-de-hidrogeno-alternativa-energetica
		Convocatoria 879 para energía sostenible y su aporte a la planeación minero-energética (Colombia)	https://minciencias.gov.co/convocatorias/

Current H_2 technology is based on consecutive steps that are addressed independently: (i) production, (ii) purification, (iii) distribution, (iv) storage, and (v) use [8]. This kind of models are designed for centralized power production, which requires a large production plant and interconnected distribution systems. The centralized production of H_2 from natural gas and oil is standardized, achieving annually more than 75 million metric tons [9] that are mainly destined to the petrochemical industry and the production of oils and fertilizers. Nevertheless, the use of non-renewable resources and the technical challenges related to delivery and storage of H_2 [9,10] impacts the sustainability of the technology, restricting its use in mobile applications or in remote places that are not connected to the distribution network. An alternative is to produce H_2 in a decentralized way (called on-site production [9]), where the H_2 is produced in lesser amounts in compact units assembled close to the end-use devices. Besides, H_2 on-site production can be integrated with several renewable resources depending on the area where the technology is implemented.

Emerging H_2-based technologies for centralized [11] and decentralized [12] power production is coupled to solar and wind systems. However, the implementation of these systems in developing countries is still scarce [13]. Likewise, as the use of a single type of energy resource may not be enough to supply the total energy demand to continue with the economic development of Latin America [13] energy sources must be diversified using the alternative resources available in each region. Therefore, a combined strategy between solar, wind and biomass energy could be the key to the development of sustainable energy models in Latin America [14]. Nonetheless, biomass presents important challenges to develop H_2-based technologies. Firstly, government policies in Latin America for the energy production from biomass are mainly focused on obtaining biofuels as ethanol and diesel [15], which do not effectively reduce the pollution [16], leaving cleaner alternatives such as the FC in the background. Secondly, H_2 obtained from biomass requires complex purification processes to be used in FC [17], demanding a rigorous engineering design. Finally, the investment for the implementation of H_2-based technologies is high because they are not massively widespread [18]. Despite this, technical, economic and environmental evaluations [3,5,7,19–21] show that it is possible to develop sustainable energy models based on H_2 obtained from biomass if some aspects are carefully managed.

Recently, the research group in Energies, Materials and Environment (GEMA) of Univer-

sidad de La Sabana and the research group in Environmental Catalysis (GCA) of Universidad de Antioquia have worked on the development of a decentralized H_2-based technology to obtain power, using residual biomass from the Colombian agroindustry. The framework project includes economic, social, environmental and technical aspects, which involve the integration and cooperation with several organizations from both the academic and productive sectors, as shown in Figure 1.1.1. The core of this technology is a bioethanol fuel processing unit (B-FPU) that is a device where the H_2 is produced and purified sequentially using catalytic processes.

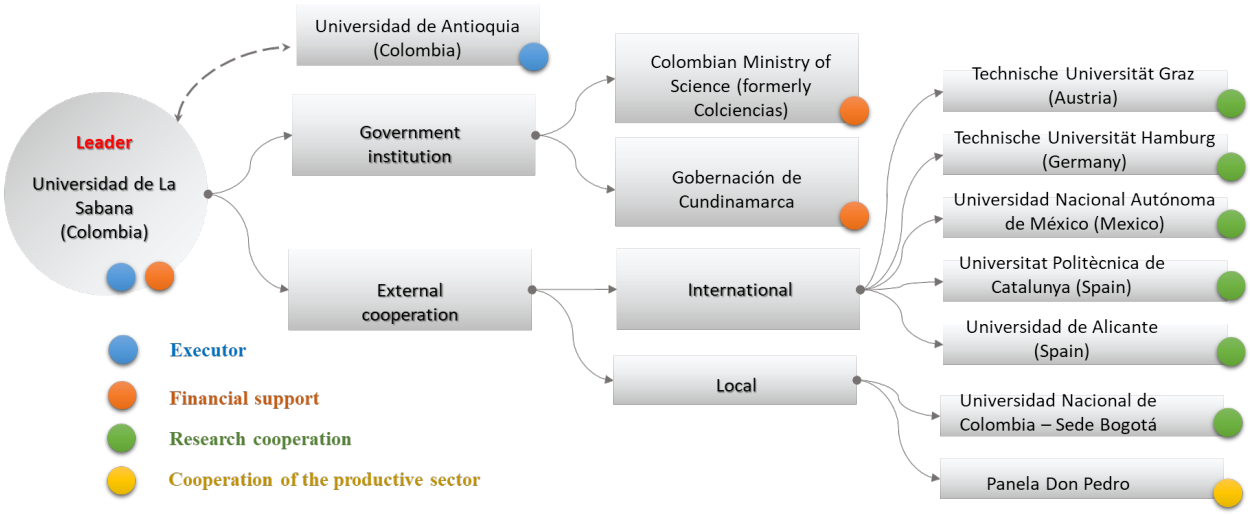

Figure 1.1.1. Cooperation network in the framework project for the power and heat production from residual biomass that involves a H_2-based technology.

This document details the development of a lab-scale prototype of a B-FPU to produce H2 adequate for FC. The project builds on the previous work conducted by the research groups [22–24], namely, an optimized RhPt/CeO_2-SiO_2 powder catalyst for SRE. The previous optimization of the catalyst for the SRE included (i) the selection of the CeO2 support among other options such as ZrO_2 and La_2 O_3 [22], (ii) the study of the effect of the Rh/Pt ratio on the catalytic performance [23] and (iii) the evaluation of the inclusion of SiO_2 in the RhPt/CeO_2 catalyst [24]. Thus, the Thesis begins with the evaluation of the CO elimination from an actual syngas coming from RhPt/CeO_2-SiO_2-based reactor, using only one catalytic system based on AuCu/CeO_2 powder catalyst. The use of a single catalytic reactor to carry out the CO removal (i.e., CO elimination by simultaneous preferential oxidation of CO, water gas shift and methanation) could contribute to reduce the size and complexity of B-FPU. In particular, an optimum Au:Cu weight ratio was found (Chapter 2/Section 1), and the use of mixed supports was studied as a means to reduce deactivation resulting from structural changes of the support (Chapter 2/Section 2). In addition, the nanoshape of the support was found to play a crucial role in the performance of the system (Chapter 2/Section 3). Once the powder catalysts were optimized, the Thesis focused on the monolith reactors. Therefore, the performance of the RhPt/CeO_2-SiO_2 and AuCu/CeO_2 catalysts washcoated on cordierite monoliths was assessed for SRE (Chapter 3/Section 1) and CO removal (Chapter 3/Section 2) Finally, the lab-scale prototype is described and a brief economical assessment of its use

into a sugarcane press-mud process (locally known as Panela) is presented (Chapter 4).

Consequently, the objectives of the Thesis are the following.

1.2 Objectives

1.2.1 General

Develop a stable, active and selective monoliths-based, lab-scale prototype of a catalytic system to produce H_2 suitable for fuel cells, coupling the steam reforming of bioethanol and the CO removal.

1.2.2 Specific

- ✓ Evaluate the catalytic performance of Au-Cu catalysts (powder) in the CO removal from actual syngas streams.
- ✓ Evaluate monoliths washcoated with a RhPt/CeO_2-SiO_2 in the syngas production from bioethanol reforming.
- ✓ Evaluate monoliths washcoated with AuCu catalysts in the CO removal from syngas streams.
- ✓ Perform a preliminary economic analysis of the H_2 production in a bioethanol fuel processor unit to assess the potential of developed prototype.

1.3 Document structure

The development of a lab-scale prototype to produce H_2 suitable for fuel cells was divided into 3 chapters. The results of the powder-based catalytic system are presented in the Chapter 2, which is divided into three sections, each presented as a paper. This chapter corresponds to the first specific objective of the Thesis.

- ✓ **Section 2-1:** This section presents a description of the proposed catalytic system to produce H_2 suitable for fuel cells. The study focuses on the evaluation of CO removal from an actual syngas using a powder catalyst of AuCu/CeO_2 with several Au/Cu ratios.
  This section corresponds to an article published in the *International Journal of Hydrogen Energy, (2018), 43, 17216 - 17229.* - DOI:10.1016/j.ijhydene.2018.07.139 Raw and processed data of this section can be downloaded from https://data.mendeley.com/datasets/scwxcw4gcz/1 - DOI:10.17632/scwxcw4gcz.1
- ✓ **Section 2-2**: This section presents a catalytic screening of several metal oxides as supports for an Au–Cu based catalytic system for the CO removal from an actual syngas. The study aims to identify alternatives to overcome the shortcomings of the AuCu/CeO_2 catalyst identified in section 2-1.
  This section corresponds to an article published in *Catalysts, (2019) 9, 10, 852–877.* - DOI:10.3390/catal9100852

Raw and processed data of this section can be downloaded from: https://data.mendeley.com/datasets/6pxcn5k3sx/1 - DOI: 10.17632/6pxcn5k3sx.1

✓ **Section 2-3**: This section presents a modification in the CeO_2 morphology as an alternative strategy to improve the catalytic performance of $AuCu/CeO_2$. Thus, the performance of several nanostructures of CeO_2 as supports of an Au-Cu catalyst for CO removal is shown.
This section corresponds to an article published in *Applied Catalysis A: General, (2020) 598, 117568.* - DOI: 10.1016/j.apcata.2020.117568
Raw and processed data of this section can be downloaded from: https://data.mendeley.com/datasets/38c6gy3t4r/2 - DOI: 10.17632/38c6gy3t4r.2

The results obtained using monolithic reactors are presented in Chapter 3, which is divided into 2 sections.

✓ **Section 3-1**: This section presents the evaluation of a system of monolithic reactors washcoated with a $RhPt/CeO_2$-SiO_2 catalyst for the reforming of ethanol. Stability of structured system was evaluated with several bioethanol samples: (i) synthetic (a mixing between water and ethanol), (ii) obtained from fermentation of glucose patrons, and (iii) obtained from fermentation of residual biomass. This chapter corresponds to the second specific objective of the Thesis.
This section corresponds to a paper in preparation.
Raw and processed data of this section can be downloaded from: https://data.mendeley.com/datasets/k2jb73b39z/1 - DOI: 10.17632/k2jb73b39z.2

✓ **Section 3-2**: This section presents the evaluation of a system of monolithic reactors coated with an $AuCu/CeO_2$ catalyst for the CO removal from syngas streams. In addition, the cost of the catalyst and a simulation of structured system in a multiphysics software are presented. This chapter corresponds to the third specific objective of the Thesis.
This section corresponds to a paper submitted to *International Journal of Hydrogen Energy* (www.journals.elsevier.com/international-journal-of-hydrogen-energy) on July 9, 2020.
Raw and processed data of this section can be downloaded from: https://data.mendeley.com/datasets/rw8drwgv8p/1 - DOI: 10.17632/rw8drwgv8p.2

Chapter 4 presents a description of the developed lab-scale prototype. In particular, the cost of the prototype is estimated.

Finally, Conclusions and Supplementary Material are found at the end of the document.

1.4 Academic products

1. Research papers: first author

   ✓ Cifuentes, B.; Bustamante, F.; Araiza, D. G.; Diaz, G.; Cobo, M. Hydrogen purification of actual syngas streams for energy applications: Au-Cu supported over nano-shaped CeO_2 as stable catalysts for the carbon monoxide removal. *Appl. Catal. A Gen. (2020), 598, 117568.*

- ✓ Cifuentes, B.; Bustamante, F.; Cobo, M. Single and Dual Metal Oxides as Promising Supports for Carbon Monoxide Removal from an Actual Syngas: The Crucial Role of Support on the Selectivity of the Au/Cu System. *Catalysts (2019), 9, 10, 852–877.*
- ✓ Cifuentes, B.; Bustamante, F.; Conesa, J.; Córdoba, L; and Cobo, M. Fuel-cell grade hydrogen production by coupling steam reforming of ethanol and carbon monoxide removal. *Int. J. Hydrogen Energy (2018), 43, 17216 - 17229.*
- ✓ Cifuentes, B.; Figueredo, M.; Cobo, M. Response Surface Methodology and Aspen Plus Integration for the Simulation of the Catalytic Steam Reforming of Ethanol. *Catalysts (2017), 7, 15 - 35.*

2. Research papers: co-author

   - ✓ Sanchez, N.; Ruiz, R. Y.; Cifuentes, B.; Cobo, M. Controlling sugarcane pressmud fermentation to increase bioethanol steam reforming for hydrogen production. *Waste Management (2019), 98, 1–13.*

3. Patent application
   M. Cobo, B. Cifuentes, F. Bustamante. *Catalizador bimetálico de Au-Cu soportado en un soporte de óxido de cerio (CeO_2) con una nanoestructura de poliedros* (Bimetallic Au-Cu catalyst supported on a cerium oxide (CeO_2) with a polyhedral nanostructure)". Patent application presented to *Superintendencia de Industria y Comercio de Colombia* on June 11, 2019. Patent number/Filed: NC2019/0006060.

4. Presentations: oral

   - ✓ Cifuentes, B.; Bustamante, F.; and Cobo, M. (2019). Remoción de CO en gas de síntesis: Efecto de los soportes en el catalizador de AuCu. XI Simposio Colombiano de Catálisis (SICCAT), September, Popayán, Colombia.
   - ✓ Cifuentes, B.; Sánchez, N.; Gómez, J.; and Cobo, M. (2019). Producción sostenible de gas de síntesis para aplicaciones energéticas: Una tecnología basada en biohidrógeno. 1er Congreso Nacional de Investigación e Innovación Ambiental CNIIA, May, Bogotá, Colombia.
   - ✓ Cifuentes, B.; Bustamante, F.; Conesa, J.; and Cobo, M. (2018). Eliminación de monóxido de carbono en una corriente de post-reformado con catalizadores bimetálicos de Au-Cu. XXVI Congresso Ibero-Americano de Catálise, September, Coímbra, Portugal.
   - ✓ Cifuentes, B., Camargo, J., Manrique, A., Córdoba, L., Bustamante, F., Cobo, M. (2017).Integration of Ethanol Steam Reforming and COPROX Reactions for H_2 Production. 25th North American Catalysis Meeting (NAM), June, Denver, USA.

5. Presentations: posters

   - ✓ Cifuentes, B.; Gómez, J.; Sánchez, N.; Bustamante, F.; and Cobo, M. (2019). Monolitos de RhPt/CeO $_2$/SiO_2 como catalizadores promisorios para la producción de hidrógeno a partir de bioetanol real. XI Simposio Colombiano de Catálisis (SICCAT), September, Popayán, Colombia.
   - ✓ Cifuentes, B.; Araiza, D.; Bustamante, F.; Díaz, G.; and Cobo, M. (2019). CO removal from actual syngas streams over Au-Cu catalysts supported on shaped CeO_2 nanoparticles. 26^{th} North American Catalysis Meeting (NAM), June, Chicago, USA.
   - ✓ Sánchez, N.; Cifuentes, B.; Ruiz, R. Y.; and Cobo, M. (2018). Efecto de las condiciones de fermentación de biomasa en la actividad del catalizador durante el reformado con vapor de bioetanol. XXVI Congresso Ibero-Americano de Catálise, September, Coímbra, Portugal.
   - ✓ Cifuentes, B., Figuredo, M., Cobo, M. (2017). Effect of the Catalyst Active Metal Ratio on the Energy Efficiency of a H_2 Fuel Cell Model. Poster. 25^{th} North American Catalysis Meeting (NAM), June, Denver, USA.

6. Distinctions

   - ✓ Scholarship for PhD program in Chemical Engineering. Scholarship granted by Colombian Department of Science, Technology, and Innovation (Colciencias) through call 727-2015. Medellin, Colombia (2016 - 2020).
   - ✓ Scholarship for research stay. Scholarship granted by Fundación Carolina through SEGIB-2019 program. Madrid, Spain (2019 – 2020).

7. Others

   - ✓ Research stay: Catalysis and Energy Laboratory of the Institute of Energy Technologies of Universitat Politècnica de Catalunya (UPC). Barcelona, Spain. September 2019 to January 2020.
   - ✓ Research stay: Catalysis and Energy Laboratory of the Institute of Energy Technologies of Universidad Nacional Autónoma de México (UNAM). Ciudad de Mexico, Mexico. July 2018 to August 2018.
   - ✓ Academic internship: Universidad de Los Andes. Bogotá, Colombia. August 2017 to December 2017.

1.5 References

[1] S. Williams, J. Robinson, Environ. Sci. Policy 103 (2020) 58–66.
[2] K. Wasniewski, Energy 191 (2020) 116500–116508.
[3] R. Chaubey, S. Sahu, O. James, S. Maity, Renew. Sustain. Energy Rev. 23 (2013) 443–462.
[4] M. Mortazaei, M. Rahimi, Energy Convers. Manag. 126 (2016) 132–141.

[5] N.P. Brandon, Z. Kurban, Philos. Trans. R. Soc. London A Math. Phys. Eng. Sci. 375 (2017) 1–17.
[6] U. Lucia, Renew. Sustain. Energy Rev. 30 (2014) 164–169.
[7] T.S. Moraes, H.N. Cozendey da Silva, L.P. Zotes, L.V. Mattos, L.E. Pizarro Borges, R. Farrauto, F.B. Noronha, Int. J. Hydrogen Energy 44 (2019) 21205–21219.
[8] F. Dawood, M. Anda, G.M. Shafiullah, Int. J. Hydrogen Energy 45 (2020) 3847–3869.
[9] D. Apostolou, G. Xydis, Renew. Sustain. Energy Rev. 113 (2019) 109292–109304.
[10] I. Sreedhar, K.M. Kamani, B.M. Kamani, B.M. Reddy, A. Venugopal, Renew. Sustain. Energy Rev. 91 (2018) 838–860.
[11] G. Liu, Y. Sheng, J.W. Ager, M. Kraft, R. Xu, EnergyChem 1 (2019) 100014–100065.
[12] M. Burhan, S.J. Oh, K.J.E. Chua, K.C. Ng, Appl. Energy 194 (2017) 255–266.
[13] J. Armijo, C. Philibert, Int. J. Hydrogen Energy 45 (2020) 1541–1558.
[14] C. Washburn, M. Pablo-Romero, Energy Policy 128 (2019) 212–222.
[15] J.B. Heo, Y.-S. Lee, C.-H. Chung, Biotechnol. Adv. 37 (2019) 107422–107442.
[16] A.H. Sebayang, H.H. Masjuki, H.C. Ong, S. Dharma, A.S. Silitonga, F. Kusumo, J. Milano, Fuel 210 (2017) 914–921.
[17] M.A. Ashraf, G. Ercolino, S. Specchia, V. Specchia, Int. J. Hydrogen Energy 39 (2014) 18109–18119.
[18] B. Gim, W.L. Yoon, Int. J. Hydrogen Energy 37 (2012) 19138–19145.
[19] B. Cifuentes, M. Figueredo, M. Cobo, Catalysts 7 (2017) 1–20.
[20] T. Wilberforce, A. Alaswad, A. Palumbo, M. Dassisti, A.G. Olabi, Int. J. Hydrogen Energy 41 (2016) 16509–16522.
[21] R. Roldán, Int. J. Hydrogen Energy 40 (2015) 2035–2046.
[22] B. Cifuentes, M.F. Valero, J. a. J. Conesa, M. Cobo, Catalysts 5 (2015) 1872–1896.
[23] B. Cifuentes, M. Hernández, S. Monsalve, M. Cobo, Appl. Catal. A Gen. 523 (2016) 283–293.
[24] N. Sanchez, R.Y. Ruiz, B. Cifuentes, M. Cobo, Int. J. Hydrogen Energy 41 (2016) 5640–5651.

2 Catalytic system based on powder catalysts

2.1 Catalytic system to produce and purify syngas

The objective of this chapter is to present the initial advances in the development of a catalytic system that integrates the production and purification of syngas to obtain fuel-cell grade hydrogen. This chapter corresponds to the first specific objective of the Thesis: "Evaluate the catalytic performance of Au-Cu catalysts (powder) in the CO removal from actual syngas streams". Thus, this first section focuses on the study of the Au/Cu ratio in powder catalysts of $AuCu/CeO_2$ for CO removal from an actual syngas.

This section corresponds to an article published in the *International Journal of Hydrogen Energy, (2018), 43, 17216 - 17229.* - DOI:10.1016/j.ijhydene.2018.07.139

Raw and processed data of this study can be downloaded from https://data.mendeley.com/datasets/scwxcw4gcz/1 - DOI:10.17632/scwxcw4gcz.1

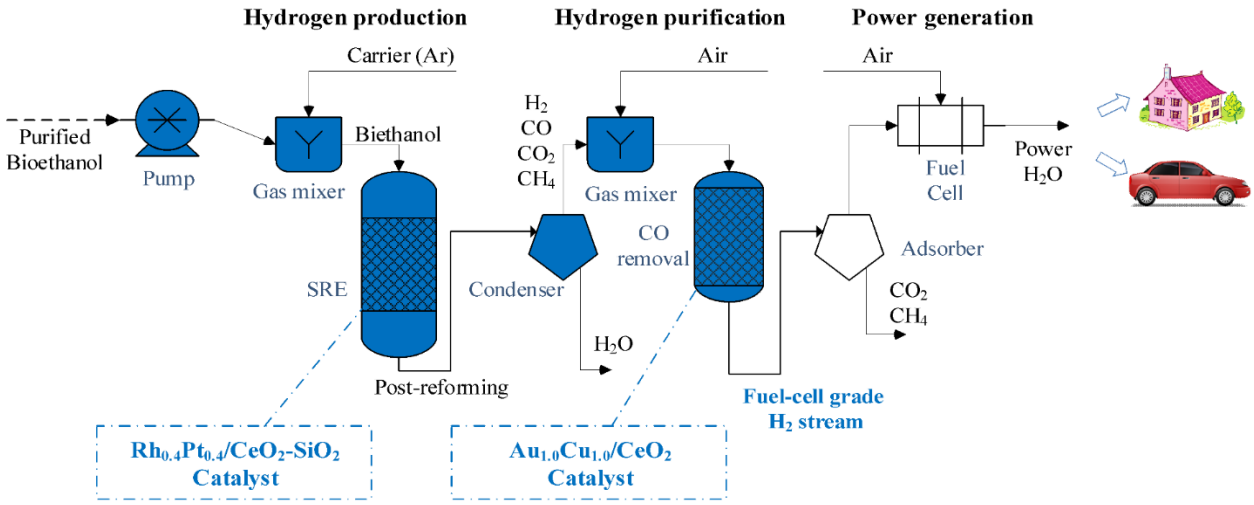

Graphical abstract

Fuel-cell grade hydrogen production by coupling steam reforming of ethanol and carbon monoxide removal

Bernay Cifuentes[1,4], Felipe Bustamante[1], Juan A. Conesa[2], Luis F. Córdoba[3] and Martha Cobo[4]*

[1]Environmental Catalysis Laboratory, Department of Chemical Engineering, Universidad de Antioquia UdeA, Calle 70 No. 52 - 21, Medellín, Colombia.

[2]Department of Chemical Engineering, Universidad de Alicante, P.O. Box 99, Alicante E-03080, Spain.

[3]Chemical and Biochemical Processes Laboratory, Department of Chemical Engineering, Universidad Nacional de Colombia, Carrera. 30 Calle 45, Bogotá, Colombia.

[4]Energy, Materials, and Environment Laboratory, Department of Chemical Engineering, Universidad de La Sabana, Campus Universitario Puente del Común, Km. 7 Autopista Norte, Bogotá, Colombia.

*Corresponding author: Email: martha.cobo@unisabana.edu.co, Tel: +571 8615555 Ext. 25207, Fax: 571 8615555

2.1.1 Abstract

Challenges of coupling steam reforming of ethanol (SRE) and carbon monoxide (CO) removal to continuous fuel-cell grade hydrogen (H_2) production were assessed. A SRE reactor, based on a previous optimized $RhPt/CeO_2$-SiO_2 catalyst, was coupled to a CO removal reactor, based on $AuCu/CeO_2$ catalysts with different Au:Cu weight ratios. Fuel-cell grade H_2 was achieved with an $Au_{1.0}Cu_{1.0}/CeO_2$ catalyst at 210 °C on the CO removal reactor. $AuCu/CeO_2$ catalysts characterization suggests that Au favors CO conversion by the formation of possible Au^0-CO_{ad} species, and Cu improves CO_2 yield by promoting oxygen vacancies on CeO_2. However, *operando* DRIFTS by 95 h showed that $Au_{1.0}Cu_{1.0}/CeO_2$ catalyst is susceptible to deactivation by the diminish on the CO_{ad} species and oxygen vacancies, and the formation of carbonate species. These results allowed us to propose a cyclic reduction treatment to prevent catalyst deactivation of $Au_{1.0}Cu_{1.0}/CeO_2$ (95 h of time-on-stream) while producing fuel-cell grade H_2.

Keywords: Methanation; Preferential Oxidation of CO; Surface Response Methodology; Thermogravimetric Analysis; X-ray Photoelectron Spectroscopy.

2.1.2 Introduction

Hydrogen (H_2) is a promising fuel to develop a cleaner energy system because it can be used in fuel cells (FC) to decarbonizing both mobile and stationary applications [1]. Water, heat, and electricity are the only products in FC fed with H_2. Also, this technology can be integrated with local renewable resources to improve energy efficiency and security. For instance, H_2 can be obtained from fermentable biomass, which is widely present in industrial and agricultural wastes, allowing to close the CO_2 cycle [2].

The general process for energy production from biomass may be divided into four stages, as shown in Figure 2.1.1. Traditionally, these stages are considered separately, and information of process integration is still missing. Bioethanol production is well-studied and depends strongly on the kind of the biomass fermented and the purification steps, but ethanol and water are the main products expected. In H_2 production from bioethanol, steam reforming of ethanol (SRE) stands out for having higher H_2 yield compared to other alternatives, such as partial oxidation or oxidative steam reforming [3]. Depending on the operating conditions and catalyst, SRE yields different amounts of H_2, carbon monoxide (CO), carbon dioxide (CO_2), and methane (CH_4) [4]. Therefore, purification of the H_2 stream is required but, as the purification requirements depends on the end-use of H_2, this stage is usually studied independently from the SRE.

CO_2, CH_4, and CO should be removed from post-reforming streams to reduce the environmental impact of the process and to protect FCs [5]. Thus, several strategies have been proposed to H_2 purification. Strategies such as chemical looping steam reforming (CLSR) of ethanol [6] and parallel plate reactors (PPR) [7] avoid the formation of undesirable products, increasing H_2 selectivity. Also, the inclusion of a sorbent in CLSR favors CO_2 capture with low cost [8]. However, emission of other undesirable products such as CO and CH_4 are still present. On the other hand, membrane reactors could simultaneously remove CO_2 and

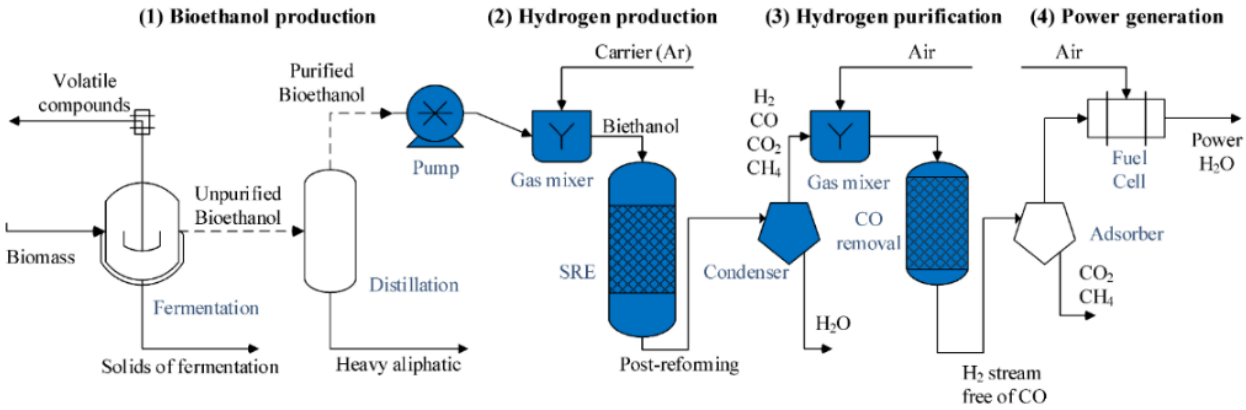

Figure 2.1.1. Overall process for energy production from biomass. Solid lines indicate continuous processes, while dotted lines indicate batch processes. The processes of interest in this paper are highlighted in blue.

CH_4 during reaction [9–11]. Nevertheless, the presence of CO reduces the permeability and selectivity of the membrane [12]. The use of selective membranes for CO removal has been previously proposed, but a membrane with high perm-selectivity is needed [13], which is expensive; thus, this technology is still in development. Therefore, CO removal from post-reformed streams could be currently the biggest barrier to connect H_2-reach streams to commercially available FCs devices.

FC represents a great opportunity to develop and deploy environmentally friendly devices. Among FC, proton exchange membranes FC (PEM-FC) have the larger share of the market because they can be used in a wide range of temperatures with high efficiency [14], making them suitable for diverse applications. Also, recent energy and economic simulations in Aspen Plus software show the potential of coupling SRE and PEM-FC technologies [15,16]. As the presence of CO is highly undesirable in PEM-FC applications due to its deleterious effect on the cell electrodes, these studies include several stages to remove CO, followed by membranes to remove CO_2 and CH_4. However, an experimental study that integrates directly SRE and PEM-FC have not been reported because CO-removal is a bulky step [17]. Removal of CO from the H_2 stream prior to its purification with membranes and use in PEM-FC is a key aspect in implementing this technology.

Chemical treatment is a promising way to remove CO from post-reforming streams due to it achieves low CO concentration (<100 ppm) [18]. Table 2.1.1 shows the reactions that would be involved in CO-removal from H_2 streams, along with the main side-reactions. Conventionally, CO-removal from post-reforming streams is carried out by a partial conversion through water gas shift reaction (WGSR) (R.1) to ensure an outlet CO content close to 2000-5000 ppm [19] -which may require two reactors-, followed by a final stage to ensure low CO (<100 ppm [20]) -which could also include several reactors-. Preferential oxidation of CO (CO-PROX, R.2) and CO methanation (R.3) are the most common methods used in the final stage [21]. Nevertheless, high H_2 loss is common during the final stage by the presence of secondary reactions (R.4 and R.5). Therefore, the conventional H_2 purification is extremely complex and bulky, limiting the application of the existing H_2 production technology in mobile and small FC applications [17]. Thus, an integration of the CO-removal process

in the same reactor, which would be promising for the development of new applications with PEM-FC, has been proposed recently [22]. The challenge to integrate H_2 production and purification lies on finding a catalytic system that ensures fuel-cell grade hydrogen production, reducing the number of reactor units.

Table 2.1.1. Chemical reactions involved in the CO-removal of post-reforming streams

Reaction	Description	
$CO + H_2O \rightleftharpoons CO_2 + H_2$	Water gas shift reaction, WGSR	R.1
$2CO + O_2 \rightarrow 2CO_2$	Preferential oxidation of CO, CO-PROX	R.2
$CO + 3H_2 \rightleftharpoons CH_4 + H_2O$	CO methanation	R.3
$CO_2 + 4H_2 \rightleftharpoons CH_4 + 2H_2O$	CO_2 methanation	R.4
$2H_2 + O_2 \rightarrow 2H_2O$	H_2 oxidation	R.5

In previous works, our Group designed an active and stable catalyst for the SRE by assessing different supports (CeO_2, ZrO_2, and La_2O_3) [23] and Rh:Pt ratios [24], as well as a novel mixed Ce:Si support [25]. In particular, a RhPt/CeO_2-SiO_2 catalyst with 0.4 wt% Rh, 0.4 wt% Pt, and a Ce/Si molar ratio of 2 in the support yields a H_2-rich stream (71% of H_2, 18% of CO, 3% of CO_2, and 7% of CH_4), making it a promising material for mobile and stationary applications. Now, it is our intent to clean this stream (i.e., remove CO) to be able to connect it to a PEM-FC.

Mono- and bi-metallic Au-Cu supported on CeO_2 have been reported as favorable catalysts for the CO-removal in synthetic post-reforming streams (containing CO, H_2, CO_2, and H_2O) because they promote WGSR [22,26,27], CO-PROX [28], and methanation [29]. However, CO-removal depends strongly on temperature and active metals ratio [25]. Also, catalysts assessment of the CO-removal in a stream that comes directly from the reformer have not been reported yet, which is necessary to implement a hydrogen technology in mobile and small devices. Therefore, the challenge is to evaluate the CO-removal in an actual post-reforming stream and identify operational variables that promote high activity and stability, preventing H_2 losses.

This study aimed to evaluate a system for CO-free H_2 production that couples SRE and CO-removal reactors, looking forward to designing an in-line process to produce electricity in PEM-FC (see Figure 2.1.1). SRE was carried out over a RhPt/CeO_2-SiO_2 catalyst previously reported [25], and AuCu/CeO_2 catalysts were evaluated for CO-removal. The effect of the Au:Cu ratio and temperature on activity and selectivity was studied by surface response methodology (RSM). Stability tests in continuous operation were conducted in the coupled system and some strategies for catalyst reactivation were assessed. Characterization tests, such as Brunauer–Emmett–Teller (BET) surface area, X-ray photoelectron spectroscopy (XPS), transmission electron microscopy (TEM), thermogravimetric analysis (TGA), and *operando* diffuse reflectance infrared Fourier transform spectroscopy (DRIFTS) were carried out to determine possible changes on the surface of AuCu/CeO_2 catalysts during CO-removal from actual post-reforming streams.

2.1.3 Experimental

Catalyst synthesis

RhPt/CeO_2-SiO_2 catalyst for SRE was prepared according to [25]. Firstly, the CeO_2-SiO_2 support was prepared by mixing $Ce(NO_3)_3{\cdot}6H_2O$ (99.5%, Alfa Aesar, USA) and SiO_2 (Merck, Germany), using water as solvent and achieving a Ce/Si molar ratio of 2. The support was dried at 105 °C for 24 h and calcined at 500 °C in a muffle for 4 h. Subsequently, aqueous solutions of rhodium (III) chloride hydrate ($RhCl_3{\cdot}H_2O$) (Aldrich Chem. Co., USA) and chloroplatinic acid hexahydrate ($H_2PtCl_6{\cdot}6H_2O$) (Aldrich Chem. Co., USA) were used to load Rh and Pt on the support by incipient wetness co-impregnation, achieving 0.4 wt% of each noble metal (Rh and Pt). After drying at 105 °C for 24 h and calcination at 700 °C in a muffle for 2 h, the catalysts were sieved to ensure particle sizes between 74 and 177 μm.

Au-Cu/CeO_2 catalysts for CO-removal were prepared with different nominal Au:Cu weight ratios (1:0, 3:1, 1:1, 1:3, and 0:3) by a two-step procedure. Firstly, $HAuCl_4{\cdot}3H_2O$ (99.9%, Sigma Aldrich, USA) was dissolved in water and the pH of the solution was adjusted to 6 with NaOH (0.1 M); then, CeO_2 (labeled as "Ce") was added and heated to 80 °C under continuous stirring for 2 h [30];]; the resulting slurry was filtrated, washed with water until constant pH, and dried at 105 °C for 24 h. This precipitation method has been reported as effective to load Au and promote more dispersed particles [30]. Afterwards, the required amount of $Cu(NO_3)_2{\cdot}3H_2O$ (99%, Sigma Aldrich, USA) was used as Cu precursor and loaded to the previously prepared Au/CeO_2 catalyst by incipient wetness impregnation. This procedure has been reported to favor a Cu enrichment on the catalytic surface and allow similar values between nominal and experimental Au/Cu ratio [31]. The nominal total metal loading (Au+Cu) was 2 wt% in all catalysts. Catalysts were dried at 100 °C for 24 h, calcined in a muffle at 500 °C for 2 h, and sieved to ensure a particle size between 74 and 177 μm. These samples were labeled as "fresh" (F) catalysts. The prepared AuCu/CeO_2 catalysts were represented as Au_xCu_{2-x}/Ce (x= 0, 0.5, 1.0, 1.5, and 2.0), where x indicates Au loading (wt%).

Catalytic tests

SRE was carried out over a RhPt/CeO_2-SiO_2 catalyst in a fixed-bed reactor (ID of 12 mm) at 700 °C, atmospheric pressure, and under kinetic control (i.e., avoiding external and internal mass transfer limitations), according to the procedure described elsewhere [25]. The catalytic bed was made of 50 mg of RhPt/CeO_2-SiO_2 and 250 mg of inert quartz particles. RhPt/CeO_2-SiO_2 catalyst was reduced *in-situ* with 8% H_2/N_2 (300 mL/min) at 700 °C for 1 h. SRE was conducted at 6.4 ± 0.2 $L{*}g_{cat}^{-1}{*}min^{-1}$ of space velocity (SV) (GHSV=63,500 h^{-1}) to avoid mass transfer limitations. The feed was 0.03 mL/min of synthetic bioethanol (water/ethanol with a stoichiometric molar ratio of 3). Before entering the reactor, the feed was diluted in Ar to achieve 1.8 and 5.4 mol% of ethanol and water, respectively, in the inlet stream. The SRE catalytic stability test was conducted for 120 h time-on-stream (TOS) using the conditions described above. Steady state SRE product distribution was reached after 30 min (see Supplementary Material, Figure SM.1), achieving yields of 5.1 for H_2, 1.3 for CO, 0.5 for CO_2, and 0.2 for CH_4, with a deviation less than 7%.

When the SRE's product distribution was stable (i.e., after 30 min), the SRE output was directly connected to the CO-removal reactor to carry out the catalytic evaluation of CO conversion in the actual post-reforming stream. The effluent stream from SRE was mixed with dry air, to achieve a O_2/CO molar ratio of 0.9 ± 0.04 in the inlet of the CO-removal reactor: O_2/CO ratio was selected based on preliminary tests (see Supplementary Material, Figure SM.2), where the 0.9 ratio favors CO conversion and mitigates H_2 losses, similarly to results reported by [32]. Likewise, water in post-reforming was not condensed because activity and selectivity were slightly improved above 180 °C by water presence (see Supplementary Material, Figure SM.3), in agreement with [31]. Catalytic tests were started at 300 °C and the temperature was decreased in 20 °C intervals until 60 °C (continuous sequence, 20 min at each temperature) in a plug flow reactor (ID=12 mm). External and internal mass transfer limitations were controlled as reported in [25]. The catalytic bed was made of 50 mg of catalyst sample of Au-Cu/Ce catalysts and 250 mg of inert quartz particles. A SV of 6.5 ± 0.2 $L*g_{cat}^{-1}*min^{-1}$ (GHSV=64,100 h^{-1}) was used in the CO-removal reactor. All catalyst samples were reduced *in-situ* with 8 mol% H_2/Ar at 300 °C for 1 h, degassed in Ar at 300 °C for 30 min, and stabilized in 10% air/Ar at 300 °C for 30 min. These samples were labeled as "reduced–oxidized" (R-O) catalysts. Samples used in catalytic evaluation were labeled as "used" (U) catalysts.

Contribution of the main reactions involved during CO removal and listed in Table 2.1.1 was individually evaluated on $Au_{1.0}Cu_{1.0}$/Ce using synthetic feeds. Inlet concentrations where simulated from those found at the SRE outlet for the species relevant to each reaction. Table SM.1 of Supplementary Materials shows the experimental details of each reaction. Briefly, for CO-PROX, the feed was 2.0% CO, 7.8% H_2, 1.8% O_2, and 6.8% N_2 in Ar balance; for WGSR, 2.0% CO and 1 % H_2O in Ar balance; for CO methanation, 2.0% CO and 7.8% H_2 in Ar balance; for CO_2 methanation: 1% CO_2 and 8.2% H_2 in Ar balance; and, for H_2 oxidation, 1.8% O_2, 8.0% N_2, and 8.2% H_2 in Ar balance. Besides, thermodynamic equilibrium of each reaction (see Supplementary Material, Figure SM.4) was evaluated using a Gibbs reactor in Aspen Plus V9.0 (Aspen Tech, USA, 2016). NRTL-RK was used as thermodynamic package in simulations to model all species present in hydrocarbon reforming [16,33].

CO-removal stability tests with several reactivation treatments were conducted on $Au_{1.0}$ $Cu_{1.0}$/Ce at 210 °C for 95 h TOS, as described in Table SM.2 of Supplementary Material. The sample used during this initial stability tests was labeled as "ST". The reactivation treatment 4, namely *in-situ* catalyst reduction with 8 mol% H_2/Ar stream (300 mL/min) at 300 °C for 1 h followed by a degasification in Ar at 300 °C for 30 min, was selected as the most appropriate to keep the catalyst active. This reactivation treatment was applied during a new stability test by 95 h, in which the reactivation treatment was applied every 24 h. This sample was labeled as "R-ST" catalyst.

The outlet products of the SRE and CO-removal reactors were measured on-line by gas chromatography (GC, Perkin Elmer, USA). The GC was equipped with an Innowax column (30 m, 0.53 mm ID, Perkin Elmer, USA) connected to a flame ionization detector (FID) and a Carboxen 1010 plot column (30 m, 0.53 mm ID, Restek, USA) connected to a thermal conductivity detector (TCD), using Ar as carrier. This configuration allowed measuring CO, CO_2, H_2, CH_4, ethylene, and ethanol. Carbon elemental balances between inlet and outlet of each reactor were measured in all tests.

CO conversion (x_i) and yield for each detected product were calculated by 1 and 2.

$$x_i = \frac{F_{i,inlety} - F_{i,outlety}}{F_{i,inlety}} \times 100 \quad (1)$$

$$\text{Yield}_i = \frac{F_{i,outlet\,CO-removal}}{C_{inlet\,SRE}} \quad (2)$$

Where $F_{i,inlety}$ is the mole flow (mol/min) of species i (ethanol, H_2, CO, CH_4, or CO_2) entering the reactor y (SRE or CO-removal) and $F_{i,outlety}$ is the mole flow (mol/min) of unreacted species i detected by GC in the outlet of the corresponding reactor.

Catalytic performance of AuCu/Ce catalysts was evaluated by RSM using Design Expert 8 software (Stat-Ease Inc, USA). The adjustment of the response surfaces was validated by the probability ("Prop. F"), "Lack of fit" test, "Adeq precision", and variability with respect to the experimental data (R^2), as reported in [24].

AuCu/CeO_2 catalyst characterization

AuCu/CeO_2 catalyst surface area was determined by the single-point BET surface method in a ChemBET Pulsar TPR/TPD unit (Quantachrome Instruments, Boynton Beach, FL, USA). 70 mg of sample was previously degassed in He (20 mL/min) at 120 °C for 1 h; surface area was measured with 30% N_2 /He (20 mL/min) as the adsorption gas, at liquid nitrogen temperature. The measurement was repeated until a deviation lower than 5% was obtained.

XPS spectra of catalysts were obtained using an VG-Microtech Multilab electron spectrometer (Thermo-Scientific, Waltham, MA, USA) with a twin anode radiation source in the Mg Kα (1253.6 eV) constant energy analysis mode and an energy flow of 50 eV. The analysis chamber was maintained at 5.10×10^{-8} Pa. The C 1s line was set at 284.6 eV. The binding energy (BE) values were obtained with a precision of 0.2 eV using the Peak Fit program of the spectrometer control program.

TEM was carried out in a JEOL JEM-2010 microscope at 200 kV coupled to energy-dispersive X-ray spectroscopy (EDS, INCA Energy TEM100, Oxford Instruments, Abingdon, UK) with a Si(Li) detector, 30 mm^2 detection area, and 142 eV resolution. Samples were dispersed in ethanol by ultrasonic vibration and dropped on a carbon film-coated copper grid. The active metal particles were measured with ImageJ software. The mean particle diameter was calculated according to 3, where n_i is the number of particles and d_i is the particle diameter [34].

$$\overline{d}_p = \frac{\sum_i n_i d_i^3}{\sum_i n_i d_i^2} \quad (3)$$

TGA using a thermogravimetric analyzer (Mettler Toledo, Columbus, OH, USA) were performed to measure residues and deposits on catalyst samples. Each sample (20 mg) was previously degassed in N_2 (20 mL/min) at 100 °C for 1 h and then heated from 30 to 1000 °C in air (5 °C/min, 100 mL/min flow rate). Weight loss reported for used samples includes the subtraction of the weight loss obtained in R-O samples.

Stability of $Au_{1.0}Cu_{1.0}$/Ce was evaluated for 95 h at 210 °C by *operando* DRIFTS. The outlet stream of SRE was connected to a Thermo Scientific Nicolet iS10 spectrum (USA)

equipped with a diffuse reflection attachment DRK-3 Praying Mantis (Harrick, USA) in the range of 4000–400 cm^{-1}, with an average of 32 scans each 1.5 min and a resolution of 4 cm^{-1}. About 40 mg of powder $AuCu/CeO_2$ catalyst were loaded into the high temperature Harrick reaction cell equipped with ZnSe windows. Each spectrum was obtained by subtracting the background collected for R-O sample.

2.1.4 Results and discussion

Activity and selectivity of $AuCu/CeO_2$ catalysts during CO-removal

Catalytic performance of AuCu/Ce during CO-removal of the post-reforming stream was evaluated by RSM. Figure 2.1.2 shows response surfaces for CO conversion, CO_2 yield, H_2 loss, and CH_4 yield over several AuCu/Ce catalysts between 60 and 300 °C. A volcano-shape trend is observed in CO conversion with temperature (Figure 2.1.2a), likely due to a competition between CO-PROX and hydrogen oxidation at high temperature[35,36]. Besides, when Au loading increased, CO conversion was favored (Figure 2.1.2a), probably due to the fact that Au has been reported as 9 times more active than Cu in WGSR (R.1) and CO-PROX (R.2) [37].

CO_2 yield displays a similar trend that CO conversion with temperature (Figure 2.1.2b), suggesting that CO-PROX is the main reaction that consumes CO and produces CO_2. Moreover, larger CO_2 yield was observed in those catalysts with higher Cu content. It has been reported that dispersed Cu on catalytic surface favors CO adsorption, promoting high CO_2 yield during CO-PROX [38].

Au:Cu ratio in the AuCu/Ce catalysts also affects H_2 loss, which is undesirable (Figure 2.1.2c). Between 175 and 260 °C, a pronounced decrease in H_2 loss is observed on bimetallic $Au_{1.5}Cu_{0.5}/Ce$ and $Au_{1.0}Cu_{1.0}/Ce$. The lower H_2 loss was recorded over $Au_{1.0}Cu_{1.0}/Ce$ at 210 °C (25%, see Figure 2.1.2c), achieving a CO concentration of 70 ppm in the outlet gas. H_2 loss, which is still elevated compared to the recommended goal for CO-PROX (<5% [39]), may be correlated mainly to CH_4 formation. Figure 2.1.2d shows that CH_4 formation follows the H_2 loss profile. Although Au-Cu catalysts are recognized for avoiding methanation during CO-PROX of synthetic post-reforming streams [37], this reaction appears to be important in the cleaning of the actual post-reforming stream. Wang at al. [40] also reported CO and CO_2 methanation at 160 °C during CO-PROX over Au-supported catalysts, using a synthetic post-reforming stream (CO, O_2, and H_2). Thus, AuCu/Ce catalysts could favor methanation under certain conditions, resulting in H_2 losses in the coupled SRE-CO-removal system.

To identify the specific contribution of each reaction in carbon selectivity and H_2 loss, independent evaluation using synthetic feeds of all the reactions listed in Table 2.1.1, namely CO-PROX, WGSR, H_2 oxidation, CO-methanation, and CO_2-methanation, was carried out over the catalyst that displayed the lowest H_2 loss, i.e., $Au_{1.0}Cu_{1.0}/Ce$. Results are shown in Figure 2.1.3; the behavior of the actual post-reforming stream cleaning is also included. CO-PROX (R.2), which is favored between 140-210 °C, and WGSR (R.1), favored at high temperatures [22], are the main ways to remove CO over $Au_{1.0}Cu_{1.0}/Ce$ catalyst (see Figure 2.1.3a), whereas CO methanation has a slight participation in CO conversion, mostly at lower temperature. When compared with CO-removal of the actual post-reforming stream,

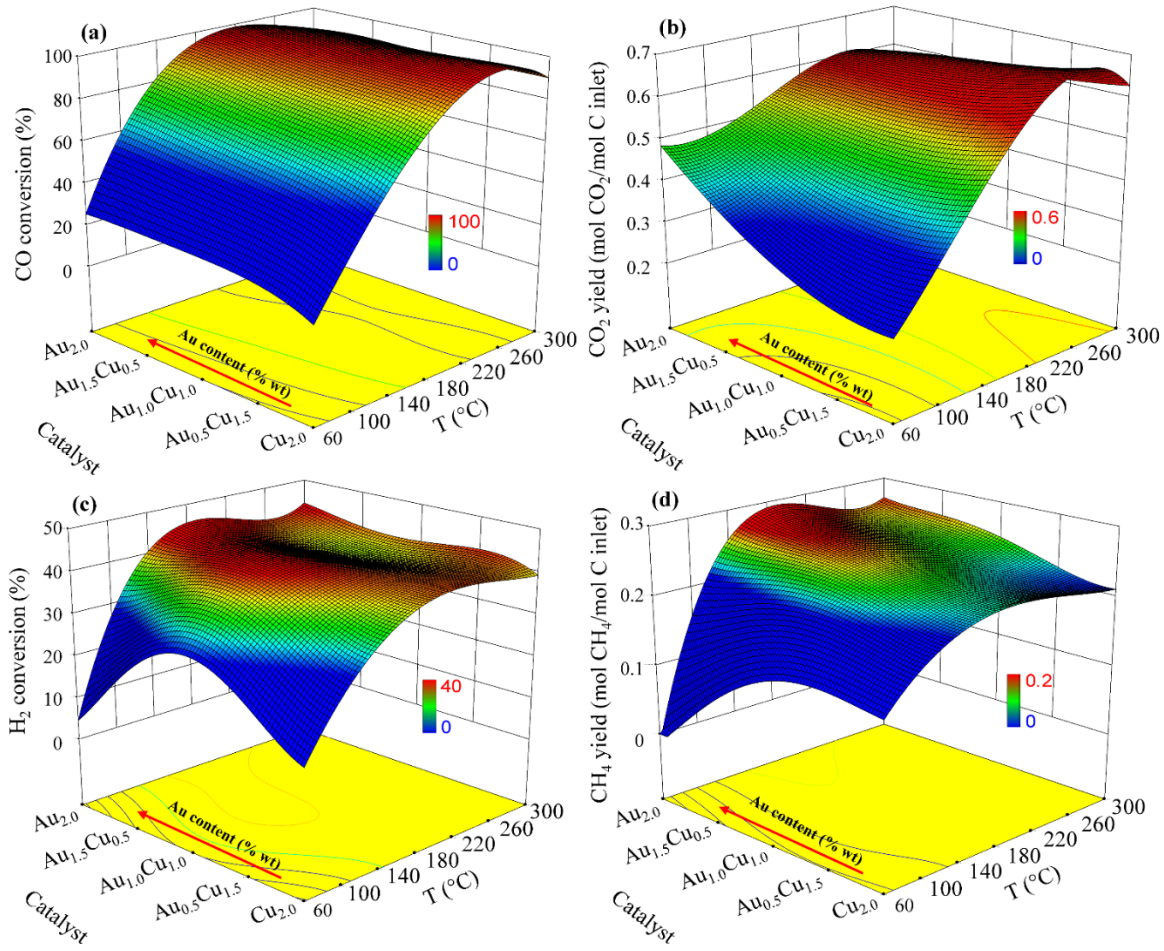

Figure 2.1.2. (a) CO conversion, (b) CO_2 yield, (c) H_2 loss, and (d) CH_4 yield for CO-removal of a post-reforming stream on $AuCu/CeO_2$ catalysts. Inlet stream: 7.8% H_2, 2.0% CO, 0.5% CO_2, 0.3% CH_4, 1.4% H_2O, 1.8% O_2, 6.8% N_2, and 79.4% Ar. Total metal loading (Au+Cu) = 2 wt% in all catalysts. Response surface: Quartic model, $R^2 > 0.82$, Adjusted $R^2 > 0.8$, Prop. F<<0.1 (significant), and Lack of Fit>>3 (nonsignificant). The regression analysis for the response surfaces is available in Supplementary Material, Table SM.3

it is observed that at temperatures lower than 180 °C, total CO conversion is not a sum of the different reactions involved, but it is lower than CO-PROX conversion. It seems that CO-PROX is mitigated at lower temperatures in this complex post-reforming stream. A higher CO_2 content in the post-reforming could favor a competitive adsorption of CO with CO_2, decreasing CO conversion [41]. However, at temperatures higher than 180 °C, CO-removal is a combination of CO-PROX and WGSR, increasing the CO-removal. Likewise, CO_2 yield (see Figure 2.1.3b) is directly related to CO conversion for CO-PROX and WGSR. But, CO_2 yield in post-reforming stream has a drastic decreasing, especially between 100 and 180 °C. In this way, some additional reactions are not only mitigating CO-PROX, but also consuming the CO_2 formed during the actual post-reforming stream cleaning.

Again, H_2 and CH_4 behavior could provide some insight into decreasing of CO_2 yield and CO-PROX mitigation in the actual post-reforming stream. In independent reactions, high H_2 loss is observed at the lower and higher temperatures (see Figure 2.1.3c) during CO-PROX; interestingly, high H_2 losses match low CO conversions (see Figure 2.1.3a). Oppositely to CO-PROX and actual post-reforming stream, H_2 loss is not significant in CO_2 and CO methanation. Furthermore, the same trend is observed in CH_4 formation (see Figure 2.1.3d). Then, the large amount of CO_2 formed by CO oxidation would promote its methanation, thus consuming H_2. Yet, CH_4 yield in the actual post-reforming stream is larger than the sum of the independent reactions at temperatures lower than 180 °C. Thermodynamic calculations for each reaction (see Supplementary Material, Figure SM.4) show that CH_4 is the main product in most of the scenarios, except during WGSR, where CH_4 is not formed. Thus, according to thermodynamics, the favorability for the hydrogenation of the carbon species leads to a high loss of hydrogen.

On the other hand, since the amount of CH_4 formed is lower than the sum of each independent reaction, H_2 consumption in post-reforming would not be the sole result of methanation at temperatures higher than 220 °C. Thence, in that temperature range, H_2 oxidation is the main contributor to H_2 loss. In an intermediate zone, between 180 and 220 °C, methanation is mitigated, delivering a minimum of 25% H_2 loss at 210 °C in the post-reforming stream treatment. Thermodynamics show a clear favorability for this hydrogen loss (see Supplementary Material, Figure SM.4), reaching more than 40% under the conditions of the actual post-reforming stream, but the catalyst can mitigate the hydrogenation of carbonated species, controlling the hydrogen loss until 25%. Therefore, CO-removal on the actual post-reforming stream is not a cumulative contribution of the CO-removal reactions. The high CO concentration, and subsequent CO_2 formation, and the complex network of reactions in an actual post-reforming stream could favor H_2 loss greater than the 5% goal. This behavior has not been observed in synthetic streams [37], where a simple system allows catalysts to be more effective to control the hydrogenation of carbon species.

Therefore, catalyst characterization was employed to identify how the AuCu/Ce ratio on the catalyst affects the complex phenomena occurring during the CO-removal of post-reforming streams.

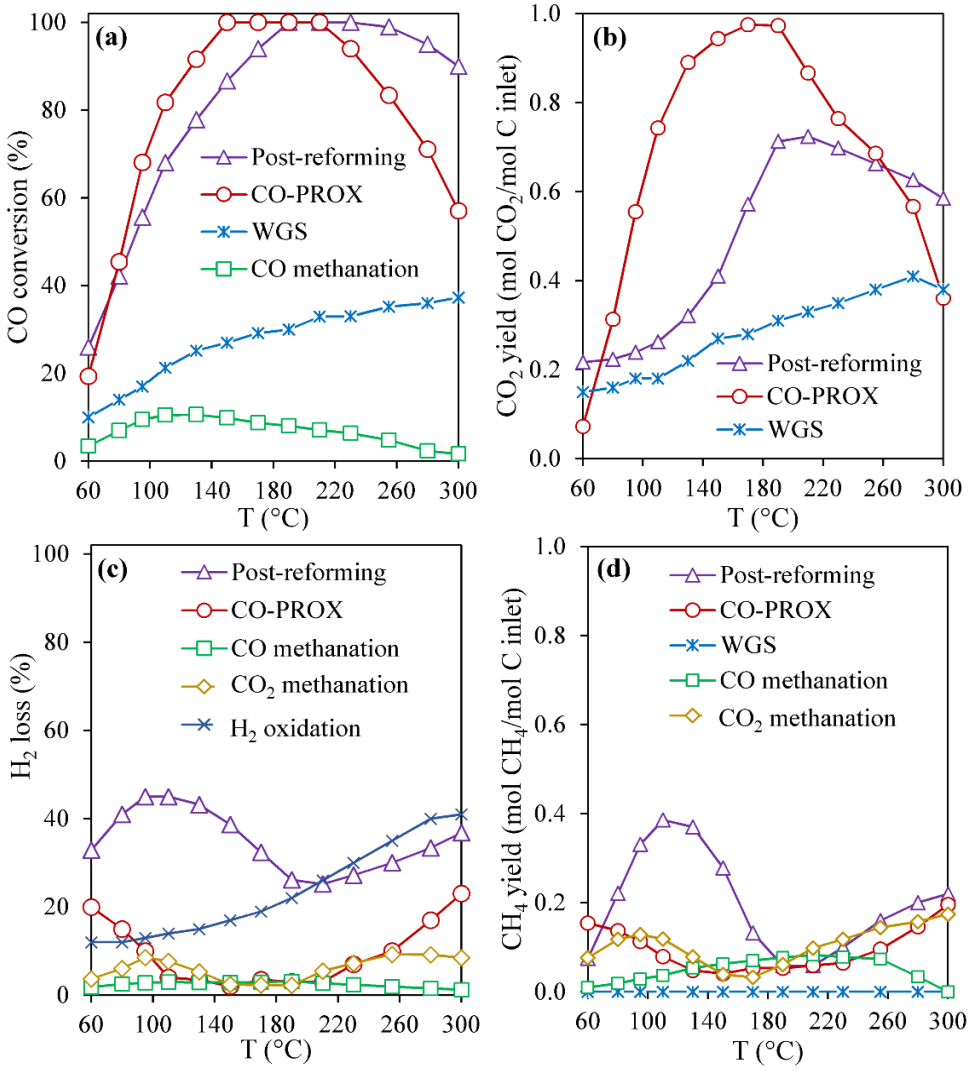

Figure 2.1.3. Individual contribution of the main CO-removal reactions on (a) CO conversion, (b) CO_2 yield, (c) H_2 lost, and (d) CH_4 yield on $Au_{1.0}Cu_{1.0}$/Ce catalyst. Lines identified as CO-PROX, WGS, H_2 oxidation, and CO and CO_2 methanation correspond to independent evaluation using synthetic feeds. Post-reforming corresponds to actual post-reforming stream cleaning. SV was fixed in 6.5 ± 0.2 $L*g_{cat}^{-1}*min^{-1}$.

Catalysts characterization

BET surface area Table 2.1.2 shows textural and morphological characteristics of AuCu/Ce catalysts. Surface area of the catalysts, which were activated by reduction-oxidation (R-O), increased with Cu content, reaching a maximum of 83.6 m^2/g_{cat} for $Cu_{2.0}$/Ce. Formation of irregular and highly dispersed Cu particles may favor this higher catalyst surface area [42]. A direct relationship between catalytic activity and catalysts surface area was not detected in this study, but the high CO_2 yield found in Cu catalysts could be attributed to their larger specific surface areas. However, BET surface area decreased after use (U samples), suggesting that catalysts could be susceptible to surface changes and formation of carbonaceous deposits under operation, as it will be shown in Section 3.2.4.

XPS Oxidation states of the elements on AuCu/Ce catalysts were evaluated by XPS. Figure 2.1.4 shows the XPS spectra of Au, Ce, and O in AuCu/Ce catalysts before (R-O) and after (U) CO-removal process. The amount of each species was determined by integration of each characteristic peak. Since Cu can be easily reduced under ultra-high vacuum chamber of XPS unit its reduction state is difficult to follow with this test. Thus, Cu spectra were not including to avoid speculative interpretations. Figure 2.1.4a shows XPS spectra of Au 4f for fresh, R-O samples. The characteristic peak of Au^0 around 84 eV is observed. Au^0 interacts with adsorbed CO (CO_{ad}) to form Au^0-CO_{ad} species, which is an intermediate in CO oxidation [43]. The possible formation of Au^0-CO_{ad} species could be related to the elevated CO-PROX on Au-containing catalysts (see Figure 2.1.2a and Figure 2.1.3a). However, it is expected that the Au-CeO_2 interaction involves a charge transfer, leading to Au oxidized species [44]. However, oxidized species as Au^+ (85 eV [31]) and Au^{3+} (86eV [44]) were not detected, indicating a weak interaction of Au with CeO_2 when Cu is present. This Au reductive state was kept in used samples (Figure 2.1.4b).

Figure 2.1.4c and d show XPS spectra of Ce; symbols V and U represent the spin−orbit coupling of $3d_{5/2}$ and $3d_{3/2}$, respectively, associated with Ce^{3+} and Ce^{4+} species. Deconvoluted peaks of V^0, V´, U^0, and U´ could be ascribed to Ce_2O_3 (Ce^{3+}), while V, V´´, V´´´, U, U´´, and U´´´ correspond to CeO_2 (Ce^{4+}) [45,46]. Ten peaks are observed in all AuCu/Ce catalysts, indicating that CeO_2 is partially reduced. Partial reduction of Ce^{4+} to Ce^{3+} generates oxygen vacancies, which dissociate CO into CO_{ad} species [47], and favor oxygen mobility, which can act as an oxidizing agent [48]. The Ce^{3+}/Ce^{4+} ratio for AuCu/Ce catalysts (see Table 2.1.2) increases with Cu loading, which could be linked to the incorporation of Cu species into the lattice of CeO_2 [49] to form CuO and oxygen vacancies [50]. Thus, high selectivity of AuCu/Ce catalysts with high Cu loading could be associated to a synergetic effect of the redox characteristics of Cu and CeO_2, to promote oxygen vacancies. In addition, possible interaction between Cu and Ce could be related to the increase in BET (see Table 2.1.2). In used samples, Ce^{+3}/Ce^{+4} ratio decreases in $Cu_{2.0}$/Ce and $Au_{0.5}Cu_{1.5}$/Ce, remains constant in $Au_{1.0}Cu_{1.0}$/Ce, and increases in $Au_{2.0}$/Ce and $Au_{1.5}Cu_{0.5}$/Ce, indicating that Cu promotes the oxidation of CeO_2 under operation. $Au_{1.0}Cu_{1.0}$/Ce shows favorable Cu and Au loadings to promote and retain oxygen vacancies on the catalysts. Correspondingly, oxygen vacancies on $Au_{1.0}Cu_{1.0}$/Ce can activate H_2O (in WGSR) and O_2 (in CO-PROX) to

Table 2.1.2. Textural and morphological characteristics of AuCu/Ce catalysts

Catalysts[1]	BET surface area (m^2/g catalyst)		Ce^{3+}/Ce^{4+} molar ratio[2]		(O_s +OH^-)/Ce molar ratio[2]		Metal average surface-area-weighted diameter of Au (d_p, nm)[3]		Weight loss of used samples (%)[4]
	R-O	U	R-O	U	R-O	U	R-O	U	U
$Cu_{2.0}$/Ce	83.6	75.5	0.9	0.7	0.5	0.6	-	-	2.2
$Au_{0.5}Cu_{1.5}$/Ce	75.9	71.7	0.7	0.6	0.4	0.5	4.93	4.81	1.4
$Au_{1.0}Cu_{1.0}$/Ce	70.8	68.0	0.6	0.6	0.5	0.9	4.80	5.12	1.6
$Au_{1.0}Cu_{1.0}$/Ce (ST)	70.8	56.8	0.6	0.4	0.5	0.9	4.80	5.63	3.0
$Au_{1.0}Cu_{1.0}$/Ce (R-ST)	70.8	67.5	0.6	0.6	0.5	0.8	4.80	5.24	1.3
$Au_{1.5}Cu_{0.5}$/Ce	62.8	61.1	0.5	0.7	0.4	0.9	4.66	5.02	1.9
$Au_{2.0}$/Ce	61.1	60.4	0.5	0.6	0.4	0.8	4.40	5.24	2.4

[1]Subscript in catalysts corresponds to the nominal metal loading. R-O: reduced-oxidized fresh sample; U: used sample with post-reforming gas; ST: sample used during stability tests; and R-ST: reactivated sample during stability test by *in-situ* reduction. [2]Obtained from XPS. [3]Obtained from TEM. [4]Measured by TGA

promote CO oxidation trough both reactions (WGSR and CO-PROX) [22], as was observed during synthetic feeds evaluation (Figure 2.1.3a). Likewise, oxidation state of CeO_2 surface affects methanation, excess in oxygen vacancies could inhibit hydrogenation of carbon intermediates, mitigating CH_4 formation [29]. Thus, oxidation of CeO_2 promoted by Cu could prevent methanation, as was observed in synthetic feeds evaluation (see Figure 2.1.3d).

XPS spectra of O (Figure 2.1.4e and f) indicate the presence of three main species: O^{-2} (related to the lattice oxygen in CeO_2) at 529 eV, surface oxygen (O_s), and surface OH^- species, both associated to the peak at 531 eV [44]. O_s and OH^- groups play an important role in the catalytic activity and selectivity. O_s can react with CO in the gas phase or with the CO_{ad}, formed by interaction of CO with the oxygen vacancies, to produce CO_2 [26]. OH^- species are intermediates required in CO-PROX on Au catalysts [51]. In R-O samples, significant changes in O_s and OH^- species by Au:Cu ratio are not identified and, in average, a 0.45 of (O_s and OH^-)/Ce molar ratio is observed in AuCu/Ce catalysts (see Table 2.1.2). However, in used samples, the amount of O_s and OH^- species increases, particularly when the Au loading is higher than 1 wt%. Au is recognized to promote OH^- formation from water decomposition [31] or from reactants in the gas phase [51]. Despite the participation of OH^- groups is considered an effective way to CO oxidation in CO-PROX [37], the excess in OH^- species could promote high amount of carbon intermediates [52], which could be easily hydrogenated [53], as observed by thermodynamic calculations (see Supplementary Material, Figure SM.4). In fact, the presence of OH^- species has been linked to simultaneous WGSR and CO-methanation [53]. OH^- species on $Au_{1.0}Cu_{1.0}$/Ce could be linked to the occurrence of both WGSR and methanation during CO-removal of the synthetic and post-reforming streams (see Figure 2.1.3a and d). Therefore, the inclusion of Au in AuCu/Ce catalysts could favor the formation of OH^- species under reaction conditions, which increases the activity but could also affect the selectivity by hydrogenated carbon intermediates.

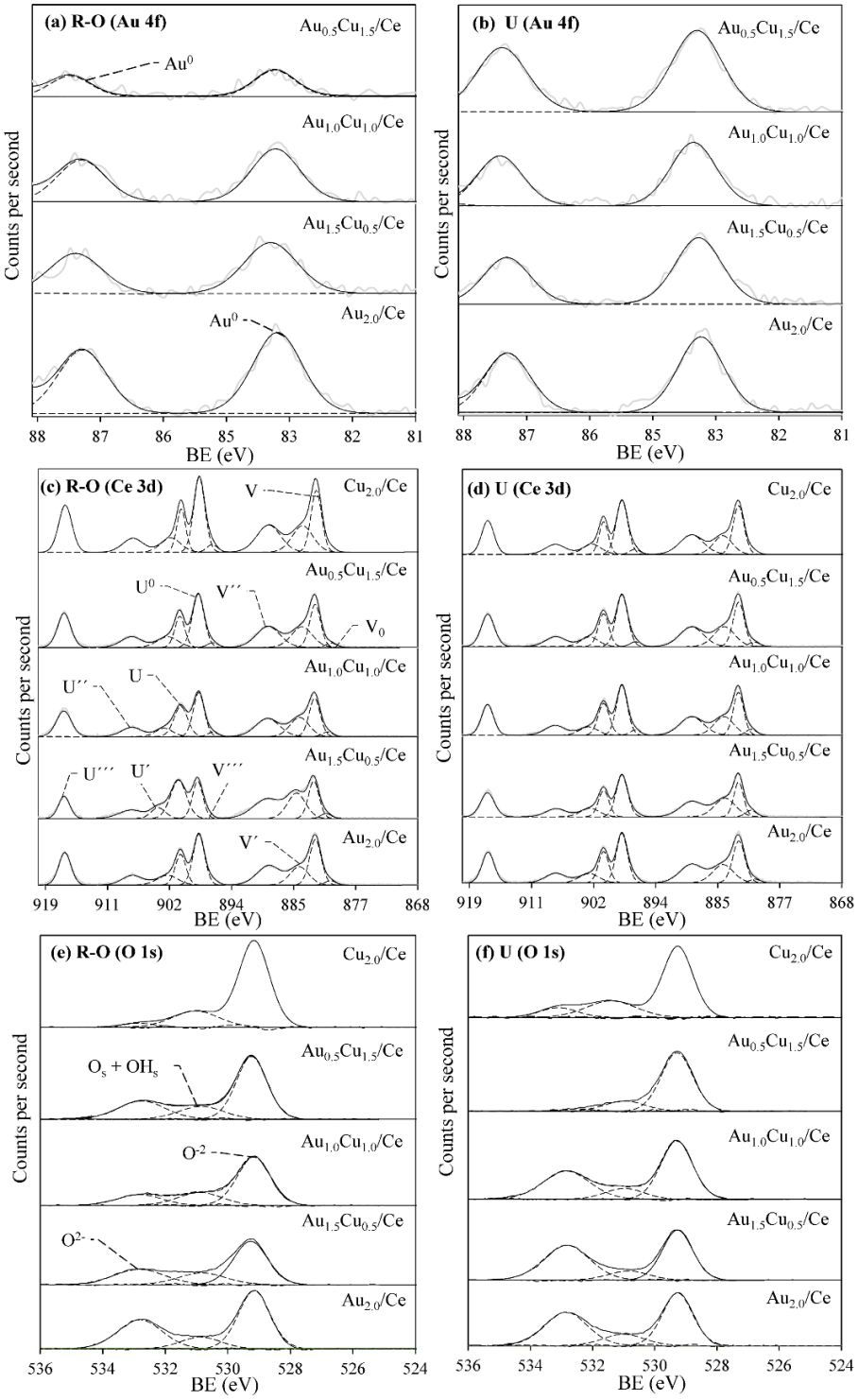

Figure 2.1.4. XPS spectra of Au 4f (a and b), Ce 3d (c and d), and O 1s (e and f) for reduced-oxidized (R-O) and used (U) samples of $AuCu/CeO_2$ catalysts.

TEM TEM micrographs and particle size distribution of AuCu/Ce catalysts are show in Supplementary Material (Figure SM.5). As Cu may form irregular, highly dispersed particles [42], it was not clearly identified in TEM micrographs; moreover, there is not enough contrast between active particles and support. Therefore, this study only evaluated the Au average particle sizes obtained from the TEM, which are listed in Table 2.1.2. In R-O samples, Au average active particle diameter increased with Cu loading, suggesting that Cu promotes a slight Au agglomeration, which could be ascribed to the low interaction between Au and Ce, as was discussed in the XPS section. In used samples (U), Au average active particle diameter increased with respect to R-O samples. Therefore, TEM results show that AuCu/CeO_2 catalysts are susceptible to a slight agglomeration of Au active particle sites under operation, especially with high Au content; but this agglomeration is not clearly increased with TOS (ST and R-ST samples), probably due to it is just an initial Au particle rearrangement.

TGA The amount of adsorbed and deposited species was evaluated by TGA. Table 2.1.2 shows the weight loss of used samples. Mitigation of deposits is most significant in bimetallic $Au_{0.5}Cu_{1.5}$/Ce and $Au_{1.0}Cu_{1.0}$/Ce. As discussed in previous sections, carbon intermediates were favored by OH^- species, which are formed on CeO_2 and Au. These intermediates favor CO oxidation, but also promotes surface carbon during CO-PROX [54]. Thus, OH^- groups could contribute to produce CH_4 or carbonaceous deposits. Therefore, $Au_{1.0}Cu_{1.0}$/Ce catalyst has a proper Au:Cu ratio to favor enough OH^- species on surface, which favor CO removal, and oxygen vacancies, which improve CO_2 selectivity, mitigating carbonaceous deposits.

Thus, despite the high H_2 loss, CO-removal of post-reforming streams on $Au_{1.0}Cu_{1.0}$/Ce catalyst at 210 °C ensures low CO concentrations ($\sim$ 70 ppm). Therefore, stability tests were carried out to evaluate this FC-grade H_2 production, to identify the catalyst stabilization time, and to check the possible changes that could shift the behavior of the catalyst outside the narrow operation window observed in Figure 2.1.2.

Stability of the coupled SRE/CO-removal system

***Operando* DRIFTS** Catalysts stability and productivity are the most relevant industrial parameters [55]. So, these characteristics must be established prior to the extensive application of a catalyst. Thence, $Au_{1.0}Cu_{1.0}$/Ce catalyst was subjected to a stability tests at 210 °C by 120 h TOS. Figure SM.6 of Supplementary Material showed that $Au_{1.0}Cu_{1.0}$/Ce catalyst presented rapid deactivation after 40 h TOS, accompanied by a high CH_4 production, which matches with the thermodynamic predictions (see Supplementary Material, Figure SM.4). Then, stability of $Au_{1.0}Cu_{1.0}$/Ce catalyst was evaluated with *operando* DRIFTS for 95 h to determinate the main species involved in catalyst deactivation. Figure 2.1.5 shows the DRIFTS spectra for the gas phase during the CO-removal of an actual post-reforming stream; the spectra in shown every 5 h. Intensity of OCO stretching vibration at 1736 and 1300 cm^{-1}, which is related to CO_{ad} on active metal [56], decreases over 45 h, indicating that the catalyst loses its capacity to interact with CO. Increasing in metal active particles diameter by sintering in ST sample (see Table 2.1.2), which corresponds to the sample used

in stability test, could cause the deficiency in the CO_{ad} formation. Additionally, peak at 1648 cm^{-1}, which is associated to water on Au/CeO_2 [44], also decreases with TOS. The high concentration of oxidants, such as water, on the catalytic surface during the first hours of operation could be related to the reduction in oxygen vacancies (Ce^{3+}/Ce^{4+}) in ST sample (see Table 2.1.2) and consequently to the lost in CO_2 yield with TOS (see Figure SM.6 of Supplementary Material).

Peaks at 1300 and 1500 cm^{-1} are linked to the presence of $[COOH]_s$ formates, while peak at 1450 cm^{-1} corresponds to carbonate species [51]. Both species, formates and carbonates, are intermediate in the formation of CO_2, CH_4, and other stable carbon species [41,56]. Peaks of formate species decrease slightly with TOS possibly due to the reduction of $v_s(OCO)$ of $[COOH]_s$ by the deficiency in CO_{ad} formation. Meanwhile, carbonates species remain stable, suggesting that carbonates are the main intermediates in CO-removal of post-reforming stream on $Au_{1.0}Cu_{1.0}/Ce$. Band intensities of surface bidentate carbonate species (1150 to 1279 cm^{-1} [44]) increased after 45 h TOS. Carbonate species, such as bidentate carbonate, have been previously associated with carbon deposition [31,57], which contributes to decrease in catalytic activity. The formation of a new peak around 1000 cm^{-1} would confirm the formation of n-alkanes [58] on the surface of the catalyst. In fact, weight loss of ST sample (see Table 2.1.2) was higher compared to the other samples. Therefore, reduction in oxygen vacancies by oxidation of the catalytic surface with TOS and elevated formation of carbonate species with subsequent carbonizing to n-alkenes, could be the main causes of deactivation of $Au_{1.0}Cu_{1.0}/Ce$ catalyst with TOS.

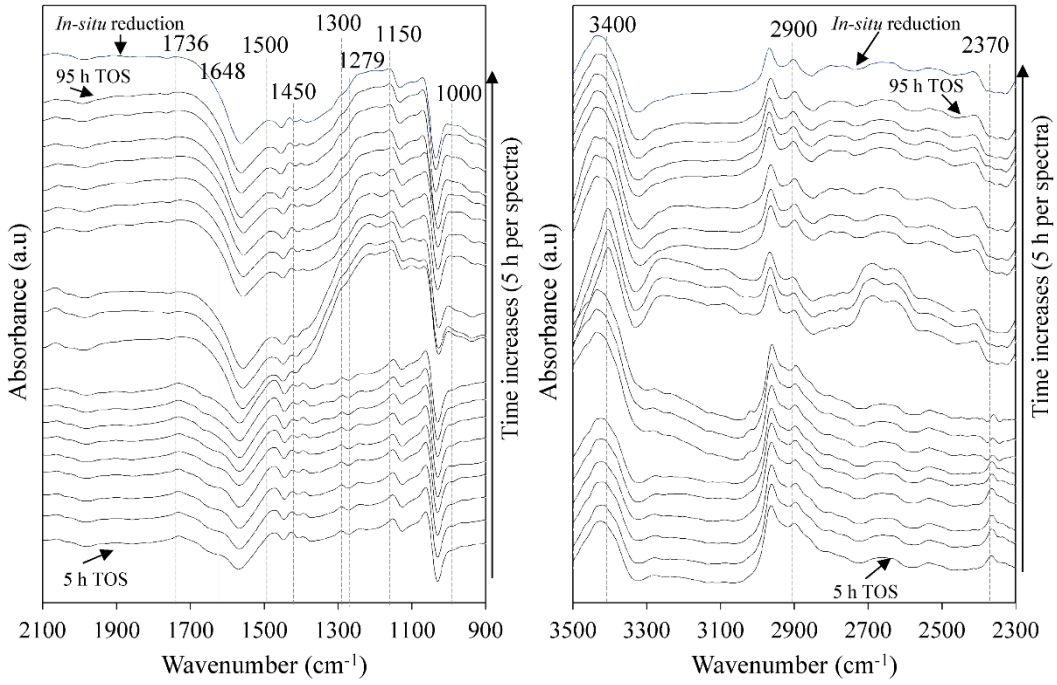

Figure 2.1.5. *Operando* DRIFTS spectra for CO-removal of a post-reforming stream on $Au_{1.0}Cu_{1.0}/Ce$ catalyst. Each spectrum was taken every 5 h t a total of 95 h.

Additionally, peak about 3400 cm^{-1} corresponds to a hydroxyl group, which is related

to formate and carbonate species [52]. Then, formation of carbonate intermediates and subsequent deposition on $Au_{1.0}Cu_{1.0}$/Ce catalyst could be favored by the excess of hydroxyl groups on the catalyst surface (see (Os + OH^-)/Ce molar ratio in Table 2.1.2). On the other hand, the CO_2 peak, observed between 2450–2300 cm^{-1} [59], shows a continuous decrease which is consistent with the loss in the CO_2 yield observed during stability test (see Supplementary Material, Figure SM.6). However, C–H stretching vibration at 2900 and 3000 cm^{-1} [44], which are related to CH_4 formation [59], increased with time, indicating that CH_4 formation was not affected by carbon deposition and seems to be favored by catalyst oxidation In fact, CH_4 formation is thermodynamically favorable (see Supplementary Material, Figure SM.4) and the role of the catalysts could mitigate the hydrogenation of carbon species. Thus, reduction in oxygen vacancies by cumulative surface oxidation and deposition of carbonate compounds could be related to the decrease in CO_2 formation and the increase in CH_4 formation.

Finally, this catalyst was *in-situ* reduced using an 8 mol% H_2/Ar stream by 1 h at 300 °C. The last spectra on Figure 2.1.5 was taken after this treatment. Significant changes were not observed after reduction, indicating that, if the reactivation process is delayed, the catalyst could be irreversibly deactivated.

Reactivation tests Based on *operando* DRIFTS results, several reactivation treatments were carried out to $Au_{1.0}Cu_{1.0}$/Ce catalyst (see Supplementary Material, Table SM.3 and Figure SM.4 to easily identify their effect on the recovery of catalytic activity. An *in-situ* reduction (treatment 4 in Table SM.2) with 8 mol% H_2/Ar stream (300 mL/min) at 300 °C for 1 h, followed by a degasification in Ar at 300 °C for 30 min was selected as treatment to prevent catalysts deactivation. Moreover, this reactivation treatment was carried out every 24 h to prevent the irreversible deactivation observed by *operando* DRIFTS. Figure 2.1.6 shows the catalytic performance of the $Au_{1.0}Cu_{1.0}$/Ce catalyst undergoing the reactivation treatment every 24 h. Low concentration of CO (70 ppm) is achieved when the catalysts was periodically reduced (see Figure 2.1.6a), suggesting that a reduced catalyst surface is paramount in the CO-removal. Excessive surface oxidation by the presence of oxidants in the gas phase could quickly affect catalytic activity due to reduced surface oxygen vacancies [20].

H_2 loss is also shown in Figure 2.1.6a. After 1 h, H_2 loss decreases rapidly, achieving 9% at 9 h, followed by increasing and decreasing intervals. After the first reduction treatment, H_2 conversion is kept below 14%. Bimetallic catalysts supported on CeO_2 tend to experience surface rearrangements under both reducing and oxidizing atmospheres [60], affecting the catalytic performance. These rearrangements have been linked to the modification in the number of oxygen vacancies [61] which are involved in the oxidation mechanism [40]. In fact, preventive *in-situ* reduction treatment succeeds in retaining oxygen vacancies on R-ST sample compared to fresh sample (R-O sample), avoiding oxidation of surface of CeO_2 and mitigating carbonaceous depositions observed in ST sample (see Table 2.1.2).

Figure 2.1.6b shows CO_2 and CH_4 yield with TOS and reactivation cycles. Decrease of CH_4 and increase of CO_2 production are observed at the same time than H_2 loss decreases. Thus, methanation activity of the catalyst declined with TOS; furthermore, CH_4 consumption was observed in the reduced sample, indicating that CH_4 decomposition or reverse

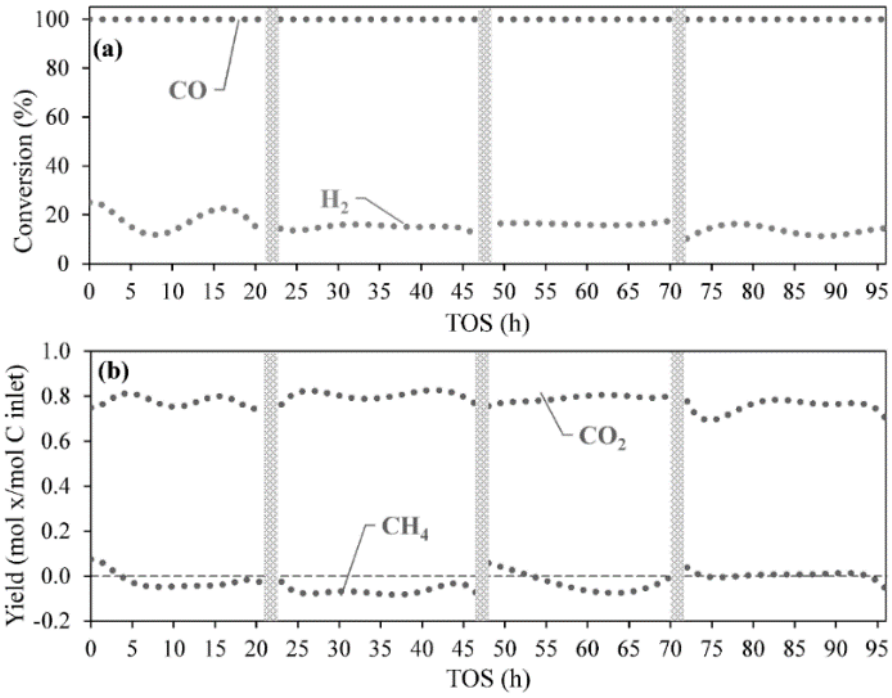

Figure 2.1.6. (a) CO and H_2 conversion, and (b) CO_2 and CH_4 yield during the CO-removal of a post-reforming stream of a post-reforming stream over $Au_{1.0}Cu_{1.0}$/Ce catalysts. Inlet stream: 7.8% H_2, 2.0% CO, 0.5% CO_2, 0.3% CH_4, 1.4% H_2O, 1.8% O_2, 6.8% N_2, and 79.4% Ar. Reaction conditions: SV=6.5 ± 2 $L*g_{cat}^{-1}*min^{-1}$; 50 mg of catalyst and 250 mg of inert quartz; 210 °C. Vertical lines show reactivation treatments every 24 h with an *in-situ* reduction with 8 mol% H_2/Ar (300 mL/min) at 300 °C for 1 h followed by degassing in Ar at 300 °C for 30 min.

methanation could be taking place, favored by catalyst reactivation by reduction. This behavior may explain the increasing CO_2 yield and the mitigation of H_2 loss with TOS. Indeed, CH_4 increased rapidly in ST sample after 23 h (see Supplementary Material, Figure SM.6). Caputo et al. [42] reported that a reduction treatment contributes to Cu redistribution and stabilization on CuO/CeO_2. Thus, TOS could favor a rearrangement on the catalyst surface, which reduces CH_4 formation and H_2 loss. Nonetheless, oxidant species such as O_2 and water could affect the catalyst activity and selectivity, favoring a rapid deactivation. Periodic *in-situ* reduction would mitigate this accumulative surface oxidation, achieving high activity with less H_2 loss.

Table 2.1.3 compares the catalytic results obtained in this work with recent literature reports dealing with the CO removal of H_2-rich streams. Although reaction conditions, catalytic regimes, and feed compositions were different, all catalytic systems reported a high activity in CO conversion ($> 90\%$), using a total metal loading lower than 3 wt%, except for studies reported by Castañeda et al. [35] and Lee et al. [62], where a higher metal loading was used. However, a distinct feature of this work is the evaluation of catalysts for CO elimination directly from a post-reforming stream. Most of the studies use a model mixture for this purpose. Likewise, the model mixture commonly used corresponds to the outlet of the primary step (traditionally a reactor of WGSR), when most of the CO has been removed [19] and H_2/CO ratio is higher. Therefore, the feasibility of integrating CO removal with reforming using only two reactors is presented in this work, avoiding several reactors [31,62]. Also, the percent of H_2 lost was explicit in this work because it is an important criterium in catalysts selection [63]; however, this information is usually missing in the literature. Similarly, stability tests and reactivation treatment are important to maintain and improve catalyst performance over time [55]. In this work, a continuous stability test of 95 h TOS was performed (the longest of all studies included in Table 2.1.3) and several activation methods (see Table SM.2 of Supplementary Material) were evaluated.

2.1.5 Conclusions

CO-removal in an actual post-reforming stream over $AuCu/CeO_2$ catalysts with different Au:Cu ratios was investigated. The concentration of the post-reforming stream remained constant due to the stable $RhPt/CeO_2$-SiO_2 catalyst used during the SRE. This stream was subjected to the CO catalytic cleaning. Response surfaces allowed to identify that Au presence in the $AuCu/CeO_2$ catalyst favors CO conversion but affects CO_2 yield. $Au_{1.0}Cu_{1.0}/Ce$ catalyst showed the lowest H_2 loss (25%) achieving low CO concentration (70 ppm) at 210 °C. However, H_2 loss is higher than that reported for synthetic feeds because a complex network of reactions is present in the actual post-reforming stream cleaning. Independent evaluation of CO-PROX, WGSR, H_2 oxidation, CO-methanation, and CO_2-methanation on $Au_{1.0}Cu_{1.0}/Ce$ catalyst shows that CO_2 formed by CO oxidation during post-reforming cleaning could be vulnerable to hydrogenation, producing CH_4 and consuming H_2.

Characterization tests indicated that CeO_2 interacts mainly with Cu to form surface oxygen vacancies on CeO_2. Au favors OH^- formation, improving the catalytic activity, whereas Cu increases the catalyst surface area and promotes CO_2 formation, increasing the selectivity of the catalyst. However, an excess of carbon intermediates as a result of the presence of OH^- species promotes both undesirable CH_4 formation and the presence of carbonaceous deposits

Table 2.1.3. Comparison of various catalytic systems for CO removal

Description	This work	Other authors					
		Liao et al. [31]	Castañeda et al. [35]	Zhang et al. [36]	Fiorenza et al. [64]	Lee et al. [62]	Miao et al. [65]
Catalysts	$AuCu/CeO_2$	$AuCu/CeO_2$	CeO_2/CuO	$Au/CuO\text{-}CeO_2$	$AuAg/CeO_2$	$Au/CuO\text{-}CeO_2$	$Au/CeO_2/Al_2O_3$
Total metal loading (wt%)	2	2.2	41.4	3	2	1	1.3
GHSV (h^{-1})	64,100	NR	80,000	29,300	8,400	NR	30,000
Kind of feed	Post-reforming	Model mixture	Model mixture	Model mixture	Model mixture	Model mixture	Model mixture
Composition in the feed (mol%)	H_2 (7.8), O_2 (1.8), N_2 (6.8), CO (2.0), CO_2 (0.5), CH_4 (0.3), H_2O (1.4) and Ar (79.4)	H_2 (35), O_2 (1), CO (1), CO_2 (10), H_2O (10) and He (48)	H_2 (50), O_2 (1.25), CO (1), H_2O (0.2) and Ar (48.55)	H_2 (50), O_2 (1), CO (1), and N_2 (48)	H_2 (98), O_2 (1), and CO (1)	H_2 (65.3), O_2 (1.3), CO (1.3), and He (32.1)	H_2 (40), O_2 (1), CO (1), and N_2 (58)
CO conversion (%)	100	100	92	100	90	100	100
H_2/CO mol ratio	3.9	35	50	50	98	50.2	40
H_2 conversion (%)	14	NR	NR	NR	NR	NR	NR
Stability test (h)	95	NR	NR	80	14	NR	NR
Reactivation treatment	Yes	NR	NR	None	None	NR	NR

NR: not reported.

on the catalyst. Finally, stability tests and *operando* DRIFTS showed that $Au_{1.0}Cu_{1.0}/CeO_2$ catalyst is susceptible to rearrangements and cumulative surface oxidation during operation, which promote high carbon deposition and catalytic deactivation. Nevertheless, periodic *in-situ* reduction treatment contributes to stabilize and maintain high activity, decreasing H_2 loss with time. $Au_{1.0}Cu_{1.0}/Ce$ catalyst was active for 95h TOS, when is reduced every 24 h, achieving fuel-cell grade hydrogen with a 14% H_2 loss.

2.1.6 Acknowledgments

The authors are grateful to Colciencias (Francisco Jose de Caldas Fund) and Universidad de La Sabana for the financial support of this work through the Project ING-163 (Colciencias contract 174-2016). The authors also acknowledge Universidad de Antioquia, Universidad de Alicante, and Universidad Nacional de Colombia for their support to this project. B. Cifuentes acknowledges Colciencias for the doctoral scholarship (grant number 727-2015).

2.1.7 References

[1] N.P. Brandon, Z. Kurban, Philos. Trans. R. Soc. London A Math. Phys. Eng. Sci. 375 (2017) 1–17.
[2] R. Roldán, Int. J. Hydrogen Energy 40 (2015) 2035–2046.
[3] W. Cai, F. Wang, E. Zhan, A. Vanveen, C. Mirodatos, W. Shen, J. Catal. 257 (2008) 96–107.
[4] D. Zanchet, J.B.O. Santos, S. Damyanova, J.M.R. Gallo, J.M. C. Bueno, ACS Catal. 5 (2015) 3841–3863.
[5] H.J. Alves, C. Bley Junior, R.R. Niklevicz, E.P. Frigo, M.S. Frigo, C.H. Coimbra-Araújo, in: Int. J. Hydrogen Energy, Pergamon, 2013, pp. 5215–5225.
[6] B. Dou, H. Zhang, G. Cui, Z. Wang, B. Jiang, K. Wang, H. Chen, Y. Xu, Int. J. Hydrogen Energy 42 (2017) 26217–26230.
[7] E.M. Izurieta, D.O. Borio, M.N. Pedernera, E. López, Int. J. Hydrogen Energy 42 (2017) 18794–18804.
[8] B. Dou, H. Zhang, G. Cui, Z. Wang, B. Jiang, K. Wang, H. Chen, Y. Xu, Energy Convers. Manag. 155 (2018) 243–252.
[9] L. Shao, S. Quan, X.Q. Cheng, X.J. Chang, H.G. Sun, R.G. Wang, Int. J. Hydrogen Energy 38 (2013) 5122–5132.
[10] H.H. Tseng, H.W. Chuang, G.L. Zhuang, W.H. Lai, M.Y. Wey, Int. J. Hydrogen Energy 42 (2017) 11379–11391.
[11] Z. Liao, G. Tu, J. Lou, B. Jiang, J. Wang, Y. Yang, Int. J. Hydrogen Energy 41 (2016) 5243–5249.
[12] H.Z. Chen, T.S. Chung, Int. J. Hydrogen Energy 37 (2012) 6001–6011.
[13] M. Teixeira, L.M. Madeira, J.M. Sousa, A. Mendes, Int. J. Hydrogen Energy 35 (2010) 11505–11513.
[14] U. Lucia, Renew. Sustain. Energy Rev. 30 (2014) 164–169.
[15] U. Gardemann, M. Steffen, A. Heinzel, Int. J. Hydrogen Energy 39 (2014) 18135–18145.
[16] I. Rossetti, M. Compagnoni, M. Torli, Chem. Eng. J. 281 (2015) 1036–1044.
[17] T. V. Choudhary, D.W. Goodman, Catal. Today 77 (2002) 65–78.

[18] A.M. Abdalla, S. Hossain, O.B. Nisfindy, A.T. Azad, M. Dawood, A.K. Azad, Energy Convers. Manag. 165 (2018) 602–627.
[19] R.J. Farrauto, Chem. Eng. J. 238 (2014) 172–177.
[20] L. Ilieva, P. Petrova, G. Pantaleo, R. Zanella, L.F. Liotta, V. Georgiev, S. Boghosian, Z. Kaszkur, J.W. Sobczak, W. Lisowski, A.M. Venezia, T. Tabakova, Appl. Catal. B Environ. 188 (2016) 154–168.
[21] O. Pozdnyakova, D. Teschner, A. Wootsch, J. Kröhnert, B. Steinhauer, J. Catal. 237 (2006) 1–16.
[22] T.R. Reina, S. Ivanova, O.H. Laguna, M.A. Centeno, J.A. Odriozola, Appl. Catal. B Environ. 197 (2016) 67–72.
[23] B. Cifuentes, M.F. Valero, J. a. J. Conesa, M. Cobo, Catalysts 5 (2015) 1872–1896.
[24] B. Cifuentes, M. Figueredo, M. Cobo, Catalysts 7 (2017) 1–20.
[25] B. Cifuentes, M. Hernández, S. Monsalve, M. Cobo, Appl. Catal. A Gen. 523 (2016) 283–293.
[26] O. Jakdetchai, T. Nakajima, J. Mol. Struct. Theochem 619 (2002) 51–58.
[27] C. Ratnasamy, J.P. Wagner, Catal. Rev. 51 (2009) 325–440.
[28] O.H. Laguna, W.Y. Hernández, G. Arzamendi, L.M. Gandía, M. a. Centeno, J. a. Odriozola, Fuel 118 (2014) 176–185.
[29] D.C. Upham, A.R. Derk, S. Sharma, H. Metiu, E.W. McFarland, T. Onishi, P. Fornasiero, M. Peressi, A. Baldereschi, R. Rosei, G. Comelli, Catal. Sci. Technol. 5 (2015) 1783–1791.
[30] L.F. Córdoba, A. Martínez-Hernández, Int. J. Hydrogen Energy 40 (2015) 16192–16201.
[31] X. Liao, W. Chu, X. Dai, V. Pitchon, Appl. Catal. B Environ. 142–143 (2013) 25–37.
[32] Y. Choi, H.G. Stenger, J. Power Sources 129 (2004) 246–254.
[33] T.A. Adams, P.I. Barton, Fuel Process. Technol. 92 (2011) 639–655.
[34] N. Krishnankutty, M.A. Vannice, J. Catal. 155 (1995) 312–326.
[35] R. Castañeda, L. Pascual, A. Martínez-Arias, Catal. Commun. 108 (2018) 88–92.
[36] A. Zhang, L. Zhang, G. Jing, H. Zhang, S. Wang, H. Su, S. Zeng, Int. J. Hydrogen Energy 43 (2018) 10322–10333.
[37] J.D.S.L. Fonseca, H.S. Ferreira, N. Bion, L. Pirault-Roy, M.D.C. Rangel, D. Duprez, F. Epron, Catal. Today 180 (2012) 34–41.
[38] H.C. Lee, D.H. Kim, Catal. Today 132 (2008) 109–116.
[39] R.J. M. J. Kahlich, H.A. Gasteiger, Iournal New Mater. Electrochem. Syst. 1 (1998) 39–46.
[40] H. Wang, H. Zhu, Z. Qin, G. Wang, F. Liang, J. Wang, Catal. Commun. 9 (2008) 1487–1492.
[41] H. Jin, R. You, S. Zhou, K. Ma, M. Meng, L. Zheng, J. Zhang, T. Hu, Int. J. Hydrogen Energy 40 (2015) 3919–3931.
[42] T. Caputo, L. Lisi, R. Pirone, G. Russo, Appl. Catal. A Gen. 348 (2008) 42–53.
[43] S. Chen, L. Luo, Z. Jiang, W. Huang, ACS Catal. 5 (2015) 1653–1662.
[44] S. Zhang, X. Li, B. Chen, X. Zhu, C. Shi, A. Zhu, ACS Catal. (2014) 3481–3489.
[45] K.I. Maslakov, Y.A. Teterin, A.J. Popel, A.Y. Teterin, K.E. Ivanov, S.N. Kalmykov, V.G. Petrov, P.K. Petrov, I. Farnan, Appl. Surf. Sci. 448 (2018) 154–162.
[46] D.M. Gu, Y.Y. Chu, Z.B. Wang, Z.Z. Jiang, G.-P. Yin, Y. Liu, Appl. Catal. B Environ. 102 (2011) 9–18.

[47] E.J. Choi, Y.H. Lee, D.W. Lee, D.J. Moon, K.Y. Lee, Mol. Catal. 434 (2017) 146–153.
[48] S. Poulston, P.M. Parlett, P. Stone, M. Bowker, Surf. Interface Anal. 24 (1996) 811–820.
[49] Y. Luo, K. Chen, J. Wang, J. Lu, L. Zhong, R. Chen, Y. Lei, S. He, G. Wan, C. Han, Mol. Catal. 443 (2017) 241–252.
[50] T.R. Reina, S. Ivanova, M. a. Centeno, J. a. Odriozola, Int. J. Hydrogen Energy 40 (2015) 1782–1788.
[51] T. Sakwarathorn, A. Luengnaruemitchai, S. Pongstabodee, J. Ind. Eng. Chem. 17 (2011) 747–754.
[52] X. Wang, J.A. Rodriguez, J.C. Hanson, D. Gamarra, A. Martínez-Arias, M. Fernández-García, A. Rodriguez, J.C. Hanson, D. Gamarra, M. Ferna, J. Phys. Chem. B 110 (2006) 428–434.
[53] S.H. Kim, S.W. Nam, T.H. Lim, H.I. Lee, Appl. Catal. B Environ. 81 (2008) 97–104.
[54] G. Marbán, I. López, T. Valdés-Solís, Appl. Catal. A Gen. 361 (2009) 160–169.
[55] P. Lanzafame, G. Centi, S. Perathoner, Catal. Today 234 (2014) 2–12.
[56] Q. Pan, J. Peng, S. Wang, S. Wang, Catal. Sci. Technol. 4 (2014) 502–509.
[57] A. Abd El-Moemen, A.M. Abdel-Mageed, J. Bansmann, M. Parlinska-Wojtan, R.J. Behm, G. Kučerová, J. Catal. 341 (2016) 160–179.
[58] J.P. Gorce, S.J. Spells, Polymer (Guildf). 43 (2002) 4043–4046.
[59] A. Westermann, B. Azambre, M.C. Bacariza, I. Graça, M.F. Ribeiro, J.M. Lopes, C. Henriques, Catal. Today 283 (2017) 74–81.
[60] N.J. Divins, I. Angurell, C. Escudero, V. Pérez-Dieste, J. Llorca, Science. 346 (2014) 620–623.
[61] M. Ozawa, M. Haneda, M. Hattori, IOP Conf. Ser. Mater. Sci. Eng. 18 (2011) 1–4.
[62] D.S. Lee, Y.W. Chen, Int. J. Hydrogen Energy 41 (2016) 3605–3612.
[63] T.R. Reina, C. Megías-Sayago, A.P. Florez, S. Ivanova, M.Á. Centeno, J.A. Odriozola, J. Catal. 326 (2015) 161–171.
[64] R. Fiorenza, C. Crisafulli, S. Scirè, Int. J. Hydrogen Energy 41 (2016) 19390–19398.
[65] Y.X. Miao, J. Wang, W.C. Li, Cuihua Xuebao/Chinese J. Catal. 37 (2016) 1721–1728.

2.2 Selection of support for CO removal

In the previous chapter $AuCu/CeO_2$ with a mole ratio of Au/Cu = 1 was presented as a promising catalyst to CO removal. However, $AuCu/CeO_2$ is susceptible to deactivation due to structural changes in the support. For this, in this chapter, several alternatives of metal oxides were evaluated as supports for the Au-Cu system, looking for an active, selective, and stable material for CO removal from an actual syngas.

This section corresponds to an article published in *Catalysts, (2019) 9, 10, 852–877.* - DOI:10.3390/catal9100852

Raw and processed data of this study can be downloaded from: https://data.mendeley.com/datasets/6pxcn5k3sx/1 - DOI: 10.17632/6pxcn5k3sx.1

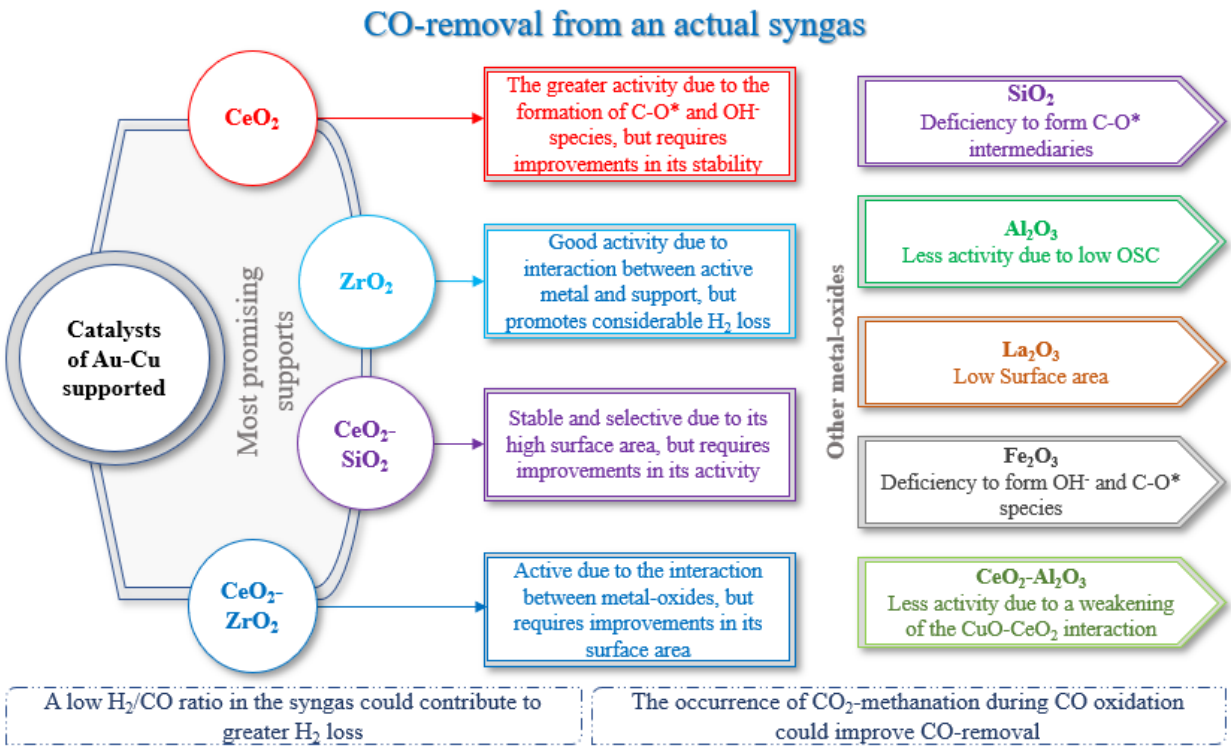

Graphical abstract

Single and dual metal oxides as promising supports for carbon monoxide removal from an actual syngas: the crucial role of support on the selectivity of the Au–Cu system

Bernay Cifuentes[1], Felipe Bustamante[2] and Martha Cobo[1*]

[1]Energy, Materials, and Environment Laboratory, Chemical Engineering Department, Universidad de La Sabana, Campus Universitario Puente del Común, Km. 7 Autopista Norte, Bogotá, 250001, Colombia. bernay.cifuentes@unisabana.edu.co

[2]Environmental Catalysis Laboratory, Chemical Engineering Department, Universidad de Antioquia UdeA, Calle 70 No. 52-21, Medellín, 050010, Colombia. felipe.bustamante@udea.edu.co

*Correspondence: martha.cobo@unisabana.edu.co, Tel: +571 8615555 Ext. 25207, Fax: 571 8615555

2.2.1 Abstract

A catalytic screening was performed to determine the effect of the support on the performance of an Au–Cu based system for the removal of CO from an actual syngas. First, a syngas was obtained from reforming of ethanol. Then, the reformer outlet was connected to a second reactor, where Au–Cu catalysts supported on several single and dual metal oxides (i.e., CeO_2, SiO_2, ZrO_2, Al_2O_3, La_2O_3, Fe_2O_3, CeO_2-SiO_2, CeO_2-ZrO_2, and CeO_2-Al_2O_3) were evaluated. AuCu/CeO_2 was the most active catalyst due to an elevated oxygen mobility over the surface, promoting CO_2 formation from adsorption of C–O* and OH^- intermediates on Au^0 and CuO species. However, its lower capacity to release the surface oxygen contributes to the generation of stable carbon deposits, which lead to its rapid deactivation. On the other hand, AuCu/CeO_2-SiO_2 was more stable due to its high surface area and lower formation of formate and carbonate intermediates, mitigating carbon deposits. Therefore, use of dual supports could be a promising strategy to overcome the low stability of AuCu/CeO_2. The results of this research are a contribution to integrated production and purification of H_2 in a compact system.

Keywords: CO-PROX; CO-SMET; CO_2 methanation; Hydrogen purification; Process integration.

2.2.2 Introduction

Synthesis gas (syngas) is used as a chemical building block in the synthesis of commodity chemicals and for energy applications. Specifically, syngas can be used in combustion processes [1], gas turbines [2], or hydrogen fuel cells (H_2-FC) [3] to produce energy. The H_2-FC are promising systems to provide sustainable energy for households, industry, transportation, and small devices. Likewise, the use of H_2-FC has been proposed as an alternative to supply energy in places that are not connected to the electrical network and for remote installations [4].

The syngas composition varies depending on the production source, but mostly contains H_2, carbon monoxide (CO), and light hydrocarbons. Bioethanol reforming is one of the most used pathways to produce syngas due to its high yield to H_2 [5]. In a previous study [6], we obtained a syngas containing H_2, CO, CO_2, CH_4, and H_2O from ethanol steam reforming (ESR) using a RhPt/CeO_2-SiO_2 catalyst. Syngas production remained stable for 72 h of continuous operation and on/off cycles. This syngas could be used for sustainable energy production in H_2-FC. However, CO must be removed from the syngas because of its harmful effect on fuel cell electrodes [7].

One of the most used strategies of CO removal from syngas is via chemical pathways, which includes preferential oxidation of CO (CO-PROX) [8,9], water gas shift reaction (WGSR) [10], and selective CO methanation (CO-SMET) [10]. Traditionally, the objective of the CO cleanup step is to ensure CO concentrations below 10 ppm, which requires several catalytic reactors in series [11] and presents a high operating cost. However, recent research studies have allowed the development of H_2-FC systems that tolerate CO concentrations above 100 ppm [12–14]. These contributions facilitate the use of less complex systems for syngas purification, which could lead to the development of more compact and economic H_2 technology.

Anticipating the commercialization of a new generation of more CO-tolerant H_2-FC, it has been proposed to redesign the CO removal stage to reduce the number of process units in syngas purification. The new approach seeks to carry out CO removal using a single catalytic reactor, where several reactions occur simultaneously (i.e., CO-PROX, WGSR, and CO-SMET). Kugai et al. [15] studied Pt–Cu and Pd–Cu bimetallic catalysts supported on CeO_2 for oxygen-enhanced water gas shift (OWGS), where WGSR and CO-PROX occur concurrently, reporting higher CO removal from a model reformate gas (synthetic syngas) in the OWGS compared to the WGSR carried out individually. Similarly, Xu and Zhang [16] reported that the presence of CO-SMET during CO-PROX on a commercial Ru/Al_2O_3 catalyst allows for wider temperature windows that ensure the CO removal of a synthetic syngas. Despite these valuable contributions, the CO removal from syngas in a compact system is still at laboratory scale. Among the limitations for evaluation at the pilot scale is the lack of consensus regarding the catalyst and the most appropriate operating conditions to carry out the syngas purification.

Au is recognized as a promising catalyst in the three cleaning reactions of syngas (i.e., CO-PROX, WGSR, and CO-SMET) [17,18]. Reina et al. [19] evaluated bimetallic catalysts of Au–M (M = La, Ni, Cu, Fe, Cr, Y), reporting that CO oxidation is favored by the Au–Cu combination because Cu interacts strongly with the support, favoring the oxygen mobility in the catalyst. Also, in a previous study [20], we evaluated Au–Cu bimetallic catalysts supported on CeO_2 for CO removal from a syngas obtained from ESR. It was possible to reduce the CO concentration below 100 ppm, but the catalyst showed rapid deactivation after 40 h. Deactivation was related to structural changes in the support and to the accumulation of carbonaceous compounds during continuous operation. Thus, this study illustrated that the support plays a key role in CO removal from an actual syngas and led us to evaluate different supports for CO removal from a syngas in the search for a stable material.

Figure 2.2.1 shows the supports most used in the CO removal processes (i.e., WGSR, CO-PROX, CO-SMET, or their combinations). CeO_2, Fe_2O_3, ZrO_2, TiO_2, and Al_2O_3 are the most commonly used single supports in CO removal from synthetic syngas. However, there is a growing interest in mixed supports (dual metal oxides) because they may have characteristics not observed in individual supports [21]. Most combinations of dual metal oxides include CeO_2 in the matrix, usually combined with supports that provide larger surface area, such as Al_2O_3 [22] and SiO_2 [23], or with basic oxides, such as ZrO_2, to generate new active sites [24]. TiO_2 is mainly used in CO removal by photocatalytic processes [25] and was not considered in this study. On the other hand, although La_2O_3 is not among the most used supports in CO removal, it was recently reported that La_2O_3 is effective for avoiding carbon deposits during CO-SMET [26].

Although several supports for syngas cleanup have been proposed, each investigation was carried out under different experimental conditions and using synthetic syngas, which makes it difficult to select the most suitable support for the CO removal. Therefore, the objective of this work was to study the CO removal from an actual syngas using bimetallic catalysts of AuCu-supported on single and dual metal oxides. Specifically, CeO_2, ZrO_2, La_2O_3, Fe_2O_3, Al_2O_3, and SiO_2 were selected as single metal oxides, and CeO_2-SiO_2, CeO_2-ZrO_2, and CeO_2-Al_2O_3 as dual metal oxides. The catalytic performance of the supports with and without active metals (i.e., Au and Cu) was evaluated. Then, the activity, selectivity, and stability were established as criteria for selecting the most suitable support for the CO elimination. In

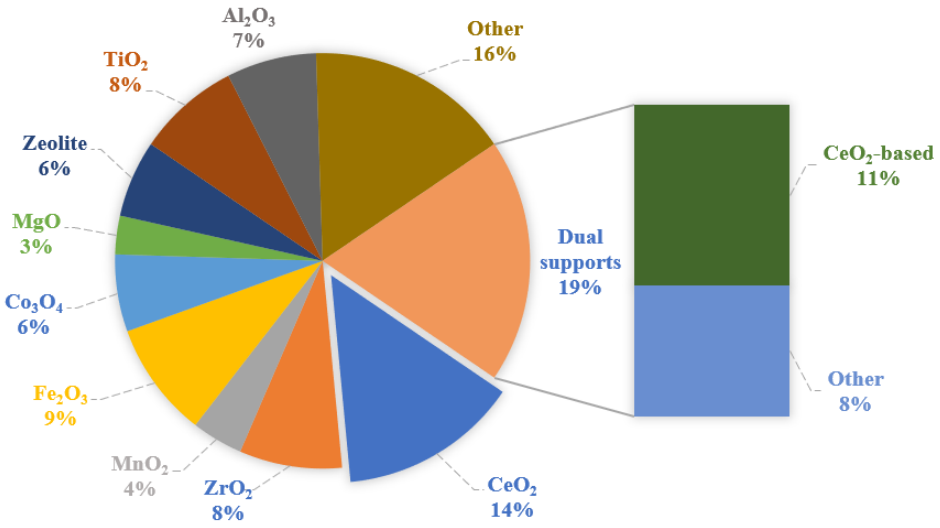

Figure 2.2.1. Supports used in CO removal from syngas streams using CO-PROX, WGSR or CO-SMET reactions.

addition, characterization tests were conducted, such as temperature programmed reduction (TPR), surface area tests using the Brunauer-Emmett-Teller (BET) method, oxygen storage capacity (OSC) tests, thermogravimetric analysis (TGA), and *in-situ* diffuse reflectance infrared Fourier transform spectroscopy (DRIFTS).

2.2.3 Experimental

Support selection

The supports evaluated in this work were selected according to a literature review and are summarized in Figure 2.2.1. Scientific articles published between 2012 and 2019 that included at least one of the following reactions were reviewed: CO-PROX, WGSR, and CO-SMET. The detailed list of reviewed articles can be consulted in Table SM.5 (see Supplementary Material).

Catalyst synthesis

The single supports of CeO_2, ZrO_2, and Fe_2O_3 were obtained by calcination at 500 °C for 2 h of $Ce(NO_3)_3{\cdot}6H_2O$ (CAS: 10294-41-4, Sigma Aldrich, St. Louis, MO, USA), $ZrO(NO_3)_2{\cdot}xH_2O$ (CAS: 14985-18-3, Sigma Aldrich, St. Louis, MO, USA), and $Fe(NO_3)_3{\cdot}9H_2O$ (CAS: 7782-61-8, Merck, Darmstadt, HE, Germany), respectively. Also, commercial oxides of La_2O_3 (CAS: 1312-81-8, Sigma Aldrich, St. Louis, MO, USA), Al_2O_3 (CAS: 1344-28-1, Sigma Aldrich, St. Louis, MO, USA), and SiO_2 (CAS: 60676-86-0, Merck, Darmstadt, HE, Germany) were used, which were also calcined at 500 °C in a muffle for 2 h.

Dual supports of CeO_2-ZrO_2, CeO_2-Al_2O_3, and CeO_2-SiO_2 were obtained from aqueous solutions of Ce $Ce(NO_3)_3{\cdot}6H_2O$ (CAS: 10294-41-4, Sigma Aldrich, St. Louis, MO, USA) with

$ZrO(NO_3)_2{\cdot}H_2O$ (CAS: 14985-18-3, Sigma Aldrich, St. Louis, MO, USA), Al_2O_3 (CAS: 1344-28-1, Sigma Aldrich, St. Louis, MO, USA), and SiO_2 (CAS: 60676-86-0, Merck, Darmstadt, HE, Germany), respectively, ensuring a molar ratio of Ce/M = 1 (M = Si, Zr and Al). Each solution was dried at 80 °C for 24 h and calcined at 500 °C in a muffle for 4 h. All supports (i.e., single and dual metal oxides) were screened with a 140-mesh sieve.

Bimetallic Au–Cu catalysts supported on each single and dual metal oxide were prepared according to the procedure described in [20], ensuring active metal loads of Au (1 wt%) and Cu (1 wt%). Au was first impregnated on each support by the precipitation-deposition method at pH 6 and 80 °C, using a solution of $HAuCl_4{\cdot}3H_2O$ (CAS: 16961-25-4 Sigma Aldrich, USA). The filtered solid was dried at 80 °C for 24 h. Subsequently, Cu was included in the Au catalysts by the incipient wetness impregnation method, using a solution of $Cu(NO_3)_2{\cdot}3H_2O$ (CAS: 10031-43-3, Sigma Aldrich, St. Louis, MO, USA). The catalyst obtained was dried at 80 °C for 24 h, calcined at 500 °C in a muffle for 2 h, and screened with a 140-mesh sieve.

The $RhPt/CeO_2{\text{-}}SiO_2$ catalyst for ESR was prepared according to the methodology described in [6]. Briefly, $CeO_2{\text{-}}SiO_2$ support was obtained from $Ce(NO_3)_3{\cdot}6H_2O$ (CAS: 10294-41-4, Sigma Aldrich, St. Louis, MO, USA) and SiO_2 (CAS: 60676-86-0, Merck, Darmstadt, HE, Germany) solutions, ensuring a molar ratio of Ce/Si = 2. Rh and Pt were deposited on the CeO_2-SiO_2 support by the incipient wetness co-impregnation method, using $RhCl_3{\cdot}H_2O$ (CAS: 20765-98-4, Sigma Aldrich, St. Louis, MO, USA) and $H_2PtCl_6{\cdot}6H_2O$ (CAS: 10025-65-7, Sigma Aldrich, St. Louis, MO, USA) solutions. The catalyst obtained was dried at 80 °C for 24 h, calcined at 700 °C for 2 h, and screened with a 140-mesh sieve.

Obtaining syngas

The syngas was obtained from ESR with a $RhPt/CeO_2{\text{-}}SiO_2$ catalyst at 700 °C in the first reactor (ESR reactor). The plug flow conditions in the ESR reactor were maintained ensuring L/Dp >50 ratios (i.e., catalytic bed height (L) and catalyst particle size (Dp)) and D/Dp >60 (i.e., diameter internal to the reactor (D)), as recommended in [27]. The catalyst bed consisted of 0.050 g of $RhPt/CeO_2{\text{-}}SiO_2$ and 0.250 g of inert quartz. The reactor feed consisted of 0.3 L/min of a mixture of ethanol (1.8 mol%), water (5.4 mol%), and Ar as carrier gas. The space velocity (SV) was set at 6.4 ± 0.2 L/g_{cat}*min. The syngas obtained in the ESR reactor, containing H_2 (8.4 mol%), CO (2.2 mol%), H_2O (1.6 mol%), CO_2 (0.6 mol%), CH_4 (0.3 mol%), and Ar (86.9 mol%), remained stable, with a variation <6.8%.

Catalytic test

The supports and Au–Cu catalysts for the CO removal from the syngas were evaluated in a second reactor (cleanup reactor) between 100 and 300 °C. For this, the ESR reactor outlet was mixed with dry air, ensuring an excess oxygen factor (λ) of 1.8 ± 0.05 [20], and connected to the cleanup reactor inlet. The plug flow conditions in the cleanup reactor were maintained as previously described for the ESR reactor. The catalyst bed consisted of 0.050 g of catalyst (i.e., supports or Au–Cu catalysts) and 0.250 g of inert quartz. The SV in the

cleanup reactor was set at 6.5 ± 0.3 L/g_{cat}*min. Before the reaction, the supports and Au–Cu catalysts were pretreated *in-situ* at 300 °C with streams of 8% H_2/Ar for 1 h, followed by Ar for 0.5 h, and finally 10% air/Ar for 0.5 h. These samples were labeled as "activated catalyst" (AC). Also, the samples used to obtain the light-off curves were labeled "U", while those used in the stability test were labeled "S".

The species at the outlet of each reactor (i.e., ESR reactor and cleanup reactor) were quantified by gas chromatography (GC) in a Clarus 580 (Perkin Elmer, Waltham, MA, USA), equipped with a Carboxen 1010 plot column (30 m, 0.53 mm ID, Restek, Bellefonte, PA, USA) connected to a thermal conductivity detector (TCD). Ar was used as carrier gas and N_2 as internal reference. The reaction conditions and GC data processed in Excel can be consulted in detail and downloaded from [28].

The conversion of CO (x_{CO}), the production of the main products (Y_{CO_2}, Y_{CH_4}), and the H_2 obtained (Y_{H_2}) from the integrated system were obtained considering the molar flows (F_i) to the output of each reactor (i.e., ESR reactor and cleanup reactor), according to 4, 5 and 6. Production of CO, CH_4, and H_2 were normalized with the amount of carbon entering the system ($F_{C,inlet}$), which remained constant at 5.2×10^{-4} mol/min of C.

$$x_{CO} = \frac{F_{CO,ESR-reactor} - F_{CO,cleanup-reactor}}{F_{CO,ESR-reactor}} \tag{4}$$

$$Y_{CH_4;CO_2} = \frac{F_{CH_4;CO_2,cleanup-reactor} - F_{CH_4;CO_2,ESR-reactor}}{F_{C,inlet}} \tag{5}$$

$$Y_{H_2} = \frac{F_{H_2,cleanup-reactor}}{F_{C,inlet}} \tag{6}$$

Characterization tests

The reducibility of supports and Au–Cu catalysts was determined by TPR. The experiments were carried out in a ChemBET Pulsar unit (Quantachrome Instruments, Boynton Beach, FL, USA) equipped with a TCD. Prior to the reduction, 0.07 ± 0.01 g of AC samples was pretreated with N_2 (0.02 L / min) at 120 °C for 1 h and then cooled to room temperature. Subsequently, 5 % H_2/N_2 was passed, and the temperature was increased to 700 °C (5 °C/min). The H_2 uptake was calculated by integrating the peaks associated with the reduction of active metals (i.e., Au and Cu). The apparent active metal dispersion (H/M ratio) was also determined [29], assuming that the adsorption stoichiometry is one hydrogen atom for one active metal atom (Au + Cu).

The surface area of the samples was determined by standard physisorption of N_2 in a ChemBET Pulsar unit (Quantachrome Instruments, Boynton Beach, FL, USA). For this, 0.06 ± 0.01 g of sample was pretreated with N_2 (0.02 L/min) at 100 °C for 1 h and then cooled to room temperature for 0.5 h. Subsequently, the sample was immersed in a liquid N_2 bath. The BET area was measured with a single point, using 30% N_2/He (0.02 L/min). The measurements were repeated until deviations lower than 5% were obtained.

The OSC values of the samples were measured in a ChemBET Pulsar unit (Quantachrome Instruments, Boynton Beach, FL, USA), according to the procedure described in [30]. Briefly,

0.06 ± 0.01 g of sample was degassed in Ar (0.02 L/min) at 300 °C for 1 h. OSC was measured at 300 and 100 °C with independent samples. For this, 10 pulses of pure O_2 (0.25 mL) were injected to oxidize the sample, followed by a 20 min purge with Ar. Then, pulses of a 5 % CO/Ar mixture (0.25 mL) were injected until a constant signal was obtained. The OSC value was calculated by the CO consumed in the first pulse, and the OSCC value was determined by the total CO consumed.

The weight loss, associated with the presence of impurities, moisture, and carbon deposition in samples, was measured by TGA. The change in mass was determined using a thermogravimetric analyzer (Mettler Toledo, Columbus, OH, USA). For this, 0.02 ± 0.01 g of sample was pretreated with a N_2 (0.1 L/min) at 100 °C for 1 h and then cooled to 40 °C for 0.5 h. Subsequently, the sample was heated to 1000 °C (5 °C/min) in a dry air stream (0.1 L/min). Then, the rate of carbon formation was calculated according to 7.

$$\text{Rate of carbon formation} = \frac{\text{Weight loss in terms of C (mg)}}{\text{mass of catalyst (g)} \times \text{Reaction time (h)}} \tag{7}$$

The CO adsorption on supports and catalysts was studied by *in-situ* DRIFTS in a Nicolet iS10 spectrum device (Thermo Scientific, Waltham, MA, USA) equipped with a diffuse reflection attachment DRK-3 Praying Mantis (Harrick Scientific Products, New York, NY. USA). Spectra were taken between 400 and 4000 cm^{-1}, with 64 scans per minute and a resolution of 4 cm^{-1}. The sample holder was sealed with an airtight hood with ZeSn windows. In addition, the airtight hood was isolated with an Ar stream to avoid interference from the environment. Approximately 0.02 g of AC samples were degassed in Ar (15 mL/min) at 50 °C for 30 min. Then, 10 pulses of 30 μL of CO, obtained from a certified 5% CO/Ar mixture, were injected into the cell; between each pulse, Ar (15 mL/min) was passed for 10 min. Raw and processed Excel data for characterization tests can be downloaded from [28].

2.2.4 Results and discussion

Activity, selectivity, and stability Figure 2.2.2 shows the CO conversion in the cleanup reactor on the bare supports (i.e., without Au and Cu) and Au–Cu-supported catalysts. CeO_2 and ZrO_2 display the larger CO conversion between single metal oxides (Figure 2.2.2a). Indeed, the presence of oxygen vacancies on the surface of an oxide could favor a support showing high activity in the CO oxidation, despite the absence of active metals [31]; on the other hand, supports with low OSC, such as Al_2O_3 [32], present lower activity. The use of dual metal oxides has been proposed as a strategy to overcome the deficiencies of single supports [21]. Figure 2.2.2b shows that CeO_2-SiO_2 increases the CO conversion compared to SiO_2, which could be associated with the interaction between the two oxides. However, no significant improvement in the CO conversion with CeO_2-Al_2O_3 was observed, and even for CeO_2-ZrO_2, the combination of the two metal oxides leads to a less active material. Furthermore, below 260 °C the dual metal oxides showed less activity that single CeO_2, suggesting that the combination of several metal oxides does not always lead to more active materials in the syngas cleaning.

On the other hand, catalytic systems based on Au, Cu and Au–Cu have been studied extensively for the CO oxidation, CO-PROX, WGSR, and CO-SMET. In-depth descriptions for Cu/CeO_2 [9], $AuCu/CeO_2$ [33], $AuCu/SiO_2$ [34], $AuCu/Al_2O_3$ [35], Au/Fe_2O_3 [36],

$Au/La_2O_3/Al_2O_3$ [37], and Au/CeO_2-ZrO_2 [38,39] are available in the literature. In general, Au favors the CO conversion through a mechanism that involves Au–CO and Au–OOH species [40], where the formation of C–O* intermediates determines the selectivity of the process [20], while CuO acts through a redox mechanism [8], promoting oxygen mobility in the oxide lattice [41] and facilitating the CO oxidation. A synergistic Au–Cu effect has also been proposed [19,33,42]. Therefore, the inclusion of 1 wt% Au and 1 wt% Cu in the single and dual metal oxides promotes greater CO conversion (Figure 2.2.2). Despite having the same active metals (i.e., Au and Cu), the catalysts showed maximum CO conversion at different temperatures, indicating that the properties of the support have a key role in the syngas cleaning. Table 2.2.1 shows that only $AuCu/CeO_2$ reached CO concentrations below 100 ppm in the actual syngas at 210 °C, whereas minimum CO concentrations of the other catalysts were above 500 ppm.

On the other hand, the selectivity in the CO removal has been attributed to the support rather than the active metal [43], being the consumption of H_2 an important criterion in catalyst selection [43]. Figure 2.2.3 shows that H_2 consumption increases with temperature, particularly in the supports and catalysts based on ZrO_2. The deficiency of ZrO_2 to adsorb/desorb bidentate carbonates above 150 °C has been associated with a promotion of the H_2 combustion over the CO oxidation [44]. Likewise, H_2 loss increases in the majority of the supported Au–Cu catalysts (Figure 2.2.3c and d) compared to their respective bare support (Figure 2.2.3a and b), possibly due to affinity of the Au–Cu system to form intermediates in the H_2 oxidation (e.g., hydroxyl groups [33,30]) and methane formation (e.g., C–O* species [18,20,45]). Also, the most active catalysts in the CO removal (i.e., $AuCu/CeO_2$, $AuCu/ZrO_2$, $AuCu/CeO_2$-SiO_2, and $AuCu/CeO_2$-ZrO_2) promote higher H_2 consumption. That is, an active catalyst in the CO conversion possibly has an inherent tendency to consume H_2.

The high H_2 consumption, which in some cases exceeds 20%, could be associated with the syngas composition [20,41], specifically with the H_2/CO ratio. Table 2.2.2 shows the results obtained in the CO removal with catalytic systems based on Au–Cu. High H_2/CO ratios (>>10 [46]) are used in CO-PROX with synthetic syngas to favor CO oxidation [47] and reduce the H_2 consumption. To achieve such high H_2/CO ratios before CO-PROX several WGSR reactors are required, however [11]. Thence, aiming at reducing the number of units used in the traditional process, it has been proposed to carry out CO removal reactions in a single reactor using the syngas that comes directly from the reformer [15,20,39]. Nevertheless, the syngas obtained directly from the ESR contains larger amounts of CO. H_2/CO ratios around 4 have been reported for syngas obtained from ESR using Ir/CeO_2 [48] and $RhPd/CeO_2$ [49] catalysts. Thus, the low H_2/CO ratio in the actual syngas (e.g., the syngas used in this work has an $H_2/CO = 4$) could conduce to a high H_2 loss in the cleanup reactor. Simultaneous production of CO_2 and CH_4 was observed in all catalysts evaluated (Figure SM.7 and Figure SM.8 in Supplementary Material), suggesting that CO-SMET and CO_2 methanation occur together with CO-PROX and WGSR. Then, H_2 oxidation and carbon hydrogenation would be the main causes of H_2 loss during the CO removal from an actual syngas.

Although CH_4 formation implicitly involves an undesirable H_2 consumption, it has been reported that a combination of CO-PROX and methanation improves CO removal compared to the CO-PROX alone, because of favoritism in the activation of adsorbed CO [16]. Then,

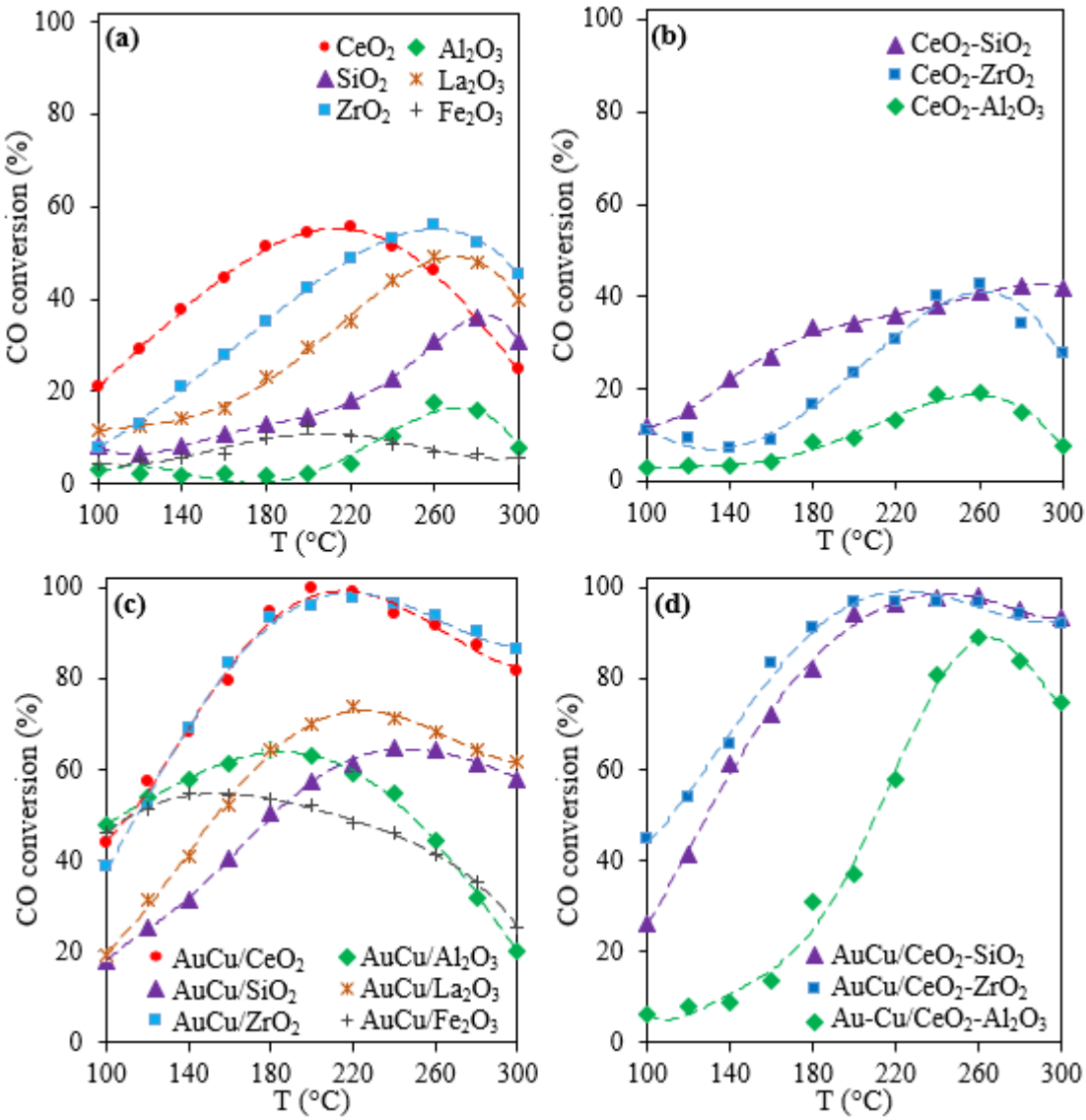

Figure 2.2.2. CO conversion obtained in the Cleanup reactor with supports (a,b) and supported 1 wt% Au–1 wt% Cu catalysts (c,d). Syngas feed: 7.8% H_2, 2.0% CO, 0.5% CO_2, 0.3% CH_4, 1.4% H_2O, 1.8% O_2, 6.8% N_2, and 79.4% Ar. Reaction conditions: The space velocity (SV) = 6.5 ± 0.2 L/g_{cat}*min and 0.3 g of the catalytic bed.

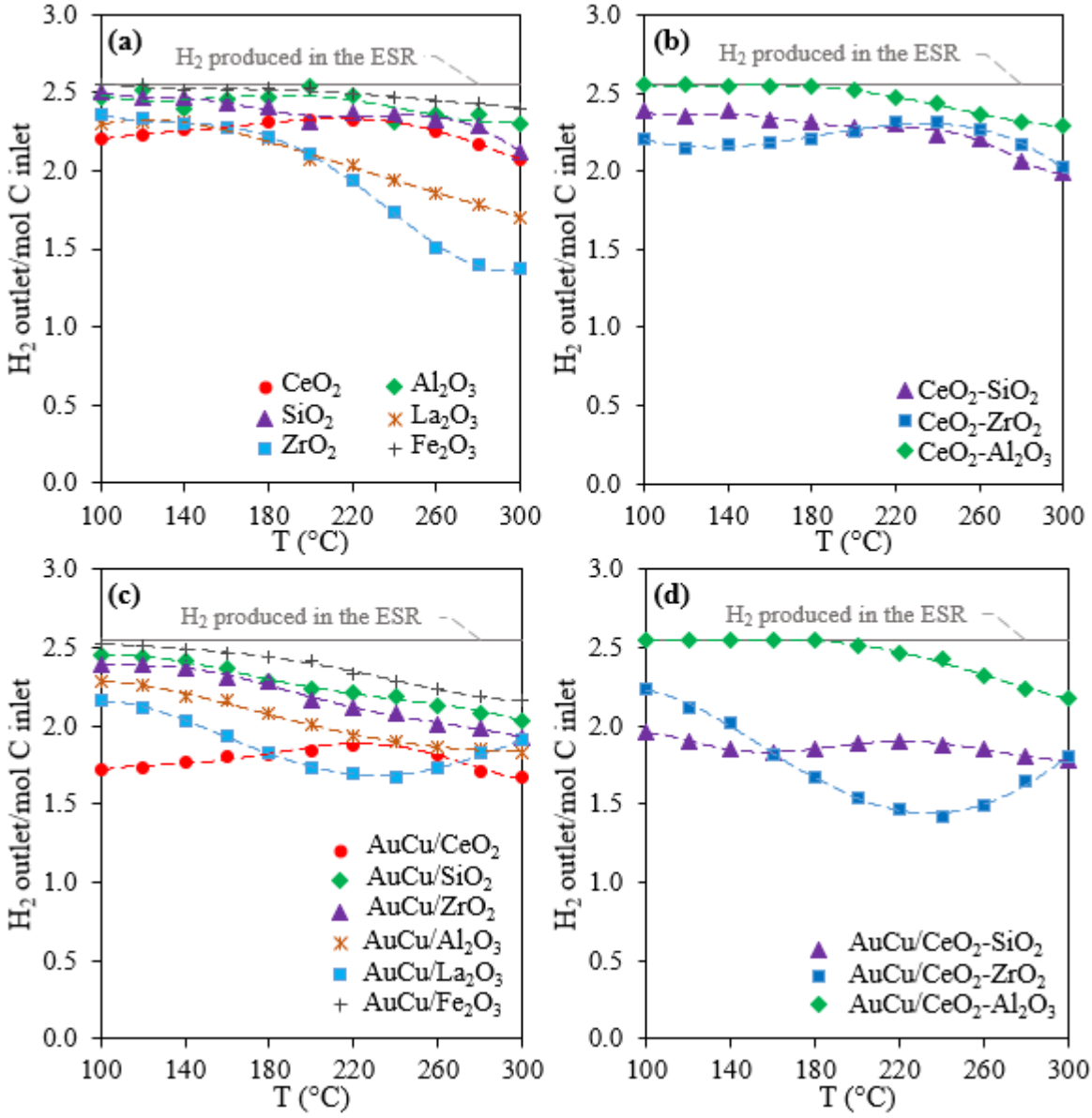

Figure 2.2.3. H_2 yield obtained from a system that integrate the ethanol steam reforming (ESR) reactor and the cleanup reactor, where the CO removal is performed with bare supports (a,b) and supported 1 wt% Au–1 wt% Cu catalysts (c,d). Reaction conditions: SV = 6.5 ± 0.2 L/g_{cat}*min and 0.3 g of the catalytic bed in both reactors.

Table 2.2.1. Minimum concentration of CO obtained in syngas, the apparent active metal dispersion (H/M ratio), surface area, OSC, and OSCC of Au–Cu catalysts supported on single and dual supports.

Catalyst[a]	Minimum CO concentration in outlet gas (ppm)[b]	H/M index	BET surface area (m^2/g_{cat})		OSC in AC samples (μmol O_2/g_{cat})		OSCC at 300 °C (μmol O_2/g_{cat})	
			AC	Spent	100 °C	300 °C	Fresh	Spent
$AuCu/CeO_2$	75 at 210 °C	0.9	60	58 (U) 50 (S)	41	91	230	121 (U) 93 (S)
$AuCu/SiO_2$	8320 at 240 °C	0.7	364	277 (U)	21	37	45	41 (U)
$AuCu/ZrO_2$	507 at 225 °C	0.8	58	47 (U)	39	76	185	84 (U)
$AuCu/Al_2O_3$	745 at 180 °C	0.8	90	65 (U)	31	35	75	41 (U)
$AuCu/La_2O_3$	5365 at 225 °C	0.4	19	18 (U)	21	41	90	24 (U)
$AuCu/Fe_2O_3$	9416 at 140 °C	0.4	16	5 (U)	NR	NR	NR	NR
$AuCu/CeO_2$-SiO_2	861 at 230 °C	1.6	110	75 (U) 74 (S)	34	78	146	121 (U) 126 (S)
$AuCu/CeO_2$-ZrO_2	941 at 210 °C	0.9	42	30 (U)	42	94	210	162 (U)
$AuCu/CeO_2$-Al_2O_3	1521 at 260 °C	1.2	65	56 (U)	32	79	155	121 (U)

[a] Nominal metal loading: 1 wt% Au and 1 wt% Cu. [b] Value includes the carrier gas. AC: activated catalyst, which were reduced with H_2 and stabilized in air before activity tests. U: sample used to obtain light-off curves. S: sample evaluated in the stability test. Note: NR = Not reported; OSC = oxygen storage capacity; OSCC = oxygen storage complete capacity; BET: Brunauer-Emmett-Teller test.

Table 2.2.2. Comparison of various catalytic systems for the CO removal using Au–Cu catalysts.

Catalyst	Syngas type	H_2/CO	T (°C)	CO conversion (%)	H_2 loss (%)	Ref.
$AuCu/CeO_2$	Synthetic	30	220	90	2	[33]
AuCu/SBA-15	Synthetic	>50	25	$\sim$ 100	$\sim$ 5[a]	[50]
Au/CuO-CeO_2/Al_2O_3	Synthetic	4.5	350	$\sim$ 75	NR	[17]
Au/CeO_2-CuO_2/Al_2O_3	Synthetic	50	110	$\sim$ 95	$\sim$ 3[a]	[19]
Au/Al_2O_3	Synthetic	>50	80	$\sim$ 99	$\sim$ 2[a]	[40]
Au/CeO_2-ZrO_2	Actual	30	100	99	$\sim$ 2[a]	[39]
$AuCu/CeO_2$	Actual	4	210	99	17	This work
$AuCu/CeO_2$-SiO_2	Actual	4	230	97	19	This work

[a] Calculated by O_2 mass balance. NR: Not reported.

C and H mass balances were carried out to determine the effect of CH_4 production on H_2 consumption and CO conversion. Figure 2.2.4 shows the H_2 and CO converted with respect to the CH_4 formed in the cleanup reactor. CH_4 formation appears to be directly proportional to H_2 loss (Figure 2.2.4a), but the amount of H_2 consumed is larger than the amount of H_2 contained in the formed CH_4 (yellow line); moreover, in most catalysts, H_2 loss is larger than the H_2 required by CO_2 methanation (green line). Hence, the remnant of H_2 loss may be associated with the production of water or hydrogenated compounds not detected by GC, indicating that methanation would have a secondary role in the H_2 loss during the syngas cleanup. On the other hand, CO conversion grows faster compared to the contribution of methanation (Figure 2.2.4b). Xu et al. [16] studied a Rh/Al_2O_3 catalyst and proposed that at temperatures above 150 °C, the methanation of CO_2 formed during the CO-PROX facilitates the CO oxidation caused by changes in the C–O* and H* adsorbed species. This possible beneficial effect of CO-PROX and subsequent CO_2 methanation seems to be stronger in some catalysts (e.g., $AuCu/CeO_2$-Al_2O_3 and $AuCu/CeO_2$-SiO_2), which would explain their higher activity at high temperatures (Figure 2.2.2d), where most CH_4 was produced (Figure SM.8 in Supplementary Material). $AuCu/CeO_2$ and $AuCu/La_2O_3$ show an atypical trend (Figure 2.2.4b), where the CO conversion decreases with the CH_4 formation, which could depend on the intermediates of C–O* formed on theses catalysts, as will be discussed later. Therefore, these results would confirm the beneficial effect of CO_2 methanation during the CO-PROX proposed in [16], but it was also identified that this effect depends on the support and composition of the syngas.

Although the main objective in the cleaning of the syngas is the CO removal, differences in the activity and selectivity could lead to changes in product distribution over prolonged periods of operation. Therefore, the stability of Au–Cu catalysts loaded on the best single (CeO_2) and dual support (CeO_2-SiO_2) was evaluated. Figure 2.2.5 shows the product distribution over time obtained from a system consisting of ESR and cleanup reactors, the latter of which is packed with either $AuCu/CeO_2$ or $AuCu/CeO_2$-SiO_2. In both cases, a H_2-rich stream is obtained. However, $AuCu/CeO_2$ shows more variability in product distribution, and after around 42 h of operation deactivation was observed, at which point the test was stopped. In contrast, the $AuCu/CeO_2$-SiO_2 catalyst ensures a stable operation for longer periods of time (at least 30% more time-on-stream, Figure 2.2.5b) with CO concentration of about 1000 ppm. The results of the stability test show that the use of dual metal oxides leads to less active (i.e., CO concentration of 1000 ppm versus 75 ppm) but more stable materials, which could be more interesting in extended processes.

Activity, H_2 consumption, and stability were used as criteria for comparison among the Au–Cu-supported catalysts for the CO removal from an actual syngas. Now, catalytic properties, such as reducibility, surface area, OSC, carbon deposit formation, and the CO-support interactions, will be related to the activity, selectivity, and stability of the Au–Cu catalysts supported in single and dual metal oxides.

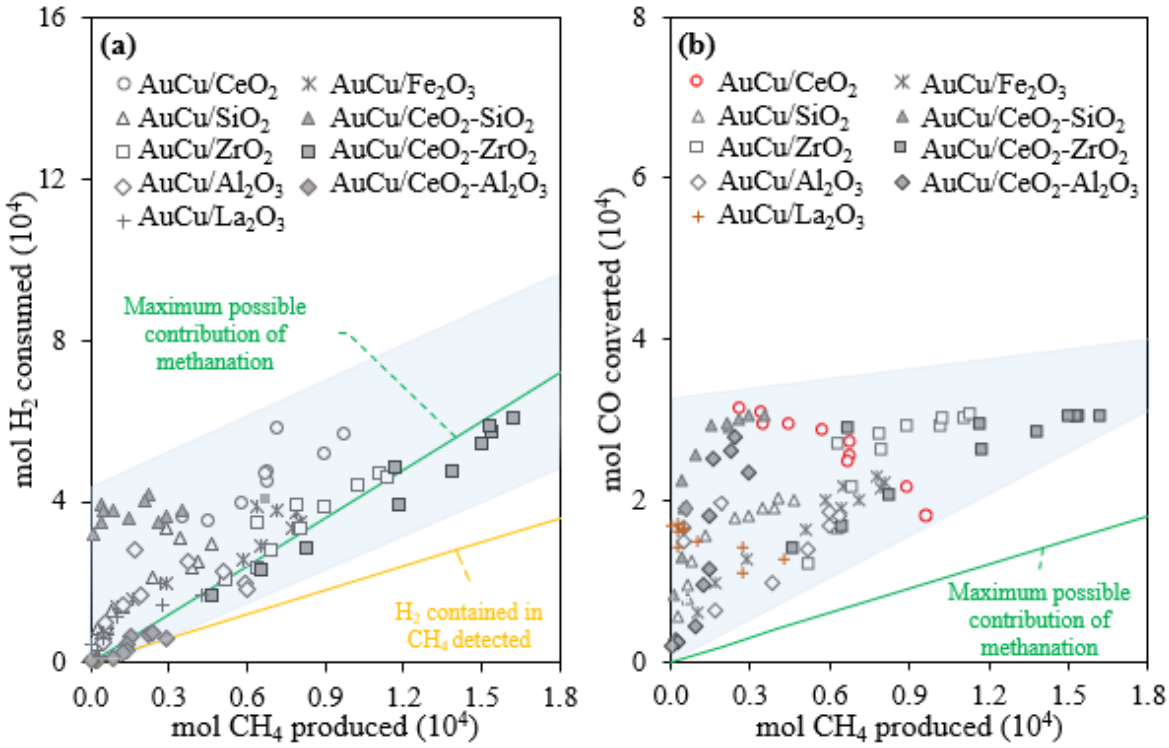

Figure 2.2.4. Contribution of methanation in (**a**) the H_2 consumption and (**b**) CO conversion during the CO removal from an actual syngas. The shaded area conveys the trend of the experimental data.

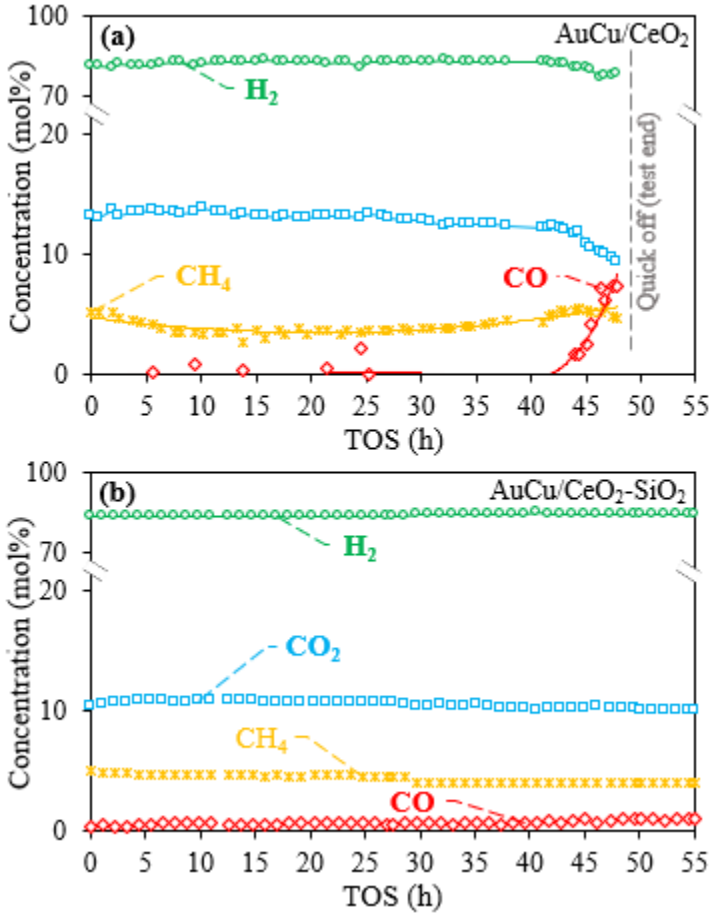

Figure 2.2.5. Products distribution obtained from a system that integrate the ESR reactor and the cleanup reactor, where the CO removal is performed with (a) $AuCu/CeO_2$ and (b) $AuCu/CeO_2$-SiO_2 catalysts. Syngas feed: 7.8% H_2, 2.0% CO, 0.5% CO_2, 0.3% CH_4, 1.4% H_2O, 1.8% O_2, 6.8% N_2, and 79.4% Ar. Reaction conditions: The space velocity (SV) = 6.5 ± 0.2 L/g_{cat}*min and 0.3 g of the catalytic bed. Note: TOS = Time-on-stream.

Catalysts characterization

TPR The redox properties of catalysts have a significant effect on CO oxidation and metal-support interactions [17]. Figure 2.2.6 shows the H_2-TPR profiles for the Au–Cu catalysts supported on single and dual metal oxides. Deconvolution peaks are presented to identify possible individual contributions in each reduction zone, but they are not intended to be exact. Contrary to bare supports (Figure SM.9 in Supplementary Material), discrepancies are observed between supported Au–Cu catalysts. The specific reduction temperatures for Au and Cu are very diverse in the literature, possibly because the reduction of metals strongly depends on the interaction with other species [51]. In this study, a first zone (<130 °C) observed was attributed to the reduction of Au^{3+} and Au^{+} nanoparticles [30]. The second zone (130 to 430 °C) was associated with the reduction of Cu, where at least three species [52] can be identified: (α) easily reducible CuO nano particles, (β) particles of CuO dispersed that interact moderately with the support, and (γ) isolated particles of Cu [53]. In the last zone (>430 °C), the reduction of surface layers and bulk of the support is likely happening [38]. The α and β species promote the formation of oxygen vacancies [54], contributing to the CO oxidation. Thus, preferential formation of CuO species in single and dual metal supports would explain the increase in CO_2 production over Au–Cu-supported catalysts compared to bare supports (Figure SM.7 and Figure SM.8 in Supplementary Material).

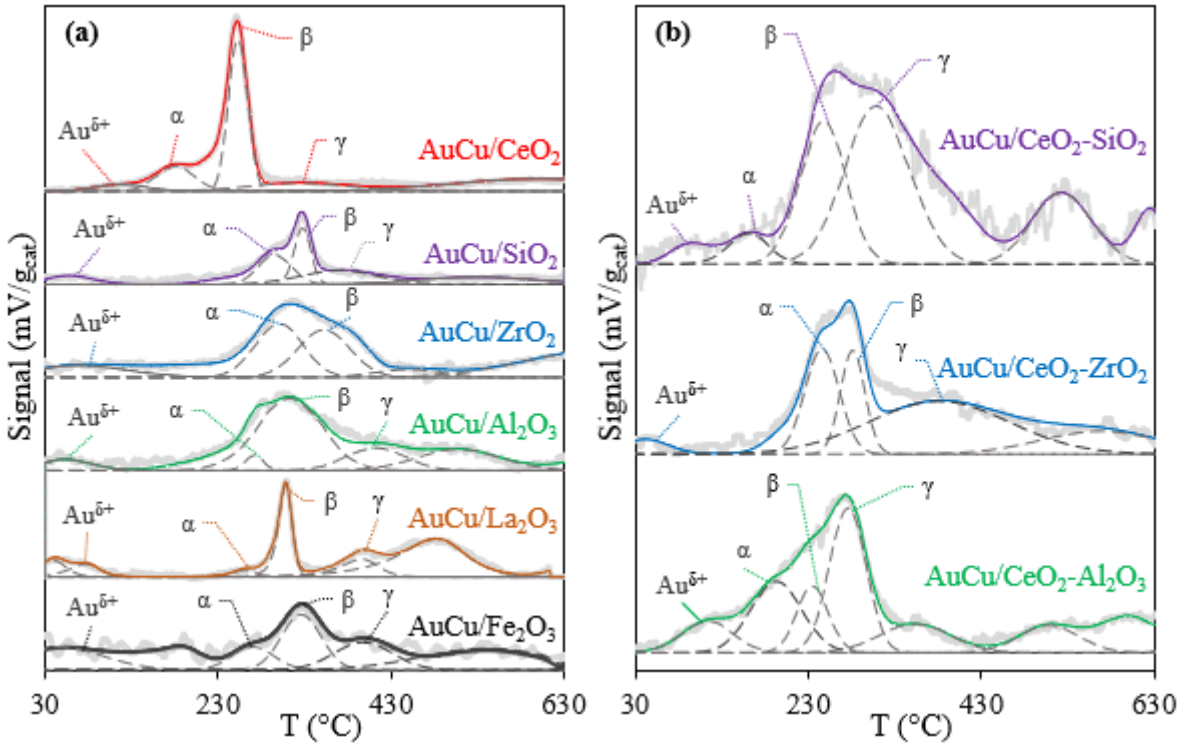

Figure 2.2.6. H_2-temperature programmed reduction (TPR) profiles for Au–Cu catalysts supported on (a) single and (b) dual metal oxides.

On the other hand, the displacement of the reduction peaks to lower temperatures has been associated with changes in metal-support interactions [51]. CeO_2 shows an exceptional

ability to facilitate the reduction of Cu and the formation of (mostly) β species. This effect has been previously studied [9,55], correlating a stronger CuO-CeO_2 interaction with high activity during CO-PROX. However, the increase in the contribution of γ-species and a slight shift of reduction peaks to higher temperatures could indicate a variation of the CuO-CeO_2 interaction in the Au–Cu catalysts supported in dual oxides. Thus, a change in the redox properties of the support caused by the presence of a second metal oxide could explain why the Au–Cu catalysts supported on dual oxides (i.e., AuCu/CeO_2-SiO_2, AuCu/CeO_2-ZrO_2, and AuCu/CeO_2-Al_2O_3) showed less activity compared to AuCu/CeO_2 (Figure 2.2.2). However, an exceedingly strong CuO-support interaction could also mitigate the formation of selective Au–Cu alloys [35]. In fact, AuCu/ZrO_2 and AuCu/CeO_2-ZrO_2 show a significant contribution of α species, which could be related to the high H_2 loss observed in these catalysts (Figure 2.2.3c and d). On the contrary, the combination of inert metal oxides such as Al_2O_3 with CeO_2 could facilitate the migration of CuO towards Au particles [35], leading to lower H_2 loss compared to single CeO_2 support. Then, the change in redox properties of CeO_2 by the presence of inert metal oxides (e.g., SiO_2) could lead to less active but more selective materials during CO removal.

Table 2.2.1 shows the H/M index, which has been associated with apparent active metal dispersion [29]. The H/M index in AuCu/Fe_2O_3 and AuCu/La_2O_3 is particularly low, indicating that these catalysts are not as effective for dispersing active metals [29]. In the other catalysts, the H/M index was close to or larger than 1.0 (i.e., complete reduction of Au and Cu), which could be associated with a higher dispersion of Au and Cu on the catalytic surface. However, a high H/M value could also indicate an additional effect of superficial reduction of the supports by the interaction between metal oxides and active metals [56]. Au–Cu catalysts supported on dual metal oxides showed higher H/M index compared to their respective single supports, which could be associated with a favoring in the reduction of both active metals and support due to the interaction between metal oxides. If so, then the redox properties of Au–Cu catalysts supported on dual oxides would depend on several interactions: (i) active metal-active metal; (ii) active metal-support, and (iii) oxide I-oxide II. The variation of these interactions influences catalytic performance during CO removal.

BET area The surface area of the catalysts is key to the availability of the active sites and catalytic performance [57]. The BET area (Table 2.2.1) of the catalysts supported on basic oxides (i.e., CeO_2, ZrO_2 and La_2O_3 [58]) is larger than their respective bare supports (Table SM.4 in Supplementary Material), which has been previously associated with the formation of high disperse β species [20,59]. On the other hand, AuCu/Fe_2O_3 and AuCu/La_2O_3 show low surface areas, which match to the low capacity of these metal oxides to disperse active metals (low H/M index, Table 2.2.1). The synthesis method of the catalysts could influence the surface area of the support, overcoming some drawbacks of metal oxides such as Fe_2O_3 by using alternative synthesis methods [32,60]. In contrast, the higher surface area of AuCu/CeO_2-Al_2O_3 and AuCu/CeO_2-SiO_2 could favor the dispersion of Au and Cu, which is reflected by a larger H/M index (Table 2.2.1).

Although an increase in the surface area could contribute to improving the catalytic activity [57], the trend for surface area of the catalysts does not match their activity (Figure 2.2.2), indicating that the supports have other features that could be more relevant

during the CO removal. Figure 2.2.7 shows the conversion rate of CO normalized by the surface area of catalysts. $AuCu/La_2O_3$ has a high normalized activity, possibly because the basic supports promote the formation of Au nanoparticles [37] and formation of β species [20,59], which are active in the CO conversion. In fact, basic oxides, such as CeO_2 and ZrO_2, also have higher normalized activity compared to less basic supports, such as Al_2O_3 and SiO_2. Also, the normalized activity of the $AuCu/CeO_2$-ZrO_2 catalyst increases compared to their respective single supports. Recently, it was reported that the replacement of Zr^{4+} ions in the lattice of the CaO-CeO_2 system leads to the formation of highly basic sites [61]. Then, we speculate that the high interaction in CeO_2-ZrO_2 observed by TPR could lead to the formation of sites with greater basicity. However, the low surface area of basic supports is a well-known limitation that affects their activity [6]. So, because of the possible role of basic sites in CO removal, the design of catalysts for CO removal should include a support with both a high surface area and elevated basicity. Modifications in the morphology of metal oxides have been proposed as a successful strategy to achieve this objective in other catalytic processes [62]. Then, preparation of Au–Cu catalysts supported on single and dual metal oxides can be optimized to improve their catalytic properties during CO removal.

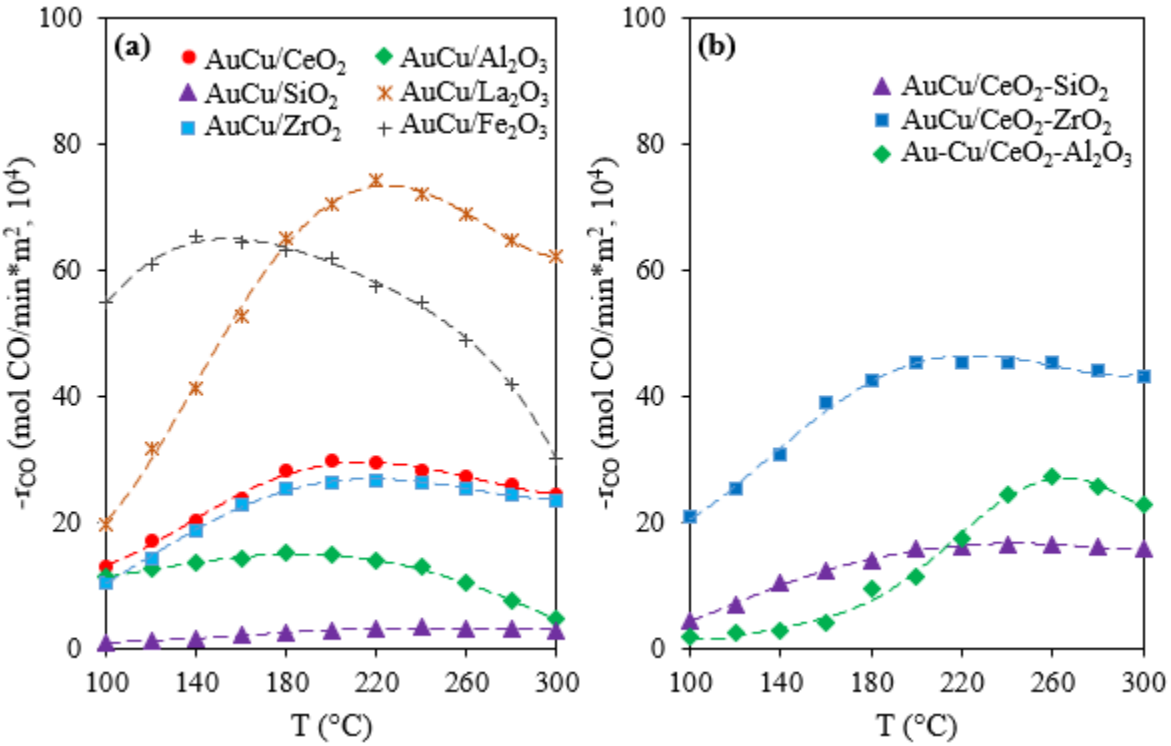

Figure 2.2.7. CO conversion rate normalized by the surface area of the Au–Cu catalysts supported in (a) single and (b) dual metal oxides.

OSC measurements The OSC of the support plays a central role in the oxidation of CO adsorbed on active sites [31]. Table 2.2.1 shows the OSC of Au–Cu catalysts supported on single and dual metal oxides. In general, the OSC of supported Au–Cu catalysts is higher than that of the bare supports (Table SM.4 in Supplementary Material), indicating

that the presence of Au and Cu favors greater oxygen mobility in the catalyst. Also, the presence of α and β species has been associated with the formation of oxygen vacancies on the catalytic surface [55]. Catalysts that have a higher OSC at 300 °C (i.e., AuCu/CeO_2-ZrO_2, AuCu/CeO_2, AuCu/CeO_2-SiO_2, and AuCu/ZrO_2) were the most active (Figure 2.2.2), but also those that showed the highest consumption of H_2 (Figure 2.2.3). However, the OSC depends strongly on the temperature: at 100 °C, all catalysts except AuCu/Al_2O_3 showed an OSC up to 60% lower compared to 300 °C, which could be related to the lower activity of catalysts at low temperatures (Figure 2.2.2).

Likewise, the CO_2 formation depends on the availability of surface oxygen [15]. The first CO pulse (OSC) in AuCu/CeO_2 only corresponds to 39% of its oxygen storage complete capacity (OSCC), indicating that oxygen adsorbed on CeO_2 may not be easily released. The possible deficiency of CeO_2 to release the oxygen absorbed on its surface could limit the oxidation of carbon intermediates, which could, in turn, be related to the atypical trend observed in Figure 2.2.4b. The OSC in supports with larger surface area (i.e., AuCu/SiO_2, AuCu/Al_2O_3, AuCu/CeO_2-SiO_2, and AuCu/CeO_2-Al_2O_3), on the other hand, corresponds to more than 50% of their OSCC. A higher availability of surface oxygen (> OSC/OSCC) could be associated with the strong effect of CO_2 methanation on the CO removal for AuCu/CeO_2-SiO_2 and AuCu/CeO_2-Al_2O_3, as previously discussed. If so, then the beneficial effect of methanation during the CO-PROX proposed by [16] could be enhanced in catalysts that combine a high OSC and readiness to release their adsorbed oxygen (i.e., high OSC/OSCC ratio), which would require a high surface area.

On the other hand, the OSCC of the catalysts used decreases with respect to the fresh, activated ones (AC samples), reaching up to 73% reduction with AuCu/La_2O_3. This reduction could be associated with progressive oxidation of the catalyst surface by the presence of oxidants in the gas stream and deposits on the catalytic surface [20], conducive of a progressive deactivation. To clarify this, a TGA study was conducted.

TGA Table 2.2.3 shows the weight loss of Au–Cu catalysts supported on single and dual metal oxides. Most AC samples show a weight loss of less than 1% that could correspond to a remnant of the precursors of the active metals. However, AuCu/Fe_2O_3 and AuCu/CeO_2-SiO_2 show an increase in weight that can be associated with an oxygen adsorption; specifically, the CeO_2-SiO_2 system can form a $Ce_{9.33}(SiO_4)\cdot 6O_2$ phase that is susceptible to consume oxygen above 600 °C [6]. The used catalysts have a higher weight loss than the fresh, activated ones (AC samples), indicating the presence of compounds deposited on the catalytic surface during the reaction. To determine the nature of the deposits, the TGA results were analyzed by weight loss in terms of rate of carbon equivalent formed in each temperature interval (Table 2.2.3). In the first interval (40–250 °C), light compounds, such as water, and adsorbed OH^- and gases are released [36]; in this interval, AuCu/SiO_2 and AuCu/Al_2O_3 showed the highest weight loss, which could be related to their high surface area, which favors moisture adsorption. In the second interval (250–600 °C), light hydrocarbons are oxidized [26]; AuCu/La_2O_3 and AuCu/Fe_2O_3 had the highest rate of carbon formation in this interval, which would explain the strong decrease in the OSCC and surface area, respectively, observed in these samples (Table 2.2.1). In the last interval (600–1000 °C), heavy hydrocarbons are oxidized, which are the type of deposits that could favor a faster deactivation of the catalyst

[58]; in this zone, $AuCu/CeO_2$ showed a higher rate of carbon formation. Thus, rapid deactivation observed in $AuCu/CeO_2$ (Figure 2.2.5) could be associated with the decrease in surface area (17%, Table 2.2.1) and OSCC (59%, Table 2.2.1) promoted by the accumulation of deposits on the catalytic surface (Table 2.2.3). The formation of stable deposits could be associated with the formation of intermediates during the CO removal [32]; therefore, *in-situ* DRIFTS was carried out to identify how the interaction between CO and support affects the performance of the supported Au–Cu catalysts.

Table 2.2.3. Weight loss of Au–Cu catalysts supported on single and dual supports evaluated in CO removal from an actual syngas.

Catalyst	Total weight loss (%)		Weight loss of spent catalyst samples by temperature intervals (mg of C/g_{cat}*h)		
	AC	Spent	40–250 °C	250–600 °C	600–1000 °C
$AuCu/CeO_2$	0.7	3.8 (U)	17.1 (U)	6.8 (U)	11.8 (U)
		5.6 (S)	14.5 (S)	15.1 (U)	18.1 (U)
$AuCu/SiO_2$	0.3	3.7 (U)	35.5 (U)	3.4 (U)	3.9 (U)
$AuCu/ZrO_2$	0.9	1.6 (U)	9.2 (U)	2.1 (U)	4.7 (U)
$AuCu/Al_2O_3$	0.5	3.7 (U)	28.9 (U)	2.1 (U)	9.4 (U)
$AuCu/La_2O_3$	0.6	2.1 (U)	9.2 (U)	7.5 (U)	2.4 (U)
$AuCu/Fe_2O_3$	−0.3	2.5 (U)	18.4 (U)	8.9 (U)	NR
$AuCu/CeO_2$-SiO_2	−0.9	0.3 (U)	3.9 (U)	4.8 (U)	NR
		1.3 (S)	15.8 (S)	4.1 (U)	NR
$AuCu/CeO_2$-ZrO_2	0.5	1.7 (U)	9.2 (U)	6.2 (U)	0.8 (U)
$AuCu/CeO_2$-Al_2O_3	0.6	2.6 (U)	17.1 (U)	2.7 (U)	7.1 (U)

Note: AC = activated catalyst, which were reduced with H_2 and stabilized in air before activity tests; U = sample used to obtain light-off curves; S = sample evaluated in the stability test; NR = Not reported.

***In-situ* DRIFTS** Figure 2.2.8 shows the DRIFTS spectra of CO adsorption on bare supports and supported Au–Cu catalysts. CeO_2 and ZrO_2 show higher intensity in the area associated with hydroxyl groups (~ 3500 cm^{-1}) that contributes to the CO conversion [40], which would explain their high activity among single metal oxides (Figure 2.2.2). Although the CO pulses were free of H_2 or water, hydroxyl groups may be formed from the interaction of H_2 with the surface of the support [63], which could occur during the H_2 reduction that was performed on the AC samples. In fact, Zhou et al. [64] studied the CO adsorption on bare ZrO_2 by DRIFTS and Fourier transform infrared spectroscopy (FTIR), identifying up to three families of hydroxyl groups in the zone from 3675 to 3772 cm^{-1}, which are activated by the adsorption of CO, even at room temperature, and have an active role in the formation of surface intermediates. CeO_2 favors the formation of hydroxyl groups even with the first pulse of CO, which could be decisive in ensuring a syngas with a lower CO concentration.

In the C–O* zone (1200 to 1700 cm^{-1} [65]), the formation of bidentate carbonates (1600 cm^{-1}) and formates (1300 and 1500 cm^{-1}) are observed, which are also intermediates in the CO conversion [20,54,65]. The formation of hydroxyl groups and C–O* species were lower than dual supports when compared to CeO_2; specifically, CeO_2-Al_2O_3 shows a significant reduction in the formation of C–O* intermediates, which would correspond to its lower activity among the dual supports (Figure 2.2.2).

The inclusion of Au–Cu in the single oxides (Figure 2.2.8c) favors the presence of hydroxyls and the formation of C–O* intermediates, possibly due to the ability of Au to form Au–CO and Au–OOH species [40]. In fact, most catalysts show an increase in CO adsorbed (2100 cm^{-1}), which is associated with CO–Au^0 species [66], indicating that Au could be present mostly as Au^0 on the catalytic surface, as previously reported for systems such as Au/CeO_2 [20] and Au/La_2O_3/Al_2O_3 [37], evaluated by XPS. However, in AuCu/CeO_2-SiO_2 and AuCu/CeO_2-ZrO_2, a weak peak of CO adsorption between 2075 and 2050 cm^{-1} is also observed, which has been associated with the formation of CO–$Au^{\delta-}$ species [67]. In the case of AuCu/CeO_2-ZrO_2, the formation of these species only occurs after several CO pulses. The presence of $Au^{\delta-}$ has been related to a stronger support-metal interaction, which could be ascribed to the high stability of AuCu/CeO_2-SiO_2 (Figure 2.2.5).

The formation of C–O* intermediates may occur on different active sites, including Au^0, Au^{δ}, and CuO, but the formation of carbonate species at approximately 1470 cm^{-1} occurs preferably on Cu^+ species [68], which are very active in CO-PROX [69]. The peak associated with Cu^+ is well defined in AuCu/CeO_2. Furthermore, the formation of active Cu^+ species due to the high affinity in CuO-CeO_2 has been extensively studied by XPS and DRIFTS [25,70]. Thus, a smaller amount of Cu^+ species on the other catalysts could explain their inability to ensure CO concentrations below 100 ppm (Table 2.2.1). Besides, the peaks associated with formate species, which are related to CH_4 formation, are better defined on CeO_2. It is accepted that CH_4 formation is promoted on several oxides (e.g., Al_2O_3, ZrO_2, Y_2O_3, MgO, and CeO_2 [71]), but the special ability to adsorb and activate carbon species makes CeO_2 an adequate support in CO_2 methanation and CO-SMET [72]. Nevertheless, during the CO removal the Boudouard reaction and the CH_4 decomposition could contribute to the production of carbon deposits [26], favoring the catalyst deactivation. Then, the ability of CeO_2 to form C–O* intermediates (Figure 2.2.8) assisted by Cu^+ species and its lower capacity to release the surface oxygen (low OSC/OSCC) could contribute to the generation of stable carbon deposits, as was observed by TGA, leading to its rapid deactivation (Figure 2.2.5). Besides, the deficiency of AuCu/CeO_2 to mitigate carbon deposition due to the excessive formation of C–O* intermediates could be also related to the atypical behavior of CH_4 formation (Figure 2.2.4b). However, the less active materials show low formation of intermediates (e.g., AuCu/La_2O_3, AuCu/Fe_2O_3, and AuCu/SiO_2). Thus, the selection of the support for the CO removal from a syngas must consider the balance between activity and stability.

The results of DRIFTS support the notion that the use of dual metal oxides favors less active but more stable catalysts. Therefore, in this study, CeO_2 is presented as the most promising support for developing a compact system to carry out the CO removal from an actual syngas. However, the selectivity and stability of CeO_2 require improvements. Furthermore, it was shown that the use of dual supports, specifically CeO_2-SiO_2 and CeO_2-ZrO_2, could be a promising strategy to overcome the deficiencies presented by CeO_2.

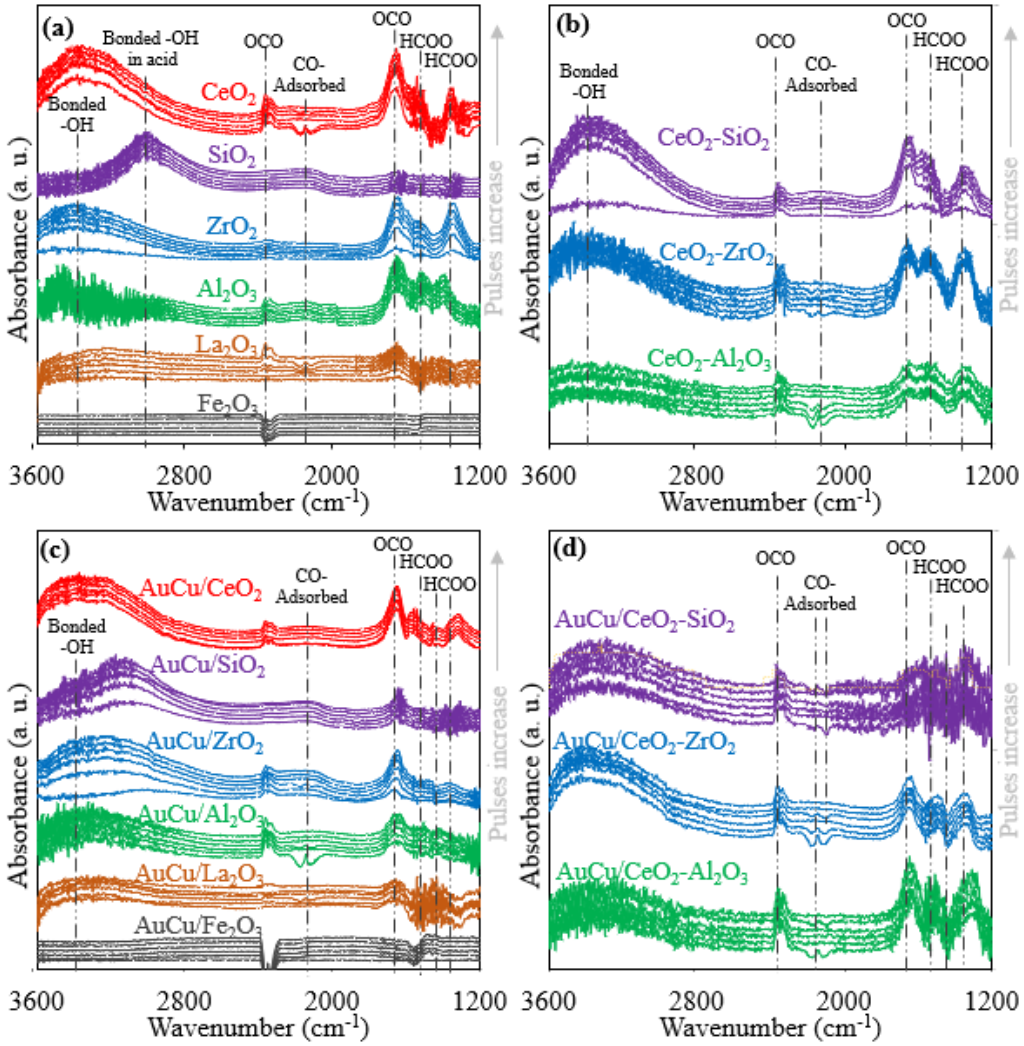

Figure 2.2.8. *In-situ* diffuse reflectance infrared Fourier transform spectroscopy (DRIFTS) of CO adsorption of (a, b) bare supports and (c, d) supported Au–Cu catalysts.

2.2.5 Conclusions

Several single and dual metal oxides were investigated as supports in a catalytic system based on Au–Cu for the CO removal from an actual syngas. The use of a syngas obtained directly from the ESR affects the effectiveness in the CO removal; specifically, a low H_2/CO ratio could favor greater H_2 loss. AuCu/CeO_2 was identified as the most active catalyst in the CO removal, but it also contributes to a higher H_2 consumption. H_2 is lost mainly by the formation of water and CH_4, where the occurrence of CO_2 methanation affected the CO removal differently. Over CeO_2-Al_2O_3 and CeO_2-SiO_2, methanation seems to improve CO removal because the CO-PROX product, CO_2, is constantly consumed to produce CH_4. On the contrary, methanation has a negative effect on CeO_2 and La_2O_3 because the formed CH_4 favors carbon deposition.

Differences among the catalysts were evaluated by several characterization techniques. DRIFTS spectra of CO adsorption showed that CeO_2 has a superior activity because it favors the formation of C–O* and OH^- intermediates, but it promotes the formation of carbon deposits that lead to its deactivation. Similarly, TPR showed that ZrO_2 has a high interaction with active metals (Au–Cu), which makes it active but less selective, favoring a high H_2 oxidation. In addition, the low OSC of Al_2O_3 and SiO_2, and the lower surface area of Fe_2O_3 and La_2O_3 make these metal oxides less active. Regarding dual supports, the inclusion of a second metal oxide weakens the interaction of CeO_2 with the active metals, reducing activity. However, dual metal oxides are more selective and stable than single CeO_2 because they mitigate the excess of C–O* species, as was observed by DRIFTS; specifically, CeO_2-SiO_2 mitigates the formation of stable carbon deposits that deactivate the catalyst. Thus, AuCu/CeO_2 was identified as a promising catalyst for carrying out the CO removal from a syngas using just one catalytic reactor, but improvements in CeO_2 stability are still required. Therefore, the use of dual supports (e.g., CeO_2-SiO_2) could be a strategy to overcome single CeO_2 deficiencies. Thus, the development of more compact systems for the purification of H_2 suitable for FC implicitly promotes greater H_2 consumption. The results of this work aim to contribute to the development and establishment of sustainable energies based on H_2.

2.2.6 Acknowledgments

B. Cifuentes acknowledges Colciencias for the doctoral scholarship (grant number 727-2015).

2.2.7 References

[1] K. Zhang, X. Jiang. Fuel 220 (2018) 283–295.
[2] M. Renzi, F. Patuzzi. Appl. Energy 206 (2017) 697–707.
[3] A. Rosa. Academic Press, Cambridge, United States (2013) 371–428.
[4] H. Mohammed, A. Al-Othman, P. Nancarrow, M. Tawalbeh, M. El Haj Assad. Energy 172 (2019) 207–219.
[5] S. Sengodan, R. Lan, J. Humphreys, D. Du, W. Xu, H. Wang, S.Tao. Renew. Sustain. Energy Rev. (2018) 761–780.
[6] B. Cifuentes, M. Hernández, S. Monsalve, M. Cobo. Appl. Catal. A Gen. 523 (2016) 283–293.

[7] Y. Xie, J. Wu, G. Jing, H. Zhang, S. Zeng, X. Tian, X. Zou, J. Wen, H. Su, C.J. Zhong, et al. Appl. Catal. B Environ. 239 (2018), 665–676.
[8] T. Kou, C. Si, Y. Gao, J. Frenzel, H. Wang, X. Yan, Q. Bai, G. Eggeler, Z. Zhang. RSC Adv. 4 (2014) 65004–65011.
[9] T. Kou, C. Si, J. Pinto, C. Ma, Z. Zhang. Nanoscale 9 (2017) 8007–8014.
[10] Ashraf, M.A.; Ercolino, G.; Specchia, S.; Specchia, V. Int. J. Hydrogen Energy 2014, 39, 18109–18119.
[11] I. Rossetti, M. Compagnoni, M. Torli. Chem. Eng. J.281 (2015) 1036–1044.
[12] D. Gubán, A. Tompos, I. Bakos, Á. Vass, Z. Pászti, E.G. Szabó, I.E. Sajó, I. Borbáth. Int. J. Hydrogen Energy 42 (2017) 13741–13753.
[13] H. Narayanan, S. Basu. Int. J. Hydrogen Energy 42 (2017) 23814–23820.
[14] Y. Devrim, A. Albostan, H. Devrim. Int. J. Hydrogen Energy 43 (2018) 18672–18681.
[15] J. Kugai, E.B. Fox, C. Song. Appl. Catal. A Gen. 497 (2015) 31–41.
[16] G. Xu, Z.G. Zhang. J. Power Sources 157 (2006) 64–77.
[17] T.R. Reina, S. Ivanova, O.H. Laguna, M.A. Centeno, J. Odriozola. A. Appl. Catal. B Environ. 197 (2016) 67–72.
[18] F. Wang, J. Zhang, W. Li, B. Chen. J. Energy Chem. 39 (2019) 198–207.
[19] T.R.R. Reina, S. Ivanova, M.A.A Centeno, J.A.A. Odriozola. Int. J. Hydrogen Energy 40 (2015) 1782–1788.
[20] B. Cifuentes, F. Bustamante, J.A. Conesa, L.F. Córdoba, M. Cobo. Int. J. Hydrogen Energy 43 (2018) 17216–17229.
[21] X. Yao, F. Gao, L. Dong. Cuihua Xuebao/Chin. J. Catal.34 (2013) 1975–1985.
[22] C.G. MacIel, L.P.R. Profeti, E.M. Assaf, J.M. Assaf. J. Power Sources 196 (2011) 747–753.
[23] G. Águila, F. Gracia, P. Araya. Appl. Catal. A Gen. 343 (2008) 16–24.
[24] Z. Zhao, X. Lin, R. Jin, Y. Dai, G. Wang. Catal. Commun. 12 (2011) 1448–1451.
[25] E. Moretti, E. Rodríguez-Aguado, A.I. Molina, E. Rodríguez-Castellón, A. Talon, L. Storaro, Catal. Today 304 (2018) 135–142.
[26] S. Li, H. Tang, D. Gong, Z. Ma, Y. Liu. Catal. Today 297 (2017) 298–307.
[27] D.R. Sahoo, S. Vajpai, S. Patel, K.K. Pant. Chem. Eng. J. 125 (2007) 139–147.
[28] B. Cifuentes, F. Bustamante, M. Cobo. Mendeley Datasets (2019) 1-10, doi:10.17632/6pxcn5k3sx.1.
[29] T. Mallát, S. Szabó, J. Petró, S. Mendioroz, M.A. Folgado. Appl. Catal. 53 (1989) 29–40.
[30] J.D. Fonseca, H.S. Ferreira, N. Bion, L. Pirault-Roy, M. do Carmo Rangel, D. Duprez, F. Epron. Catal. Today 180 (2012) 34–41.
[31] S. Liu, X. Wu, D. Weng, R.J. Ran. Rare Earths 33 (2015) 567–590.
[32] L.M. Martínez, O.H. Laguna, C. López-Cartes, M.A. Centeno. Mol. Catal. 440 (2017) 9–18.
[33] N.K. Gamboa-Rosales, J.L Ayastuy, M.P. González-Marcos, M.A. Gutiérrez-Ortiz. Today 176 (2011) 63–71.
[34] P. Destro, S. Marras, L. Manna, M. Colombo, D. Zanchet. Catal. Today 282 (2017) 105–110.
[35] P. Destro, T.M. Kokumai, A. Scarpellini, L. Pasquale, L. Manna, M. Colombo, D. Zanchet. ACS Catal. 8 (2017) 1031–1037.

[36] J.L. Ayastuy, A. Gurbani, M.A. Gutiérrez-Ortiz. Int. J. Hydrogen Energy 41 (2016) 19546–19555.
[37] P. Lakshmanan, E. Park. Catalysts 8 (2018) 183–193.
[38] L.F. Córdoba, A. Martínez-Hernández. Int. J. Hydrogen Energy 40 (2015) 16192–16201.
[39] J.D. Arévalo, Á. Martinez-Hernández, J.C. Vargas, L.F. Córdoba. Tecciencia 13 (2018) 55–64.
[40] Z. Chen, C.J. Pursell, B.D. Chandler, J. Saavedra, T. Whittaker, R.M. Rioux. Nat. Chem. 8 (2016) 584–589.
[41] V.D.B.C. Dasireddy, J. Valand, B. Likozar. Renew. Energy 116 (2018) 75–87.
[42] W. Zhan, J. Wang, H. Wang, J. Zhang, X. Liu, P. Zhang, M. Chi, Y. Guo, Y. Guo, G. Lu, et al. J. Am. Chem. Soc. 139 (2017) 8846–8854.
[43] T.R. Reina, C. Megías-Sayago, A.P. Florez, S. Ivanova, M.Á. Centeno, J.A. Odriozola. J. Catal. 326 (2015) 161–171.
[44] M.M. Yung, Z. Zhao, M.P. Woods, U.S. Ozkan. J. Mol. Catal. A Chem. 279 (2008) 1–9.
[45] L. Proaño, E. Tello, M.A. Arellano-Trevino, S. Wang, R.J. Farrauto, M. Cobo. Appl. Surf. Sci. 479 (2019) 479, 25–30.
[46] A. Jhalani, L.D. Schmidt. Catal. Lett. 104 (2005) 103–110.
[47] K.I. Tanaka, H. He, M. Shou, X. Shi. Catal. Today 175 (2011) 467–470.
[48] F. Wang, L. Zhang, J. Zhu, B. Han, L. Zhao, H. Yu, Z. Deng, W. Shi. Appl. Catal. A Gen. 564 (2018) 226–233.
[49] N.J. Divins, A. Casanovas, W. Xu, S.D. Senanayake, D. Wiater, A. Trovarelli, J. Llorca, Catal. Today 253 (2015) 99–105.
[50] X. Li, S.S. Fang, J. Teo, Y.L. Foo, A. Borgna, M. Lin, Z. Zhong. ACS Catal. 2 (2012) 360–369.
[51] O.H. Laguna, W.Y. Hernández, G. Arzamendi, L.M. Gandía, M.A. Centeno, J.A. Odriozola. Fuel 118 (2014) 176–185.
[52] E.A. Redina, A.A. Greish, I.V. Mishin, G.I. Kapustin, O.P. Tkachenko, O.A. Kirichenko, L.M. Kustov. Catal. Today 241 (2015) 246–254.
[53] J. Wang, L. Zhong, J. Lu, R. Chen, Y. Lei, K. Chen, C. Han, S. He, G. Wan, Y. Luo. Mol. Catal. 443 (2017) 241–252.
[54] X. Wang, J.A. Rodriguez, J.C. Hanson, D. Gamarra, A. Martínez-Arias, M. Fernández-García. J. Phys. Chem. B 110 (2006) 428–434.
[55] F. Wang, R. Büchel, A. Savitsky, M. Zalibera, D. Widmann, S.E. Pratsinis, W. Lubitz, F. Schüth. ACS Catal. 6 (2016) 3520–3530.
[56] P.S. Barbato, S. Colussi, A. Di Benedetto, G. Landi, L. Lisi, J. Llorca, A. Trovarelli. J. Phys. Chem. C 120 (2016) 13039–13048.
[57] F. Schüth, M.D. Ward, J.M. Buriak. Chem. Mater. 30 (2018) 3599–3600.
[58] B. Cifuentes, M. Valero, J. Conesa, M. Cobo. Catalysts 5 (2015) 1872–1896.
[59] B.M. Nagaraja, A.H. Padmasri, B.D. Raju, K.S.R. Rao. J. Mol. Catal. A Chem. 265 (2007) 90–97.
[60] J. Li, Y. Zhan, X. Lin, Q. Zheng. Acta Phys.-Chim. Sin. 24 (2008) 932–938.
[61] F. Liu, Y. Xiao, X. Sun, G. Qin, X. Song, Y. Liu. Chem. Eng. J. 369 (2019) 205–214.
[62] W. Chen, R. Ran, D. Weng, X. Wu, J. Zhong, S. Han. J. Rare Earths 35 (2017) 970–976.

[63] A.S. Malik, S.F. Zaman, A.A. Al-Zahrani, M.A. Daous, H. Driss, L.A. Petrov. Catal. Today (2019), in press, doi:10.1016/j.cattod.2019.05.040.
[64] W. Zhou, Z. Ma, S. Guo, M. Wang, J. Wang, M. Xia, L. Jia, B. Hou, D. Li, Y. Zhao. Appl. Surf. Sci. 427 (2018) 867–873.
[65] S. Agarwal, B.L. Mojet, L. Lefferts, A.K. Datye. Elsevier: Amsterdam, The Netherlands, (2015) 31–70.
[66] A. Leba, T. Davran-Candan, Z.I. Önsan, R. Yildirim. Catal. Commun.29 (2012) 6–10.
[67] S. Fernández-García, S.E. Collins, M. Tinoco, A.B. Hungría, J.J. Calvino, M.A. Cauqui, X. Chen. Catal. Today 336 (2019) 90–98.
[68] D. Gamarra, A. Martínez-Arias. J. Catal. 263 (2009) 189–195.
[69] E. Moretti, M. Lenarda, L. Storaro, A. Talon, R. Frattini, S. Polizzi, E. Rodríguez-Castellón, A. Jiménez-López. Appl. Catal. B Environ. 72 (2007) 149–156.
[70] C.S. Polster, H. Nair, C.D. Baertsch. J. Catal. 266 (2009) 308–319.
[71] J. Suzuki, K. Hayakawa, C. Fukuhara, R. Watanabe, W. Kawasaki. Appl. Catal. A Gen. 532 (2016) 12–18.
[72] T.A. Le, M.S. Kim, S.H. Lee, T.W. Kim, E.D. Park. Catal. Today 293-294 (2017) 89–96.

2.3 Modification of CeO_2 morphology

In the previous section the effect of several single and dual metal oxides as supports for a catalytic system based on Au-Cu in the CO removal from an actual syngas was presented. It was identified that the inclusion of a second metal oxide in the CeO_2 matrix impact in the activity of the $AuCu/CeO_2$ system. For this reason, in this section a different approach was evaluated, which seeks to obtain both active and stable catalyst of $AuCu/CeO_2$ by modifying the nanomorphology of CeO_2.

This section corresponds to an article published in *Applied Catalysis A: General, (2020) 598, 117568.* - DOI: 10.1016/j.apcata.2020.117568

Raw and processed data of this section can be downloaded from: https://data.mendeley.com/datasets/38c6gy3t4r/2 - DOI: 10.17632/38c6gy3t4r.2

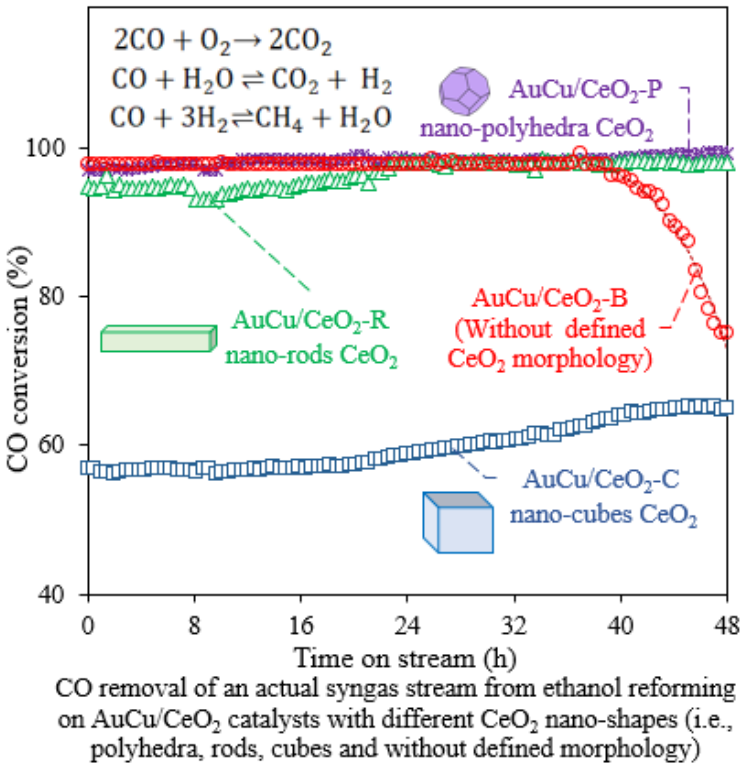

CO removal of an actual syngas stream from ethanol reforming on $AuCu/CeO_2$ catalysts with different CeO_2 nano-shapes (i.e., polyhedra, rods, cubes and without defined morphology)

Graphical abstract

Hydrogen purification of actual syngas streams for energy applications: Au-Cu supported over nano-shaped CeO_2 as stable catalysts for the carbon monoxide removal

Bernay Cifuentes[1,2], Felipe Bustamante[2], Daniel G. Araiza[3], Gabriela Diaz[3] and Martha Cobo[1*]

[1]Energy, Materials and Environment Laboratory, Chemical Engineering Department, Universidad de La Sabana, Campus Universitario Puente del Común, Km. 7 Autopista Norte, Bogotá, Colombia.

[2]Environmental Catalysis Laboratory, Chemical Engineering Department, Universidad de Antioquia UdeA, Calle 70 No. 52 - 21, Medellín, Colombia.

[3]Instituto de Física, Universidad Nacional Autónoma de México, Circuito de la Investigación Científica s/n, Cd. Universitaria, Ciudad de México 04510, México.

*Corresponding author: Email: martha.cobo@unisabana.edu.co, Tel: +571 8615555 Ext. 25207, Fax: 571 8615555

2.3.1 Abstract

Nano-shaped CeO_2 (i.e., polyhedra, rods and cubes) and CeO_2 without defined morphology were compared as supports of $AuCu/CeO_2$ catalysts in the CO removal of actual syngas streams. Catalyst characterization indicates that oxygen vacancies, exposed CeO_2 crystal planes, surface area and the interaction between active metals and support translate into changes in the catalytic performance on each nano-shape of CeO_2. CeO_2 nano-polyhedra and nano-rods show the higher activity and selectivity due to their high surface area and the presence of both {111} and {100} lattice planes. However, nano-rods are susceptible of losing CO_2-selectivity under continuous operation due to the presence of an additional and unstable {110} lattice plane. Therefore, an AuCu catalyst supported on nano-polyhedra CeO_2 ensures complete CO removal (i.e., <100 ppm) from an actual syngas stream for 48 h. These results are a contribution to the development of a simple, continuous, and robust system for fuel-cell grade H_2 production.

Keywords: Fuel-cell grade hydrogen; in-situ DRIFTS; Post-reforming stream cleaning; XRD; XPS.

2.3.2 Introduction

Hydrogen fuel cells (H_2-FC) are promising devices for pollution-free and efficient power production, which would favor their integration in commercial applications. However, obtaining H_2 from renewable resources is a key step in the establishment of the H_2-FC technology. In particular, production of H_2 from bioethanol obtained from agroindustrial wastes [1] is an attractive alternative because bioethanol from residual biomass is cheaper than that from food-crops and does not endanger food security [2,3].

Bioethanol conversion to H_2 is usually carried out via ethanol steam reforming (ESR) due to its high H_2 yield. The main products in the ESR include H_2, carbon monoxide (CO) and carbon dioxide (CO_2); hydrogenated species such as methane (CH_4) or ethylene (C_2H_4) could also be present in lesser amounts. Then, the post-reforming gas (syngas) should be purified depending on the final use of H_2. For the specific use of H_2 in proton exchange membranes FC (PEM-FC), which are the FC currently commercially available, CO must be removed due to its poising effect on the FC electrodes. Thus, the ESR is followed by a purification process to reduce the CO level in the syngas streams. Currently, CO is eliminated in two stages involving the chemical reactions presented in Table 2.3.1: a water gas shift reaction (WGS, R.1) is first used to remove most of the CO, followed by a final step that could include CO oxidation (R.2) or CO methanation (R.4) to ensure CO levels of parts per million (ppm). Each of these stages may require several reactors [4], making CO removal a complex and bulky process.

Recently, miniaturization has become a key aspect for the implementation of emerging technologies in the commercial sector [5]. Consequently, several technologies have been proposed to reduce the number of units used in the suitable production of PEM-FC grade H_2. For instance, advances in the design of PEM-FC have contributed to the development of more CO-tolerant devices. Narayanan and Basu [6] proposed the use of a solution of $KMnO_4$ to regenerate the PEM-FC electrodes, recovering the initial current density of a FC poisoned with a H_2 stream containing more than 100 ppm of CO. Similarly, Devrim et al. [7]

Table 2.3.1. Reaction network for the CO removal from syngas streams

Reaction	Description	
$CO + H_2O \rightleftharpoons CO_2 + H_2$	Water gas shift reaction, WGS	R.1
$2CO + O_2 \rightarrow 2CO_2$	CO oxidation	R.2
$2H_2 + O_2 \rightarrow 2H_2O$	H_2 oxidation	R.3
$CO + 3H_2 \rightleftharpoons CH_4 + H_2O$	CO methanation	R.4
$CO_2 + 4H_2 \rightleftharpoons CH_4 + 2H_2O$	CO_2 methanation	R.5

reported that an increase in the operating temperature of the PEM-FC mitigates the effect of CO poisoning, achieving a proper functioning at 160 °C for 500 h of a PEM-FC fed with a gas containing 3% of CO. Thus, 100 ppm of CO in the H_2 streams represents a conservative concentration for the most recent models of PEM-FC [8].

Integration of catalytic CO removal in a single reactor has also been studied. Ayastuy et al. [9] evaluated a CuO/CeO_2 catalyst in a system that integrated WGS and CO-PROX reactions in the same reactor, achieving the removal of most of the CO from a syngas (CO, H_2O, H_2, CO_2 and He). Similar results were reported by Reina et al. [10], who found that an $Au/CeFe_2/Al$ catalyst is promising for carrying out both WGS and CO-PROX reactions, but without complete CO conversion. Then, catalytic process integration would simplify the bulky CO removal step, but improvements in the catalysts design are required to ensure a CO-free H_2 stream.

Recently, we evaluated a system for CO removal of an actual syngas stream coming from ESR using only one catalytic reactor based on an AuCu catalysts supported on several metal oxides [11]. That work focused on the understanding of the effect of the support in CO removal. Complete CO removal (i.e., <100 ppm) was only achieved on $AuCu/CeO_2$ catalyst, but the catalyst was deactivated due to progressive changes in the CeO_2 structure. We also studied the Au/Cu ratio in CeO_2 [12], identifying that a weight ratio of Au/Cu = 1 provides a balance between CO removal and H_2 loss. Therefore, our intention now is to evaluate several CeO_2 nanostructure configuration to develop a stable $AuCu/CeO_2$ catalyst for the CO removal of actual syngas streams.

The modification of the support nanostructure has been reported as a novel strategy to develop more active, selective, and stable catalysts. Si et al. [13] assessed Cu catalysts supported on nano-cubes and nano-rods of CeO_2 in the WGS, reporting that the morphology affects the active metal dispersion and the oxygen vacancies of CeO_2. Similarly, Yi et al. [14] and Soler et al. [15] evaluated Au/CeO_2 catalysts with polyhedra, rods and cubes morphologies for the CO-PROX, reporting that CeO_2 morphology influences the CO adsorption/desorption properties and Au-CeO_2 interaction, which alters the catalytic activity. Therefore, modification of CeO_2 nanostructure would promote an active, selective, and stable catalyst for CO removal of a syngas coming directly from the ESR. Although there are reports on the effect of CeO_2 morphology on the CO-PROX and WGS, all these studies have been conducted with synthetic feeds. Catalysts evaluation using actual syngas streams could show catalytic phenomena that would be otherwise not observed, such as a high formation of formates and carbonates that increase carbon deposits and H_2 consumption [12]. Thus,

the effect of CeO_2 nanostructure in the CO removal should be evaluated using actual syngas streams. In addition, none of the previous studies have assessed specifically the bimetallic $AuCu/CeO_2$ system.

Therefore, this study aimed to evaluate the effect of CeO_2 nanostructure, looking to develop an active, selective, and stable $AuCu/CeO_2$ catalyst for CO removal from an actual syngas stream. To this end, several CeO_2 morphologies were assessed, including polyhedra, rods and cubes; besides, a CeO_2 without a defined morphology was used as reference. Catalytic performance and stability tests were carried out in a system that couples ESR and CO removal in line. Characterization by X-ray photoelectron spectroscopy (XPS), transmission electron microscopy (TEM), N_2 adsorption (BET), energy-dispersive X-ray spectroscopy (EDS), Atomic Absorption Spectroscopy (AAS), thermogravimetric analysis (TGA), *in-situ* diffuse reflectance infrared Fourier transform spectroscopy (DRIFTS), X-ray diffraction (XRD) and Raman spectroscopy were performed to identify structural changes of $AuCu/CeO_2$ catalysts during CO removal.

2.3.3 Experimental

Catalyst synthesis

AuCu catalysts were prepared over CeO_2 with different morphologies (i.e., polyhedra, rods and cubes); a sample without defined morphology was used as a reference to establish a base line for comparison. CeO_2 supports with a specified nano-shape were prepared by hydrothermal method according to [16]. Briefly, 0.3 M NaOH and 9.0 M NaOH solutions were mixed with $Ce(NO_3)_3{\cdot}6H_2O$ (Sigma Aldrich, USA) for polyhedra and rods/cubes synthesis, respectively, under continuous stirring for 1 h at 600 rpm. The slurry obtained was heated in an airtight container for 24 h at 100, 120 and 160 °C for polyhedra, rods and cubes, respectively. The precipitate was neutralized with water and calcined at 500 °C for 2 h. Blank CeO_2 was obtained from $Ce(NO_3)_3{\cdot}6H_2O$ calcined at 500 °C for 2 h. All supports were sifted using a 140-mesh sieve.

Au (1 wt%) and Cu (1 wt%) metals were impregnated according to the procedure described elsewhere [12]. Briefly, Au was included in specified nano-shaped CeO_2 by precipitation-deposition method, using a solution of $HAuCl_4{\cdot}3H_2O$ (Sigma Aldrich, USA). Afterwards, Cu was loaded into the previously prepared Au/CeO_2 catalyst by incipient wetness impregnation method, using a solution of $Cu(NO_3)_2{\cdot}3H_2O$ (Sigma Aldrich, USA). Catalysts were calcined at 500 °C for 2 h. The prepared $AuCu/CeO_2$ catalysts were labeled as AuCu/Ce–X, where X indicates morphology (X = P for polyhedra, R for rods, C for cubes and B for the blank).

Actual syngas streams were provided by ESR reaction using a $RhPt/CeO_2$-SiO_2 catalyst prepared according to previous reports [17]. Briefly, the dual CeO_2-SiO_2 support was prepared by incipient wetness co-impregnation of SiO_2 (Merck, Germany), using solutions of $Ce(NO_3)_3{\cdot}6H_2O$ (Alfa Aesar, USA). Subsequently, Rh and Pt active metals (each metal content is 0.4 wt%) were loaded into the support by incipient wetness co-impregnation, using solutions of $RhCl_3{\cdot}H_2O$ (Sigma Aldrich, USA) and $H_2PtCl_6{\cdot}6H_2O$ (Sigma Aldrich, USA) in water.

Catalytic tests

The actual syngas was generated from the ESR, using a fixed-bed catalytic reactor fed with 0.03 mL/min of synthetic bioethanol (water/ethanol molar ratio = 3) and 300 mL/min of Ar as carrier gas. Reaction was carried out at 700 °C, atmospheric pressure, and 6.4 ± 0.1 L/g_{cat} min of space velocity (SV). The catalyst bed was made of 0.050 g of $RhPt/CeO_2$-SiO_2 and 0.250 g of inert quartz particles. The molar composition of the syngas obtained, excluding carrier gas, was: H_2 (70.8%), CO (18.1%), CO_2 (8.3%), and CH_4 (2.8%), with a deviation lower than 7.3%.

The ESR output was mixed with dry air and directly connected to the CO-removal reactor, where AuCu catalysts supported over CeO_2 with different morphologies were evaluated. According to our previous study [12], an O_2 excess factor (λ) [18] of 1.8 ± 0.05 at the inlet of the CO-removal reactor was used to ensure a high CO conversion, reducing the H_2 loss. The catalytic bed was made of 0.050 g of Au-Cu/CeO_2 and 0.250 g of inert quartz particles, achieving a 6.5 ± 0.2 L/g_{cat} min of SV. Before activity tests, catalysts samples were reduced *in-situ* at 300 °C with 8 mol% H_2/Ar (330 mL/min) for 1 h, followed by a purge with Ar (300 mL/min) for 30 min and ended by a stabilization in 10% air/Ar (330 mL/min) for 30 min. These samples were labeled as "Activated" catalysts (AC). Light-off curves for each $AuCu/CeO_2$ catalyst were built from 300 to 100 °C, decreasing the temperature every 30 min in sequence of 20 °C. Samples used in catalytic evaluations were labeled as "Used" (U) catalysts. Finally, stability tests were conducted at 210 °C for 48 h time-on-stream (TOS) under the same conditions described above for the activity tests. Samples used in stability tests were labeled as "S". External and internal mass transfer limitations were controlled in both reactors as reported in [17]. Reaction conditions and processed Excel data of all activity and stability tests can be observed in detail and downloaded from [data set] [19].

Outlet streams of the ESR and CO-removal reactors were quantified by a Clarus 580 gas chromatograph unit (GC, Perkin Elmer, USA). Conversion (x_i) and yield for each detected product were calculated using 8 and 9.

$$x_i = \frac{F_{i,inlet} - F_{i,outlet}}{F_{i,inlet}} \times 100 \tag{8}$$

$$Yield_i = \frac{F_{i,outlet} - F_{i,inlet}}{C_{inlet\,ESR}} \tag{9}$$

Where F_i is the mole flow (mol/min) of species i (i.e., CO, CO_2, H_2, and CH_4) entering or leaving the reactor *of* CO removal and $C_{inlet\,ESR}$ is the total carbon flow (mol/min) fed into the system. Elemental carbon balances were calculated in each temperature and reported in Table SM.6 (see Supplementary Material).

Catalyst characterization

The catalytic surface of activated catalysts was studied by XPS in a NAP-XPS unit (Specs group, Germany) with a PHOIBOS 150 1D-DLD analyzer, using a monochromatic Al-Kα source (1486.7 eV, 13 kV, 100 W) and a pass energy of 20 eV for high resolution spectra. The binding energy (BE) reference was taken at the C1s transition at 284.8 eV. An estimated

error of 0.1 eV can be assumed for measurements. Data processing was performed with the CasaXPS program (Casa Software, UK), ensuring an adjustment parameter (R^2) $\geq$ 0.9.

The morphology of the samples was verified by TEM using a JEM 2010 F FasTem analytical electron microscope equipped with a Z-contrast annular detector working at 200 kV (Oxford Instruments, UK). Samples were previously dispersed on a carbon-film-coated copper grid using a syringe at high pressure. The particle size was measured using the ImageJ software.

Surface area of samples was estimated by N_2 adsorption tests in a ChemBET Pulsar unit (Quantachrome Instruments, USA), using a single point of 30% N_2/He (20 mL/min). The repeatability of the test was confirmed by a standard error $<$ 5%.

Au and Cu presence in AC samples of AuCu/CeO_2 catalysts was initially confirmed by EDS analysis in a Noran microanalysis system (Thermo Electron Corporation, USA) connected to a SEM JSM 5600 microscope. Afterwards, actual Au and Cu loadings in AC samples were measured by AAS using a Solaar S4 spectrometer (Thermo Electron Corporation, USA).

Deposits on catalyst samples were measured by TGA using a thermogravimetric analyzer (Mettler Toledo, USA). Test was performed between 30 to 1000 °C (5 °C/min) in dry air (150 mL/min). Weight loss of the AC samples was subtracted to the weight loss obtained in the spent catalysts.

In-situ DRIFTS was used to evaluate CO adsorption on AC samples in a Nicolet iS10 unit (Thermo Scientific, USA). 0.02 g of samples were put on a sampler holder, which consisted in a DRK-3 Praying Mantis (Harrick, USA) equipped with ZeSn windows. Then, the sample holder was sealed and aisled to avoid interference from the environment using an external flow of Ar (20 mL/min), which remained during the entire test. Afterwards, the sample was flushed with Ar (15 mL/min) at 50 °C [20] for 30 min. Finally, 10 pulses of 30 μL of CO, obtained from a certified 5% CO/Ar mixture, were injected into the sampler holder; between each pulse, Ar (15 mL/min) was passed for 10 min. Signal was collected between 4000–400 cm^{-1}, 2 cm^{-1} of resolution and 64 scans/min.

The crystalline structure of catalysts was determined by XRD in a D-8 diffractometer (Bruker Corporation, USA). Rietveld refinement of XRD data was performed using a FullProf suite software. Statistical parameters were used to validate the data adjustment: Chi-square test (Chi^2) $<$2.2 and R-weighted pattern (R_{wp}) $<$ 30% were assured in all settings.

Structure of the materials was analyzed by Raman spectroscopy in a DRX-Raman Microscope unit (Thermo Electron Corporation, USA) with a 532-nm laser excitation source (10 mW) and a spectral resolution of 2 cm^{-1} at ambient conditions.

Raw and processed Excel data of all characterization tests can be downloaded from [data set] [19].

2.3.4 Results and discussion

Activity and selectivity Figure 2.3.1 shows CO conversion, CO_2 yield, H_2 loss and CH_4 yield as a function of temperature obtained AuCu/CeO_2 catalysts with different nano-shapes of CeO_2 (i.e., polyhedra, rods, cubes and blank). Supports were included for comparison, for which it can be seen that although CO conversion is favored by temperature in the low temperature range (Figure 2.3.1a), the exothermic nature of the reaction and the competition

with H_2 oxidation (R.3) [12] delivers a maximum in CO conversion at different temperatures, depending on the CeO_2 morphology: Ce-R (150 °C), Ce-B (210 °C), Ce-P (255 °C) and Ce-C (300 °C). The redox properties ($Ce^{3+} \leftrightarrow Ce^{4+}$) and the high oxygen storage capacity (OSC) of the support [11] favor the high activity of CeO_2 in the total oxidation reactions, even without active metals [21].

The effectiveness of the Au-Cu system in the CO oxidation has been studied extensively [22,23]: Au favors the formation of C-O* intermediaries, which favor CO oxidation [24] (R.2) and methanation (R.4 and R.5) [12]. Similarly, Cu interacts with the support to form CuO species [22] and oxygen vacancies [25], favoring CO oxidation. In a previous study [12], we found that an Au/Cu weight ratio of 1 favors an active catalyst to remove CO and reduce H_2 loss due to the formation of hydrogenated compounds, such as CH_4. Besides, a synergistic effect of Au-Cu due to a possible alloy formation was proposed [23,26]. For this, the inclusion of Au and Cu in the catalysts promotes greater CO removal from an actual syngas compared to the supports. In particular, it was possible to obtain a CO-free H_2 stream (i.e., <100 ppm including the carrier gas) with AuCu/Ce-B (CO <70 ppm at 210 °C), AuCu/Ce-P (CO <60 ppm at 230 °C) and AuCu/Ce-R (CO <80 ppm at 255 °C); while the AuCu/Ce-C sample did not reach complete CO removal (4.800 ppm at 280 °C). The support and reaction gases (actual syngas) are extrinsic factors that have a crucial role in the performance of the Au-Cu system [22]. Therefore, differences in the catalytic activity among the $AuCu/CeO_2$ catalysts with different nano-shaped CeO_2 in the CO removal from an actual syngas seem to be associated with the nanostructure of the support and its interaction with the active metals (Au and Cu), as will be discussed in the "Catalysts characterization" section.

Figure 2.3.1b shows the CO_2 yield during the CO removal. Despite having similar activities, AuCu/Ce-P and AuCu/Ce-R show higher CO_2 yield than the blank (AuCu/Ce-B). The selectivity for CO oxidation depends strongly on the availability of oxygen vacancies on the catalyst surface. Then, the variation in the CO_2 yield could be associated with the oxygen mobility [27,28] on each type of CeO_2 morphology, as it will be discussed latter.

The consumption of H_2 during the CO removal is an important aspect to consider due to its impact on the efficiency of the process. Figure 2.3.1c shows H_2 losses up to 35% depending on the catalyst and the temperature. The presence of O_2 in excess favors H_2 oxidation (R.3) [29]. In this study, a previously optimized value [12] of λ=1.8 was used, which is higher than the stoichiometric factor ($\lambda = 1$) for CO oxidation (R.2). Also, CH_4 formation is observed in all catalysts (Figure 2.3.1d), especially on AuCu/Ce-B and AuCu/Ce-P samples, suggesting the presence of hydrogenation reactions, such as methanation of CO and CO_2. CH_4 formation depends also on the oxygen vacancies on the surface of each CeO_2 morphology [30]. The elemental balance of H_2 shows that CH_4 production contributes on an average of 20% to the H_2 loss during CO removal, which increases up to 30% at low temperature (<150 °C) on AuCu/Ce-B and AuCu/Ce-P samples. The remaining H_2 loss could be attributed to the formation of H_2O and other not quantified hydrogenated carbonaceous compounds.

Therefore, the CeO_2 morphology has a strong influence on the activity and selectivity of the $AuCu/CeO_2$ catalysts evaluated in the CO removal. The interaction between the active metals (Au and Cu) and the support (nano-shaped CeO_2), in addition to possible structural changes on the different nanostructures, could also influence the catalytic performance. Consequently, catalyst characterization was used to determinate how the CeO_2 morphologies affect activity and selectivity of $AuCu/CeO_2$ catalysts in the CO removal from an actual

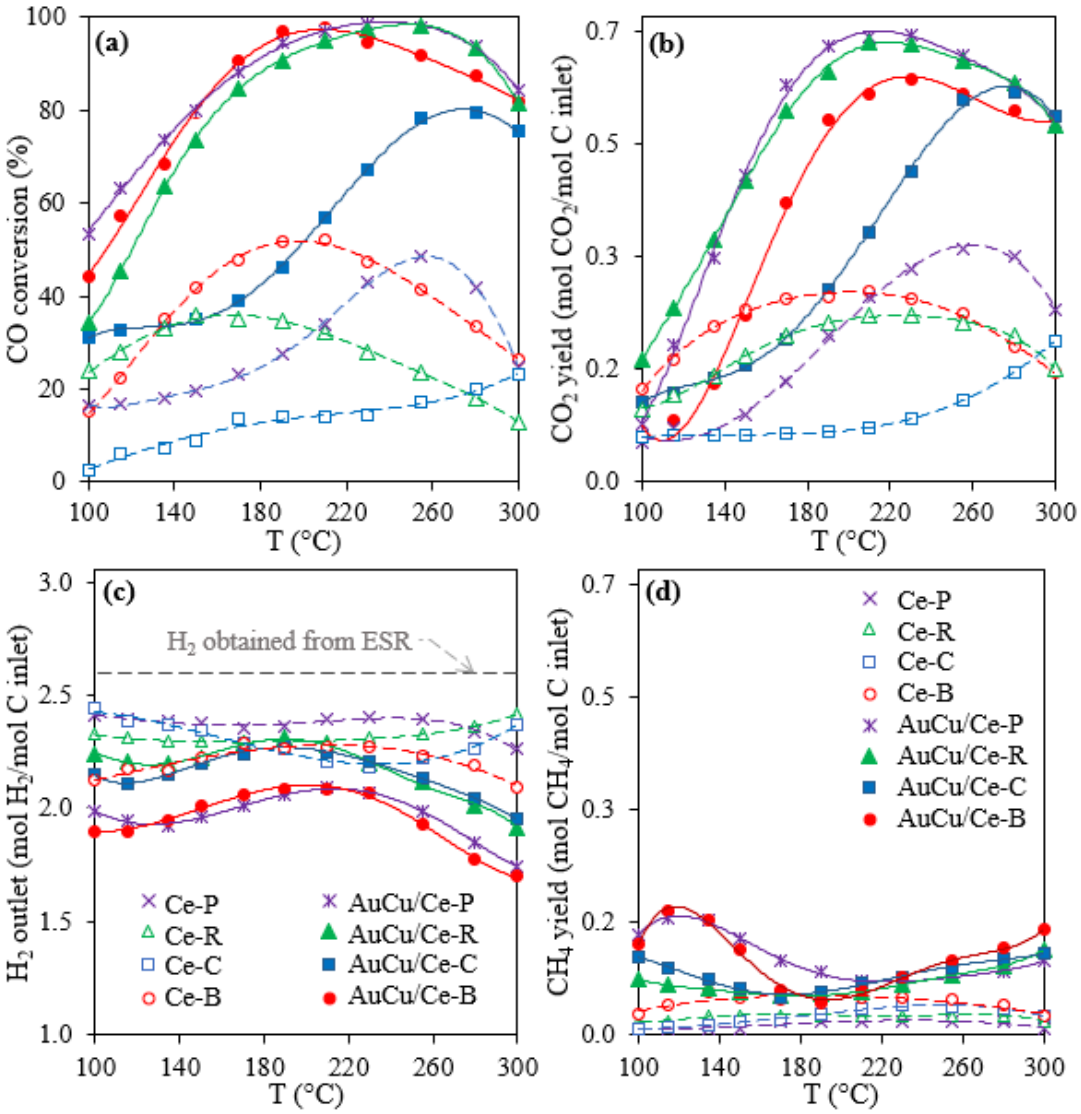

Figure 2.3.1. (a) CO conversion, (b) CO_2 yield, (c) H_2 loss and (d) CH_4 yield during the CO removal of a syngas stream over 1wt%Au-1wt%Cu/CeO_2 catalysts with different nano-shaped CeO_2: polyhedra (P), rods (R), cubes (C), and a blank (B) included for comparison. Syngas composition: 8.5% H_2, 2.2% CO, 0.5% CO_2, 0.3% CH_4, 1.5% H_2O and Ar balance. $\lambda = 1.8$.

syngas stream.

Catalysts characterization

XPS Oxidation states of Au, Cu, Ce and O on the catalyst surface of the 1wt%Au-1wt%Cu/CeO_2 catalysts with different nano-shaped CeO_2 was studied by XPS; Figure 2.3.2 shows the results. Au is identified only as Au^0 species in all AC samples (Figure 2.3.2a). AC samples were previously reduced in H_2 and oxidized in air at 300 °C, but the oxidant atmosphere was not enough to oxidize an appreciate amount of the Au loading. Au^0 promotes the CO conversion by formation of Au^0-OOH and Au^0-CO intermediates, as reported in [31]. Meanwhile, Cu shows the typical spin-orbital pair of $Cu2p_{3/2}$ zone for Cu^+ and Cu^0 (932,6 eV), and Cu^{2+} (934 eV), with two satellites of Cu^{2+} ($\sim$ 940 eV) [32]. Reduced species (e.g., Cu_2O) are the main active sites in CO-PROX over Cu/CeO_2 catalysts, as a result of its strong association with ceria (Cu-O-Ce) [33] and the fact that it acts as an effective adsorption site for C-O* intermediates, promoting a rapid conversion of CO [34]. Moreover, a certain amount of Cu^{2+} (CuO) sites is necessary to mitigate an excessive H_2 dissociation [34]. The $(Cu^+ + Cu^0)/Cu^{2+}$ ratio is shown in Table 2.3.2. AuCu/Ce-B shows a higher $(Cu^+ + Cu^0)/Cu^{2+}$ ratio that could be related to its high activity (Figure 2.3.1a). However, the possible deficiency of CuO species could influence the greater loss of H_2 observed over AuCu/Ce-B (Figure 2.3.1c). Similarly, a low $(Cu^+ + Cu^0)/Cu^{2+}$ ratio in AuCu/Ce-C could have impacted its activity. Therefore, an appropriate $(Cu^+ + Cu^0)/Cu^{2+}$ ratio, among other features discussed later, can be determinant in the activity and selectivity of the AuCu/CeO_2 system.

Figure 2.3.2c shows the XPS spectra for Ce on AuCu/CeO_2 catalysts. In addition, Table 2.3.2 presents the abundance of Ce^{3+} species (peaks v^0, v´, u^0, and u´), which are ascribed to oxygen vacancies [35], respect to the Ce^{4+} species (peaks v, v´´, v´´´, u, u´´, and u´´´). The highest availability of oxygen vacancies in AuCu/Ce-P and AuCu/Ce-R could be associated with its higher CO_2 formation (Figure 2.3.1b); while AuCu/Ce-B has 21% less vacancies, which could impact its CO oxidation capacity (less CO_2 yield, Figure 2.3.1b) and favor the hydrogenation of C-O* intermediates (high CH_4 yield, Figure 2.3.1d). Thus, a possibly enrichment of oxygen vacancies, along with a moderate $(Cu^+ + Cu^0)/Cu^{2+}$ ratio, in AuCu/Ce-P and AuCu/Ce-R would lead to active and selective catalysts for CO removal.

O spectra (Figure 2.3.2d) also show that AuCu/Ce-B has a significant difference respect to the other samples. Specifically, the amount of O_s + OH_s species, which are involved in the formation of intermediaries for CO conversion [36], is up to 4.2 times greater in AuCu/Ce-B compared to Au-Cu catalysts supported on well-defined-morphologies (Table 2.3.2). The presence of OH^- in the catalytic surface favors the formation of Au^0-OOH^-, which contributes to the CO adsorption [12], conducing to a high activity of AuCu/Ce-B (Figure 2.3.1a). However, an excess of OH^- groups and a high $(Cu^+ + Cu^0)/Cu^{2+}$ ratio also favor a greater carbon intermediates formation [37], which can be easily hydrogenated to produce CH_4 and coke [38]. Also, hydrogenation of carbon intermediates could compete with CO oxidation, reducing CO_2 formation. Therefore, a deficiency in oxygen vacancies, along with a high content of OH^- species, could explain the lower CO_2 yield of AuCu/Ce-B compared to AuCu/Ce-P and AuCu/Ce-R (Figure 2.3.1b). Changes in oxygen mobility have been associated with

the lattice planes exposed by each nanostructure of CeO_2; accordingly, the AuCu catalysts morphology will be evaluated by TEM in the following section.

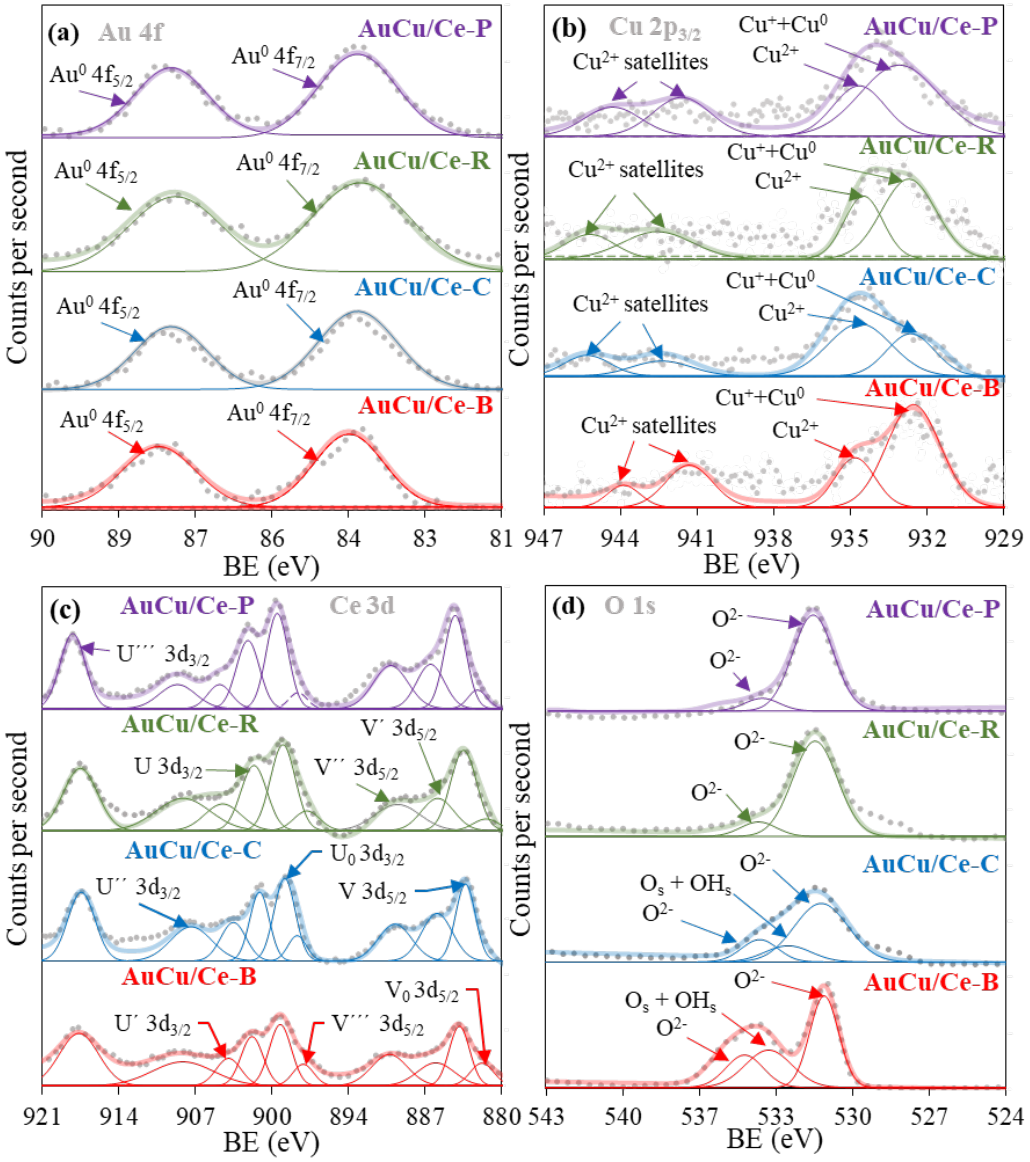

Figure 2.3.2. XPS spectra of (a) Au $4f_{5/2}$ and $4f_{7/2}$, (b) Cu $2p_{3/2}$, (c) Ce $3d_{3/2}$ and $3d_{5/2}$, and (d) O 1s for AC samples of the 1wt%Au-1wt%Cu/CeO_2 catalysts with different nano-shaped CeO_2 (polyhedra (P), rods (R), cubes (C), and a blank (B)).

TEM The morphology of the CeO_2 supports was verified by TEM (Figure SM.10 in Supplementary Material). The TEM micrographs show that each nano-shaped CeO_2 (i.e., polyhedra, rods and cubes) has a defined morphology and homogeneous distribution of CeO_2 nanoparticles. Table 2.3.2 shows the average size of particles for each morphology measured by TEM. The AuCu/CeO_2 catalysts maintain the shape (Figure SM.11 in Supplementary Material) of their corresponding CeO_2 support, indicating that the method of loading active

Table 2.3.2. Element abundance on catalyst surface, particle size and surface area of the 1wt%Au-1wt%Cu/CeO_2 catalysts with different nano-shaped CeO_2 (polyhedra (P), rods (R), cubes (C), and a blank (B)).

Catalysts	$(Cu^+ + Cu^0)/Cu^{2+}$ molar ratio[a]	Ce^{3+}/Ce^{4+} molar ratio[a]	Surface abundance of (O_s + OH_s) species (%)[a]	CeO_2 particle size[b]	BET surface area (m^2/g)			
AuCu/Ce-P	1.4	0.49	9.5	9.4 ± 1.5 nm of average diameter	84	86	76	72
AuCu/Ce-R	1.3	0.48	10.0	18 ± 1.9 nm of average diameter and 275 ± 28 nm in length	80	84	74	63
AuCu/Ce-C	1.1	0.45	14.8	38 ± 11 nm of the average edge	20	22	16	18
AuCu/Ce-B	2.1	0.38	39.9	without defined shape	66	71	61	63

SP: Support; AC: activated; U: used; and S: spent catalyst samples after stability test.
[a]Measured by XPS. [b]Measured by TEM.

metals does not affect CeO_2 morphology.

Au and Cu particles were not identified in TEM micrographs due to the low contrast between CuO and CeO_2 [12,16,39], together with a low particle size of Au [8,24]. However, Au and Cu presence in AuCu/CeO_2 catalysts was confirmed by EDS (Figure SM.12 in Supplementary Material), XPS and AAS (Table SM.7 in Supplementary Material), with values ranging 0.77 and 1.14 for Au loading and 0.82 and 0.92 for Cu loadings. Also, the concentration of active metals on the surface (measured by XPS, Table SM.7 in Supplementary Material) is greater than the concentration in the bulk (measured by AAS, Table SM.7 in Supplementary Material), indicating that Au and Cu are mostly on the surface of the AuCu/CeO_2 catalysts.

A Fast Fourier Transform (FFT) analysis to the TEM images were used to identify the lattice fringe spacing in each of the AuCu/CeO_2 catalysts, as shown in Figure 2.3.3. Interplanar distances between 0.21 to 0.24 nm can correspond to active metals (Au and Cu) [40,41]. On the other hand, the lattice planes traditionally reported for each CeO_2 nanostructure [15,42] were confirmed by interplanar distances observed in TEM micrographs. Cu/Ce-P (Figure 2.3.3a) shows stable {111} lattice planes (distances of 0.33 and 0.31 nm [43,44]) and less stable {100} lattice planes (distance of 0.27 nm [45]), associated with a high CO adsorption and the favoring of oxygen vacancies formation [46], as observed by XPS. Thus, the presence of both {111} and {100} lattice planes can improve CO_2 yield (Figure 2.3.1b).

Similarly, AuCu/Ce-R (Figure 2.3.3b) shows mainly the {111} and {100} lattice planes,

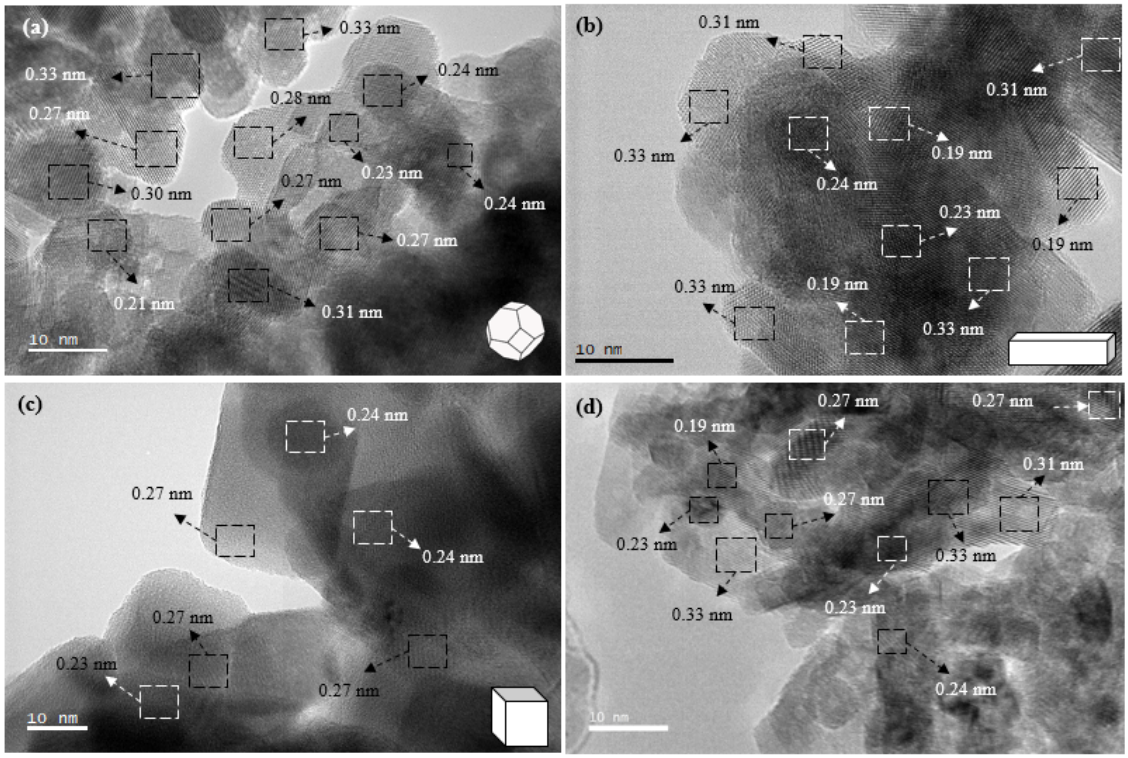

Figure 2.3.3. TEM images of 1wt%Au-1wt%Cu catalysts supported over CeO_2 with different morphologies: (a) polyhedra, (b) rods, (c) cubes and (d) blank.

which would explain why AuCu/Ce-P and AuCu/Ce-R displayed similar trends in CO conversion and CO_2 yield (Figure 2.3.1a and b). However, an additional unstable {110} plane (distance of 0.19 nm) [20], which promotes the CO oxidation even at low temperatures (<200 °C), is present in nanorods [47]. Then, the presence of the {110} lattice planes in AuCu/Ce-R could be linked to its greater effectiveness in mitigating the CH_4 formation at low temperature (<210 °C), compared to AuCu/Ce-P (Figure 2.3.1d).

The AuCu/Ce-C sample mainly exposes CeO_2 {100} lattice planes, which can favor a high CO_2 selectivity, with few {110} lattice planes associated with the corners of the cubes [48]. Nevertheless, the nano-cubes required higher temperatures to oxidize CO due to the high activation energy between the adsorbed CO and the O_2 vacancy over the {100} lattice planes [20]. Then, the presence of {100} lattice planes in the nano-cubes promotes the CO_2 selectivity, but could affect its activity at low temperature, as observed in AuCu/Ce-C (Figure 2.3.1a). Finally, AuCu/Ce-B exposes several facets, including {111}, {110} and {100} lattice planes. This combination of lattice planes could be related to the high activity of the unmodified CeO_2 (AuCu/Ce-B in Figure 2.3.1a), as was presented above. However, the presence of an excessive number of unstable lattice planes (e.g., {110} and {100}) could favor structural changes that affect the catalytic performance, as previously reported [12].

TEM test was carry out in spent samples (data not shown), observing the same lattice planes and CeO_2 morphology as in the activated samples.

Therefore, the lattice planes exposed by each CeO_2 morphology significantly affect the activity and selectivity of the AuCu/CeO_2 catalysts. However, other structural features of the supports can also contribute to the catalytic performance in the CO removal from an actual syngas stream.

BET area Table 2.3.2 shows the specific surface area of supports and AuCu/CeO_2 catalysts. It is accepted that catalytic activity scales with surface area [49], which agrees with the results of the activity test (Figure 2.3.1a). However, to assess the intrinsic activity of nano-shaped CeO_2, CO conversion rate and CO_2 formation rate were normalized by the specific BET surface area of the catalysts, Figure 2.3.4. When surface area is the main reason on the differences in catalytic activity, normalized rates measured on the different samples should be identical [49]. AuCu/Ce-P, AuCu/Ce-R and AuCu/Ce-B show a similar normalized activity and CO_2 selectivity profile (Figure 2.3.4), but they were already similar in Figure 2.3.1.

Nevertheless, the catalyst with the lowest surface area shows the highest normalized activity data (AuCu/Ce-C in Table 2.3.2 and Figure 2.3.4, respectively). Therefore, other features seem to be affecting activity and selectivity. For instance, the AuCu/Ce-C catalyst showed a larger presence of the {100} lattice planes which can be related to a higher oxygen mobility [15,50] and, therefore, to its highest normalized CO conversion rate. Similarly, the combination of multiple lattice planes could favor a slight increase in the AuCu/Ce-B normalized activity compared to AuCu/Ce-P and AuCu/Ce-R (Figure 2.3.1a). Additionally, the normalized CO_2-production rate (Figure 2.3.4b) is also favored by the presence of CeO_2 {100}, while the additional {110} lattice planes on AuCu/Ce-R and AuCu/Ce-B do not seem to contribute significantly to the CO_2 production. Therefore, activity and selectivity of AuCu supported on nano-shaped CeO_2 catalysts are greatly influenced by the surface area

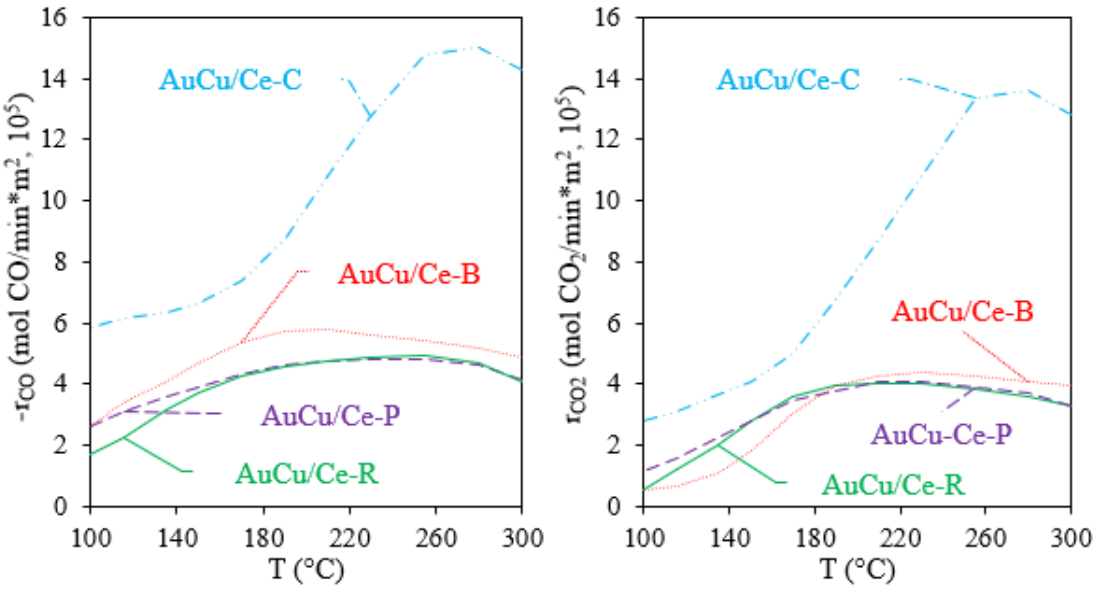

Figure 2.3.4. Normalization of (a) CO conversion rate and (b) CO_2-formation rate with respect to the surface area on the CO removal from an actual syngas streams over 1wt%Au-1wt%Cu/CeO_2 catalysts with several nano-shapes: polyhedra (P), rods (R) and cubes (C); blank (B) is included as comparison.

but this feature is not the only one when considering their differences.

On the other hand, the surface area of the catalysts decreases after the activity tests (Table 2.3.2). The decrease percentage followed the order: AuCu/Ce-C (27%) > AuCu/Ce-B (14%) > AuCu/Ce-R = AuCu/Ce-P (11%). The change in the surface area could be associated with carbon deposition and/or structural changes of the supports, as will be discussed in the following sections.

TGA The amount of reaction deposits was evaluated by TGA. Table 2.3.3 shows the weight loss of spent catalysts. AuCu/Ce-R and AuCu/Ce-P were the catalysts with the highest weight lost. A detailed review of the weight loss by temperature interval (Table SM.8 in Supplementary Material) shows that about 64% is between 80 to 250 °C [51], which can correspond to adsorbed water in the bulk of the catalysts. The H_2O content in the syngas and the H_2 oxidation during CO removal would be related to the adsorption of H_2O in the catalysts. In addition, between 250 and 600 °C, weight loss can be related to the formation of less stable carbon deposits. AuCu/Ce-P shows the lower weight loss in this zone, while AuCu/Ce-C presents the higher one. Moreover, the percentage of weight loss between 600 and 1000 °C, associated with the formation of stable carbon deposits, is lower in AuCu/Ce-C and higher in AuCu/Ce-P. The elemental carbon balances (Table SM.6 in Supplementary Material) indicate that most carbon deposits are formed between 160 to 240 °C, where the carbon balances decrease in all samples. This zone match with high CO conversion in the most samples (see Figure 2.3.1a). Then, the differences in the formation of carbon deposits could be associated with the reaction intermediates formed on each nanostructure. For this reason, the formation of intermediates during the CO removal was analyzed by CO

adsorption measured by *in situ* DRIFTS.

Table 2.3.3. TGA, XRD and Raman characterization of 1wt%Au-1wt%Cu/CeO_2 catalysts with different nano-shaped CeO_2 (polyhedra (P), rods (R), cubes (C), and a blank (B)).

Catalysts	Weight loss of used samples (%)[a]			CeO_2 average crystallite size (nm)[b]				Lattice parameter of F samples (Å)[b]		F_{2g} peak of CeO_2 (cm^{-1})[c]			
	SP	U	S	SP	AC	U	S	SP	AC	SP	AC	U	S
AuCu/Ce-P	2.0	2.4	2.5	8.9	8.9	9.3	9.0	5.4293	5.4199	465	452	459	452
AuCu/Ce-R	2.1	2.9	3.1	10.3	10	9.8	9.1	5.4294	5.4195	463	454	459	455
AuCu/Ce-C	3.4	2.2	2.6	20.5	21	20	17	5.4203	5.4202	464	452	450	457
AuCu/Ce-B	1.6	1.9	2.9	7.8	7.8	8.8	9.5	5.4295	5.4194	462	456	448	449

SP: Support; AC: activated; U: used; and S: spent catalyst samples after stability test.
[a]Measured by TGA. [b]Measured by XRD. [c]Indentified by Raman spectroscopy.

***in-situ* CO DRIFTS** Figure 2.3.5 shows the DRIFTS spectra for the CO adsorption on bare-supports and Au-Cu catalysts. The intensity of the adsorption peaks of CO as carbonyls (2147 and 2095 cm^{-1}) and CO_2 (2355 cm^{-1}) is higher in the Au-Cu catalysts compared to their respective supports. Peak at 2095 cm^{-1} has been associate with the formation of Au^0-CO species [52], confirming the presence of Au^0 evidenced by XPS (Figure 2.3.2a). It is well known that both Au and Cu favor the formation of intermediaries during CO removal [52,53]. However, the formates and carbonates zone (C-O* spectral region in Figure 2.3.5) shows that each nanostructure favors different intermediaries, which could be associated with the presence of different lattice planes exposed [20,54]. A high variety of peaks in C-O* spectral region is favored by {111} lattice planes [54], mostly present in AuCu/Ce-P, AuCu/Ce-R and AuCu/Ce-B, while {100} lattice planes exposed by the AuCu/Ce-B favor a decrease in the number of bands in this region. The presence of {100} lattice planes also favors the shift of the CO adsorption at a high wavenumber (2095 to 2103 cm^{-1}) [20]. {100} lattice planes in nano-cubes favor the regeneration of OH^- groups, mitigating carbonates formation (peaks 1395 and 1480 cm^{-1}) [50], which are intermediates in carbon deposition [37]. Thus, the presence of CeO_2 {100} in AuCu/Ce-C seems to mitigate the formation of stable carbon deposition favoring the normalized CO_2-production rate (Figure 2.3.4b). On the other hand, a high formation of carbonates and formates is promoted by CeO_2 {111} [50], favoring carbonaceous deposits during the CO removal [12]. Therefore, the presence of {111} lattice planes could be associated with a higher amount of carbon deposits on the other samples (AuCu/Ce-P, AuCu/Ce-B and AuCu/Ce-R). Although AuCu/Ce-R and AuCu/Ce-B show greater band intensities in the C-O* spectral region (1200 to 1750 cm^{-1} in Figure 2.3.5), which could be associated with the presence of highly reactive and unstable {110} lattice planes, results of TGA are not conclusive about the effect of {110} lattice planes on carbon deposition. In addition, a high resistance to carbon deposits formation has been recently attributed to nanorods [55,56]. However, it is noticeable that carbonate peaks (peaks 1395

and 1480 cm^{-1}) have a significant intensity in AuCu/Ce-B, which could lead to a high carbon deposition under long operation time.

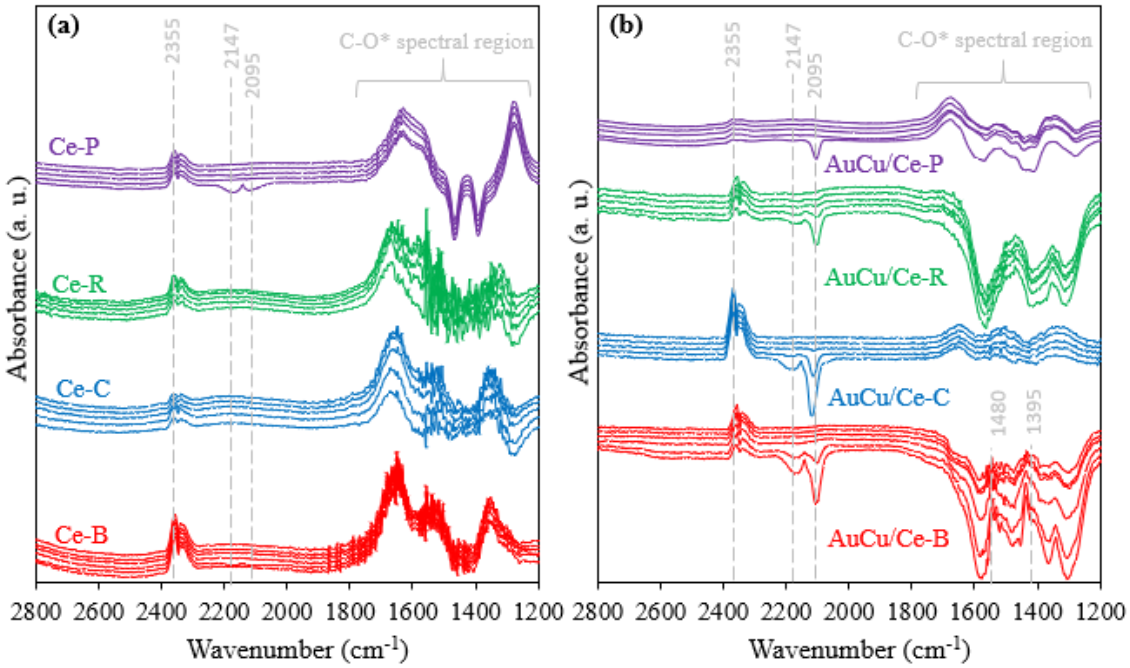

Figure 2.3.5. DRIFTS spectra for CO adsorption on (a) supports and (b) 1wt%Au-1wt%Cu catalysts supported on several CeO_2 nanoshapes: polyhedra (P), rods (R), cubes (C) and blank (B).

The adsorption and deposition of species on the catalyst surface could significantly affect the BET surface area of the catalysts. However, the tendency in weight loss does not match the decrease in surface area, so possible structural changes in the catalyst could be also taking place. Accordingly, an XRD study was performed to identify the possible changes in the crystallite size of the nanostructures of CeO_2.

XRD Figure 2.3.6 shows the XRD diffraction patterns of CeO_2 supports and AuCu/CeO_2 catalysts. A cubic fluorite structure of CeO_2 (JCPDS 34-0394 [16]) was confirmed by peaks at 2θ = 28.6°, 33°, 47.4°, 56.6°, 76.3° and 79.1° [57], however the peak intensities changed in each sample, which could be linked to a variation in the nano-CeO_2 structure. Table 2.3.3 shows CeO_2 average crystallite size obtained from Rietveld refinement of XRD patterns. Low CeO_2 crystal sizes favor higher surface areas, so the large size of the ceria crystal in AuCu/Ce-C contributes to its low surface area. On the other hand, diffraction peaks at 2θ = 35.7° and 38.9°, associated with Cu [58], were not observed by XRD, indicating that Cu would be well-dispersed [16] on AuCu/CeO_2 catalysts. Similarly, peak of Au at 2θ = 38.3° [58] was only detected in AuCu/Ce-R, suggesting that Au is also well dispersed in most of the AuCu/CeO_2 samples. Besides, Rietveld analysis showed a decrease in cell parameter of CeO_2 in the AuCu/CeO_2 catalysts compared to the corresponding supports (Table 2.3.3). The shrinkage of the CeO_2 lattice has been associated with the incorporation of some Cu^{2+}

in CeO_2 [59], as was observed by XPS, promoting high Cu dispersion and oxygen vacancies formation [60].

After the activity test, the AuCu/Ce-B catalyst showed a 13% increase in the average CeO_2 crystal size, while the variation in the other AuCu/CeO_2 samples (i.e., AuCu/Ce-P, AuCu/Ce-R and AuCu/Ce-C) was less than 5% (Table 2.3.3). Thus, the unmodified CeO_2 (AuCu/Ce-B) is susceptible to both carbon deposition and changes in crystallinity. Thus, the modification of the CeO_2 morphology (i.e., polyhedral, rods and cubes shapes) is a promising strategy to mitigate structural changes and carbon deposition during the CO removal from an actual syngas, which is in agreement with other studies [42,45,61].

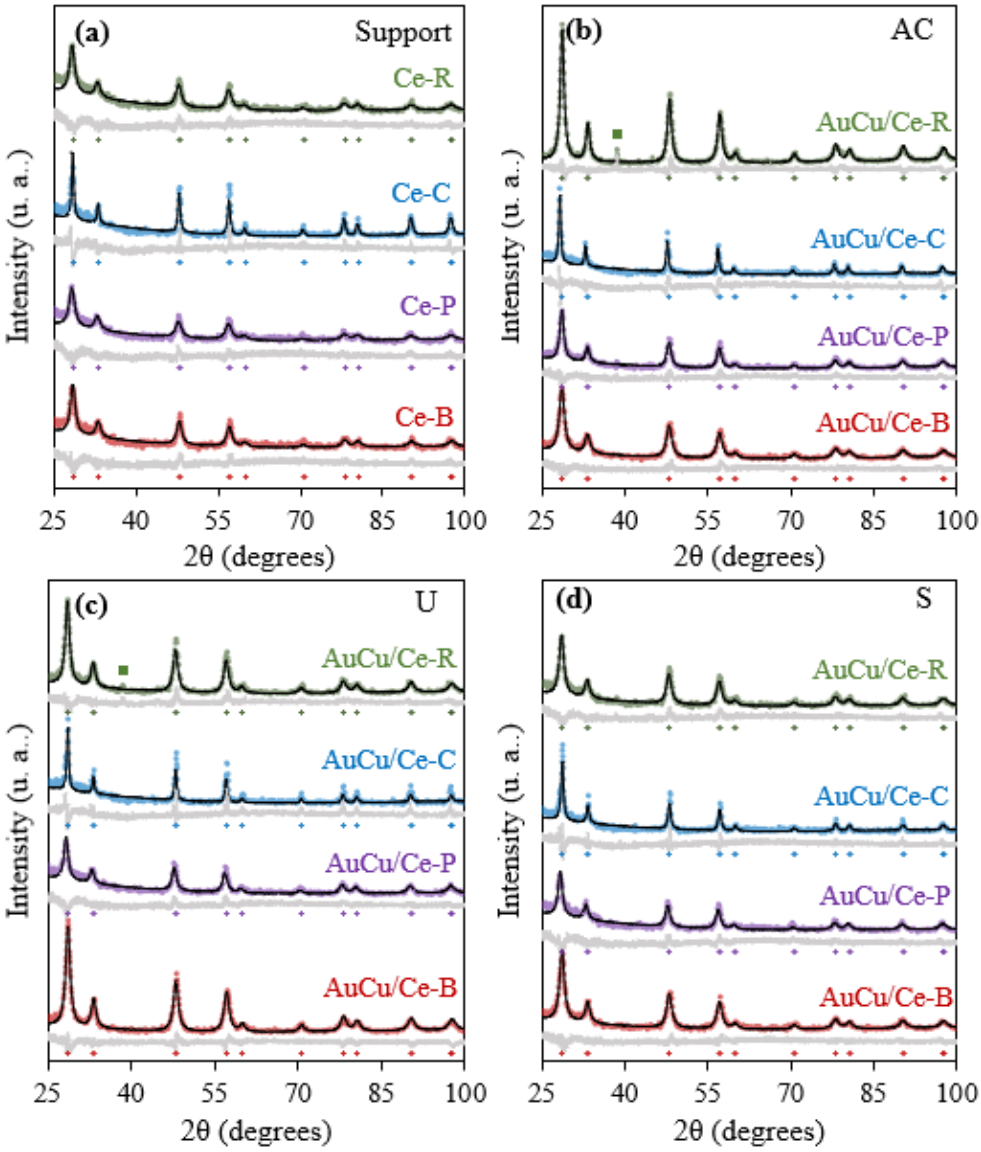

Figure 2.3.6. X-ray diffraction patterns of (a) CeO_2 supports, (b) AC samples of AuCu/CeO_2 catalysts, (c) spent AuCu/CeO_2 catalysts after the activity tests and (d) spent AuCu/CeO_2 catalysts after the stability tests. Suffix indicate the kind of nano-shaped CeO_2: polyhedra (P), rods (R), cubes (C) and blank (B).

Raman spectroscopy The structure of the catalysts was further investigated by Raman spectroscopy. Raman spectra for the AuCu/CeO_2 catalysts are shown in Figure 2.3.7. Typical Raman spectrum for fluorite crystal structure was observed in all samples [16], in agreement with XRD results. The main peak around 460 cm^{-1} is attributed to F_{2g} mode [62] and shoulders at 600 and 250 cm^{-1} correspond to longitudinal optical (LO) and transverse optical (TO) modes [8], respectively, which include contributions from oxygen vacancies [8,63]. The F_{2g} band is particularly dependent on the disorder induced in O^{2-} ion sub-lattice of the CeO_2 [8]. Table 2.3.3 shows the F_{2g} peak position displayed by AuCu/CeO_2 catalysts. After Au and Cu inclusion on nano-CeO_2, the F_{2g} band widens (Figure 2.3.7) and shifts towards lower frequencies indicating the presence of a second phase [56], possibly due to the strong interaction between CuO and CeO_2. The shift was similar in all samples, indicating that the Cu-CeO_2 interaction is morphologically non-dependent. After activity tests, slight shifts are observed in the position of the F_{2g} peak, suggesting that the operating conditions may influence the metal-support interaction. In addition, the relative intensity in the LO mode is higher in AuCu/Ce-P, confirming the enriched in oxygen vacancies in the surface of AuCu/Ce-P observed by XPS, which would be in agreement with other reports [61].

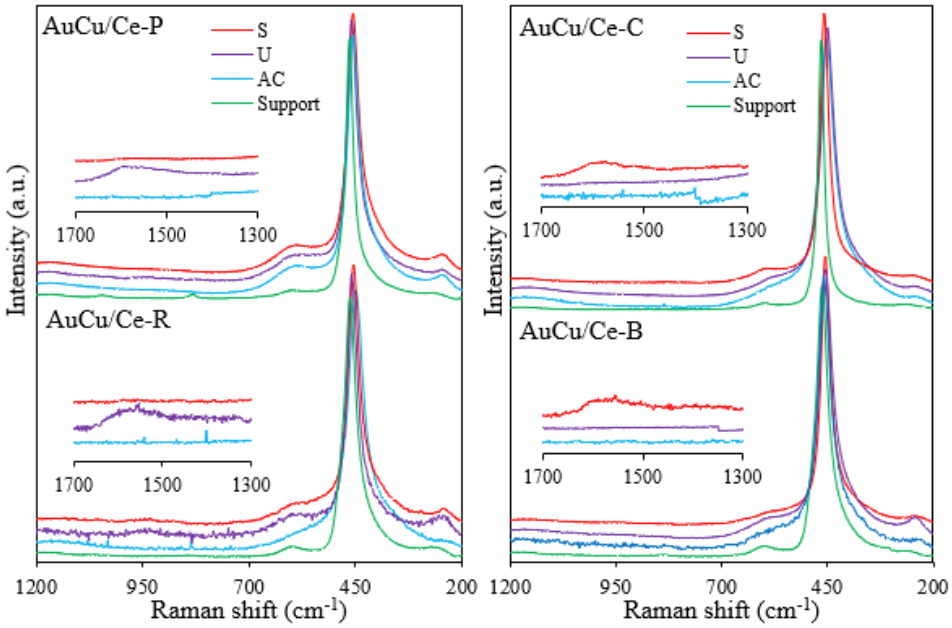

Figure 2.3.7. Normalized Raman spectra of 1wt%Au-1wt%Cu supported over CeO_2 with different morphologies: polyhedra (P), rods (R), cubes (C) and blank (B). AC catalysts (AC), spent samples after the activity tests (U) and used after the stability tests (S).

Carbon deposits on the catalysts were also investigated by G and D vibrations modes. G peak approximately at 1590 cm^{-1} is related to nano crystalline, more stable carbon, whereas D peak at about 1350 cm^{-1} is associated with amorphous, less stable carbon. D vibration was not identified by Raman spectra in any sample (Figure 2.3.7). However, TGA showed that small amounts of non-stable carbon are present in used AuCu/CeO_2 samples. Contrarily, G vibration mode was detected in used samples of AuCu/Ce-P and AuCu/Ce-R catalysts, confirming the presence of stable carbon deposits in these catalysts, as was observed in the

TGA results (Table 2.3.3).

Stability test A purpose of this research was to develop a stable catalyst for its future use in applications linked to H_2-FC. Therefore, the stability for CO removal from an actual syngas stream over AuCu/CeO_2 catalysts was evaluated, Figure 2.3.8. The stability tests of all AuCu/CeO_2 catalysts was carried out at the same temperature (210 °C), representative of the highest activity of most catalysts. At the outlet of the CO removal reactor, AuCu/Ce-P achieved a CO concentration <80 ppm during the whole stability test (Figure 2.3.8a), while AuCu/Ce-R and AuCu/Ce-C showed an improvement in CO elimination with TOS, AuCu/Ce-R reaching a concentration of CO < 95 ppm after 30 h TOS. A possible interaction between Cu and nano-shapes was analyzed above and ascribed to a F_{2g} band shift, detected by Raman spectroscopy, which promotes a more stable material [39]. Then, the high amount of oxygen vacancies, the presence of stable {111} lattice planes, a high surface area and a strong interaction with the active sites lead AuCu/Ce-P to be more active and stable in the CO removal compared to the other CeO_2 morphologies. On the other hand, despite its high initial activity, AuCu/Ce-B showed a drastic deactivation after 38 h TOS, which could be associated to: (i) a 11% reduction of the surface area (Table 2.3.2); (ii) a high carbon deposition (Table 2.3.3), of which 24% corresponds to stable carbon deposits (Figure 2.3.7 and Table SM.8 in Supplementary Material); (iii) an increase of 22% in the crystal size of CeO_2 (Table 2.3.3); and, (iv) the decrease in oxygen vacancies (Figure 2.3.7).

The CO_2 yield also changes with TOS (Figure 2.3.8b). AuCu/Ce-P and AuCu/Ce-C show a slight improvement in the CO_2 selectivity with TOS. In contrast, AuCu/Ce-R shows a decrease in CO_2 produced after 11 h. {110} lattice planes, which favor the oxidation of CO [47], are very unstable and tend to form {111} lattice planes [20], which are active but less selective. Then, the presence of unstable {110} lattice planes would lead to a loss in the selectivity of AuCu/Ce-R with TOS. Similarly, AuCu/Ce-B shows an initial increase in CO_2 yield, followed by a rapid decrease after 27 h. Drastic changes in the selectivity of AuCu/Ce-B with TOS could be ascribed to its susceptibility to structural changes, oxygen vacancies deficiency, and the excess of unstable {100} and {110} lattice planes.

In general, H_2 loss decreases with TOS, except on AuCu/Ce-R. Possible rearrangements on CeO_2 promoted by both reducing and oxidizing atmospheres [27,64] reduce the H_2 loss during CO removal [12]. At the end of the stability test, H_2 loss followed the trend AuCu/Ce-R (24%)> AuCu/Ce-C (20%)> AuCu/Ce-P (17%)> AuCu/Ce-B (15%), and only AuCu/Ce-P and AuCu/Ce-R ensured CO-free H_2 streams (<100 ppm including the carrier gas). A slight increase in the oxygen vacancies (Figure 2.3.7) and less C-O* intermediates (Figure 2.3.5) that avoid an excess in stable carbon deposition (Figure 2.3.7 and Table 2.3.3) could be related to the reduction of H_2 loss in AuCu/Ce-P.

Additionally, AuCu/Ce-P and AuCu/Ce-C showed a decrease in CH_4 yield, reducing simultaneously the H_2 loss during CO removal (Figure 2.3.8c). On the contrary, AuCu/Ce-B and AuCu/Ce-R show a significant increase in CH_4 yield, contributing to the H_2 loss. Formation of carbonates and formates in excess, as observed by DRIFTS (Figure 2.3.5), can be related to the higher CH_4 production (Figure 2.3.8d) and carbon deposits (Table 2.3.3) observed on AuCu/Ce-B and AuCu/Ce-R.

Previous studies [14,15,47] present nano-shaped CeO_2 with rods morphology as the most

appropriate support for the CO removal from synthetic-syngas streams, which only contains H_2 and CO. However, in our study we found that, despite of its high activity to remove CO (Figure 2.3.1a), the AuCu/Ce-R catalyst is prone to lose selectivity over time when is evaluated with an actual syngas stream (Figure 2.3.8). Thus, the CeO_2 morphology and the actual syngas stream influence the catalytic performance of the AuCu/CeO_2 system. Therefore, AuCu/Ce-P is shown as a promising catalyst for CO removal from an actual syngas stream during continuous operation due to: (i) the combination of {111} and {100} lattice planes that simultaneously favor high activity and selectivity; (ii) a higher surface area that contributes to active-site dispersion; and, (iii) mitigation in the formation of intermediaries that lead to carbon deposition and methanation, due to an enrichment of superficial oxygen vacancies.

2.3.5 Conclusions

CeO_2 with nano-shapes of polyhedra (P), rods (R), cubes (C) and a blank (B), i.e., without defined nano-shape, were evaluated as supports for 1wt%Au-1wt%Cu/CeO_2 catalysts in the CO removal from an actual syngas stream. It was possible obtaining a CO-free H_2 stream (i.e., <100 ppm including the carrier gas) over AuCu/Ce-P (CO <50 ppm), AuCu/Ce-B (CO <70 ppm), and AuCu/Ce-R (CO <80 ppm), while the AuCu/Ce-C sample did not achieve complete CO removal.

Activity and selectivity of the AuCu/CeO_2 catalysts was found to be related to the morphological properties of each nano-shape. Among all the samples, the presence of Au^0, Cu^{2+} and reduced Cu ($Cu^+ + Cu^0$) species on the catalyst surface favors the formation and adsorption of C-O* intermediates, improving CO conversion compared to bare-supports. However, samples with defined morphology (i.e., polyhedra, rods and cubes) are more structurally stable than the blank sample, which makes the latter susceptible to deactivation. The {111} and {100} lattice planes simultaneously shown by nano-polyhedra and nano-rods along with a high surface area, favor higher activity and selectivity over these catalysts. However, the presence of unstable {110} lattice planes in the nano-rods affects the CO_2 yield on AuCu/Ce-R in continuous operation. Conversely, the AuCu/Ce-P catalyst remained stable for 48 h of continuous operation, ensuring a CO concentration below 100 ppm in the syngas stream without loss of CO_2 selectivity. However, a H_2 loss of 17% is a consequence of an integrated reactor to eliminate CO from actual syngas streams. These results are a contribution to the development of a simple and continuous system for fuel-cell grade H_2 production.

2.3.6 Acknowledgments

The authors are grateful to Colciencias (Francisco Jose de Caldas Fund) and Universidad de La Sabana for the financial support to this work through the Project ING-221 (Colciencias contract 548–2019). The authors also acknowledge Universidad de Antioquia; M. Aguilar, S. Tehuacanero-Cuapa and R. Hernández (EDS, TEM/HRTEM), A. Morales (XRD), C. Zorrilla (Raman) and A. Gómez-Cortés (Rietveld Refinement) from Instituto de Física of Universidad Nacional Autónoma de México, for their support. Bernay Cifuentes acknowledges Colciencias for the doctoral scholarship (grant number 727-2015) and Daniel G. Araiza thanks CONACyT for the PhD scholarship No. 308329.

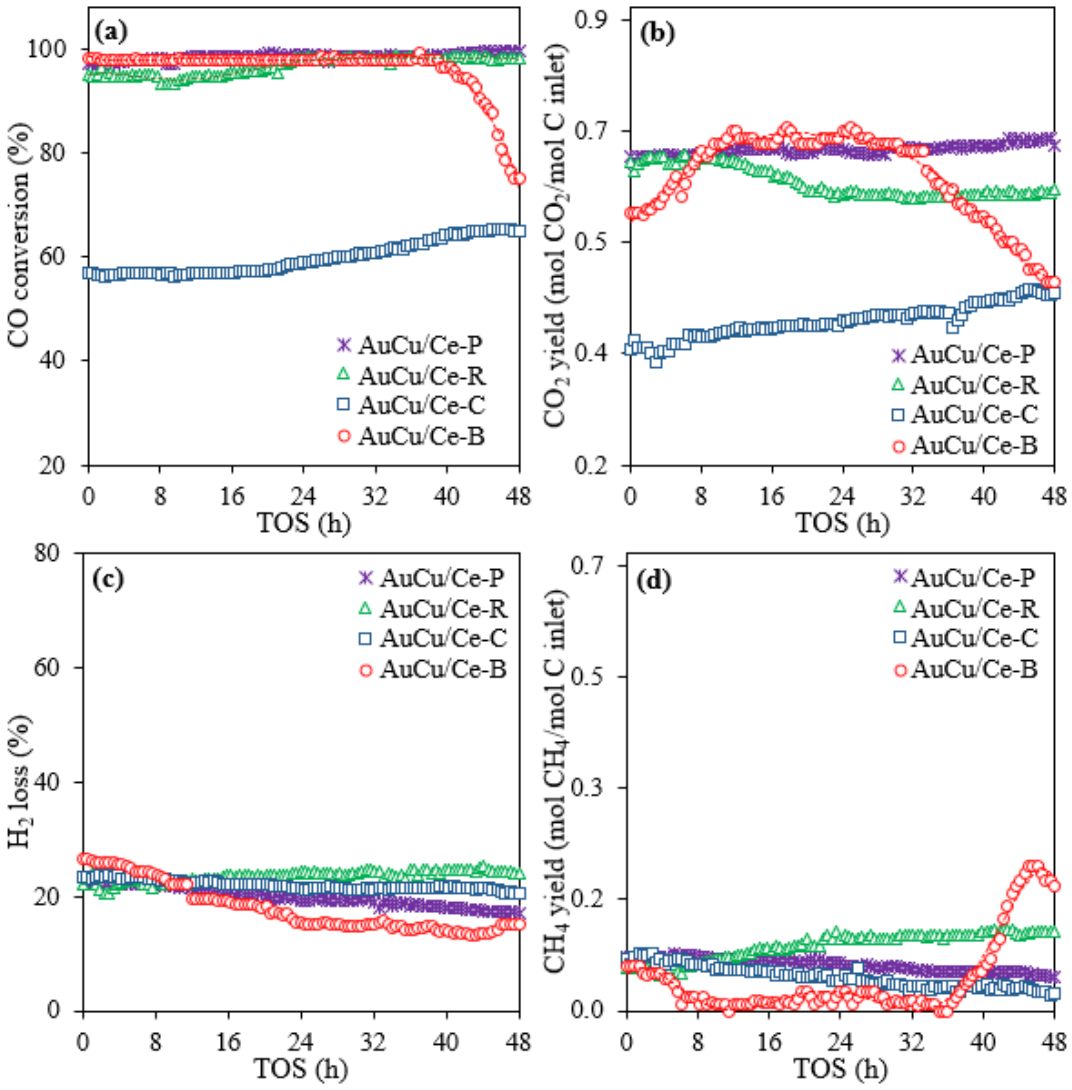

Figure 2.3.8. Stability of 1 wt%Au-1wt%Cu/CeO_2 catalyst supported on different nano-shaped CeO_2 (polyhedra (P), rods (R) and cubes (C); blank (B) is included for comparison) for CO removal of a syngas stream: (a) CO conversion, (b) CO_2 yield, (c) H_2 loss and (d) CH_4 yield. Inlet stream: 7.8% H_2, 2.0% CO, 0.5% CO_2, 0.3% CH_4, 1.4% H_2O, 1.8% O_2, 6.8% N_2 and 79.4% Ar. Reaction conditions: 210 °C, SV=6.5 ± 0.2 L/g_{cat} min; 0.050 g of catalyst and 0.250 g of inert quartz.

2.3.7 References

[1] N. Sanchez, R.Y. Ruiz, N. Infante, M. Cobo, Energies 10 (2017) 1–16.
[2] N. Sarkar, S.K. Ghosh, S. Bannerjee, K. Aikat, Renew. Energy 37 (2012) 19–27.
[3] N. Sanchez, R.Y. Ruiz, B. Cifuentes, M. Cobo, Int. J. Hydrogen Energy 41 (2016) 5640–5651.
[4] F. Barrai, M.J. Castaldi, Ind. Eng. Chem. Res. 49 (2010) 1577–1587.
[5] M.K. Moharana, N.R. Peela, S. Khandekar, D. Kunzru, Renew. Sustain. Energy Rev. 15 (2011) 524–533.
[6] H. Narayanan, S. Basu, Int. J. Hydrogen Energy 42 (2017) 23814–23820.
[7] Y. Devrim, A. Albostan, H. Devrim, Int. J. Hydrogen Energy 43 (2018) 18672–18681.
[8] L. Ilieva, P. Petrova, G. Pantaleo, R. Zanella, L.F. Liotta, V. Georgiev, S. Boghosian, Z. Kaszkur, J.W. Sobczak, W. Lisowski, A.M. Venezia, T. Tabakova, Appl. Catal. B Environ. 188 (2016) 154–168.
[9] J.L. Ayastuy, E. Fernández-Puertas, M.P. González-Marcos, M.A. Gutiérrez-Ortiz, Int. J. Hydrogen Energy 37 (2012) 7385–7397.
[10] T.R. Reina, S. Ivanova, O.H. Laguna, M.A. Centeno, J.A. Odriozola, Appl. Catal. B Environ. 197 (2016) 67–72.
[11] B. Cifuentes, F. Bustamante, M. Cobo, Catalysts 9 (2019) 852–877.
[12] B. Cifuentes, F. Bustamante, J.A. Conesa, L.F. Córdoba, M. Cobo, Int. J. Hydrogen Energy 43 (2018) 17216–17229.
[13] R. Si, J. Raitano, N. Yi, L. Zhang, S.W. Chan, M. Flytzani-Stephanopoulos, Catal. Today 180 (2012) 68–80.
[14] G. Yi, Z. Xu, G. Guo, K. ichi Tanaka, Y. Yuan, Chem. Phys. Lett. 479 (2009) 128–132.
[15] L. Soler, A. Casanovas, A. Urrich, I. Angurell, J. Llorca, Appl. Catal. B Environ. 197 (2016) 47–55.
[16] D.G. Araiza, A. Gómez-Cortés, G. Díaz, Catal. Today 282 (2017) 185–194.
[17] B. Cifuentes, M. Hernández, S. Monsalve, M. Cobo, Appl. Catal. A Gen. 523 (2016) 283–293.
[18] O.H. Laguna, M.I. Domínguez, S. Oraá, A. Navajas, G. Arzamendi, L.M. Gandía, M.A. Centeno, M. Montes, J.A. Odriozola, Catal. Today 203 (2013) 182–187.
[19] B. Cifuentes, M. Cobo, F. Bustamante, Mendeley Dataset 1 (2019) DOI: 10.17632/38C6GY3T4R.1.
[20] G. Spezzati, A.D. Benavidez, A.T. DeLaRiva, Y. Su, J.P. Hofmann, S. Asahina, E.J. Olivier, J.H. Neethling, J.T. Miller, A.K. Datye, E.J.M. Hensen, Appl. Catal. B Environ. 243 (2019) 36–46.
[21] S. Liu, X. Wu, D. Weng, R. Ran, J. Rare Earths 33 (2015) 567–590.
[22] D. Zanchet, M. Colombo, P. Destro, L. Manna, A. Scarpellini, L. Pasquale, T.M. Kokumai, ACS Catal. 8 (2017) 1031–1037.
[23] S. Najafishirtari, R. Brescia, P. Guardia, S. Marras, L. Manna, M. Colombo, ACS Catal. 5 (2015) 2154–2163.
[24] O.H. Laguna, W.Y. Hernández, G. Arzamendi, L.M. Gandía, M. a. Centeno, J. a. Odriozola, Fuel 118 (2014) 176–185.
[25] F. Wang, R. Büchel, A. Savitsky, M. Zalibera, D. Widmann, S.E. Pratsinis, W. Lubitz, F. Schüth, ACS Catal. 6 (2016) 3520–3530.

[26] W. Zhan, J. Wang, H. Wang, J. Zhang, X. Liu, P. Zhang, M. Chi, Y. Guo, Y. Guo, G. Lu, S. Sun, S. Dai, H. Zhu, J. Am. Chem. Soc. 139 (2017) 8846–8854.
[27] J.A. Hernández, S.A. Gómez, T.A. Zepeda, J.C. Fierro-González, G.A. Fuentes, ACS Catal. 5 (2015) 4003–4012.
[28] P.S. Barbato, S. Colussi, A. Di Benedetto, G. Landi, L. Lisi, J. Llorca, A. Trovarelli, J. Phys. Chem. C 120 (2016) 13039–13048.
[29] T.R. Reina, C. Megías-Sayago, A.P. Florez, S. Ivanova, M.Á. Centeno, J.A. Odriozola, J. Catal. 326 (2015) 161–171.
[30] D.C. Upham, A.R. Derk, S. Sharma, H. Metiu, E.W. McFarland, T. Onishi, P. Fornasiero, M. Peressi, A. Baldereschi, R. Rosei, G. Comelli, Catal. Sci. Technol. 5 (2015) 1783–1791.
[31] Z. Chen, C.J. Pursell, B.D. Chandler, J. Saavedra, T. Whittaker, R.M. Rioux, Nat. Chem. 8 (2016) 584–589.
[32] T.M. Ivanova, K.I. Maslakov, A.A. Sidorov, M.A. Kiskin, R. V. Linko, S. V. Savilov, V. V. Lunin, I.L. Eremenko, J. Electron Spectros. Relat. Phenomena In Press (2019) DOI:10.1016/j.elspec.2019.06.010.
[33] E. Moretti, M. Lenarda, L. Storaro, A. Talon, R. Frattini, S. Polizzi, E. Rodríguez-Castellón, A. Jiménez-López, Appl. Catal. B Environ. 72 (2007) 149–156.
[34] C.S. Polster, H. Nair, C.D. Baertsch, J. Catal. 266 (2009) 308–319.
[35] E.J. Choi, Y.H. Lee, D.W. Lee, D.J. Moon, K.Y. Lee, Mol. Catal. 434 (2017) 146–153.
[36] O. Jakdetchai, T. Nakajima, J. Mol. Struct. Theochem 619 (2002) 51–58.
[37] X. Wang, J.A. Rodriguez, J.C. Hanson, D. Gamarra, A. Martínez-Arias, M. Fernández-García, A. Rodriguez, J.C. Hanson, D. Gamarra, M. Ferna, J. Phys. Chem. B 110 (2006) 428–434.
[38] S.H. Kim, S.W. Nam, T.H. Lim, H.I. Lee, Appl. Catal. B Environ. 81 (2008) 97–104.
[39] S.Y. Yao, W.Q. Xu, A.C. Johnston-Peck, F.Z. Zhao, Z.Y. Liu, S. Luo, S.D. Senanayake, A. Martínez-Arias, W.J. Liu, J.A. Rodriguez, Phys. Chem. Chem. Phys. 16 (2014) 17183–17195.
[40] C. Ping, F. Li, Z. Jian, J. Wei, Propellants, Explos. Pyrotech. 31 (2006) 452–455.
[41] Z. Wang, S. Zhao, S. Zhu, Y. Sun, M. Fang, CrystEngComm 13 (2011) 2262–2267.
[42] G. Zhou, B. Gui, H. Xie, F. Yang, Y. Chen, S. Chen, X. Zheng, J. Ind. Eng. Chem. 20 (2014) 160–165.
[43] Y. Chen, T. Liu, C. Chen, W. Guo, R. Sun, S. Lv, M. Saito, S. Tsukimoto, Z. Wang, Ceram. Int. 39 (2013) 6607–6610.
[44] J.C. Cano-Franco, M. Álvarez-Láinez, Mater. Sci. Semicond. Process. 90 (2019) 190–197.
[45] Z. Feng, Q. Ren, R. Peng, S. Mo, M. Zhang, M. Fu, L. Chen, D. Ye, Catal. Today 332 (2019) 177–182.
[46] H.X. Mai, L.D. Sun, Y.W. Zhang, R. Si, W. Feng, H.P. Zhang, H.C. Liu, C.H. Yan, J. Phys. Chem. B 109 (2005) 24380–24385.
[47] S. Li, H. Zhu, Z. Qin, G. Wang, Y. Zhang, Z. Wu, Z. Li, G. Chen, W. Dong, Z. Wu, L. Zheng, J. Zhang, T. Hu, J. Wang, Appl. Catal. B Environ. 144 (2014) 498–506.
[48] U.M. Bhatta, D. Reid, T. Sakthivel, T.X.T. Sayle, D. Sayle, M. Molinari, S.C. Parker, I.M. Ross, S. Seal, G. Möbus, J. Phys. Chem. C 117 (2013) 24561–24569.
[49] F. Schüth, M.D. Ward, J.M. Buriak, Chem. Mater. 30 (2018) 3599–3600.

[50] S. Agarwal, L. Lefferts, B.L. Mojet, ChemCatChem 5 (2013) 479–489.
[51] M. Cobo, J. Becerra, M. Castelblanco, B. Cifuentes, J.A. Conesa, J. Environ. Manage. 158 (2015) 1–10.
[52] A. Leba, T. Davran-Candan, Z.I. Önsan, R. Yildirim, Catal. Commun. 29 (2012) 6–10.
[53] J.D.S.L. Fonseca, H.S. Ferreira, N. Bion, L. Pirault-Roy, M.D.C. Rangel, D. Duprez, F. Epron, Catal. Today 180 (2012) 34–41.
[54] D. Kang, X. Yu, M. Ge, Chem. Eng. J. 330 (2017) 36–43.
[55] N.J. Divins, A. Casanovas, W. Xu, S.D. Senanayake, D. Wiater, A. Trovarelli, J. Llorca, Catal. Today 253 (2015) 99–105.
[56] D.G. Araiza, A. Gómez-Cortés, G. Díaz, Catal. Today In Press (2018) DOI: 10.1016/j.cattod.2018.03.0
[57] Y.H. Taufiq-Yap, Sudarno, U. Rashid, Z. Zainal, Appl. Catal. A Gen. 468 (2013) 359–369.
[58] N.K. Gamboa-Rosales, J.L. Ayastuy, M.P. González-Marcos, M.A. Gutiérrez-Ortiz, Catal. Today 176 (2011) 63–71.
[59] A. Martinez-Arias, A.B. Hungria, M. Fernandez-Garcia, J.C. Conesa, G. Munuera, A. Martı, A.B. Hungrı, J. Phys. Chem. B (2004) 17983–17991.
[60] M. Zabilskiy, P. Djinović, E. Tchernychova, O.P. Tkachenko, M. Leonid, ACS Catal. 5 (2015) 5357–5365.
[61] Y. Xie, J. Wu, G. Jing, H. Zhang, S. Zeng, X. Tian, X. Zou, J. Wen, H. Su, C.-J.J. Zhong, P. Cui, Appl. Catal. B Environ. 239 (2018) 665–676.
[62] S. Parres-Esclapez, I. Such-Basañez, M.J. Illán-Gómez, C. Salinas-Martínez de Lecea, A. Bueno-López, J. Catal. 276 (2010) 390–401.
[63] S.T. Hossain, E. Azeeva, K. Zhang, E.T. Zell, D.T. Bernard, S. Balaz, R. Wang, Appl. Surf. Sci. 455 (2018) 132–143.
[64] N.J. Divins, I. Angurell, C. Escudero, V. Pérez-Dieste, J. Llorca, Science. 346 (2014) 620–623.

3 Catalytic system based on monolith reactors

3.1 Monolithic reactor for syngas production

In the previous chapter, the initial advances in the development of a prototype to H_2 production integrating the ethanol reforming and CO removal processes, using powder catalysts, were presented. The objective of the second chapter was to select the catalyst to perform the CO removal from an actual syngas coming from an ethanol reformer, finding that an AuCu catalyst supported on CeO_2 nanoparticles is promising to remove CO in a single catalytic unit. Therefore, in this third chapter, efforts focused on evaluating the structuring of catalysts used in each module of the prototype: i.e., (i) the syngas production from ethanol reforming and (ii) the CO removal from a syngas; seeking to contribute to the development of a compact and economical bioethanol fuel processor unit.

In this first section of the third chapter, the findings in the evaluation of a $RhPt/CeO_2$-SiO_2 catalyst structured in monoliths for the syngas production from bioethanol reforming are presented. This chapter links to the second specific objective of the Thesis: "Evaluate monoliths washcoated with a $RhPt/CeO_2$-SiO_2 in the syngas production from bioethanol reforming".

This section corresponds to a paper in preparation.

Raw and processed data of this section can be downloaded from: https://data.mendeley.com/datasets/k2jb73b39z/1 - DOI: 10.17632/k2jb73b39z.1

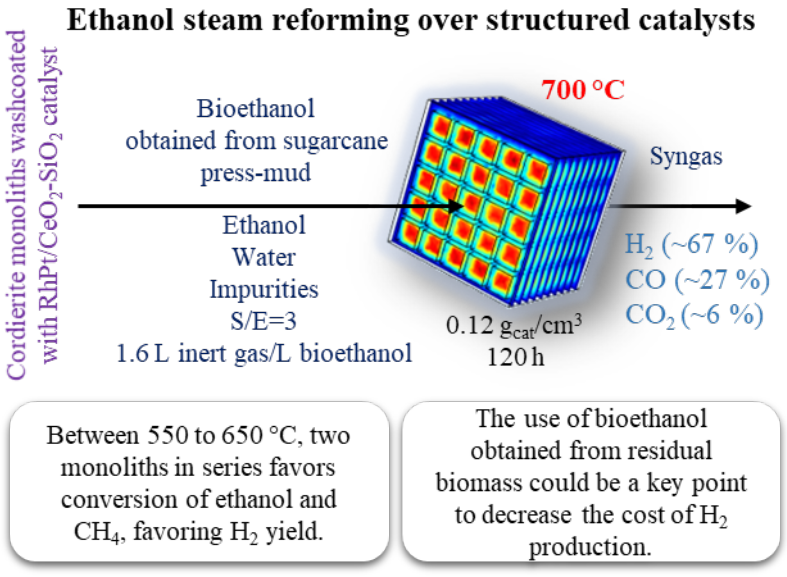

Graphical abstract

Bioethanol steam reforming over monoliths washcoated with $RhPt/CeO_2$-SiO_2: the use of residual biomass to stably produce syngas

Bernay Cifuentes[1],July Gómez[1], Néstor Sánchez[1], Laura Proaño[1], Felipe Bustamante[2], and Martha Cobo[1]*

[1]Energy, Materials and Environment Laboratory, Chemical Engineering Department, Universidad de La Sabana, Campus Universitario Puente del Común, Km. 7 Autopista Norte, Bogotá, Colombia.

[2]Environmental Catalysis Laboratory, Chemical Engineering Department, Universidad de Antioquia UdeA, Calle 70 No. 52 - 21, Medellín, Colombia.

*Corresponding author: Email: martha.cobo@unisabana.edu.co, Tel: +571 8615555 Ext. 25207, Fax: 571 8615555

3.1.1 Abstract

Effectiveness of monoliths washcoated with a $RhPt/CeO_2$-SiO_2 catalyst in ethanol steam reforming was evaluated. Initially, synthetic bioethanol (a mixture of anhydrous ethanol and water) was used to assess the performance of catalytic system, finding that ethanol conversion improved over monoliths than powder samples due to low pressure drop favored on the structured catalysts. Also, two monoliths in series with a low washcoat loading (0.08 g_{cat}/cm^3) improve conversion of ethanol and CH_4, favoring H_2 yield, compared to just one monolith with a high washcoat loading (0.16 g_{cat}/cm^3). Likewise, a decrease in the carrier gas proportion contributes to diffusion limitations into monoliths, reducing the H_2/CO ratio. Then, monoliths stability was evaluated using several bioethanol samples: (i) synthetic, (ii) obtained from the fermentation of glucose standards (glucose-bioethanol), and (iii) obtained from sugarcane press-mud (SPM-bioethanol), a local residual biomass. In all cases, a syngas with $> 60\%$ of H_2, together with CO and CO_2, was produced. For SPM-bioethanol, a 3.1 ± 0.2 mol H_2/mol EtOH was obtained, without evidence of deactivation for 120 h. Also, the use of bioethanol obtained from residual biomass could be a takeaway to decrease $\sim 20\%$ the cost of H_2 production, becoming a promising way to develop a technology for sustainable energy production.

Keywords: Bioethanol impurities**;** Biorefineries**;** Fuel processing unit**;** Non-centrifugal sugarcane waste**;** Structured catalysts.

3.1.2 Introduction

The rapid worsening of environmental quality, in both urban and rural areas, has led nations to discuss sustainable strategies that allow them to obtain chemical products, supplying energy demand and gradually reducing dependence on non-renewable sources [1]. The way to achieve this objective depends on the resources and needs of each region. However, the use of environmental friendly technologies linked to the productive sector is a growing trend [2], becoming a key point for the establishment of new chemical and energy production models. Biorefineries, where value-added products are obtained from renewable sources, are promising to integrate into the agroindustry sector. Currently, there are above 500 biorefinery facilities in the world [3], and fast growth is expected due to the need to use non-fossil-based technologies, as agreed in COP-21 [4] commitments, recently ratified in COP-25 [5].

Most biorefineries focus on the production of bioethanol and biodiesel [3], whose production has increased in recent years. Moreover, it has been proposed to use bioethanol to obtain high added-value products [6,7]; thus, avoiding its use in polluting internal combusting engines. One of the alternatives is to use bioethanol to produce syngas (H_2 + CO), which is a chemical building block to obtain energy and chemicals of high industrial demand. Generally speaking, the final use of syngas depends upon the H_2/CO ratio, i.e., a high concentration of H_2 (i.e., H_2/CO molar ratio >3) could be beneficial for power production, while a lower value is required in the most chemical synthesis. Also, the use of ethanol reforming systems to obtain syngas can promote the closing of the carbon cycle [8]. Therefore, obtaining syngas from biomass excels as a promising approach to effectively reduce the dependence on fossil fuels.

We previously reported that a powder catalyst of $RhPt/CeO_2$-SiO_2 is promising to produce a syngas containing mainly H_2, CO, CO_2 and CH_4 by ethanol steam reforming (ESR) [9]. The catalytic system was evaluated in continuous and intermittent (i.e., on/off tests) processes without observing evidence of deactivation. $RhPt/CeO_2$-SiO_2 catalyst was also evaluated with bioethanol obtained from sugarcane press-mud [10], a waste from the non-centrifugal sugarcane agroindustry. We found that the negative effect of bioethanol impurities over H_2 yield during steam reforming of bioethanol could be mitigated through proper control of residual biomass fermentation [10]. In addition, recent works with similar catalysts, such as $PtNi/CeO_2$-SiO_2 [11] and $Rh/SiCeO_2$ [12], confirm the effectiveness of these phases (i.e., Rh, Pt, CeO_2 and SiO_2) to stably syngas production from ethanol. Although the use of noble metals (i.e., Rh and Pt) is a controversial issue in the large-scale establishment of catalytic processes, Moraes et al. [13] reported that these catalyst does not significantly impact the cost of the process because the noble metals are more active, stable and require a lower than base metal options. So, the next step is to scale the technology to contribute to the development of sustainable processes. For this, it is necessary to structure the powder catalysts to have more robust systems that can be easily integrated into the extensive processes.

Pellets [14], foams [15] and monoliths [12,16] are common ways to structure powder catalysts for obtaining syngas from ethanol. Monolith structures offer lower pressure drops, high activity and more useful life compare to powder catalysts [17]. Therefore, monolithic reactors are promising to be coupled to fuel processing units (FPU), which are compact systems to supply power in small devices or remote areas [13]. In addition, the ESR needs high temperature (>500 °C) and involves strong reactive species (e.g., H_2, CO and H_2O), requiring thermally stable and chemically resistant materials. Ceramic monoliths of cordierite ($2MgO{\cdot}2Al_2O_3{\cdot}5SiO_2$) has low overall expansion, thermal shock resistance, good washcoat adherence and high chemical resistance [18]. For this, cordierite monoliths have been proposed as an adequate material for ESR [19].

Reports of syngas production from ESR with monolithic reactors are usually carried out using synthetic bioethanol (i.e., mixtures of anhydrous ethanol and water). However, the impurities present in the bioethanol obtained from fermentation (actual bioethanol) can influence the performance of the catalyst during ESR [10,20].

Based on the above, the aim of this work is to study cordierite monoliths washcoated with a $RhPt/CeO_2$-SiO_2 catalyst in the syngas production from actual bioethanol steam reforming. First, the operating conditions of a monolith catalytic system were evaluated for the syngas production using synthetic bioethanol. Afterwards, the stability of the catalytic system was tested in continuous tests, using different kinds of bioethanol: (i) synthetic bioethanol, (ii) bioethanol obtained from the fermentation of glucose standards and (iii) bioethanol obtained from sugarcane press-mud, a local residual biomass. The study also includes complementary characterization tests such as scanning electron microscopy (SEM), diffuse reflectance infrared Fourier transform spectroscopy (DRIFTS) and thermogravimetric analysis (TGA). This work is a contribution to the scaling up of a clean and compact technology to obtain energy and high added-value products from residual biomass.

3.1.3 Experimental

Synthesis of RhPt/CeO_2-SiO_2 catalyst

The RhPt/CeO_2-SiO_2 catalyst was prepared according to the methodology detailed in [9]. Briefly, the dual CeO_2-SiO_2 support was prepared by incipient wetness impregnation method using SiO_2 (Merck, Germany) and $Ce(NO_3)_3{\cdot}6H_2O$ (Sigma Aldrich, USA) as precursors. Then, 0.4 wt% of Rh and 0.4 wt% of Pt were loaded into the CeO_2-SiO_2 support by incipient wetness co-impregnation, using aqueous solutions of $RhCl_3{\cdot}H_2O$ (Sigma Aldrich, USA) and $H_2PtCl_6{\cdot}6H_2O$ (Sigma Aldrich, USA). Catalysts were dried in an oven at 80 °C for 24 h, calcined at 700 °C for 2 h (5 °C/min) and sifted using a 140-mesh sieve. Several characterization tests, including X-ray diffraction (XRD), high-resolution transmission electron microscopy (HRTEM), CO_2-temperature programmed desorption, N_2 adsorption, TGA and energy-dispersive X-ray (XPS) of the RhPt/CeO_2-SiO_2 powder catalyst were reported in [9].

Monolith washcoating

Cordierite monoliths (Corning Inc., USA) with 400 CPSI (cells per square inch), 0.018 cm average wall thickness, edges with 8 channels and 1 cm long, were used. All square cordierite monoliths were immersed in a HNO_3 solution (20 wt%) for 3 h. Then, the monoliths were washed with deionized water until neutral, dried at 100 °C for 24 h, immersed in acetone for 24 h, calcined at 600 °C for 2 h (2 °C/min) in muffle and stored in a hermetic container.

Monoliths were washcoated with RhPt/CeO_2-SiO_2 catalyst by the dip-coating method using an aqueous slurry with 25 wt% solids. The slurry was previously grinding for 36 h in a ball mill programmed at 36 rpm (2 balls/g of slurry), achieving an average particle size of solid in the slurry of 776 ± 13 nm, measured in a Zetasizer NanoZS unit (Malvern Instruments, UK) [21], and a viscosity of 19 mPa*s, measured in a MCR 502 rheometer unit (Anton Parr, Austria).

External walls of the monoliths were covered with tape and then the samples were submerged in the slurry for 5 s, partially dried in a gentle flow of N_2, dried at 100 °C for 1 h, blown with abundant air (500 mL/min) and weighed. The process was repeated to ensure the proper washcoat loading. Then, monoliths coated with RhPt/CeO_2-SiO_2 were calcined at 700 °C for 1 h (10 °C/min) and the final loadings were determined. Several catalyst loadings were evaluated: 0.08 ± 0.02 (∼ 0.100 g_{cat}), 0.12 ± 0.03 (∼ 0.140 g_{cat}) and 0.16 ± 0.04 g_{cat}/cm^3 (∼ 0.180 g_{cat}). Monoliths were labeled as M-X, where X is the catalyst loading (X=0.12, 0.16 and 0.18 g_{cat}/cm^3). Also, the remnant slurry was dried at 120 °C for 24 h and sifted using a 140-mesh sieve. This sample was labeled as dried slurry. The resistance and stability of the coating was assessed in an ultrasound unit (pulses of 10 s with amplitude of 40%) and controlled atmospheres of water (1.3 L/min) and N_2 (2 L/min). Figure SM.13 (see Supplementary Material) shows that the coating remained stable, losing less than 20% of the catalyst in all tests. In addition, SEM micrographs (Figure SM.14 in Supplementary Material), obtained in a JSM 6490LV microscope (Jeol Geo Solutions, USA), of the monoliths with a loading of 0.12 g_{cat}/cm^3 show that the washcoating does not obstruct the monolithic channels, forming a homogeneous film (∼ 23 μm of thick) on the walls.

Bioethanol production

Bioethanol was obtained through alcoholic fermentation using a previously standardized process [22], which seeks to mitigate the formation and reduce the concentration of impurities, such as 2-methyl-1-propanol, 3-methyl-1-butanol, 1-butanol and ethyl acetate, which negatively impact the performance of the catalyst during ESR. Briefly, bioethanol was obtained in an Erlenmeyer (400 mL) at 30 °C, 200 rpm and 48 h, using a Saccharomyces cerevisiae strain (Fermentis, Ethanol Red, France). Glucose standards and sugarcane press-mud were used as substrates at a concentration of 160 g/L. Sugarcane press-mud is a residual biomass obtained from non-centrifugal sugar mills in the Colombian Andean region. The sugarcane press-mud was previously hydrolyzed at 130 °C for 1 h [10]. Bioethanol samples were purified on a rotary evaporator at 70 °C until getting a steam to ethanol ratio (S/E) of 3. The bioethanol obtained from glucose was labeled as glucose-bioethanol and the bioethanol obtained from sugarcane press-mud was labeled as SPM-bioethanol. Bioethanol composition was determined by gas chromatography (GC) in a Clarus 580 unit (Perkin Elmer, USA), equipped with an Elite Wax ETR column (60 m, 0.25 mm, Perkin Elmer, USA) connected to a flame ionization detector (FID). The GC oven was programmed at 80 °C for 1min, followed a heating to 230 °C (8 °C/min). Table 3.1.1 shows the composition of the actual bioethanol samples used in this study.

Table 3.1.1. Composition of actual bioethanol samples

Component	Glucose-bioethanol (mol%)	SPM-bioethanol (mol%)
Ethanol	26.3	24.8
Ethyl acetate	0.006	0.017
1-propanol	0.024	0.018
2-methyl-1-propanol	0.071	0.063
3-methyl-1-butanol	0.105	0.114
1-butanol	0.002	0.002
Total impurities	0.208	0.214

SPM-bioethanol: bioethanol obtained from sugarcane press-mud fermentation.

Activity tests

Powder samples of $RhPt/CeO_2$-SiO_2 catalysts were evaluated in a quartz tubular reactor at atmospheric pressure (Chía, Colombia: elevation above sea level of 2,564 m and atmospheric pressure $\sim$ 550 mmHg). External and internal mass transfer limitations were controlled according to reported in [9,23]. The inlet was 0.06 mL/min of liquid synthetic-bioethanol (i.e., bioethanol obtained of the mixture between anhydrous ethanol and water with S/E=3), which was evaporated and mixed with inert gas (Ar), ensuring 5.0 L Ar/mL bioethanol before entering the reactor. The catalyst bed consisted of 0.100 g of catalyst and 0.250 g of ground

quartz as a diluent, achieving 3.5 ± 0.2 L/g_{cat}*min (∼ 0.28 g_{cat}*h/g_{EtOH}) of space velocity (SV).

Monoliths washcoated with $RhPt/CeO_2$-SiO_2 were evaluated into a quartz reactor at the same atmospheric pressure reported above. Several operating conditions were assessed: (i) catalyst loading, (ii) proportion of carrier gas (inert gas) in the feed and (iii) type of bioethanol sample (i.e., synthetic-bioethanol, glucose-bioethanol, and SPM-bioethanol). Before entering the reactor, bioethanol (0.06 mL/min) was evaporated and mixed with inert gas. Initially, washcoat loadings (between 0.08 and 0.16 ± 0.04 g_{cat}/cm^3) and proportion of inert gas in the feed (proportion of 0.8, 1.6, 3.3 and 5.0 L Ar/mL bioethanol) were evaluated, using synthetic-bioethanol. Subsequently, the catalytic stability of the monoliths was evaluated in continuous operation test at 700 °C, using several kinds of bioethanol samples (i.e., synthetic-bioethanol sample, glucose-bioethanol, and SPM-bioethanol). In all tests, both powder and monoliths samples of $RhPt/CeO_2$-SiO_2 catalyst were reduced in-situ with an 8% H_2/Ar stream at 700 °C for 1h. This samples were labeled as reduced samples.

Outlet stream of the reactor was quantified by GC in a Clarus 580 unit (Perkin Elmer, USA), using N_2 as an internal reference [9]. GC unit was equipped with a Carboxen 1010 column (30 m, 0.53 mm, Restek, USA) coupled to a thermal conductivity detector (TCD) and an Innowax column (30 m, 0.53 mm, Perkin Elmer, USA) connected to an FID. The oven temperature in the CG unit started at 60 °C for 6 min, follow by an increase to 120 °C (10 °C/min). Carbon balances between the inlet and outlet streams of the reactor were performed, reaching balances of 95 ± 0.5 % C. Conversion (x_i), yield (Y_i) and mol ratios between products (N_i) for detected species were calculated by 10 to 12.

$$x_i = \frac{EtOH_{\,inlet} - EtOH_{\,outlet}}{EtOH_{\,inlet}} imes 100 \tag{10}$$

$$Y_i = \frac{F_{i,outlet}}{EtOH_{\,inlet}} \tag{11}$$

$$N_i = \frac{F_{i,outlet}}{F_{j,outlet}} \tag{12}$$

Where $EtOH_{\,outlet}$ is the ethanol flow (mol/min) leaving the reactor, $EtOH_{\,inlet}$ is the ethanol flow (mol/min) inlet into the system, and $F_{i/j,outlet}$ is the flow (mol/min) of product i (i.e., H_2, CO, CO_2 and CH_4) leaving the reactor.

Reaction conditions and processed Excel data of activity and stability tests can be observed in detail and downloaded from [data set] [24].

Catalysts characterization

The washcoating on the monolith walls was carefully removed with a soft bristle brush, avoiding removing the cordierite walls. Then, DRIFTS was used to evaluate the catalytic surface of removed washcoating from used monoliths in a Nicolet iS10 unit (Thermo Scientific, USA). 0.020 g of sample were put on a DRK-3 Praying Mantis accessory (Harrick, USA). Then, the DRK-3 Praying Mantis was sealed and aisled with an external flow of Ar (20 mL/min). Subsequently, the sample was purged with Ar (15 mL/min) for 15 min at

room temperature. Spectra of removed washcoating from reduced monolith was used as background. Spectra were collected from 4000 to 400 cm^{-1} with 64 scans/min and 2 cm^{-1} of resolution. Also, carbon deposits in the removed washcoating from used monoliths were determined by TGA in a TGA/DSC1 unit (Mettler Toledo, USA). 0.020 g of removed washcoating was used. The weight change in the samples was examined between 30 and 1000 °C (5 °C/min) in dry air (100 mL/min). The change in weight of the corresponding reduced sample was subtracted from the final weight change of the spent samples.

3.1.4 Results and discussion

Effect of the washcoat loading on catalytic performance

Figure 3.1.1a shows the ethanol conversion during ESR over powder catalysts and monoliths with several washcoat loadings, evaluated with synthetic bioethanol. A similar trend in ethanol conversion was observed between the powder sample (CP) and the dried slurry (DS), indicating that slurry preparation does not affect the performance of the catalyst. On the other hand, ethanol conversion is higher on monoliths compared to powder catalysts, gradually increasing with the washcoat loading. Lower drop pressure favors conversion into endothermic processes [25], which would favor the ethanol conversion during ESR over monoliths. Simson et al. [26] evaluated cordierite monoliths coated with a commercial catalyst based on Rh-Pt, finding that between 660 and 680 °C the ethanol conversion increases more than 5 times when the washcoat loading increases from 0.03 to 0.12 g_{cat}/cm^3. The authors suggest that at low washcoat loadings there is competition between ethanol and reaction intermediates (e.g., acetaldehyde) for active catalyst sites. However, an excessive increase in washcoat loading leads to thicker coatings promoting greater pressure drops and mass transfer limitations [26,27]. For this reason, two monoliths were evaluated in series with a washcoat loading of 0.08 g_{cat}/cm^3 (sample 2M-0.08 in Figure 3.1.1a). The use of two monoliths with a low washcoat loading (i.e., 0.08 g_{cat}/cm^3) is more effective in increasing ethanol conversion than using a single monolith with a high washcoat loading (e.g., 0.16 g_{cat}/cm^3). We speculate that a greater area of contact between the reaction gas and the catalytic surface could play a crucial role in this result.

Figure 3.1.1b shows H_2 yield in the ESR over monoliths washcoated with a $RhPt/CeO_2$-SiO_2 catalyst, using synthetic-bioethanol. Two zones of operation are observed: (i) at temperatures <650 °C, H_2 yield is higher on monoliths with a washcoat loading ≥0.12 g_{cat}/cm^3, possibly due to the higher ethanol conversion over these monoliths at this zone (Figure 3.1.1a); and (ii) at higher temperatures, H_2 yield is superior on powder catalysts. Cifuentes et al. [28] simulated the ESR on cordierite monoliths washcoated with a $RhPd/CeO_2$ catalyst by computational fluid dynamics (CFD), finding a change in the temperature profile and in the flux of the products (i.e., H_2, CO, CO_2 and CH_4) along the monolith. In fact, the CFD profiles show a variation of ∼ 10 °C between the outer walls and the center of the monolith at 677 °C; the authors suggest that this change is due to the endothermic character of the ESR and well-known heat transfer limitations of cordierite. However, the use of two monoliths in series (sample 2M-0.08) manages to slightly mitigate this effect and increases ∼ 5% the H_2 yield compared to the other monolith configurations (Figure 3.1.1b), which

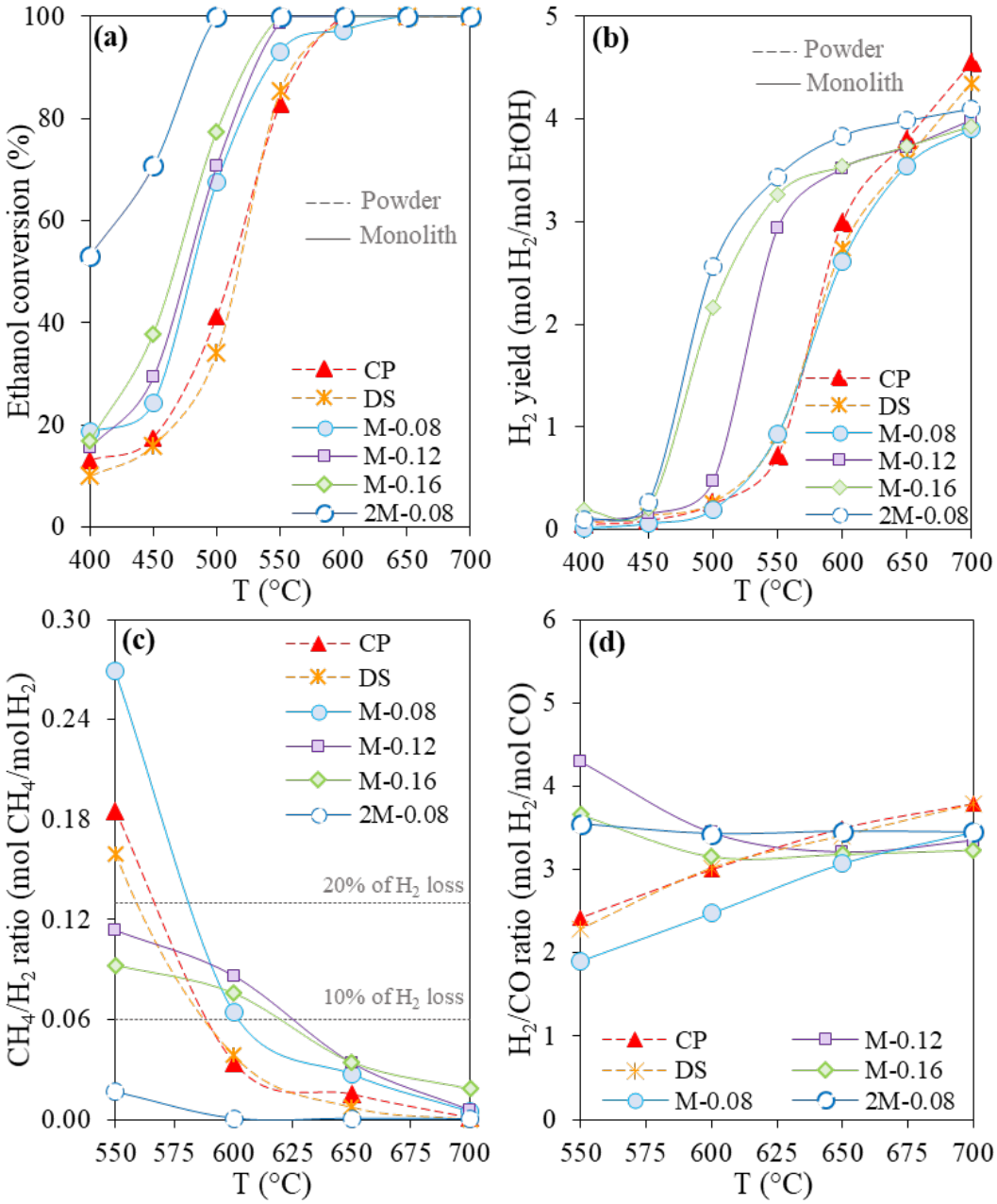

Figure 3.1.1. (a) Ethanol conversion, (b) H_2 yield, (c) CH_4/H_2 molar ratio and (d) H_2/CO molar ratio obtained in the ESR over washcoated monoliths (solid lines) and powder catalysts (dashed lines) of $RhPt/CeO_2$-SiO_2, using synthetic-bioethanol. Reaction conditions: 5.0 L Ar/mL bioethanol inlet and S/E=3. CP: fresh powder catalyst, DS: dried slurry of catalyst, M-X: Monolith, where X is the washcoat loading in g_{cat}/cm^3.

could be associated with a longer contact between ethanol and reaction intermediaries on the monolith walls.

H_2 yield depends on the ability of the catalyst to reform CH_4, which is one of the main intermediaries in the ESR [29,30]. CH_4/H_2 ratio was carefully measured in the zone of high ethanol conversion (i.e., temperatures >550 °C, where X_{EthOH} was >80%), where it is expected that CH_4 production increases (Figure 3.1.1c) [26,29]. The dotted horizontal lines in Figure 3.1.1c indicate the percentage of H_2 loss due to the CH_4 that was not converted. At intermediate temperatures (550 to 650 °C), CH_4 production (i.e., $>CH_4/H_2$ ratio) can impact H_2 yield (Figure 3.1.1b), reaching a H_2 loss greater than 20% over powder catalysts and on the monolith with a low washcoat loading (sample M-0.08). However, at higher temperatures, where CH_4 is easily reformed [31,32], H_2 loss is less than 10%. The results show that the improvement in H_2 yield at lower temperatures obtained with the two monoliths in series (sample 2M-0.08) can be due to the conversation of CH_4 with this catalytic configuration. Similar results were reported by [28], where CH_4 flux during ESR decreased proportionally with the length in the channel size of a monolith washcoated with $RhPd/CeO_2$. However, the less H_2 yield observed on monoliths at high temperatures are not related to the lack of CH_4 reforming. Recently, Kaur Sidhu et al. [27] studied the effect of the geometric parameters and coating thickness on monoliths for ethanol reformers, reporting that mass transfer resistance obtained in corners of the walls and cold spots occur inside the reformer could impact the catalytic performance. Then, decrease in H_2 yield over 650 °C respect to powder samples (Figure 3.1.1b) can be due to mass and heat phenomena that occur in structured catalysts, which could be more significant at higher temperatures due to the exothermic character of steam reforming [17,23].

Thinking about a forthcoming implementation of the syngas technology, the H_2/CO ratio was evaluated at high temperatures (>550 °C), where high ethanol conversion (i.e., >80%) was obtained (Figure 3.1.1a). Figure 3.1.1d shows that both the kind of catalytic system (i.e., powder or monolithic) and the washcoat loading in the monolith influence the H_2/CO ratio and consequently the possible final use of the syngas. Between 550 and 650 °C, monoliths with a washcoat loading $\geq$0.12 g_{cat}/cm^3 favor H_2/CO ratios greater than 3 that would make it more adequate for processes where CO is not required or desired (e.g., energy applications). Also, the use of two monoliths in series (sample 2M-0.08) favor a more stable H_2/CO ratio with less proportion of CH_4. Note that the benefits of 2M-0.08 are more significant at intermediate temperatures (550 - 650 °C) because at higher temperatures a comparable H_2 yield is obtained between monolith samples. For example, at 700 °C, 2M-0.08 favors an improvement in H_2 yield of $\sim$ 5%, but 29% more catalyst is used compared to M-0.12.

Therefore, monolithic systems show a high ethanol conversion compared to powder catalysts. However, depending on the operating conditions, mass and energy transfer limitations in these structured systems could impact H_2 yield. Now, other operational aspects to consider for scaling the technology, such as the carrier concentration and the stability of monolithic reactors, will be presented.

Effect of the carrier gas on monolith selectivity

At a laboratory scale, the use of carrier gas is common to stabilize the inlet flow and improve diffusivity and conductivity of the reactant and product molecules through the catalyst [33]. However, the use of carrier gas in scaled processes tends to be avoided due to its diluent effect on the products of interest (such as H_2) and the energy consumption in processes carried out at high temperatures [23], such as ESR. Figure 3.1.2a shows the synthetic-bioethanol conversion in ESR over a M-0.12 monolith, using several carrier gas/bioethanol ratios. M-0.12 monolith was selected to reduce the loading of catalyst compared to other alternatives, as 2M-0.08 and M-0.16, and avoid a high susceptibility to changes in temperature, as is observed with M-0.08 sample (Figure 3.1.1b). The ethanol conversion is not affected significantly by the proportion of carrier gas possibly because ethanol decomposition depends mainly on temperature and is favored even without catalyst [29]. Nevertheless, H_2 yield (Figure 3.1.2b) decreases significantly at carrier proportion <1.6 L Ar/mL bioethanol inlet. For instance, at 600 °C, despite complete ethanol conversion (Figure 3.1.2a), H_2 yield decreases $\sim$ 20 % when the carrier gas ratio is reduced by half (i.e., from 1.6 to 0.8 L Ar/mL bioethanol inlet), indicating that ESR selectivity is affected by the presence of the carrier gas. Well-known deficiencies in the diffusion of species trough channels of monoliths [17,23] could be more strong by the reduction of carrier gas [33], modifying the interaction of reactants and intermediates with the catalyst in the walls [34] or favoring temperature gradients [28], which impact the production of H_2.

Figure 3.1.2c shows the CH_4/H_2 proportion at several carrier gas ratios. The decrease in carrier gas reduces the ability of the catalytic system to convert the formed CH_4 (i.e., $>CH_4/H_2$), reducing H_2 yield (Figure 3.1.2b). CH_4 conversion depends on the temperature and the interaction with the catalyst [35]. At high temperatures (>650 °C), the impact of the carrier gas decrease on the CH_4/H_2 ratio is reduced, which could be associated with the CH_4 conversion by a thermal effect [36]. Figure 3.1.2d shows that the H_2/CO ratio also decreases when the concentration of the carrier gas is lower. A possible increasing in CO production would be linked to a preferment of the partial reforming of CH_4 ($CH_4 + H_2O \leftrightarrow CO{+}H_2$) instead to its complete reforming ($CH_4 + 2H_2O \leftrightarrow CO_2 + 4H_2$). The impact of the carrier gas on the selectivity of catalytic processes has been observed in other applications. Hu et al. [34] evaluated the effect of carrier gas flow on the decomposition of n-heptane on ZSM-5 zeolites, reporting that the increase in contact time (lower carrier gas flow) does not significantly alter the conversion of n-heptane, but favors undesirable side reactions. Kim et al. [37] studied the effect of carrier gas on cracking JP-8 with HZSM-5 zeolites, finding that the absence of carrier gas reduces the H/C ratio and favors the formation of olefins and coke, leading to rapid deactivation of the catalyst. Then, a decrease in the proportion of carrier gas influences the selectivity of the monoliths, favoring unwanted compounds (e.g., CH_4 and possibly coke) that affect the H_2/CO ratio and can have an impact on the stability of the catalytic system. However, carrier gas influences also energy demands for the ESR. For example, we calculate the energy required to heat the inlet stream to reactor (i.e., bioethanol and carrier gas) according to the methodology described in [38], finding that at 700 °C a reduction of 5 to 1.6 L Ar/mL bioethanol inlet reduces up to 40% the energy consumed to heat.

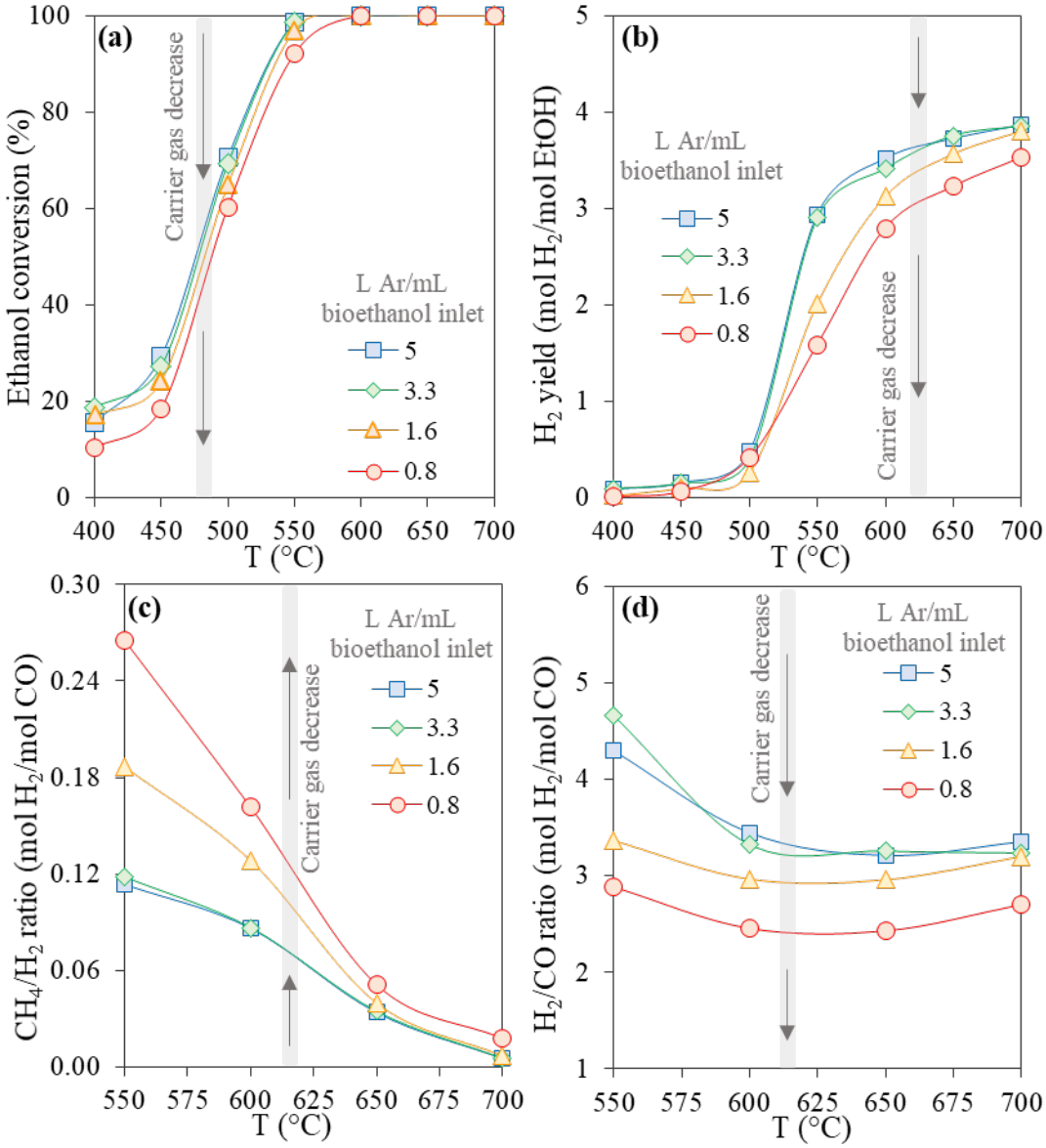

Figure 3.1.2. (a) Ethanol conversion, (b) H_2 yield, (c) CH_4/H_2 molar ratio and (d) H_2/CO molar ratio obtained in the ESR over monolith washcoated with $RhPt/CeO_2$-SiO_2 catalysts, using synthetic-bioethanol and several carrier gas/bioethanol ratios. Reaction conditions: 0.12 g_{cat}/cm^3 of washcoat loading and S/E=3.

Therefore, a decrease in the carrier gas fed to the system reduce the energy demand to heat the inlet stream, but impact negatively CH_4 reforming and favor less H_2/CO ratios, especially at temperatures < 650 °C (Figure 3.1.2c and d). However, at high temperatures (700 °C), where higher H_2 yield is expected (Figure 3.1.2b), a 1.6 L Ar/mL bioethanol inlet proportion promote a similar H_2/CO (3.4±0.2, see Figure 3.1.2d) that the obtained with higher carrier gas proportions (i.e., 3.3 and 5 L Ar/mL bioethanol inlet), but consuming less energy to heat. For this reason, the stability of the monoliths was evaluated in continuous operation at 700 °C, using a moderate amount of carrier gas (1.6 L Ar/mL bioethanol inlet).

Stability of structured catalysts during actual bioethanol reforming

Continuous stability of the monolith system was initially evaluated with synthetic- and glucose- bioethanol samples (actual bioethanol), measuring the syngas composition in small intervals (∼ 10 min between injections in the GC) to identify the variability of the system. Figure 3.1.3a shows the syngas composition obtained in the ESR with synthetic-bioethanol. The monolith washcoated with RhPt/CeO_2-SiO_2 (M-0.12 g_{cat}/cm^3) showed a similar behavior to that observed on the powder sample, which was reported in [9], remaining stable the distribution of products with a variation (100*average/standard deviation) <8% for most species, except for CH_4, whose variation was >50% due to its low amount (∼ 0.05 mol CH_4/mol EtOH). An H_2 yield of 4.1 ± 0.1 was achieved with mole ratios of 3.5 ± 0.2 of H_2/CO and 1.8 ± 0.2 of CO/CO_2. Similarly, the monolith washcoated with RhPt/CeO_2-SiO_2 catalyst evaluated with glucose-bioethanol (Figure 3.1.3b) shows a stable product distribution for 50 h, reaching a H_2 yield of 3.5 ± 0.2 with mole ratios of 2.7 ± 0.3 of H_2/CO and 2.4 ± 0.2 of CO/CO_2. Previously, we identified that the presence of 3-methyl-1-butanol (Table 3.1.1) in actual bioethanol favors the partial reforming of ethanol (CH_3CH_2OH + $H_2O \rightarrow CO + 4H_2$) [10], which increases CO/CO_2 ratio and impact the H_2 performance. Despite that, a monolith washcoated with RhPt/CeO_2-SiO_2 catalyst ensures the continuous production of syngas with a high H_2 content (∼ 65%), using either synthetic- or glucose-bioethanol.

Formation of carbon deposits is common during stability test of ESR over powder catalysts [9,39]. Moraes et al. [12] evaluated the stability of cordierite monoliths washcoated with Rh/$SiCeO_2$ during the ESR (synthetic-bioethanol with S/E=3.5) for 80 h at 750 °C, indicating that some coke formation was observed using Raman; however, it did not cause any permanent deactivation. Subsequently, to detect the possible formation of carbon deposits during stability tests, a DRIFTS analysis was carried out. Figure 3.1.4 shows the DRIFTS spectra for washcoats removed from used monoliths. A peak in the zone of OH-groups (∼ 3500 cm^{-1} [40]), which could be associated with the adsorption of water during ESR, was observed. In addition, changes in signal intensity in the spectral region associated to formates and carbonates (C-O* zone in Figure 3.1.4 [41]) are identified, indicating the presence of carbonaceous compounds on the catalytic surface. The presence of peaks associated with carbonyls species (CO* in 2147 and 2095 cm^{-1} [42]), C=O stretches (2355 cm^{-1} [40]) and, -CH_3 and -CH_2 groups (CH* around 2900 cm^{-1} [43]) can confirm the presence of carbon deposits. Subsequently, the amount of carbon deposits was also measured directly by TGA, finding that the monoliths evaluated with synthetic- and glucose-bioethanol presented

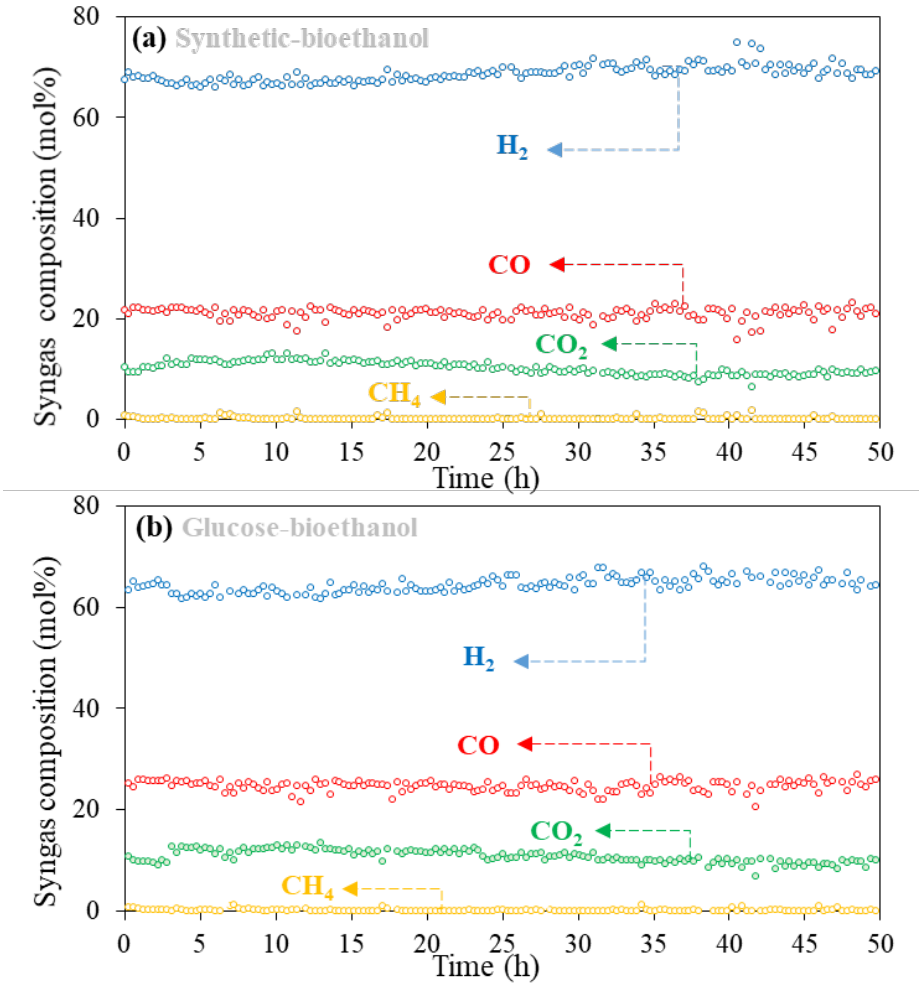

Figure 3.1.3. Syngas composition obtained in the ESR over a monolith washcoated with $RhPt/CeO_2$-SiO_2, using (a) synthetic bioethanol and (b) actual bioethanol obtaining from glucose patrons. Reaction conditions: 1.6 L Ar/mL bioethanol inlet, 0.12 g_{cat}/cm^3 of washcoat loading and S/E=3.

similar carbon deposits (5.4 ±0.1 mg C/g_{cat}*h). A lower S/E ratio (3) [44] and a low carrier gas proportion [37] (1.6 L Ar/mL bioethanol inlet) favor the formation of carbonaceous compounds during ESR over the monolith. Even though, the amount of deposits does not seem to be significantly affecting the performance of the monolith, which is consistent with reported by [12]. In addition, SEM micrographs of the walls of monolith used in stability test with synthetic-bioethanol (Figure SM.14d in Supplementary Material) show that most of the catalyst coating remains fixed, indicating that common stress due to continuous operation [45] does not have a considerable effect on stability of monoliths. Then, stability tests show that monoliths washcoated with RhPt/CeO_2-SiO_2 are promising to stably produce a syngas from ESR, using synthetic bioethanol and bioethanol obtained from glucose. Therefore, the next step was to evaluate the stability of the monolith using actual bioethanol obtained from residual biomass.

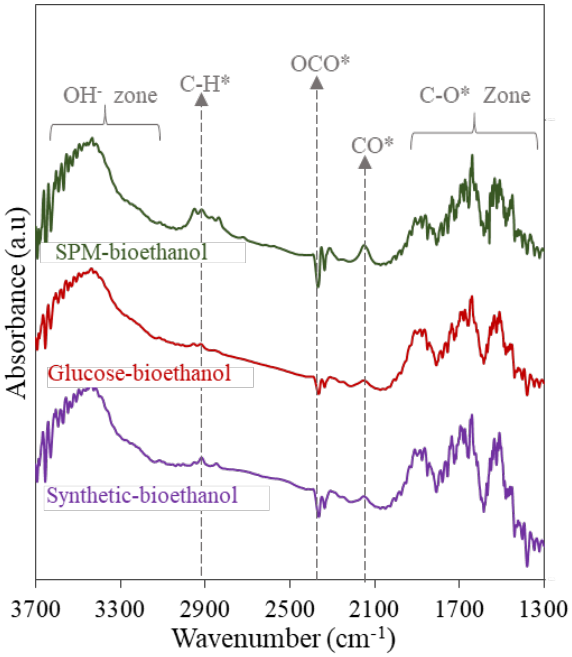

Figure 3.1.4. DRIFTS spectra of spent samples of monoliths washcoated with RhPt/CeO_2-SiO_2 catalysts evaluated in stability tests. Spectra of removed washcoating from reduced monolith was used as background.

The SPM-bioethanol was obtained from the fermentation of sugarcane press-mud, a residue of the non-centrifugal sugarcane sector. Non-centrifugal sugar has an important participation in the economy and employment generation in many Latin-American, Caribbean, Asian and African countries [46], which makes it promise for the development of a sustainable technology based on H_2. The ESR of SPM-bioethanol was evaluated in a long-term stability test, measuring the syngas composition every hour during the day, as shown in Figure 3.1.5. The monolithic system shows a variability between 5 and 10% in the distribution of the main products (i.e., H_2, CO and CO_2). In a recent report [10], we observed that bioethanol impurities influence the product distribution during ESR due to excessive coke formation. DRIFTS results (Figure 3.1.4 confirm the formation of deposits on the monolith washcoating

and the TGA indicates that the deposits in monolith evaluated with SPM-bioethanol (6.2 mg C/g_{cat}*h) increase ~ 14% compared to synthetic-bioethanol. Despite this, no evidence of a decrease in the catalytic performance of the system by coke formation was observed, as seen in the powder catalyst [10]. Then, monolithic systems appear to be resistant to the presence of carbonaceous compounds.

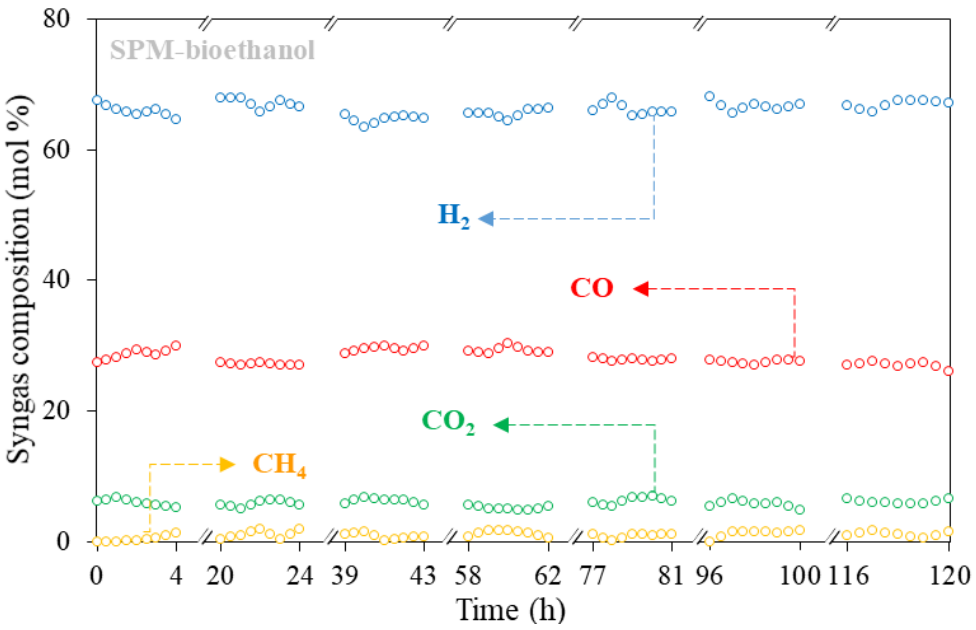

Figure 3.1.5. Syngas composition obtained in the ESR over a monolith washcoated with RhPt/CeO_2-SiO_2, using actual bioethanol obtaining from sugarcane press-mud (SPM-bioethanol). Reaction conditions: 1.6 L Ar/mL bioethanol inlet, 0.12 g_{cat}/cm^3 of washcoat loading and S/E=3.

Table 3.1.2 compares the results obtained in this study with recent ESR works on several structured catalysts. H_2 yields and H_2/CO >4 can be obtained with S/E ratios >5. An increase in S/E favors H_2 yield and avoid CO formation [44]. However, Francesconi et al. [47] simulated an ethanol-FPU, finding that an elevated S/E (>5) could impact the energy self- sufficiency of the unit. In addition, most studies with structured catalysts use synthetic bioethanol. ESR over structured catalysts using actual bioethanol was reported on [48]. These authors used a commercial bioethanol, which was previously purified to achieve only traces of impurities (i.e., 5 ppm S, 1 ppm Cl and 0.4 ppm P). However, the presence of impurities in actual bioethanol [10] and the reduced carrier gas amount used in the current study favor a lower H_2 yield, which reduces the H_2/CO ratio, as shown previously. So, despite being evaluated under severe conditions (i.e., S/E = 3, a moderate amount of carrier gas =1.6 L Ar/mL bioethanol and impurity concentrations of ~ 0.20 mol% in bioethanol), a monolith system based on a RhPt/CeO_2-SiO_2 catalyst is promising to stably produce syngas from actual bioethanol (i.e., obtained from fermentation of glucose or residual biomass).

Table 3.1.2. Comparison of various structured catalysts for ESR

Catalyst	Structured catalyst type	Bioethanol type	S/E mol ratio	T (°C)	H_2 yield (mol H_2/mol EtOH)	H_2/CO mol ratio	Stability test (h)	Ref.
$RhPd/CeO_2$	Silicon micromonolith	Synthetic	6	600	3.8	6.3	NR	[48]
$RhPd/CeO_2$	Silicon micromonolith	Actual from wine agroindustry	4	600	3.7	7.1	NR	[48]
$RhPd/CeO_2$	Silicon micromonolith	Synthetic	4	677	3.4	7.0	100	[19]
Pt-Ni/CeO_2	Ceramic foam	Synthetic	3	500	3.5	NR	NR	[49]
Pt-Ni/CeO_2ZrO_2	Ceramic foam	Synthetic	3	500	3.4	NR	8	[49]
$Rh/SiCeO_2$	Monolith of cordierite	Synthetic	3.5	750	4.2	3.5	96	[12]
Co, La	Monolith of Y_2O_3 doped with ZrO_2	Synthetic	13	600	4.3	11	NR	[50]
Co/ZnO	Monolith of cordierite	Synthetic	6	450	5.6	NR	NR	[16]
Pd/γ-Al_2O_3	Monolith of cordierite	Synthetic: modeling study	6	450	4.3	$\sim$ 6.7	NR	[51]
$RhPd/CeO_2$	Monolith of cordierite	Synthetic: modeling study	6	600	4.8	$\sim$ 6.0	NR	[28]
RhPt/CeO_2-SiO_2	Monolith of cordierite	Synthetic	3	700	4.1	3.5	50	This work
RhPt/CeO_2-SiO_2	Monolith of cordierite	Actual from glucose	3	700	3.5	2.7	50	This work
RhPt/CeO_2-SiO_2	Monolith of cordierite	Actual from sugarcane press-mud	3	700	3.1	2.5	120	This work

NR: Not reported.

Effect of the use of residual biomass on the cost of H_2 production

Cost of H_2 obtained from renewable resources is a concern for establishing H_2-based energy production systems. Figure 3.1.6 shows the levelized costs of H_2 production from various technologies. Several aspects can influence the cost of H_2: (i) *on-site* production of H_2 can reduce its cost by up to 18% due to the high delivery costs [52] (up to 10 $\$/kg_{H2}$ [53]). (ii) The commercial offer of solar panels and wind turbines also favors a low cost in H_2 obtained by electrolysis-based systems [13,54]. However, (iii) a low production (<5 kg_{H2}/h) could increase the cost of H_2 (>13 $\$/kg_{H2}$) [55]. Likewise, (iv) the low cost of raw materials contributes to reducing the costs of H_2 obtained by reforming of natural gas (NGR - a non-renewable source) [13,53], biomass gasification [56] or methanol reforming (MeOHR) [57]. However, ESR is the only technology that has failed to bring the cost of H_2 down below 8 $\$/kg_{H2}$. The price of ethanol represents up to 60% of the cost of H_2 obtained from ESR, while the catalyst, even based on noble metals, contributes less than 1% of the cost [13]. So, obtaining bioethanol from cheaper sources can contribute to significantly reducing the price of H_2 obtained from ESR.

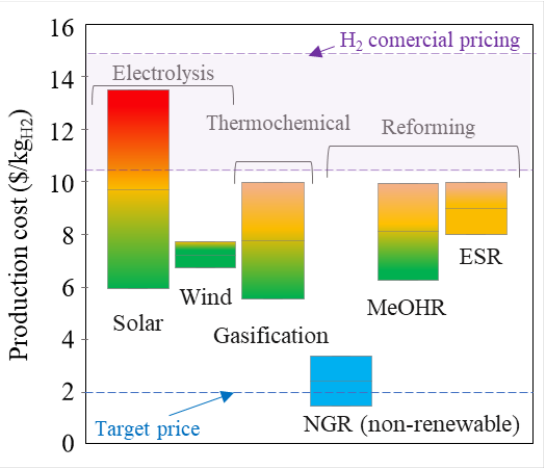

Figure 3.1.6. Levelized costs of H_2 production from several technologies. Values were obtained from several references and updated to present value at January 2020.

Most bioethanol produced in the world comes from feedstocks such as corn and sugarcane, where the cost of the raw material represents between 40 to 70% of the cost of the bioethanol produced [58]. Hence, the feedstock used to produce bioethanol could influence the cost of the ESR technology. In 2013, Quintero et al. [59] proposed that the use of residual biomass (fruit bunches) favors the production of bioethanol at a cost of 0.49 \$/L (corresponding to $\sim$ 0.54 \$/L as of 2020), which is 33% less than the cost of bioethanol in Brazil ($\sim$ 0.81 \$/L) and 10% less than bioethanol in the USA ($\sim$ 0.60 \$/L) [13]. These costs are based on bioethanol use in cars (i.e., anhydrous ethanol with purity $>$ 99.5%). However, for ESR, bioethanol does not require a high degree of purification (e.g., the SPM-bioethanol used in this study had a purity of 24.8 mol% ethanol - Table 3.1.1), supposing a reduction in the purification costs of the bioethanol. Also, the commercial cost of sugarcane press-mud is 0 \$, because it is generally discarded. However, we assume a representative value of 3 $\$/t\text{-}_{SPM}$. Then,

the cost of bioethanol was calculated using the information provided by [58,59], finding that the cost of SPM-bioethanol is $\sim$ 0.42 \$/L. Subsequently, this value was complemented with information obtained from [13] for a bioethanol FPU with a production of 2.4 L H_2/mL bioethanol, determining that levelized costs of H_2 production is $\sim$ 6.85 \$/kg_{H2}. Therefore, the use of sugarcane press-mud for H_2 production from ESR on monoliths washcoated with RhPt/CeO_2-SiO_2 could contribute to decreasing the H_2 production costs. Despite this, the production cost of H_2 obtained from clean technologies (i.e., solar, wind and biomass) is still high (>6 \$/kg_{H2}, Figure 3.1.6) compared to the proposed target for its commercialization (2 \$/kg_{H2} [56]), so it is still necessary to continue working on the design of economic processes to obtain H_2.

3.1.5 Conclusions

Several operating variables were tested in the syngas production over a monolithic reactor system based on RhPt/CeO_2-SiO_2, concluding that: (i) between 400 to 650 °C, compared to powder catalysts, monolithic reactors are more active possibly due to the lower pressure drop. However, at higher temperatures the exothermic character of ESR could favor mass and heat transfer limitations that impact the H_2 yield on the structured catalysts. (ii) At intermediate temperatures (550 to 650 °C), the use of two monoliths in line favors ethanol conversion and decrease CH_4/H_2 ratio, due to an increasing in the contact between reagents/intermediates and catalyst. (iii) A reduction in the proportion of the carrier gas increases diffusion limitations in monoliths, impacting the selectivity of the catalytic system. (iv) Monoliths showed no evidence of deactivation in the reforming of bioethanol obtained from the fermentation of sugarcane press-mud during a long stability test (120 h). (v) The use of bioethanol obtained from residual biomass, which has a lower price than commercial bioethanol, could be a key point to decrease the cost of H_2 production ($\sim$ 6.85 \$/kg_{H2}) based on ESR route. Therefore, the results of this study show that a system of monoliths washcoated with RhPt/CeO-SiO_2 can be a starting point to the development of a sustainable technology of energy production from residual biomass.

3.1.6 Acknowledgments

The authors are grateful to Colciencias (Francisco Jose de Caldas Fund), Universidad de La Sabana and Universidad de Antioquia for the financial support to this work through the project with code and ING-221 (Colciencias contracts 548-2019). Bernay Cifuentes and Nestor Sánchez acknowledge Colciencias for the doctoral scholarship (grant number 727-2015).

3.1.7 References

[1] T.A. Napp, S. Few, A. Sood, D. Bernie, A. Hawkes, A. Gambhir, Appl. Energy 238 (2019) 351–367.
[2] M.L.G. Renó, O.A. Del Olmo, J.C.E. Palacio, E.E.S. Lora, O.J. Venturini, Energy Convers. Manag. 86 (2014) 981–991.
[3] J.B. Heo, Y.-S. Lee, C.-H. Chung, Biotechnol. Adv. 37 (2019) 107422.
[4] E. Gnansounou, J.K. Raman, Bioresour. Technol. 262 (2018) 203–211.

[5] T. Schinko, One Earth 2 (2020) 20–23.
[6] F. García-Labiano, E. García-Díez, L.F. De Diego, A. Serrano, A. Abad, P. Gayán, J. Adánez, J.A.C. Ruíz, Fuel Process. Technol. 137 (2015) 24–30.
[7] J. Becerra, M. Figueredo, M. Cobo, J. Environ. Chem. Eng. 5 (2017) 1554–1564.
[8] E. López, N.J. Divins, J. Llorca, Catal. Today 193 (2012) 145–150.
[9] B. Cifuentes, M. Hernández, S. Monsalve, M. Cobo, Appl. Catal. A Gen. 523 (2016) 283–293.
[10] N. Sanchez, R.Y. Ruiz, B. Cifuentes, M. Cobo, Waste Manag. 98 (2019) 1–13.
[11] V. Palma, C. Ruocco, E. Meloni, A. Ricca, Catalysts 7 (2017) 226–241.
[12] T.S. Moraes, L.E.P. Borges, R. Farrauto, F.B. Noronha, Int. J. Hydrogen Energy 43 (2018) 115–126.
[13] T.S. Moraes, H.N. Cozendey da Silva, L.P. Zotes, L.V. Mattos, L.E. Pizarro Borges, R. Farrauto, F.B. Noronha, Int. J. Hydrogen Energy 44 (2019) 21205–21219.
[14] R. González-Gil, C. Herrera, M.A. Larrubia, F. Mariño, M. Laborde, L.J. Alemany, Int. J. Hydrogen Energy 41 (2016) 16786–16796.
[15] V. Palma, C. Ruocco, A. Ricca, Int. J. Hydrogen Energy 41 (2016) 11526–11536.
[16] A. Casanovas, C. de Leitenburg, A. Trovarelli, J. Llorca, Catal. Today 138 (2008) 187–192.
[17] R.J. Farrauto, Chem. Eng. J. 238 (2014) 172–177.
[18] J.L. Williams, Catal. Today 69 (2001) 3–9.
[19] E. López, N.J. Divins, A. Anzola, S. Schbib, D. Borio, J. Llorca, Int. J. Hydrogen Energy 38 (2013) 4418–4428.
[20] N. Sanchez, R.Y. Ruiz, B. Cifuentes, M. Cobo, Int. J. Hydrogen Energy 41 (2016) 5640–5651.
[21] L. Ricaurte, R.E.P. Correa, M. de Jesus Perea-Flores, M.X. Quintanilla-Carvajal, Food Biophys. 12 (2017) 439–450.
[22] N. Sanchez, R.Y. Ruiz, N. Infante, M. Cobo, Energies 10 (2017) 1–16.
[23] R.M. Heck, R.J. Farrauto, S.T. Gulati, Catalytic Air Pollution Control: Commercial Technology: Third Edition, 2012.
[24] B. Cifuentes, J. Gómez, N. Sánchez, F. Bustamante, L. Proaño, M. Cobo, Mendeley Dataset (2020) DOI: 10.17632/k2jb73b39z.1.
[25] B. Trewyn, Heterogeneous Catalysis for Today's Challenges: Synthesis, Characterization and Applications, 2015.
[26] A. Simson, E. Waterman, R. Farrauto, M. Castaldi, Appl. Catal. B Environ. 89 (2009) 58–64.
[27] T.P. Kaur Sidhu, S. Roy, Int. J. Hydrogen Energy 44 (2019) 11472–11487.
[28] A. Cifuentes, R. Torres, J. Llorca, Int. J. Hydrogen Energy (2019) In Press 10.1016/j.ijhydene.2019.11.034.
[29] B. Cifuentes, M.F. Valero, J. a. J. Conesa, M. Cobo, Catalysts 5 (2015) 1872–1896.
[30] D.R. Sahoo, S. Vajpai, S. Patel, K.K. Pant, Chem. Eng. J. 125 (2007) 139–147.
[31] C. Montero, A. Remiro, P.L. Benito, J. Bilbao, A.G. Gayubo, Fuel Process. Technol. 169 (2018) 207–216.
[32] B. Cifuentes, M. Figueredo, M. Cobo, Catalysts 7 (2017) 1–20.
[33] W.H. Chen, A. Pradhan, S.J. Jong, T.Y. Lee, I. Wang, T.C. Tsai, S. Bin Liu, J. Catal. 163 (1996) 436–446.

[34] X. Hu, X. Yan, R. Feng, J. Xue, Bull. Korean Chem. Soc. 38 (2017) 1129–1133.
[35] D. Zanchet, J.B.O. Santos, S. Damyanova, J.M.R. Gallo, J.M. C. Bueno, ACS Catal. 5 (2015) 3841–3863.
[36] P.Y. Sheng, W.W. Chiu, A. Yee, S.J. Morrison, H. Idriss, Catal. Today 129 (2007) 313–321.
[37] S. Kim, E. Sasmaz, R. Pogaku, J. Lauterbach, Fuel 259 (2020) 1–9.
[38] Y. Cengel, A. Ghajar, Heat and Mass Transfer: Fundamentals and Applications, 2010.
[39] J.W.C. Liberatori, R.U. Ribeiro, D. Zanchet, F.B. Noronha, J.M.C. Bueno, Appl. Catal. A Gen. 327 (2007) 197–204.
[40] L. Proaño, E. Tello, M.A. Arellano-Trevino, S. Wang, R.J. Farrauto, M. Cobo, Appl. Surf. Sci. 479 (2019) 25–30.
[41] S. Agarwal, L. Lefferts, B.L. Mojet, ChemCatChem 5 (2013) 479–489.
[42] B. Cifuentes, F. Bustamante, M. Cobo, Catalysts 9 (2019) 852–877.
[43] A. Matwijczuk, T. Oniszczuk, A. Matwijczuk, E. Chruściel, A. Kocira, A. Niemczynowicz, A. Wójtowicz, M. Combrzyński, D. Wiacek, Sustain. 11 (2019) 1–16.
[44] G. Rabenstein, V. Hacker, J. Power Sources 185 (2008) 1293–1304.
[45] T. Tabakova, Front. Chem. 7 (2019) 1–43.
[46] F. Gómez-Narváez, M. Mesías, C. Delgado-Andrade, J. Contreras-Calderón, F. Ubillús, G. Cruz, F.J. Morales, Food Chem. 301 (2019) 125256–125265.
[47] J.A. Francesconi, M.C. Mussati, R.O. Mato, P.A. Aguirre, J. Power Sources 167 (2007) 151–161.
[48] N.J. Divins, E. López, Á. Rodríguez, D. Vega, J. Llorca, Chem. Eng. Process. Process Intensif. 64 (2013) 31–37.
[49] V. Palma, C. Ruocco, F. Castaldo, A. Ricca, D. Boettge, Int. J. Hydrogen Energy 40 (2015) 12650–12662.
[50] C. Gaudillere, J.J. González, A. Chica, J.M. Serra, Appl. Catal. A Gen. 538 (2017) 165–173.
[51] E.M. Izurieta, D.O. Borio, M.N. Pedernera, E. López, Int. J. Hydrogen Energy 42 (2017) 18794–18804.
[52] Ø. Ulleberg, R. Hancke, Int. J. Hydrogen Energy 45 (2020) 1201–1211.
[53] S. Weidner, M. Faltenbacher, I. François, D. Thomas, J.B. Skùlason, C. Maggi, Int. J. Hydrogen Energy 43 (2018) 15625–15638.
[54] L. Mastropasqua, I. Pecenati, A. Giostri, S. Campanari, Appl. Energy 261 (2020).
[55] R.P. Micena, O.R. Llerena-Pizarro, T.M. de Souza, J.L. Silveira, Int. J. Hydrogen Energy (2019).
[56] M. Shahabuddin, B.B. Krishna, T. Bhaskar, G. Perkins, Bioresour. Technol. 299 (2020).
[57] J.X. Weinert, L. Shaojun, J.M. Ogden, M. Jianxin, Int. J. Hydrogen Energy 32 (2007) 4089–4100.
[58] J.A. Quintero, M.I. Montoya, O.J. Sánchez, O.H. Giraldo, C.A. Cardona, Energy 33 (2008) 385–399.

3.2 Monolithic reactor for CO removal

In the previous section, the assessment of monolithic reactors for the first module of the bioethanol fuel processor unit (i.e., the syngas production from bioethanol reforming) was presented. Consequently, this section presents the outcomes of the evaluation of a monolithic reactor for the second module of the prototype (i.e., the CO removal from the syngas). The study starts from the findings presented in Chapter 2. The objective the section is to develop a monolith coated with an AuCu-based catalyst, considering the activity, stability, and cost of the catalytic system. This chapter corresponds to the third specific objective of the Thesis: "Evaluate monoliths washcoated with AuCu catalysts in the CO removal from syngas streams".

This section corresponds to a paper submitted to *International Journal of Hydrogen Energy* (https://www.journals.elsevier.com/international-journal-of-hydrogen-energy) on July 9, 2020.

Raw and processed data of this section can be downloaded from: https://data.mendeley.com/datasets/rw8drwgv8p/1 - DOI: 10.17632/rw8drwgv8p.2

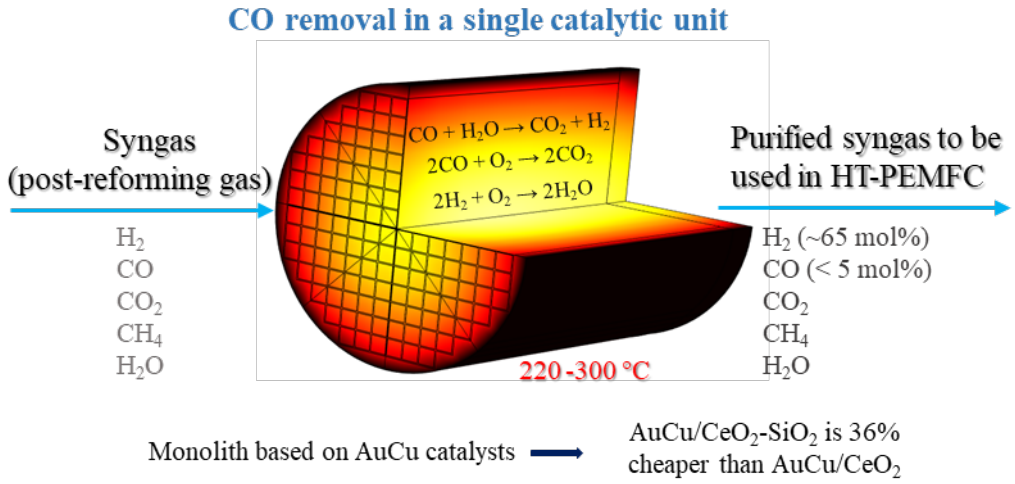

Graphical abstract

Monoliths washcoated with AuCu catalysts for CO removal in an ethanol fuel processor: effect of CeO_2-SiO_2 dual support on the catalytic performance and reactor cost

Bernay Cifuentes[1], Alejandro Cifuentes[2], Felipe Bustamante[3], Lluis Soler[2], Jordi Llorca[2], and Martha Cobo[1]*

[1]Energy, Materials and Environment Laboratory, Chemical Engineering Department, Universidad de La Sabana, Campus Universitario Puente del Común, Km. 7 Autopista Norte, Bogotá, Colombia

[3]Institute of Energy Technologies, Department of Chemical Engineering and Barcelona Research Center in Multiscale Science and Engineering, Universitat Politècnica de Catalunya, EEBE, Eduard Maristany 10-14, 08019, Barcelona, Spain

[2]Environmental Catalysis Laboratory, Chemical Engineering Department, Universidad de Antioquia UdeA, Calle 70 No. 52 - 21, Medellín, Colombia

*Corresponding author: Email: martha.cobo@unisabana.edu.co, Tel: +571 8615555 Ext. 25207, Fax: 571 8615555

3.2.1 Abstract

Monoliths washcoated with AuCu/CeO_2-SiO_2 catalysts were evaluated in the CO removal from a syngas, using a single catalytic unit. Initially, powder catalysts of AuCu supported on mixed CeO_2-SiO_2 oxides with several SiO_2 loadings (0, 25, 50, 75 and 100 mol%) were assessed. SiO_2 addition into AuCu/CeO_2 increased the surface area of catalysts by up to 3.4 times and reduced its cost by up to 60 %, but also impacts CO conversion. However, structured catalysts were most effective to remove CO compared to powder samples. Computational fluid dynamics simulations of the monoliths showed that the improvement in heat diffusion and an intimate contact between the reactant gases and the catalytic monolith walls contribute to their high activity. Moreover, stability tests in on/off cycles at 220 °C for 100 h confirmed that outlet CO concentrations from monoliths washcoated with AuCu/CeO_2 (CO < 0.2 %) and AuCu/CeO_2-SiO_2 with 75 mol% of SiO_2 (CO < 3.6 %) is adequate to feed high temperature fuel cells. Besides, the cost of the Au/CeO_2-SiO_2 monolith (14 USD/g_{cat}) is 36 % lower compared to the AuCu/CeO_2 monolith, paving the way to the development of compact and economic systems to remove CO in bioethanol fuel processor units.

Keywords: CO cleanup; CO oxidation; H_2 oxidation; Structured catalysts; WGS.

3.2.2 Introduction

Hydrogen (H_2)-based technologies are promising to supply power to homes, industrial plants, vehicles, and small devices [1,2]. H_2 production in large-scale centralized facilities from non-renewable resources, such as natural gas [3], is well standardized. However, obtaining H_2 from renewable resources is a key point for the development of sustainable energy systems. Furthermore, difficulties in H_2 delivery and storage have sparked interest in on-site production systems [3], where H_2 is produced using existing fuels, favoring decentralized energy production, even in places that are not connected to the electrical network or in remote installations [1]. The growth of biorefineries to produce biofuels, such as bioethanol and biodiesel [4], that can be used as a starting point to produce H_2 [5,6], offers an opportunity to implement sustainable energy models using H_2.

Power production based on H_2 on-site systems is carried out in compact devices known as fuel processors units (FPU) [7,8], in which syngas (gas containing mainly H_2 and CO) is produced from a liquid fuel and subsequently purified to obtain H_2 suitable for fuel cells (FC) [9]. FC fed with H_2 (H_2-FC) produce electricity, heat and water, without pollutants [10]. Recently, technoeconomic evaluations of FPU fed with bioethanol (B-FPU) have shown that these devices allow to produce H_2 economically competitive to current prices for H_2-powered car refueling stations [3,11]. Figure 3.2.1 shows the steps involved in a B-FPU (i.e., syngas production by ethanol reforming and CO removal from the syngas). Ethanol reforming has been extensively studied [12,13], including the assessment of catalysts structured in foams [14], pellets [15] and monoliths [7,16]. However, CO removal still presents several challenges for catalysis and engineering process design.

Figure 3.2.1 shows that the steps to remove CO in the syngas depend on the type of H_2-FC to which the B-FPU will be connected. For FC with low CO tolerance, such as proton-exchange membrane FC (PEMFC), a low CO content (< 50 ppm [17]) in the syngas

is required. Figure 3.2.1 shows that to ensure a low CO concentration two approaches have been proposed: (i) a traditional approach [18], where a series of catalytic reactions are carried out, including a reactor for a high temperature water gas shift (HT-WGS), followed by a reactor for a low temperature water gas shift (LH-WGS) and, finally, a reactor for CO selective methanation (CO-SMET) and/or CO preferential oxidation (CO-PROX). The advantage of the traditional approach is that it ensures low CO concentrations (< 20 ppm [19]). However, the use of several units increases the volume and cost of the B-FPU, constraining its use in some compact applications. Alternative (ii) is based on the use of a pressure swing adsorption (PSA) unit [3] or selective membranes [20,21] after the WGS reactor. These processes significantly reduce the volume of B-FPU, but they are usually expensive.

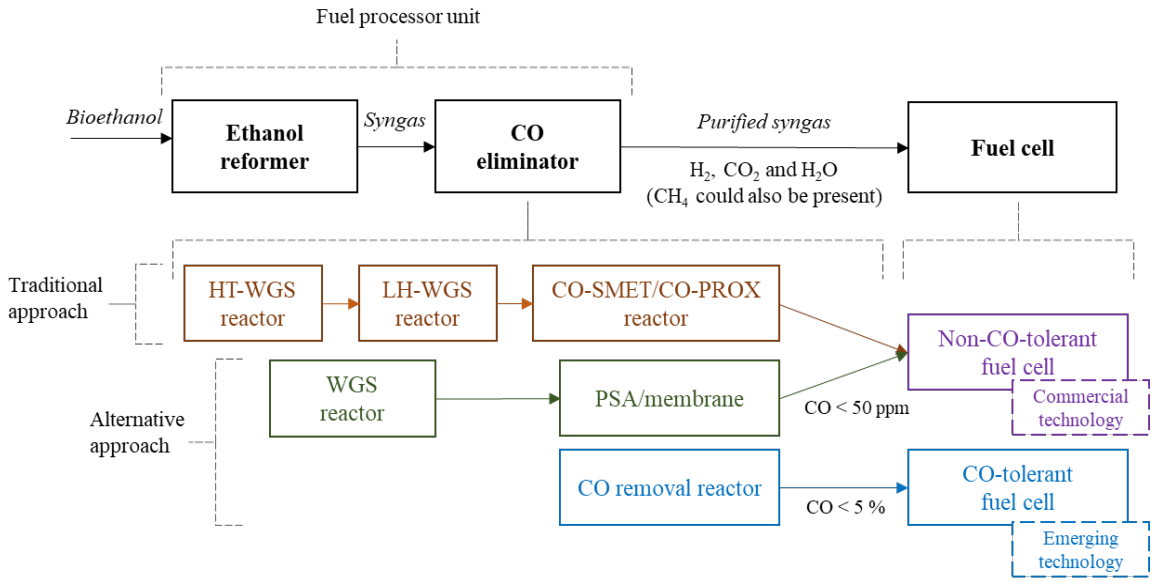

Figure 3.2.1. Strategies to remove CO in a bioethanol fuel processor unit according to the type of fuel cell used. HT-WGS: high temperature water gas shift, LH-WGS: low temperature water gas shift, CO-SMET: CO selective methanation, CO-PROX: CO preferential oxidation, PSA: pressure swing adsorption.

The emergence of a new generation of more CO-tolerant H_2-FC, such as high-temperature PEMFC (HT-PEMFC) that withstands up to 5 % of CO [22], has encouraged the development of new approaches to design simpler B-FPU [23]. Therefore, envisioning an early commercialization of CO-tolerant FC, we have worked on the development of a B-FPU that contains a single catalytic unit for CO removal. Firstly, we developed an active catalyst of $RhPt/CeO_2$-SiO_2 for stable syngas production from actual bioethanol (i.e., obtained from fermentation of residual biomass) [6,24]. Secondly, we identified an Au-Cu catalyst (with an Au/Cu molar ratio = 1 [25]) supported on nanoparticles of CeO_2 [26] as promising to perform CO removal from an actual syngas in a single unit. We chose CeO_2 as support among other alternatives (i.e., CeO_2, SiO_2, ZrO_2, Al_2O_3, La_2O_3, Fe_2O_3, CeO_2-SiO_2, CeO_2-ZrO_2 and CeO_2-Al_2O_3 [27]) due to its greater activity to oxidize CO; CeO_2 morphology was also studied, finding that a polyhedra nano-shape is an active and stable support for CO

removal over a $AuCu/CeO_2$ system [26]. Now, our intention is to structure the $AuCu/CeO_2$ catalyst to favor the development of a compact B-FPU [3].

Recently, monolith reactors washcoated with powder catalysts supported on CeO_2 have been shown as promising for H_2-cleanup. Lacoste et al. [28] tested $CuO\text{-}CeO_2/SBA\text{-}15$ catalysts deposited over cordierite monoliths in the CO-PROX suggesting that the macropores of cordierite walls conferred mechanical resistance to catalysts, contributing to high stability of the structured system. González-Castaño et al. [29] evaluated monoliths washcoated with a $Pt/CeO_2/Al_2O_3$ catalyst for WGS, reporting that the structured system favors water diffusion on metal-support interface, which could be a relevant point in the actual WGS process intensification. Landi et al. [30] studied monoliths washcoated with a CuO/CeO_2 catalyst for CO-PROX, showing that coated monoliths provided both conversion and selectivity higher than the reference powder catalyst. Then, cordierite monoliths washcoated with catalysts based on CeO_2 are attractive to develop a compact technology for the CO removal in syngas streams.

Most economic assessments of B-FPU have focused on the bioethanol reformer [11], finding few reports on the cost associated with cleaning H_2 through catalytic systems. In general, the use of noble metals such as Au is controversial in the CO removal process: some authors recommend avoiding Au due to its high cost [31], while others suggest that the high performance of noble metals translates into a most cost-effective catalyst [32]. Also, the cost of the catalyst associated with the support goes into the background. However, the high demand of CeO_2 for environmental applications and industrial processes [33] has increased its price. Figure 3.2.2a shows that the average cost of CeO_2 doubles other supports used in CO removal, such as ZrO_2, Al_2O_3, FeO_2 and SiO_2 [27]. Likewise, considering the overall price of the catalyst (i.e., active metals plus support) , the $AuCu/CeO_2$ has a cost 73 % higher when compared to the other options (Figure 3.2.2b). The higher cost of CeO_2 has led us to look for alternatives to reduce its amount in the structured catalyst, seeking to decrease the cost of the catalytic system without significantly impacting its catalytic performance.

Figure 3.2.2a shows that SiO_2 is the cheapest support. Besides, in a preliminary study [27] it was identified that although the inclusion of a second metal oxide (i.e., ZrO_2, Al_2O_3 and SiO_2) in the CeO_2 matrix decreases its activity in CO removal, this effect is less significant in the $CeO_2\text{-}SiO_2$ system. The evaluation was carried out by fixing a Ce/Si molar ratio of 1 in the catalysts. Thus, prior to catalyst structuring, an evaluation of the effect of SiO_2 inclusion into the $AuCu/CeO_2$ catalyst over both the cost and the catalytic performance may be required.

In this contribution, CO removal from syngas was evaluated using a monolith reactor washcoated with AuCu-based catalysts, seeking to identify the potential of this catalytic system to be integrated in a B-FPU. Firstly, the effect of dual supports of $CeO_2\text{-}SiO_2$ with several SiO_2 loadings over the cost and activity of powder Au-Cu catalysts was determined. Then, activity and selectivity of structured catalysts were compared to powder samples. Also, a computational fluid dynamics (CFD) simulation of the monolithic reactors was carried out to identify profiles of temperature and concentration of chemical species throughout the channels of monolithic reactors. Finally, the stability of monoliths washcoated with $AuCu/CeO_2$ and $AuCu/CeO_2\text{-}SiO_2$ catalysts in the CO removal from a syngas was assessed. The study also included the use of characterization techniques such as high-resolution transmission electron microscopy (HR-TEM), UV-visible diffuse reflectance spectroscopy (UV-vis), X-

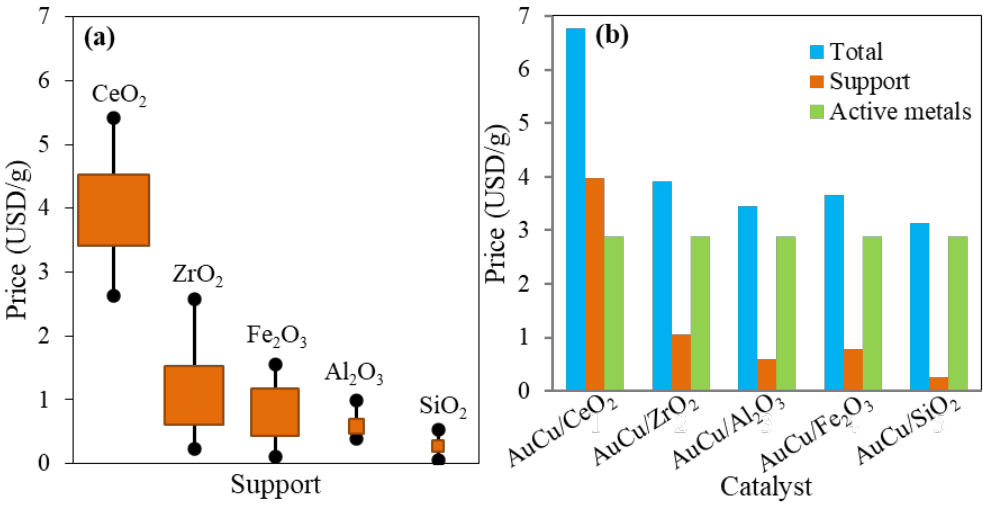

Figure 3.2.2. Cost of (a) metal oxides and (b) AuCu based catalysts commonly used for CO removal in a B-FPU. Values obtained from Sigma Aldrich (www.sigmaaldrich.com), Merck (www.merckmillipore.com), Fisher Scientific (www.fishersci.com) and Alfa Aesar (www.alfa.com) in February 2020 for presentations between 50-1000 g and purity > 99 %.

ray photoelectron spectroscopy (XPS), X-ray diffraction (XRD), Raman spectroscopy, BET analysis, ultrasonic pulse test and thermal shock test.

3.2.3 Experimental

Synthesis of powder catalysts

Polycrystalline CeO_2 nanoparticles were obtained by the hydrothermal method as described in [26]. A solution 0.3 M of NaOH (Merck, Germany) was mixed slowly with an aqueous solution of $Ce(NO_3)_3{\cdot}6H_2O$ (Sigma Aldrich, USA), stirring at 500 rpm for 1 h. Then, the mixing was passed to an airtight container and heated at 100 °C for 24 h. The obtained slurry was filtered, washed with abundant water and calcined at 500 °C for 2 h. Formation of nanoparticles of CeO_2 was confirmed by HRTEM. CeO_2 occurs as polyhedral particles with an average diameter of 9±2 nm (Figure SM.15 in Supplementary Material). Afterwards, the dual supports of CeO_2-SiO_2 with several contents of SiO_2 (i.e., 0, 25, 50, 75 and 100 mol%) were prepared. For this, nanoparticles of CeO_2 were added into a slurry of SiO_2 (Merck, Germany). The mixing was dried at 80 °C for 12 h, carefully crushed in a mortar and calcined at 500 °C for 2 h. This preparation method was selected based on initial tests (Method 1, Figure SM.16 and Table SM.9 in Supplementary Material), where several alternatives to obtain the dual supports of CeO_2-SiO_2 were assessed. CeO_2-SiO_2 samples were labeled as CeSi-X, where X indicates the SiO_2 percent content in the support (X = 25, 50 and 75 mol% SiO_2).

1 wt% Au and 1 wt% Cu were impregnated onto the CeO_2-SiO_2 supports by deposition-precipitation and incipient wetness impregnation methods, respectively, using the procedure described in [25]. $HAuCl_4{\cdot}3H_2O$ (Sigma Aldrich, USA) and $Cu(NO_3)_2{\cdot}3H_2O$ (Sigma Aldrich,

USA) were used as precursors of active metals. Catalysts were calcined at 500 °C for 4 h and sifted using a 140-mesh sieve. Before reaction, an activation pretreatment was performed in all catalyst samples [25], which consisted in a reduction at 300 °C with 8 % H_2/Ar stream for 1 h, followed by a purge with pure Ar stream for 30 min and ended by a stabilization in 10 % air/Ar stream for 30 min. AuCu/CeO_2-SiO_2 samples were labeled as "Activated" catalysts.

Preparation of catalytic monoliths

Cordierite monoliths (Corning Inc.) with 400 CPSI (cells per square inch) and 2 cm long were used. Monoliths were washcoated by repetitive immersion in a slurry of powder catalyst (25 wt% of catalyst in the slurry), followed by drying at 105 °C for 1 h under continuous rotation (60 rpm), and calcination in muffle at 500 °C for 4 h. Polyvinyl alcohol (PVA) was used as a binder with a proportion of 0.6 g_{PVA}/g_{cat}. A net catalyst loading of 3.3 mg_{cat}/cm^2 in the monoliths was achieved. Before reaction, the washcoated monoliths were activated using the same procedure described for powder samples. Stability of monolith coatings was assessed by ultrasonic pulses. In particular, washcoated monoliths were submerged into acetone in a ultrasonic bath (Fisher Scientific, USA) for 10 s, then dried at 70 °C for 1 h and weighted [34]; the procedure was repeated to achieve 100 s. Adhesion of the washcoat was assessed by a thermal shock test [7]. For this, monoliths were heated at 700 °C for 1 h and then quickly cooled down with abundant N_2 (500 mL/min). The procedure was repeated three times, determining catalyst losses in each cycle. The data of all characterization tests are available at the website [data set] [35].

Activity and stability tests

Powder samples of AuCu supported on dual oxides of CeO_2-SiO_2 were evaluated in CO removal with a syngas containing H_2 (19.9±0.3 mol%), CO (6.3±0.1 mol%), CO_2 (5.2±0.5 mol%), O_2 (5.6±0.3 mol%), H_2O (7.8±0.2 mol%) and N_2 (55.2±0.6 mol%). Syngas composition was defined in preliminary tests where a cordierite monolith washcoated with a RhPt/CeO_2-SiO_2 catalyst was evaluated in the ethanol steam reforming. Besides, an excess oxygen factor (λ) of 1.8 was fixed, which was optimized in a previous work [25]. Channeling and back mixing through the catalyst bed were avoided using a ratio of 50 between the catalyst bed height (L) and catalyst particle size (D_p), and a ratio of 60 between the reactor internal diameter (D) and D_p [36,37]. 0.200 g of catalyst with 0.200 g of ground quartz as a diluent were used in all tests, achieving a space velocity (SV) of 5.6 ± 0.3 L/g_{cat}*min. Species at the outlet stream of the catalytic system were continuous monitored, using a Clarus 580 gas chromatograph (GC, Perkin Elmer, USA) equipped with a Carboxen 1010 plot column (30 m, 0.53 mm, Restek, USA) connected to a thermal conductivity detector (TCD), using N_2 (20 mL/min) as internal reference. An isothermal method at 60 °C was used in the GC unit.

CO removal was also assessed over monoliths washcoated with AuCu/CeO_2 and AuCu/CeO_2-SiO_2 (75 mol% of SiO_2), using a syngas with the same composition described in the evaluation of powder samples. Activity was tested between 100 to 300 °C and stability was

evaluated in on/off tests at 220 °C. The species at the outlet stream were quantified online, using a 490 micro-GC (Agilent Technologies, USA) equipped with three columns connected with several TCD. N_2 (60 mL/min) was used as internal reference and isothermal method at 60 °C was used. Elemental balances between the inlet and the outlet streams of the reactor were quantified in all tests, achieving balances of C, H and O > 90 %. Conversion (x_i) of CO and H_2, and the molar composition (y_i of outlet streams were calculated by 13 and 14, respectively.

$$x_i = \frac{N_{inlet} - N_{outlet}}{N_{inlet}} imes 100 \tag{13}$$

$$y_i = \frac{N_{j,outlet}}{\sum_0^n N_{j,outlet}} \times 100 \tag{14}$$

Where N_{inlet} is the flow (mol/min) of CO or H_2 inlet into the reactor, N_{outlet} is the flow (mol/min) of CO or H_2 leaving the reactor, and $N_{j,outlet}$ is the flow (mol/min) of species j (i.e., H_2, CO, CO_2, O_2 and N_2) leaving the reactor. The data of activity and stability tests are available at the website [data set] [35].

Catalysts characterization

HRTEM micrographs of CeO_2 nanoparticles were obtained in a Tecnai F20 Super Twin unit (FEI, USA). UV-vis spectroscopy was carried out using a UV-VIS-NIR 3600 spectrophotometer (Shimadzu, Japan) equipped with PMT, InGaAs, PbS light detectors and an ISR-3100 accessory. The spectra were recorded at room temperature in the wavelength range of 200–800 nm with 0.1 nm of resolution. Barium sulphate was used as a reflectance standard. XPS spectra of catalysts were obtained using a SPECS system (SPECS group, Germany) equipped with a XR-50 X-ray source and a Phoibos 150 EP hemispherical energy analyzer with MCD-9 detector. The binding energy (BE) values were obtained with a precision of 0.1 eV, maintaining the analysis chamber below 10^{-7} Pa. XPS data was processed in CasaXPS software, adjusting the adventitious C 1s line at 284.8 eV. XRD was conducted in a D5000 diffractometer (Siemens, Germany) using Cu Kα radiation (45 kV, 35 mA). Profiles were collected in 2θ at range of 20 to 100°, using a step of 0.02° and 1 s/step. The lattice parameter and the average crystallite size of CeO_2 were determined by a Rietveld refinement of diffraction patterns in FullProf suite software (2019 version, France), ensuring a Chi-square test (Chi^2) < 2.0 and a R-weighted pattern (R_{wp}) < 30 %. Raman spectroscopy was carried out in a RE 0.4 in Via Qontor confocal microscope (Renishaw, UK) equipped with a 532.1 ± 0.3 nm laser. Spectra were collected using an exposure time of 2 s, 1 % of laser power and 48 accumulated scans. Surface area of powder samples was determined by BET method in a ChemBET Pulsar unit (Quantachrome Instruments, USA). 0.1 g of sample was degassed at 120 °C for 2 h in inert gas (N_2, 20 mL/min). BET surface area was determined with a 30 % N_2/He stream in a liquid N_2 bath.

CFD simulation

CFD simulation of the catalytic system, considering the actual dimensions of the monoliths, was carried out in COMSOL Multiphysics commercial software (V5.5), according to methodology detailed in [38]. A mesh independence test was performed to ensure an accurate numerical solution, identifying that more than 12,000 elements are enough for the CFD model. Thermodynamic and transport assumptions for reactive gas and monolith are summarized in Table SM.10, Supplementary Material. Table 3.2.1 shows the governing equations ((1)–(4)), kinetic model ((5)–(7)), and chemical reactions (8–(10)) considered in the CFD model. Kinetic models based on power law ((5) in Table 3.2.1) are widely accepted for the CO removal on Au and Cu catalysts [39–41]. Thermodynamic and transport properties were modeled by polynomial approximations, using NASA coefficients [42].

Table 3.2.1. Governing equations, kinetic model and reaction network involved in CFD simulations.

Equation/Reaction [a]	Description	
$\nabla\left(\rho_f \bullet u\right) = 0$	Continuity equation	(1)
$-\nabla p + \nabla\bullet(\mu.$	Momentum balance	(2)
$\rho_f C_p u \bullet \nabla T + \nabla\bullet(-k_{con}\nabla T) = Q + Q_r$	Energy balance	(3)
$\nabla\bullet\left(-D_i\nabla c_i + uc_i\right) = R_i$	Convection-diffusion equation	(4)
$r_n = k_n \sum c_i^{\gamma_i} - \frac{k_n}{K_n}\sum c_i^{\gamma_i}$	Power law equation	(5)
$k_n = k_{\infty j} e^{\frac{-E_{aj}}{RT}}$	Arrhenius equation	(6)
$K_n = e^{\frac{-\Delta G^\circ}{RT}} \prod \left(C_t \frac{P^\circ}{P}\right)^{\gamma}$	Chemical equilibrium	(7)
$CO(g) + H_2O(g) \rightleftharpoons CO_2(g) + H_2(g)$	WGS reaction	(8)
$CO(g) + \frac{1}{2}O_2(g) \rightarrow CO_2(g)$	CO oxidation	(9)
$H_2(g) + \frac{1}{2}O_2(g) \rightarrow H_2O(g)$	H_2 oxidation	(10)

[a] ρ_f = density, u= velocity vector, p = pressure, I= indent matrix, μ = dynamic viscosity, F = external forces, C_p = heat capacity, T= temperature, k_{con} = thermal conductivity, Q = external heat, Q_r = reaction heat, D_i= diffusion coefficient, i = specie (i.e., CO, H_2O, CO_2, O_2 or H_2), c_i= molar concentration, R_i= species surface rate, r_n = reaction rate, n = chemical equation (i.e., WGS, CO oxidation or H_2 oxidation), k_n= reaction rate constant, γ_i = stoichiometric coefficient, K_n = reaction rate constant of equilibrium, $k_{\infty j}$= pre-exponential factor, E_{aj}= activation energy, R= universal gas constant, ΔG°= Gibbs free energy (including formation terms), C_t= sum of all concentration species, P°= standard pressure.

3.2.4 Results and discussion

Relationship between cost and activity of the powder catalysts

Table 3.2.2 shows the total price of catalysts (1 wt% Au and 1 wt% Cu) supported on several CeO_2-SiO_2 supports. Costs were calculated according to the information detailed in Table SM.11 (Supplementary Material), considering the losses during the synthesis of catalysts and actual market prices of each reagent. The cost associated with active metals (Cu + Au) is $\sim$ 3.5 USD/g_{cat} for all samples. Thus, the catalysts cost associated to the support would range between 21 and 84 %, depending mainly on the CeO_2 content. The high cost of CeO_2 is the result of its high market price (Figure 3.2.2a) and the losses during its synthesis to ensure homogeneous nanoparticles; cheaper CeO_2, namely, without a homogeneous and well-defined morphology, would lead to a rapid deactivation, as shown in [26]. Therefore, inclusion of SiO_2 in AuCu/CeO_2 have a positive effect in terms of the cost of the catalysts, achieving a price up to 1.6 times lower for AuCu/CeSi-75 compared to AuCu/Ce.

Table 3.2.2. Price of catalysts and the minimum CO concentration obtained in the outlet stream of the reactor.

Catalyst	Total price (USD/g_{cat})	Cost associated with the support (%)	T (°C)	CO concentration achieved (mol%)
AuCu/Ce	21	84	220	0.4
AuCu/CeSi-25	19	82	220	0.6
AuCu/CeSi-50	17	80	220	1.7
AuCu/CeSi-75	13	73	260	1.1
AuCu/Si	4	21	260	4.0
Monolith washcoated with AuCu/Ce	22	82	260	0.2
Monolith washcoated with AuCu/CeSi-75	14	71	300	0.3

Figure 3.2.3 shows the CO conversion from a syngas stream over the bare supports and supported AuCu catalysts. Volcano type curves [34] are observed for the CO conversion over both bare supports (Figure 3.2.3a) and AuCu catalysts (Figure 3.2.3b). Inclusion of active metals (Au and Cu) improves CO conversion; however, the activity of catalysts decreases with the SiO_2 content in the support. Notwithstanding, most of AuCu catalysts (except AuCu/CeSi-50 and AuCu/Si) favor a CO conversion > 85 % (Figure 3.2.3b). While highly active catalysts are desirable, complete CO removal is not required for a B-FPU connected to a FC with high CO tolerance, as recent research has allowed for the development of HT-PEMFC that resist up to 5 % of CO in the cleaned H_2 stream [22]. Table 3.2.2 shows the minimum CO concentration in the outlet stream obtained with each sample. Most catalysts (except AuCu/Si) ensured CO concentrations < 5 %, paving the way to carry out CO removal from syngas using a single catalytic unit. Despite being the most active, the cost of AuCu/Ce is 9 % higher than that of AuCu/CeSi-25 and 61 % higher than AuCu/CeSi-75.

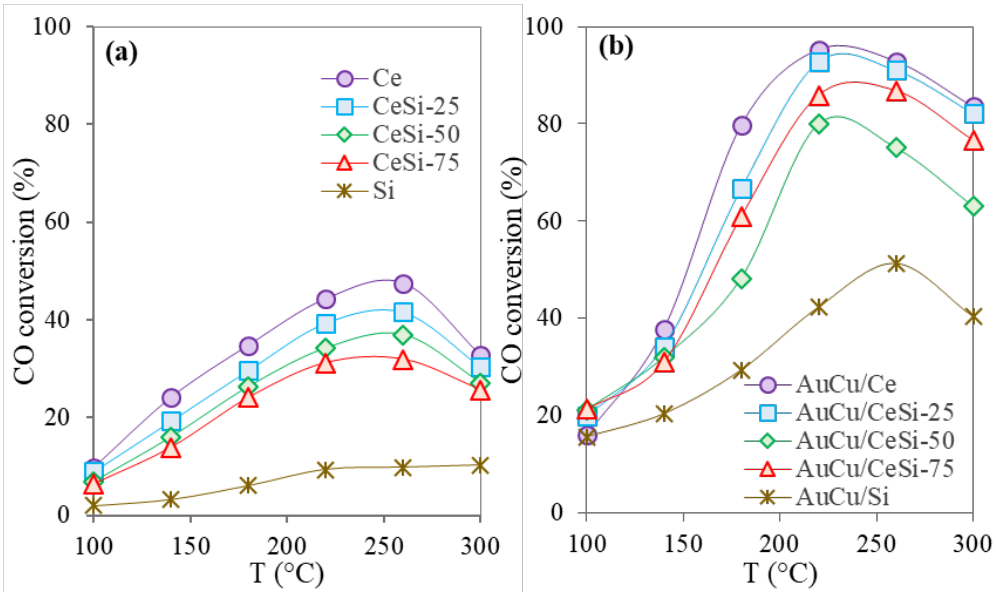

Figure 3.2.3. CO conversion obtained over (a) bare supports and (b) supported AuCu catalysts. CeO_2-SiO_2 supports were labeled as CeSi-X, where X indicates the SiO_2 percent content (X = 25, 50 and 75 mol% SiO_2). Syngas feed: H_2 (19.9±0.3 mol%), CO (6.3±0.1 mol%), CO_2 (5.2±0.5 mol%), O_2 (5.6±0.3 mol%), H_2O (7.8±0.2 mol%), and N_2 (55.2±0.6 mol%). Reaction conditions: SV of 5.6 ± 0.3 L/g_{cat}*min and 0.35 g of the catalytic bed.

Therefore, AuCu/CeO_2-SiO_2 catalysts show promising features in terms of cost and activity to be integrated into a B-FPU to produce H_2 streams adequate for HT-PEMFC.

The effectiveness of the AuCu system to promote CO oxidation has been well documented by other researchers [43–45]. Additionally, in previous studies [25,27] we identified that Au contributes to the formation of CO* intermediates while Cu provides reactive oxygen on the catalytic surface, and this combined effect favors the CO conversion on AuCu/CeO_2 catalysts, as seen in Figure 3.2.3b. However, dilution of CeO_2 with a second support as SiO_2 impacts its ability to convert CO [27]. Nevertheless, AuCu/CeSi-75 sample shows a CO conversion higher than that of AuCu/CeSi-50 (Figure 3.2.3b), indicating that the SiO_2 inclusion in the AuCu/CeO_2 system could alter several properties of the catalysts. Consequently, to understand the effect of the presence of SiO_2 in the catalyst, several characterization tests were carried out on the powder samples before monolith evaluation.

Effect of SiO_2 on surface and structure of AuCu/CeO_2-SiO_2 catalysts

UV-vis spectroscopy Catalyst surface of the activated samples of AuCu catalysts was assessed by UV-vis spectroscopy. Figure 3.2.4a shows the UV-vis spectra of the AuCu catalysts. Catalysts based on CeO_2 show the typical absorptions for $O^{2-} \rightarrow Ce^{4+}$ charge transfer (277 nm) and cerium inter-band transitions (347 nm) [46]. However, the presence of a second oxide as SiO_2 can alter the optical absorption of CeO_2, favoring a slight shift in wavelength [47]. Moreover, absorption with $\lambda \geq 470$ nm confirms the presence of active metals (Au and Cu [48,49]). The intensity and width of the bands are usually related to the

size and shape of the active particles on the catalyst surface. Signal related to spherical Au particles ($\lambda \sim 528$ nm) can present a red-shift towards higher wavelength due to changes in particle size and morphology of Au [49]. Similarly, bands associated with Cu^{+} (472 nm) and Cu^{2+} (692 nm) are susceptible to a red-shift due to changes on the interaction of Cu with the support [48]. AuCu/Ce-50 and AuCu/CeSi-75 catalysts show wider and less intense bands than the other samples (Figure 3.2.4a), indicating the formation of active particles of several morphologies and sizes on the catalytic surface. Thus, SiO_2 is likely producing a change in the distribution of active particles on the catalyst surface, which promotes variations in the activity of AuCu catalysts (Figure 3.2.3b). Consequently, the catalytic surface was also studied by XPS (*vide infra*).

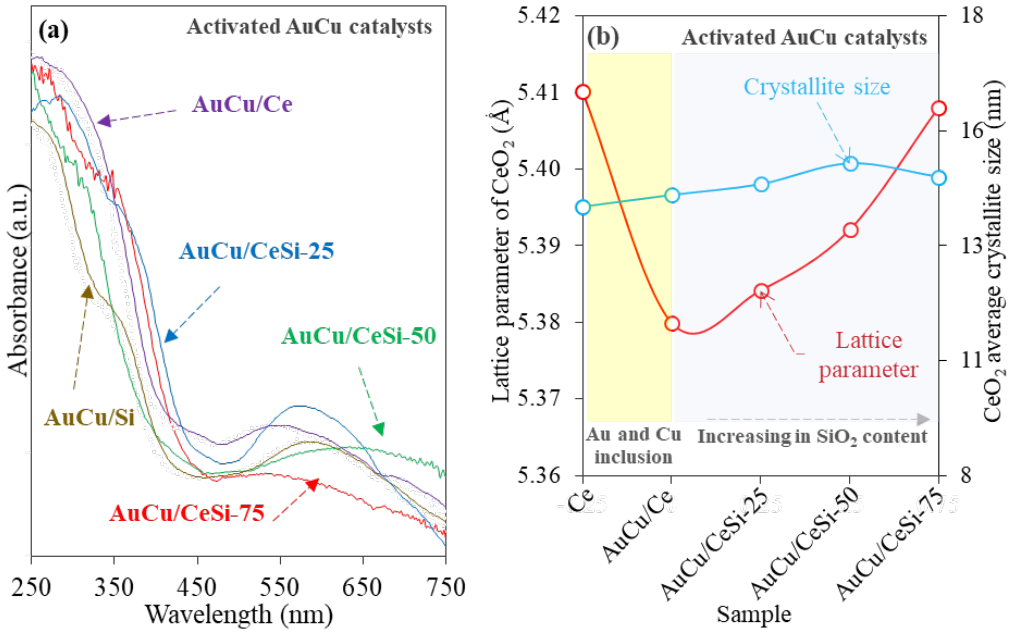

Figure 3.2.4. (a) UV-vis spectra for activated samples of Au-Cu catalysts. (b) Correlation of the lattice parameter and the average crystallite size of CeO_2 obtained by a Rietveld refinement of XRD patterns of Au-Cu catalysts. CeO_2-SiO_2 supports were labeled as CeSi-X, where X indicates the SiO_2 percent content (X = 25, 50 and 75 mol% SiO_2).

XPS The surface composition of AuCu catalysts was studied by XPS. Figure 3.2.5 shows the XPS spectra for Au, Cu and Ce, and Table 3.2.3 shows the surface concentration of Au and Cu. The amount of Au and Cu exposed decreases with the SiO_2 content in the support, indicating that SiO_2 could favor the adsorption of active metals towards the bulk of the support or the formation of larger particles [37], which would confirm the presence of particles of Au and Cu with several morphologies, as proposed in the UV-vis spectroscopy section.

Figure 3.2.5a shows the XPS spectra for Au $4f_{5/2}$ and $4f_{7/2}$. The characteristic peak at 83.8 eV shows the presence of only Au^0 species [50], which act as CO adsorption sites [25,51]. Also, Figure 3.2.5b shows the XPS spectra for Cu $2p_{3/2}$. The well-known Cu^{2+} satellites around 940 eV confirm the presence of oxidized Cu species (CuO), which is in line

Table 3.2.3. Atomic surface content, Auger parameter, Ce^{3+}/Ce^{4+} ratio, TO/F_{2g} index and BET surface area of $AuCu/CeO_2$-SiO_2 catalysts

Catalyst	Surface content (at%) [a]		Auger parameter[a]	Ce^{3+}/Ce^{4+} [a]	TO/F_{2g} index (10^2) [b]		BET surface area (m^2/g_{cat}) [c]
	Au	Cu			Activated	Used	
AuCu/Ce	1.7	5.0	1849.4	0.21	7.3	6.9	81
AuCu/CeSi-25	1.1	4.0	1849.0	0.18	5.5	5.3	115
AuCu/CeSi-50	1.4	3.2	1849.6	0.18	4.0	3.9	160
AuCu/CeSi-75	1.0	2.4	1849.1	0.18	2.9	2.8	275
AuCu/Si	0.6	2.2	1849.4	N/A	N/A	N/A	453

A: activated; U: Used; N/A: Not applicable. [a]measured by XPS; [b]measured by Raman spectroscopy; [c]measured by N_2 adsorption.

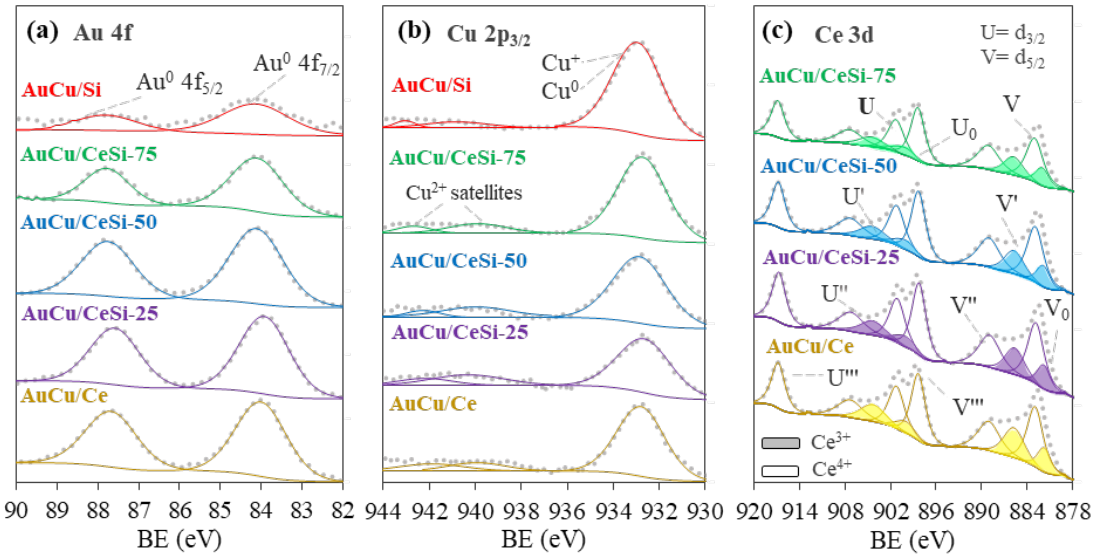

Figure 3.2.5. XPS spectra for (a) Au 4f, (b) Cu $2p_{3/2}$ and (c) Ce 3d in activated samples of AuCu catalysts supported on CeO_2-SiO_2 with several SiO_2 loadings. CeO_2-SiO_2 supports were labeled as CeSi-X, where X indicates the SiO_2 percent content (X = 25, 50 and 75 mol% SiO_2).

with previous reports [25,44]. However, the identification of reduced Cu species (i.e., Cu^0 and Cu^+), associated with the 932.6 eV peak, is difficult or impossible only by the Cu2p XPS spectra [52]. For this, we used the Cu LMM Auger spectra to identify the presence of reduced Cu species. Table 3.2.3 shows the modified Auger parameters for the AuCu catalysts. Most of the samples has an Auger parameter corresponding to the Cu^+ species (1849.2 to 1849.8 eV [52]). No evidence of the presence of Cu^0 ($\sim$ 1851.2 eV [52]) was identified. Both Cu^{2+} and Cu^+ species have been associated with the enhancement of CO oxidation during H_2 cleanup [25,53]. Then, the alteration in the concentration of Au and Cu in the catalytic surface by SiO_2 presence could favor changes on the activity of catalysts (Figure 3.2.3b).

The oxidation state of Ce is frequently used to determine the interaction of active metals with CeO_2 [51]. Figure 3.2.5c shows the XPS spectra for Ce $3d_{5/2}$ and $3d_{3/2}$, where the five pairs of spin-orbit doublets are observed (V_0, V, V´, V´´ and V´´´ for Ce $3d_{5/2}$ and U_0, U, U´ , U´´ and U´´´ for Ce $3d_{3/2}$) [25,54]. The peaks V_0, V´, U_0 and U´ are associated with the presence of reduced species (Ce^{3+}), and the rest of peaks correspond to Ce^{4+} species [55]. Formation of Ce^{3+} species is favored by interaction between CeO_2 and cations such as Cu^{2+} [56,57]. Table 3.2.3 shows that the Ce^{3+}/Ce^{4+} ratio, related to the formation of oxygen vacancies [25,55], decreases by about 14 % in AuCu catalysts supported on mixed oxides (i.e., AuCu/CeSi-25, AuCu/CeSi-50 and AuCu/CeSi-75) with respect to the AuCu/Ce sample (Table 3.2.3). The decrease in the Ce^{3+}/Ce^{4+} ratio suggests that SiO_2 alter oxygen vacancies of CeO_2, decreasing the CO oxidation capacity of catalysts [58].

XRD The crystal structure of CeO_2 in the activated samples of supported AuCu catalysts was evaluated by XRD (see Figure SM.17, Supplementary Material). Figure 3.2.4b correlates the lattice parameter and the average CeO_2 crystal size obtained by a Rietveld refinement. The CeO_2 lattice size decreases in the AuCu/CeO_2 sample compared to the bare CeO_2. A decreasing in lattice size has been associated with the replacement of Ce^{4+} ions by CuO species [59,60], which favors the formation of oxygen vacancies [56]. Likewise, as the SiO_2 content increases in the AuCu/CeO_2 system, the lattice parameter of CeO_2 increases, indicating a lower CuO-CeO_2 interaction, probably because of the new interaction between Cu and SiO_2. Also, the average crystal size of CeO_2 does not change significantly by the presence of SiO_2, obtaining a size of 14.4 $\pm$ 0.4 nm for all AuCu catalysts. Therefore, the reduction of oxygen vacancies observed by XPS could be associated with an additional interaction between Cu and SiO_2, without affecting the CeO_2 structure.

Raman spectroscopy The CeO_2 structure in the activated and used samples of AuCu catalysts was studied by Raman spectroscopy. Figure 3.2.6 shows the Raman spectra for AuCu catalysts containing CeO_2. In all the samples, CeO_2 shows the typical F_{g2} mode at 464 cm^{-1} and two satellite bands at 240 (transverse optical mode, TO) and 600 cm^{-1} (longitudinal optical mode, LO), related to oxygen vacancies in CeO_2 [61,62]. Table 3.2.3 contains the TO/F_{g2} index that allows comparing the number of defects in the lattice associated with oxygen vacancies in CeO_2. The results in Table 3.2.3 show that the higher the SiO_2 content, the lower the TO/F_{g2} index value, in agreement with the XPS results, where a decrease in the Ce^{3+}/Ce^{4+} ratio was also observed in AuCu catalysts supported on dual oxides.

The variation in the TO/F_{g2} index (Table 3.2.3) between activated and used samples was

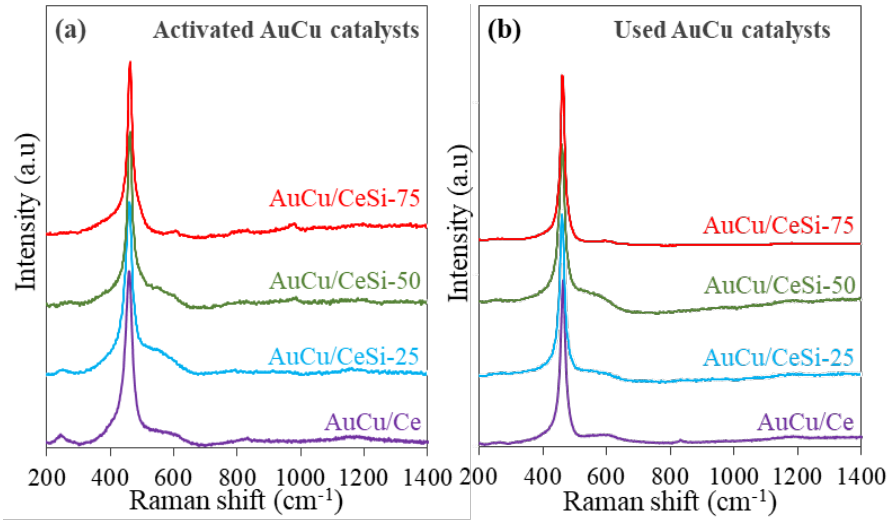

Figure 3.2.6. Raman spectra for (a) activated and (b) used samples of supported AuCu catalysts. CeO_2-SiO_2 supports were labeled as CeSi-X, where X indicates the SiO_2 percent content (X = 25, 50 and 75 mol% SiO_2).

less than 5 %. Additionally, no signal was identified in mode G (1590 cm^{-1}, associated with stable carbon deposits) and D (1350 cm^{-1}, associated with amorphous carbon) of carbon, indicating that carbon formation would not be a relevant aspect on AuCu catalysts supported on mixed CeO_2-SiO_2 oxides [27]. Thus, the characterization tests presented here and those previously reported in [26,27] show that the AuCu/CeO_2-SiO_2 supported catalysts appear not to be susceptible to significant changes during CO removal in a single unit, which could be beneficial for long term operations.

BET surface area Table 3.2.3 shows the surface area of the AuCu catalysts. The surface area of the catalysts increases with the SiO_2 content, but not linearly. For example, the increase in the surface area of AuCu/CeSi-25 is 1.4 times greater than that of AuCu/Ce, but for the AuCu/CeSi-50 and AuCu/CeSi-75 the increase is 2.0 and 3.4 times, respectively. As presented above, inclusion of SiO_2 in AuCu/CeO_2 system decreases oxygen vacancies of CeO_2, impacting oxidation capacity of catalysts. However, SiO_2 interacts also actively with active metals and promotes an increase in surface area of AuCu catalysts, which are key characteristics to favor CO adsorption on catalytic surface during CO removal [26,34]. Therefore, we speculate that with a 75 mol% of SiO_2 in the support of the AuCu/CeO_2 system, the increase in surface area mitigates the impact of the reduction of oxygen vacancies, favoring AuCu/CeSi-75 to have a higher activity than AuCu/CeO_2-50 (Figure 3.2.3b).

Monolith evaluation

In this section, monolithic reactors were evaluated in the CO removal from a syngas in a single catalytic unit. The most active catalyst (i.e., AuCu/Ce) and the most economical one (i.e., AuCu/CeSi-75) that ensured CO concentrations < 5 % (Table 3.2.2) were used to prepare the monolith catalysts.

Washcoating assessment Physical stability and adhesion of the catalyst were evaluated with ultrasonic and thermal shock tests. Figure SM.18 (Supplemental Material) shows the catalyst weight loss corresponding to the ultrasonic and thermal shock cycles. The monolith washcoated with the AuCu/CeSi-75 catalyst showed about 50 % less loss of coating in both tests, suggesting that the presence of SiO_2 favors a better adherence of the catalyst to the monolith walls. Tiscornia et al. [34] evaluated monoliths of cordierite washcoated with a $CuO/CeO_2/SiO_2$ catalysts, reporting that Aerosil (fumed silica) particles anchored to the macroporous walls of the cordierite contribute to a high mechanical stability. That is, the inclusion of SiO_2 in the $AuCu/CeO_2$ system reduces the price of the catalyst (Table 3.2.2) and improves the adhesion of the catalyst coating to the walls of the monolithic reactor.

Catalytic activity of monoliths Honeycomb monoliths present an opportunity to structure catalysts for CO removal from a syngas because they reduce the volume of the reactor, which is a critical factor for the implementation of H_2-based technology in compact applications [34]. Figure 3.2.7 shows the conversion of CO and H_2 obtained with the monoliths washcoated with AuCu/Ce and AuCu/CeSi-75, where the results using powder samples were included for comparison purposes. Over 240 °C, monolithic reactors are more effective in CO removal compared to their equivalent powder samples, which could be associated with an improvement in the transfer of mass and heat into the monoliths, as discussed later. Also, both monoliths washcoated with AuCu/Ce and AuCu/CeSi-75 have similar activity at high temperatures (> 260 °C), achieving CO conversion > 95 % and H_2 loss < 10 %. As presented in Table 3.2.2, the price of the washcoated monolith is only slightly higher than the powder samples due to the low price of cordierite. Therefore, cordierite monoliths offer an increased activity at higher temperatures with similar cost compared to non-structured samples.

Table 3.2.4 compares the activity of several structured catalysts in cordierite monoliths for CO removal. In general, it is possible to obtain a high CO conversion (> 95 %) using monolithic reactors. There were no previous reports on the CO removal of a syngas coming directly from an ethanol reformer in a single unit. That is why we reported an initial CO concentration > 6 mol%, with a H_2/CO of 3.1, which is the outlet condition of the syngas coming from a reformer. These conditions are more severe than those evaluated over monolithic reactors at CO-PROX conditions after several previous pre-cleaning units (i.e., CO < 2 mol% and $H_2/CO >> 10$). All the works reported in Table 3.2.4 used the traditional way to remove CO in fuel reformers (i.e., HT-WGS $\rightarrow$ LH-WGS $\rightarrow$ CO-SMET/CO-PROX, Figure 3.2.1), with higher H_2/CO ratios [19], which favors CO conversion during the final stage of CO-SMET and/or CO-PROX [63]. Thus, despite that they were evaluated under more severe conditions, AuCu/Ce and AuCu/CeSi-75 show similar performance to previous reports for CO removal over structured catalysts. Therefore, structured AuCu/Ce and AuCu/CeSi-75 catalysts are promising to remove CO in a single catalytic unit, showing higher activity than powder samples at temperatures higher than 240 °C. A CFD simulation was carried out to find an explanation of the observed high performance of the structured catalysts.

CFD model CO removal from syngas over washcoated monoliths was modeled by CFD, seeking to explain the improvement of catalytic activity in monoliths compared to

Table 3.2.4. Comparison of several structured catalysts for CO removal.

Coating of monolith	Gas composition in the inlet stream	Reaction	T (°C)	CO conversion (%)	Ref.
$Pt/CeO_2/Al_2O_3$	H_2 (50 mol%), CO (7 mol%), CO_2 (7 mol%), H_2O (30 mol%) and N_2 as balance.	WGS	310	$\sim$ 100*	[29]
CuO-CeO_2/SiO_2	H_2 (40 mol%), CO (1 mol%), O_2 (1 mol%) and He as balance.	CO-PROX	160	99	[34]
CuO/CeO_2	H_2 (50 mol%), CO (0.5 mol%), O_2 (0.9 mol%) and N_2 as balance.	CO-PROX	150	$\sim$ 100*	[30]
Ru/TiO_2	H_2 (60 mol%), CO (1.0 mol%), CO_2 (20 mol%), H_2O (15 mol%) and N_2 as balance.	CO-SMET	220	100	[17]
$PtCu/Al_2O_3$	H_2 (40 mol%), CO (1 mol%), O_2 (1 mol%) and He as balance.	CO-PROX	110	100	[64]
CuO/CeO_2	H_2 (50 mol%), CO (0.5 mol%), O_2 (0.9 mol%) and N_2 as balance.	CO-PROX	150	99	[65]
AuCu/CeO_2-SiO_2	H_2 (19.9±0.3 mol%), CO (6.3±0.1 mol%), CO_2 (5.2±0.5 mol%), O_2 (5.6±0.3 mol%), H_2O (7.8±0.2 mol%) and N_2 as balance.	WGS, CO-PROX	260	95	This work
$AuCu/CeO_2$	H_2 (19.9±0.3 mol%), CO (6.3±0.1 mol%), CO_2 (5.2±0.5 mol%), O_2 (5.6±0.3 mol%), H_2O (7.8±0.2 mol%) and N_2 as balance.	WGS, CO-PROX	300	96	This work

*Values obtained from graphical estimations

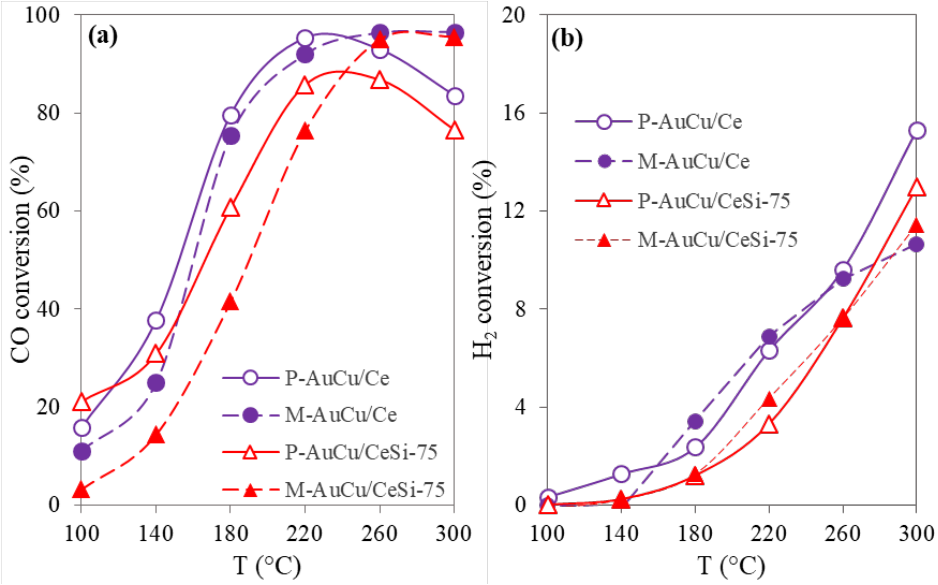

Figure 3.2.7. Conversion of (a) CO and (b) H_2 obtained in the CO removal from a syngas over powder catalysts and monoliths washcoated with AuCu/Ce and AuCu/CeSi-75 samples. Suffixes P: powder and M: monolith. Syngas feed: H_2 (19.9±0.3 mol%), CO (6.3±0.1 mol%), CO_2 (5.2±0.5 mol%), O_2 (5.6±0.3 mol%), H_2O (7.8±0.2 mol%), and N_2 (55.2±0.6 mol%). Reaction conditions: SV = 5.6 ± 0.3 L/g_{cat}*min.

powder samples at temperatures higher than 240 °C (Figure 3.2.7). Figure SM.19 (Supplementary Material) shows the excellent agreement between the experimental CO, H_2, CO_2 and O_2 flows at the outlet stream of the monolithic reactors and the results obtained in COMSOL Multiphysics. Then, CFD allows to model simultaneously mass and heat transfer and kinetics of the process [38]. Kinetic parameters obtained by non-linear regression of power law model ((5), Table 3.2.1) are presented in Table SM.12 (Supplementary Material). Parity plots (Figure SM.20 in Supplementary Material) show that CFD models adequately fit the experimental data, ensuring a deviation < 10 % in most of the values, which indicates that the models correctly predict the product distribution in both AuCu/Ce and AuCu/CeSi-75 monolithic reactors.

The temperature profile in the monoliths was also studied with the CFD simulation. Figure 3.2.8 shows that the temperature on the external walls of the monolith (which is the same as the furnace) is lower than the temperature in the internal channels of the monoliths. Actually, WGS (ΔH= -42 kJ/mol), CO oxidation (ΔH= -283 kJ/mol) and H_2 oxidation (ΔH= -241 kJ/mol) are exothermic reactions [66], which favor the increase in the temperature of the internal channels of the reactors. The temperature gradient can be up to 80 °C when the furnace operates at 300 °C. For non-reversible reactions, as CO oxidation, temperature favors an increase in reaction rate [67]. Therefore, increased temperature in internal channels could be associated with improved activity to CO removal over monolithic reactors compared to powder samples (Figure 3.2.7). In addition, the temperature increase is greater at the entrance of the monolith, since the CO conversion occurs mainly at the first 5 mm of the channels, as shown Figure 3.2.9. A high CO conversion in the initial section of

the channels also shows that the reactive gas interacts easily with catalyst adhered to the walls. Landi et al. [30] proposed that washcoated monoliths prevent the intra-particle mass transfer limitation (typically observed in powder samples), favoring CO oxidation during CO-PROX. Consequently, structured monoliths promote improvements in mass and heat transfer favoring an increase in activity, which match with previous reports [29,30,34,64]. Then, stability of structured catalysts (i.e., monoliths based on AuCu/Ce and AuCu/CeSi-75 catalysts) was evaluated in intermittent operation tests.

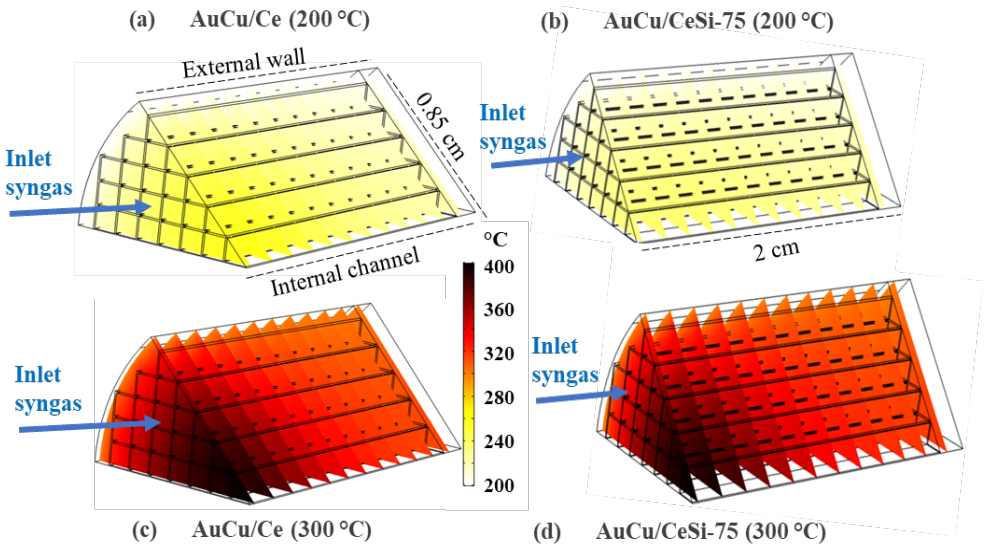

Figure 3.2.8. Temperature profiles for cross section of (a) a monolith washcoated with AuCu/Ce catalysts operating at 200 °C, (b) a monolith washcoated with AuCu/CeSi-75 catalysts operating at 200 °C, (c) a monolith washcoated with AuCu/Ce catalysts operating at 300 °C and (d) a monolith washcoated with AuCu/CeSi-75 catalysts operating at 300 °C.

Stability of monoliths in on/off test Thinking in a future implementation in fixed or mobile applications, stability of FPU is commonly evaluated by on/off stability tests (also called start-up/shutdown cycling) [7,32]. Figure 3.2.10 shows the conversion of CO and H_2 and the distribution of products obtained in an on/off test with monoliths washcoated with AuCu catalysts. Monolithic reactors were evaluated at 220 °C to prevent complete CO conversion, favoring the identification of deactivation phenomena [68]. The monolith washcoated with AuCu/Ce (Figure 3.2.10a) shows a stable conversion of CO (92 ± 2 %) and H_2 (11 ± 2 %), while the monolith washcoated with AuCu/CeSi-75 (Figure 3.2.10b) loses about 6 % of its initial CO activity (73 %). However, H_2 conversion decreases on the AuCu/CeSi-75 monolith, which is a beneficial effect, achieving only a ~ 4 % H_2 loss at the end of the test. Also, Figure 3.2.10c and d show that despite not being evaluated at the maximum CO conversion temperature, but at 220 °C, both AuCu/Ce (CO $\leq$ 0.2 %) and AuCu/CeSi-75 (CO $\leq$ 3.6 %) systems ensure a clean H_2 stream with a CO concentration $<$ 5 %. In addition, it is expected that at higher temperatures (260 to 300 °C), the monoliths based on AuCu catalysts favor a high conversion of CO ($>$ 95 %), achieving CO concentrations $<$ 1

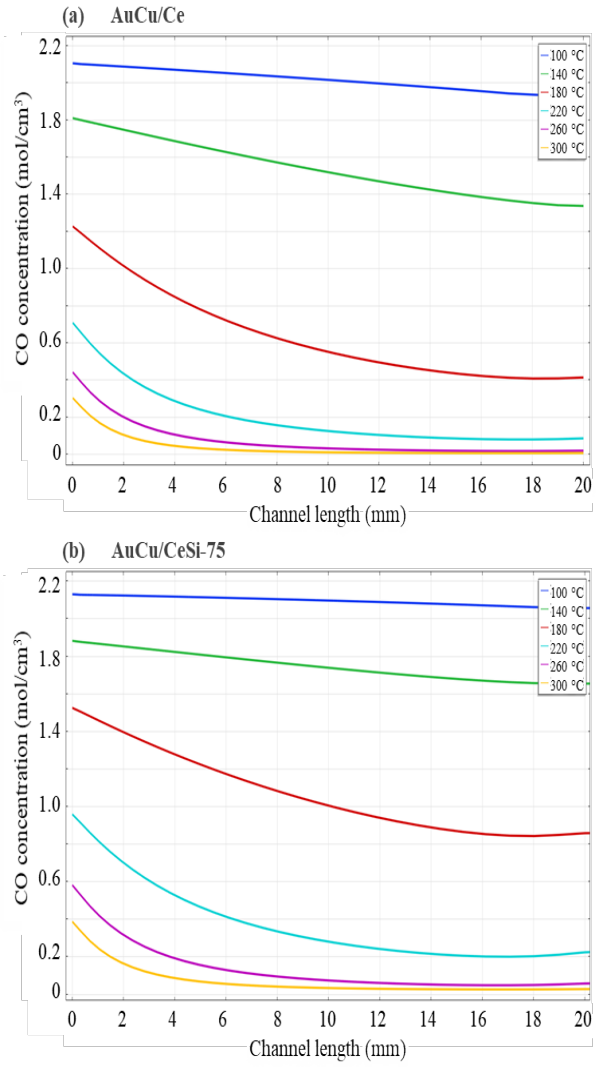

Figure 3.2.9. Molar concentration of CO at several temperatures vs. channel length of monoliths washcoated with (a) AuCu/Ce and (b) AuCu/CeSi-75 catalysts.

%. Therefore, monoliths based on AuCu catalysts are promising to be used in a compact B-FPU connected to a HT-PEMFC.

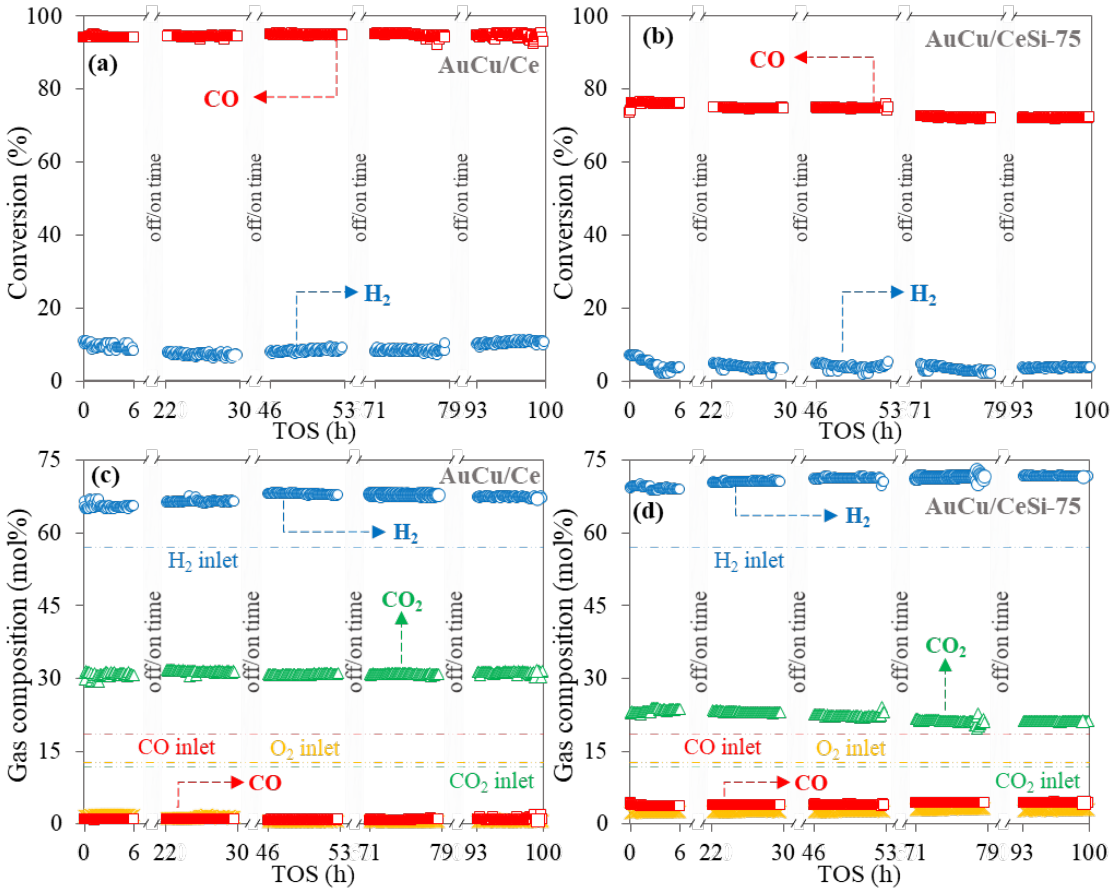

Figure 3.2.10. (a and b) Conversion of CO and H_2 and their corresponding product distribution (c and d) obtained in the CO removal over monoliths washcoated with AuCu/Ce and AuCu/CeSi-75 catalysts. Syngas feed: H_2 (19.9±0.3 mol%), CO (6.3±0.1 mol%), CO_2 (5.2±0.5 mol%), O_2 (5.6±0.3 mol%), H_2O (7.8±0.2 mol%), and N_2 (55.2±0.6 mol%). Reaction conditions: 220 °C, 3.3 g_{cat}/cm^2.

3.2.5 Conclusions

The effect of the addition of SiO_2 in the $AuCu/CeO_2$ system over both the cost and the catalytic performance for the CO removal from a syngas using only one catalytic unit was evaluated. It was identified that > 80 % of the catalyst cost relies on CeO_2, while the use of a noble metal (Au) would contribute with < 20 %. However, the inclusion of SiO_2 in the support could decrease the catalyst cost until 60 % compared to $AuCu/CeO_2$. Moreover, the $AuCu/CeO_2$-SiO_2 catalysts achieved conversion > 80 % of the initial CO in the syngas.

On the other hand, the most active catalyst (AuCu/Ce) and the cheapest (AuCu/CeSi-75) one that ensured adequate CO concentrations to be used in HT-PEMFC (i.e., < 5 %), were washcoated on monoliths of cordierite. At temperatures higher than 240 °C, monolithic

reactors were found to be more efficient to remove CO and have a similar cost compared to powdered catalysts. A CFD simulation showed that the improvement in the activity of the structured catalysts is related to enhancements in heat diffusion in the internal channels of the monolith and the easy contact between reactive gas and catalyst in the walls of monoliths. Thus, both structured catalytic systems (i.e., AuCu/Ce and AuCu/CeSi-75) allowed obtaining a syngas with concentrations of $H_2 > 65$ % and CO < 5 %. Moreover, the monolith based on AuCu/CeSi-75 is 38 % cheaper, has greater adhesion to the monolith walls and favors less H_2 losses (only 4 % of H_2 is lost), which makes it promising to be used in a compact B-FPU coupled to an HT-PEMFC.

3.2.6 Acknowledgments

The authors are grateful to Colciencias (Francisco Jose de Caldas Fund, contracts 548-2019), Universidad de La Sabana (Project code ING-221), MICINN/FEDER (projects RTI2018-093996-B-C31 and RTI2018-095498-J-I00), Generalitat de Catalunya (project GC 2017 SGR 128) and Universidad de Antioquia for the financial support to this work. B. Cifuentes acknowledge Colciencias for the doctoral scholarship (grant number 727-2015) and Fundación Carolina for grant to research stay (SEGIB-2019 program). J. Llorca is a Serra Húnter Fellow and is grateful to ICREA Academia program. A. Cifuentes is grateful to Generalitat de Catalunya and Addlink Software Científico S.L. for Industrial Doctorate grant 063/2018.

3.2.7 References

[1] H. Mohammed, A. Al-Othman, P. Nancarrow, M. Tawalbeh, M. El Haj Assad, Energy (2019) 207–219.
[2] U. Lucia, Renew. Sustain. Energy Rev. 30 (2014) 164–169.
[3] T.S. Moraes, H.N. Cozendey da Silva, L.P. Zotes, L.V. Mattos, L.E. Pizarro Borges, R. Farrauto, F.B. Noronha, Int. J. Hydrogen Energy 44 (2019) 21205–21219.
[4] J.B. Heo, Y.-S. Lee, C.-H. Chung, Biotechnol. Adv. 37 (2019) 107422.
[5] V.L. Pachapur, S.J. Sarma, S.K. Brar, Y. Le Bihan, G. Buelna, M. Verma, Biofuels 9 (2018) 129–138.
[6] N. Sanchez, R.Y. Ruiz, B. Cifuentes, M. Cobo, Waste Manag. 98 (2019) 1–13.
[7] T.S. Moraes, L.E.P. Borges, R. Farrauto, F.B. Noronha, Int. J. Hydrogen Energy 43 (2018) 115–126.
[8] L. Salemme, L. Menna, M. Simeone, Energy 57 (2013) 368–374.
[9] J. Holladay, E. Jones, D.R. Palo, M. Phelps, Y.H. Chin, R. Dagle, J. Hu, Y. Wang, E. Baker, Mater. Res. Soc. Symp. - Proc. 756 (2003) 429–434.
[10] N.P. Brandon, Z. Kurban, Philos. Trans. R. Soc. London A Math. Phys. Eng. Sci. 375 (2017) 1–17.
[11] R. Roldán, Int. J. Hydrogen Energy 40 (2015) 2035–2046.
[12] J. Llorca, V.C. Corberán, N.J. Divins, R.O. Fraile, E. Taboada, Renew. Hydrog. Technol. Prod. Purification, Storage, Appl. Saf. (2013) 135–169.
[13] N. Sanchez, R. Ruiz, V. Hacker, M. Cobo, Int. J. Hydrogen Energy 45 (2020) 11923.
[14] V. Palma, C. Ruocco, A. Ricca, Int. J. Hydrogen Energy 41 (2016) 11526–11536.

[15] R. González-Gil, C. Herrera, M.A. Larrubia, F. Mariño, M. Laborde, L.J. Alemany, Int. J. Hydrogen Energy 41 (2016) 16786–16796.
[16] A. Casanovas, C. de Leitenburg, A. Trovarelli, J. Llorca, Catal. Today 138 (2008) 187–192.
[17] C.B. Lee, S.H. Cho, D.W. Lee, K.R. Hwang, J.S. Park, S.H. Kim, Energy 78 (2014) 421–425.
[18] M. Ouzounidou, D. Ipsakis, S. Voutetakis, S. Papadopoulou, P. Seferlis, Energy 34 (2009) 1733–1743.
[19] I. Rossetti, M. Compagnoni, M. Torli, Chem. Eng. J. 281 (2015) 1036–1044.
[20] R. Koch, E. López, N.J. Divins, M. Allué, A. Jossen, J. Riera, J. Llorca, Int. J. Hydrogen Energy 38 (2013) 5605–5615.
[21] E. López, N.J. Divins, J. Llorca, Catal. Today 193 (2012) 145–150.
[22] R.E. Rosli, A.B. Sulong, W.R.W. Daud, M.A. Zulkifley, T. Husaini, M.I. Rosli, E.H. Majlan, M.A. Haque, Int. J. Hydrogen Energy 42 (2017) 9293.
[23] J.D. Arévalo, Á. Martinez-Hernández, J.C. Vargas, L.F. Córdoba, J.D. Arévalo, Á. Martinez-Hernández, J.C. Vargas, L.F. Córdoba, Tecciencia 13 (2018) 55–64.
[24] B. Cifuentes, M. Hernández, S. Monsalve, M. Cobo, Appl. Catal. A Gen. 523 (2016) 283–293.
[25] B. Cifuentes, F. Bustamante, J.A. Conesa, L.F. Córdoba, M. Cobo, Int. J. Hydrogen Energy 43 (2018) 17216–17229.
[26] B. Cifuentes, F. Bustamante, D.G. Araiza, G. Diaz, M. Cobo, Appl. Catal. A, Gen. 598 (2020) 117568.
[27] B. Cifuentes, F. Bustamante, M. Cobo, Catalysts 9 (2019) 852–877.
[28] A.M. Lacoste, I.S. Tiscornia, A. V. Boix, Int. J. Hydrogen Energy 43 (2018) 14238–14251.
[29] M. González-Castaño, S. Ivanova, O.H. Laguna, L.M. Martínez T., M.A. Centeno, J.A. Odriozola, Appl. Catal. B Environ. 200 (2017) 420–427.
[30] G. Landi, P.S. Barbato, A. Di Benedetto, L. Lisi, Appl. Catal. B Environ. 181 (2016) 727–737.
[31] L.M. Martínez T, O.H. Laguna, C. López-Cartes, M.A. Centeno, Mol. Catal. 440 (2017) 9–18.
[32] T. Tabakova, Front. Chem. 7 (2019) 1–43.
[33] F. Le Normand, L. Hilaire, K. Kili, G. Krill, G. Maire, J. Phys. Chem. 92 (1988) 2561–2568.
[34] I.S. Tiscornia, A.M. Lacoste, L.E. Gómez, A. V. Boix, Int. J. Hydrogen Energy 45 (2020) 6636–6650.
[35] B. Cifuentes, A. Cifuentes, F. Bustamante, L. Soler, J. Llorca, M. Cobo, Mendeley Dataset (2020) DOI: 10.17632/rw8drwgv8p.2.
[36] D.R. Sahoo, S. Vajpai, S. Patel, K.K. Pant, Chem. Eng. J. 125 (2007) 139–147.
[37] B. Cifuentes, M.F. Valero, J. a. J. Conesa, M. Cobo, Catalysts 5 (2015) 1872–1896.
[38] A. Cifuentes, R. Torres, J. Llorca, Int. J. Hydrogen Energy (2019) In Press 10.1016/j.ijhydene.2019.11.034.
[39] H.C. Lee, D.H. Kim, Catal. Today 132 (2008) 109–116.
[40] E. Quinet, L. Piccolo, F. Morfin, P. Avenier, F. Diehl, V. Caps, J.L. Rousset, J. Catal. 268 (2009) 384–389.

[41] G. Yi, H. Yang, B. Li, H. Lin, K.I. Tanaka, Y. Yuan, Catal. Today 157 (2010) 83–88.
[42] Bonnie J. McBride, Michael J. Zehe, Sanford Gordon, NASA Glenn Coefficients for Calculating Thermodynamic Properties of Individual Species: National Aeronautics and Space Administration, 2002.
[43] X. Li, S.S.S. Fang, J. Teo, Y.L. Foo, A. Borgna, M. Lin, Z. Zhong, ACS Catal. 2 (2012) 360–369.
[44] P. Destro, S. Marras, L. Manna, M. Colombo, D. Zanchet, Catal. Today 282 (2017) 105–110.
[45] S. Najafishirtari, R. Brescia, P. Guardia, S. Marras, L. Manna, M. Colombo, ACS Catal. 5 (2015) 2154–2163.
[46] D. Kang, X. Yu, M. Ge, Chem. Eng. J. 330 (2017) 36–43.
[47] C. Zhang, J. Lin, Phys. Chem. Chem. Phys. 13 (2011) 3896–3905.
[48] Z. Ren, F. Peng, J. Li, X. Liang, B. Chen, Catalysts 7 (2017) 48–60.
[49] A.S.A. Al-Sherbini, J. Nanomater. 2010 (2010) 1–6.
[50] X. Liu, A. Wang, L. Li, T. Zhang, C.Y. Mou, J.F. Lee, J. Catal. 278 (2011) 288–296.
[51] J.A. Hernández, S.A. Gómez, T.A. Zepeda, J.C. Fierro-González, G.A. Fuentes, ACS Catal. 5 (2015) 4003–4012.
[52] T.M. Ivanova, K.I. Maslakov, A.A. Sidorov, M.A. Kiskin, R. V. Linko, S. V. Savilov, V. V. Lunin, I.L. Eremenko, J. Electron Spectros. Relat. Phenomena 238 (2020) 146878.
[53] G. Marbán, I. López, T. Valdés-Solís, Appl. Catal. A Gen. 361 (2009) 160–169.
[54] L. Soler, A. Casanovas, A. Urrich, I. Angurell, J. Llorca, Appl. Catal. B Environ. 197 (2016) 47–55.
[55] A. Abd El-Moemen, A.M. Abdel-Mageed, J. Bansmann, M. Parlinska-Wojtan, R.J. Behm, G. Kučerová, J. Catal. 341 (2016) 160–179.
[56] J.L. Ayastuy, E. Fernández-Puertas, M.P. González-Marcos, M.A. Gutiérrez-Ortiz, Int. J. Hydrogen Energy 37 (2012) 7385–7397.
[57] H. Jin, R. You, S. Zhou, K. Ma, M. Meng, L. Zheng, J. Zhang, T. Hu, Int. J. Hydrogen Energy 40 (2015) 3919–3931.
[58] Y. Xie, J. Wu, G. Jing, H. Zhang, S. Zeng, X. Tian, X. Zou, J. Wen, H. Su, C.-J.J. Zhong, P. Cui, Appl. Catal. B Environ. 239 (2018) 665–676.
[59] A. Martinez-Arias, A.B. Hungria, M. Fernandez-Garcia, J.C. Conesa, G. Munuera, A. Martı, A.B. Hungrı, J. Phys. Chem. B (2004) 17983–17991.
[60] D.G. Araiza, A. Gómez-Cortés, G. Díaz, Catal. Today 282 (2017) 185–194.
[61] S.T. Hossain, E. Azeeva, K. Zhang, E.T. Zell, D.T. Bernard, S. Balaz, R. Wang, Appl. Surf. Sci. 455 (2018) 132–143.
[62] L. Ilieva, P. Petrova, G. Pantaleo, R. Zanella, L.F. Liotta, V. Georgiev, S. Boghosian, Z. Kaszkur, J.W. Sobczak, W. Lisowski, A.M. Venezia, T. Tabakova, Appl. Catal. B Environ. 188 (2016) 154–168.
[63] R.J.B. M. J. Kahlich, H.A. Gasteiget, Iournal New Mater. Electrochem. Syst. 1 (1998) 39–46.
[64] L.E. Gómez, B.M. Sollier, A.M. Lacoste, E.E. Miró, A. V. Boix, J. Environ. Chem. Eng. 7 (2019) 103376–103386.
[65] P.S. Barbato, A. Di Benedetto, G. Landi, L. Lisi, Top. Catal. 59 (2016) 1371–1382.
[66] D.G. Oliva, J.A. Francesconi, M.C. Mussati, P.A. Aguirre, J. Power Sources 182 (2008) 307–316.

[67] O.P. Klenov, N.A. Chumakova, S.A. Pokrovskaya, A.S. Noskov, Chem. Eng. Sci. 205 (2019) 1–13.
[68] F. Schüth, M.D. Ward, J.M. Buriak, Chem. Mater. 30 (2018) 3599–3600.

4 Technology description

In the previous chapter, syngas production by ethanol steam reforming of actual bioethanol (i.e., obtained from residual biomass) over monoliths whashcoated with a $RhPt/CeO_2$-SiO_2 catalyst, and CO removal from a syngas over monoliths washcoated with $AuCu/CeO_2$-SiO_2 catalyst were presented. These results were used as a starting point to design and built a prototype of a bioethanol fuel processor, which is described in this chapter. This chapter corresponds to the fourth specific objective of the Thesis: "Perform a preliminary economic analysis of the H_2 production in a bioethanol fuel processor unit to assess the potential of developed prototype".

This chapter is presented as a technical report.

Lab-scale prototype

4.1 Introduction

Despite the growing concern about the negative effects of fossil fuels use on human health and environment, more than 60% of the energy produced in the world still comes from coal, oil and natural gas [1]. Also, electricity, even when obtained from renewable resources, is mainly produced on large-scale facilities (e.g., thermal power stations, hydroelectric plants, and wind and solar farms) and distributed through the available local electrical network. However, governmental weaknesses and utilities indifference towards the less productive areas contribute to a low electrification in rural areas, especially in emerging countries [2]. As a consequence, more than 30% of the world population does not have clean energy systems ($\sim$ 2 billion people) and 10% does not have access to power [3] because they are in areas that are not connected to centralized power plants. Therefore, it is necessary to develop energy systems that ensure the access of the whole population to sustainable sources of electricity.

The use of multi-sites for small-scale energy production that employ micro-grids to supply the power demand of small communities has been proposed as an alternative for sustainable electrification in remote areas [2,4]. In the multi-site approach, energy is produced on site using various renewable resources available in each region (i.e., sun, wind and/or biomass). Under this scheme, hydrogen (H_2) based technologies have received great attention due to the potential of using H_2 as an integrating energy vector. Indeed, power-to-gas (P2G) systems, where H_2 is produced using solar- or wind-electrolyzers, have been successfully established in on site energy production [5]. P2G systems are connected to H_2 fuel cells (H_2-FC) to obtain electricity, heat, and water, without pollutant emissions, offering clean energy to communities. Furthermore, small-scale H_2 supply systems could be up to 18% cheaper compared to centralized H_2 production due to the high cost of H_2 distribution [6].

Advances in P2G and H_2-FC are a promising way for electrification in remote areas [7]. However, most of these technologies have been designed and established in developed countries, so their access in emerging countries is still low [8] due to the high import, adaptation and maintenance costs. Moreover, it has been proposed that only a combined strategy among solar, wind and biomass energy could ensure enough production of clean energy to supply the energy demand of emerging economies [9]. Nonetheless, commercialization of technologies for obtaining H_2 from biomass, one of the most abundant renewable resources in developing countries [10], seems to be lagged compared to P2G systems. The absence of technologies designed to take advantage of local resources and the high cost of existing methods to purify H_2 streams could be critical constraints for the implementation of H_2-based systems to obtain energy from biomass.

The on-site production of H_2 from biomass could be carried out in fuel processors units (FPU) that are devices in which H_2 is produced and purified [11]. The FPU are fed with liquid biofuels such as: methanol [12], obtained from biogas; biodiesel [13], obtained from vegetable oils; or, bioethanol [14], obtained from fermentable biomass. Among them, bioethanol is the largest produced biofuel in the world, reaching an annual production of over 97 billion liters [15] of which more than 35% come from developing regions such as Latin America and Asia-Pacific. FPU fed with bioethanol (B-FPU) contain two main modules: (i) a bioethanol reformer to produce syngas, and (ii) a separation system to obtain purified H_2. The degree of H_2 purification obtained from the B-FPU depends on the characteristics of H_2-FC to which it will be connected (i.e., the level of tolerance to CO). However, auxiliary equipment

(e.g., heat exchangers, pumps or compressors, or control systems) may be required in each module according to the configuration of the B-FPU [11]. Both modules of the B-FPU have been extensively addressed in the literature [11,16–20], making valuable contributions to the development of lab scale prototypes and pilot plants. Unfortunately, in Colombia the development of these technologies is very limited.

This research focused on developing a prototype of B-FPU based on monolithic reactors to obtain H_2 from actual bioethanol. Bioethanol was obtained from fermentation of residual biomass produced by the Colombian agroindustry. The first B-FPU module (i.e., bioethanol reformer) was assembled based on preliminary studies [21–23] and the information described above (section 1 of chapter 3). Similarly, the second module of the B-FPU (i.e., CO removal stage) was built according to the information presented in chapter 2 [14,17,24] and section 3.2 (chapter 3). The particularity of the CO removal module developed here is that it only involves a catalytic reactor, looking for the reduction of the volume of the B-FPU and the cost to purify H_2 streams. It is envisioned that, after a proof-of-concept evaluation, this technology will be connected to high CO-tolerant fuel cells (e.g., a high temperature proton-exchange membrane fuel cell) to supply power to a Colombian farm which produces *Panela* (a non-centrifugal sugar product).

This section aims to present a summary of the features of the B-FPU built during the doctoral research. For this, the details of the developed prototype are presented, including a description of equipment, process variables and cost. Then, a brief overview of the economic relevance of the panela sector, its environmental impact and its potential to produced residual biomass suitable for H_2 production are presented. Finally, possible future works associated with the prototype developed in this research are proposed.

4.2 FPU prototype

4.2.1 General description

Figure 4.2.1 shows the diagram of the prototype developed B-FPU for H_2 production from actual bioethanol. Also, Table 4.2.1 describes the main streams involved in the B-FPU. The prototype has an evaporator (E-101), two catalytic reactors (R-101 and R-201), a cooler (E-102), two mass flow controllers (M-101 and M-201), a condenser (E-201), 4 pressure sensors, 7 temperature sensors, valves, mixers and heated sections of pipeline. Most equipment (E-101, R-101, R-201) are heated electrically, and the condenser has a water chiller unit. The apparatus is made of SS304 with safety connections for handling dangerous gases (e.g., H_2, CH_4 and CO). The system also has a control panel to manipulate the temperatures of the equipment and pipelines. Line 4 serves as a relief to avoid an excessive pressure increase in E-101, while lines 9 and 16 are sampling points. Gas composition in the outlet stream of each reactor is determined with a gas analyzer or by gas chromatography. The prototype was built by local suppliers, using materials available in Colombia. Mass flow controllers (M-101 and M-201) and pump (P-101) were the only devices imported because there are no domestic manufacturers of these equipments.

Table 4.2.1. Description of the main streams of the prototype shown in Figure 4.2.1.

Stream	Description	Stream	Description
1	Bioethanol, $\sim$ 20 °C. Composition: water, ethanol and impurities (i.e., 1-propanol, 2-methyl-1-propanol, 3-methyl-1-butanol, and 1-butanol).	8, 9 and	Outlet stream from the reformer (syngas), 600-700 °C. Composition: water, CO, CO_2, CH_4, H_2 and carrier gas.
2 and 6	Carrier gas, $\sim$ 20 °C. Composition: inert gas (e.g., N_2 or Ar).	10	Cold Syngas, 120-300 °C. Composition: water, CO, CO_2, CH_4, H_2 and carrier gas.
3 and 11	Oxidant for CO removal, $\sim$ 20 °C. Composition: air or O_2.	12 and 13	Mixing between the syngas and the oxidant for CO removal, 120-300 °C. Composition: water, CO, CO_2, CH_4 and H_2, carrier gas and oxidant (i.e., air or O_2).
4	Purge stream of evaporator, $\sim$ 120 °C. Composition: water, ethanol, and impurities.	14	Outlet stream from the CO removal reactor (purified syngas), 220-300 °C. Composition: water, CO ($<$ 5%), CO_2, CH_4 and H_2, carrier gas and oxidant (i.e., air or O_2).
5	Bioethanol evaporated, $\sim$ 120 °C. Composition: water, ethanol, and impurities.	15	Water removed from purified syngas, $\sim$ 80 °C. Composition: water.
7	Inlet stream to reformer, $\sim$ 120 °C. Composition: water, ethanol, impurities, and carrier gas.	16	Dry and purified syngas, $\sim$ 80 °C. Composition: CO ($<$ 5%), CO_2, CH_4 and H_2, carrier gas and oxidant (i.e., air or O_2).

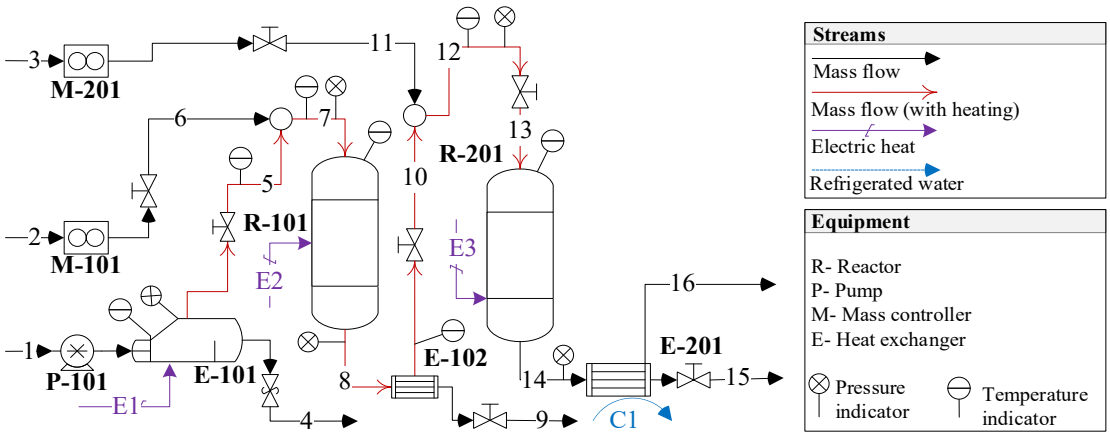

Figure 4.2.1. Diagram of the B-FPU developed in the project to H_2 production from actual bioethanol.

4.2.2 Syngas production

In the B-FPU prototype, the syngas is obtained from bioethanol reforming, which is carried out in the first reactor (R-101, Figure 4.2.1). Table 4.2.2 shows the main operating variables in the R-101 reformer. The inlet of the system (i.e., stream 1, Figure 4.2.1) consists in actual bioethanol, preferably obtained from the fermentation of residual biomass such as sugarcane press-mud [25], at <1 mL/min. Bioethanol should have a steam to ethanol (S/E) ratio between 3 and 4.2 to ensure the energy self-sufficiency of a system; this interval was determined according to a preliminary energy analysis (see Figure SM.21 in Supplementary Material). Thus, the inlet stream to the reformer is bioethanol evaporated (120 °C) and mixed with carrier gas (e.g., N_2 or Ar) in a proportion of 1.6 L inert gas/mL bioethanol, which was selected according to the results presented in section 3.1. The reformer could operate between 600 and 700 ° C, temperatures where the highest H_2 yield is obtained (>3.1 mol H_2/mol ethanol), as presented in section 3.1. The reaction system consists of two cordierite monoliths in series washcoated with a RhPt/CeO_2-SiO_2 catalyst [21] (washcoat loading = 0.1 mg_{cat}/cm^3), this configuration was selected to mitigate the formation of unwanted compounds (e.g., CH_4 and CO) and reduce the susceptibility of the system to changes in the operation temperature, as discussed in section 3A. With these operating conditions, it is expected to produce a syngas mainly containing H_2, CO, CO_2 and carrier gas (CH_4 could be present in a low proportion, <0.5%), where H_2 should be the main product (> 60%). Additionally, experimental data reported for RhPt/CeO_2-SiO_2 catalysts [21] was adjusted to the kinetic model proposed by [26]. Then, kinetic parameters for syngas production from ethanol steam reforming over RhPt/CeO_2-SiO_2 catalyst are presented in Table 4.2.3.

4.2.3 CO removal from the syngas

Syngas leaving the reformer (R-101) is mixed with air or O_2 in a proportion of 0.9 mol O_2/mol CO, as defined in section 2.1 (chapter 2) [14], and enters the second reactor (R -201) where the CO removal is carried out. Table 4.2.4 shows the main operating variables on the R-201,

Table 4.2.2. Specifications for syngas production in the ethanol reformer

Specification	**Description**	
Inlet	Bioethanol (0.06 to 1 mL/min)	
S/E	3 to 4.2	
Carrier gas	1.6 L/mL bioethanol	
Temperature	600 to 700 °C	
Reactor type	Monolith	
Material	Cordierite ($(Mg, Fe)_2Al_4Si_5O_{18}$)	
Number of reactors	2	
Configuration	In series	
Washcoat	$RhPt/CeO_2$-SiO_2 0.4 wt% Rh, 0.4 wt% Pt, and 99.2 CeO_2-SiO_2 (Ce/Si=2) [21]	
Washcoat loading	0.1 mg/cm^3	
Expected products	H_2 (> 60%), CO, CO_2 and CH_4	
Furnace type	Tubular with electric heating	Monolith size

Table 4.2.3. Kinetic parameters for syngas production from ethanol steam reforming over $RhPt/CeO_2$-SiO_2 catalyst.

Reaction	E_a/R (K)	$\ln(k_0)$
$C_2H_5OH + 3H_2O \rightarrow 2CO_2 + 6H_2$	-29008	32.7
$C_2H_5OH \rightleftharpoons CH_4 + CO + H_2$	-22918	40.2
$CO + H_2O \rightleftharpoons CO_2 + H_2$	39076	-19.2
$CH_4 + H_2O \rightleftharpoons CO + 3H_2$	-17254	35.4

Experimental data reported on [21] was adjusted to kinetic models proposed by [26]. Deterministic and metaheuristic methods were used to minimize the sum of squared errors.

which operates between 260 and 300 °C to remove more than 90% of the CO from syngas, as presented in section 3.2 (chapter 3). The reaction system consists of a cordierite monolith washcoated with an AuCu/CeO_2-SiO_2 catalyst (washcoat loading = 0.2 mg_{cat}/cm^3), a more expensive catalyst based on AuCu/CeO_2 can also be used to obtain larger CO removal (> 95%). In both cases (i.e., AuCu/CeO_2-SiO_2 and AuCu/CeO_2), CeO_2 should be present as nanoparticles with polyhedral shape [24]. H_2 loss during CO removal is expected to be <10%. The system also includes a condenser to remove the water. Thus, the syngas obtained from the B-FPU (stream 16, Figure 4.2.1) should contain mainly H_2 (> 65%), CO_2 and carrier gas, and in less proportion CO (<5%), O_2, and CH_4. The prototype of B-FPU could produce ~ 2.0 L H_2/mL actual bioethanol, which is close to the 2.4 L H_2/mL bioethanol reported for a traditional B-FPU (i.e., ethanol reformer → water gas shift reactor → a pressure swing absorption unit) that uses synthetic bioethanol (mixture of anhydrous ethanol and water) [11]. Also, experimental data reported in section 3.2 for monoliths washcoated with AuCu catalysts was adjusted to power law kinetic models; kinetic parameters for CO removal from a syngas over AuCu/CeO_2 and AuCu/CeO_2-SiO_2 catalysts are presented in Table 4.2.5.

Table 4.2.4. Specifications for CO removal from an actual syngas

Specification	**Description**	
Inlet	Syngas coming directly from ethanol reformer (0.1 to 0.6 L/min)	
$\lambda_{1/2}$	0.9 (mol O_2/mol CO)	
Temperature	260 to 300 °C	
Reactor type	Monolith	
Material	Cordierite ($(Mg, Fe)_2Al_4Si_5O_{18}$)	
Number of reactors	1	
Configuration	Single	
Washcoat	AuCu/CeO_2-SiO_2 1.0 wt% Au, 1.0 wt% Cu, and 98 CeO_2-SiO_2 (Si/Ce>3)	
Washcoat loading	0.2 mg/cm^3	
Expected products	H_2, CO (<5%), CO_2 and CH_4	
Furnace type	Tubular with electric heating	Monolith size

4.2.4 Cost of the prototype

The cost of the equipment was US$53,000, which was calculated using the actual values of its construction. Figure 4.2.2a shows the cost distribution by equipment. 22% of the cost corresponds to the furnaces (R-101 and R-201, Figure 4.2.1), which includes the control system for each equipment. In addition, the cost of imported units, mass controllers and

Table 4.2.5. Kinetic parameters for CO removal from syngas over $AuCu/CeO_2$ and $AuCu/CeO_2$-SiO_2 (Si/Ce=3) catalysts.

Reaction	$AuCu/CeO_2$		$AuCu/CeO_2$-SiO_2	
	E_a (kJ/mol)	A (pre-exponential factor)	E_a (kJ/mol)	A (pre-exponential factor)
$CO + \frac{1}{2} O_2 \rightarrow CO_2$	20	$1.6 \cdot 10^{-3}$ ($m^4/mol^* s^* g_{cat}$)	30	$2.2 \cdot 10^{-2}$ ($m^4/mol^* s^* g_{cat}$)
$C + H_2O \rightleftharpoons CO_2 + H_2$	63	$7.3 \cdot 10^{3}$ ($mol/m^* s^* g_{cat}$)	65	$5.42 \cdot 10^{3}$ ($mol/m^* s^* g_{cat}$)
$H_2 + \frac{1}{2} O_2 \rightarrow H_2O$	43	1.3 ($mol/m^* s^* g_{cat}$)	55	1.2 ($mol/m^* s^* g_{cat}$)

Kinetic models were obtained in COMSOL Multiphysics software (V5.5, Sweden) using the experimental data described in section 3-2 (chapter 3).

pump (M-101, M-201 and P-101, Figure 4.2.1), corresponds to 20% of total cost due to the high precision of these devices and the costs of import (>20% of the initial price). The costs of site preparation and the plant startup correspond to 20 and 10% of the total cost of prototype, respectively, according to those suggested in [27]. Note that the cost of monoliths for both bioethanol reforming and CO removal do not have a significant participation (<1%) in the total cost of the prototype due to the low washcoat loading, which matches with previous reports [28-30]. Therefore, the use of noble metals (e.g., Rh, Pt and Au) could not be a relevant constraint for developing B-FPU based on monoliths reactors.

Figure 4.2.2b compares the cost of the equipment associated with each module in the B-FPU (i.e., (i) syngas production in the reformer and (ii) syngas purification); the cost of imported equipment, site preparation and plant startup were labeled "others". The cost associated with equipment for CO removal (labeled as syngas purification) is 1.3 times higher than the cost to produce syngas. The use of water-gas shift reactors and pressure-swing adsorption unit to purify the syngas could be up to 3 times higher than the cost of producing syngas [11]. So, the prototype developed in this doctoral research could be a contribution to decrease the volume and cost of B-FPU. The prototype could be coupled to a high CO-tolerant H_2-FC, such as high temperature proton-exchange membrane fuel cells (HT-PEMFC), which commercial cost is $\sim$ 9,000 USD. Consequently, if bioethanol obtained from residual biomass is used, it is estimated that the cost of H_2 produced in the prototype is $\sim$ 7 USD/hgH_2, as was discussed in section 3.1 (chapter 3). Thus, it is expected that, in the medium term, this prototype will be integrated into a *panela* production farm to supply energy using bioethanol obtained from residual biomass.

4.3 Non-centrifugal sugar industry in Colombia

Non-centrifugal cane sugar agroindustry (known as *Panela*, *Chancaca*, *Piloncillo*, *Rapadura*, *Jaggery*, *Kokuto* or *Muscovado*) is widely developed in Asia and Latin America [31]. Colombia is the second largest producer of *Panela* worldwide, after India, exceeding 1.3 million

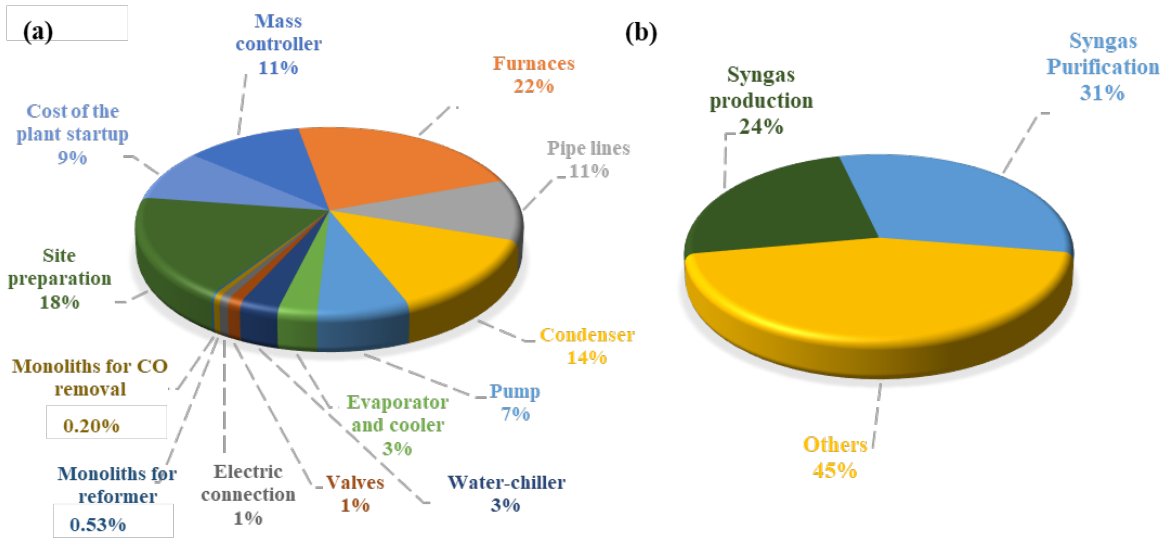

Figure 4.2.2. Cost distribution for (a) equipment and (b) modules of the B-FPU developed

ton per year [32]. In addition, *Panela* is one of the representative products of the Colombian diet because it is used in nutraceutical and medicinal products [33], and as a sweetener for drinks, sweets and traditional desserts. In Colombia, *Panela* is produced mainly on small farms called *Trapiches*, which have a low level of technification. *Trapiches* are distributed in remote areas along the country [31]. Also, *Trapiches* produce more than 500 kton of residual biomass per year [32], which could be used to produce energy. Therefore, Colombian *Panela* industry is promising to develop small-scale energy production systems based on biomass.

Production process of *Panela* is divided into three stages [31]: Initially, (i) the sugarcane is planted and harvested, followed by (ii) a grinding to extract the cane juice. Subsequently, (iii) the juice is clarified and concentrated to obtain a solid (*Panela*). Several fossil fuels, such as gasoline and diesel, are used to supply power to the grinding, producing greenhouse gas emission. Also, juice concentration is carried out in several rudimentary evaporators, where coal, wood, bagasse, and even tires are burned to provide energy to heat, significantly increasing the emissions of pollutants [34]. Consequently, the process produces about 370 kg of CO_2-eq per ton of *Panela* and 1.5 kg PM10-eq of particulate material per ton of sugarcane [35]. Thus, it is a priority to look for alternatives to face the environmental and health problems associated with *Panela* production.

The use of residual biomass from the process, such as bagasse [36] and sugarcane press-mud [25] (a solid fibrous residue obtained during the juice clarification), has been proposed to obtain biofuels that can supply part of the energy demand for the *Panela* production. Particularly, sugarcane press-mud is discarded in piles, whose leaching results in pollution of water bodies and attracts pests [37]. For this reason, the use of sugarcane press-mud as a platform for the development of clean energy technologies could reduce the use of fossil fuels in the *Panela* production process, and avoid the negative environmental impact due to its incorrect disposal.

In the framework project in which this doctoral research was carried out (as is detailed in

chapter 1), sugarcane press-mud is used to produce bioethanol by alcoholic fermentation, obtaining a yield of 40 g ethanol/kg sugarcane press-mud, which is comparable with bioethanol obtained from glucose patrons [25]. Bioethanol obtained from fermentation of sugarcane press-mud has also been evaluated in the syngas production using catalytic systems based on $RhPt/CeO_2$-SiO_2, as was presented in [38] and section 3.2 (chapter 3), achieving a syngas with high concentration of H_2 (>65%). Moreover, as discussed in section 3.1 (chapter 3) the use of bioethanol obtained from residual biomass, which have a low market price, favors the decrease in H_2 production costs.Therefore, the B-FPU developed during this research project, which takes advantage of the bioethanol obtained from sugarcane press-mud, is a contribution to the development of non-conventional technologies that could reduce the environmental impact of the *Panela* industry in Colombia.

4.4 References

[1] I. Pioro, R. Duffey, Manag. Glob. Warm. (2019) 67–114.
[2] S. Mandelli, C. Brivio, M. Moncecchi, F. Riva, G. Bonamini, M. Merlo, Energy Procedia 135 (2017) 367–378.
[3] E. Panos, M. Densing, K. Volkart, Energy Strateg. Rev. 9 (2016) 28–49.
[4] A. Pham, T. Jin, C. Novoa, J. Qin, Int. J. Prod. Econ. 218 (2019) 260–274.
[5] A. Mazza, E. Bompard, G. Chicco, Renew. Sustain. Energy Rev. 92 (2018) 794–806.
[6] Ø. Ulleberg, R. Hancke, Int. J. Hydrogen Energy 45 (2020) 1201–1211.
[7] X. Xu, W. Hu, D. Cao, Q. Huang, W. Liu, M.Z. Jacobson, Z. Chen, J. Power Sources 451 (2020) 227810.
[8] J. Armijo, C. Philibert, Int. J. Hydrogen Energy 45 (2020) 1541–1558.
[9] C. Washburn, M. Pablo-Romero, Energy Policy 128 (2019) 212–222.
[10] A. Roth, F. Riegel, V. Batteiger, Biokerosene Status Prospect. (2017) 95–122.
[11] T.S. Moraes, H.N. Cozendey da Silva, L.P. Zotes, L.V. Mattos, L.E. Pizarro Borges, R. Farrauto, F.B. Noronha, Int. J. Hydrogen Energy 44 (2019) 21205–21219.
[12] W. Wu, B.N. Chuang, J.J. Hwang, C.K. Lin, S.B. Yang, Appl. Energy 238 (2019) 401–412.
[13] G.J. Kraaij, S. Specchia, G. Bollito, L. Mutri, D. Wails, Int. J. Hydrogen Energy 34 (2009) 4495–4499.
[14] B. Cifuentes, F. Bustamante, J.A. Conesa, L.F. Córdoba, M. Cobo, Int. J. Hydrogen Energy 43 (2018) 17216–17229.
[15] S.H. Mohd Azhar, R. Abdulla, S.A. Jambo, H. Marbawi, J.A. Gansau, A.A. Mohd Faik, K.F. Rodrigues, Biochem. Biophys. Reports 10 (2017) 52–61.
[16] J. Llorca, V.C. Corberán, N.J. Divins, R.O. Fraile, E. Taboada, Renew. Hydrog. Technol. Prod. Purification, Storage, Appl. Saf. (2013) 135–169.
[17] B. Cifuentes, F. Bustamante, M. Cobo, Catalysts 9 (2019) 852–877.
[18] U. Gardemann, M. Steffen, A. Heinzel, Int. J. Hydrogen Energy 39 (2014) 18135–18145.
[19] A.M. Lacoste, I.S. Tiscornia, A. V. Boix, Int. J. Hydrogen Energy 43 (2018) 14238–14251.
[20] R. González-Gil, C. Herrera, M.A. Larrubia, F. Mariño, M. Laborde, L.J. Alemany, Int. J. Hydrogen Energy 41 (2016) 16786–16796.

[21] B. Cifuentes, M. Hernández, S. Monsalve, M. Cobo, Appl. Catal. A Gen. 523 (2016) 283–293.
[22] B. Cifuentes, M.F. Valero, J. a. J. Conesa, M. Cobo, Catalysts 5 (2015) 1872–1896.
[23] B. Cifuentes, M. Figueredo, M. Cobo, Catalysts 7 (2017) 1–20.
[24] B. Cifuentes, F. Bustamante, D.G. Araiza, G. Diaz, M. Cobo, Appl. Catal. A, Gen. 598 (2020) 117568.
[25] N. Sanchez, R.Y. Ruiz, N. Infante, M. Cobo, Energies 10 (2017) 1–16.
[26] I. Rossetti, M. Compagnoni, M. Torli, Chem. Eng. J. 281 (2015) 1036–1044.
[27] W. Seider, J.D. Seader, D. Lewin, Product and Process Design Principles. Synthesis, Analysis, and Evaluation, 3rd ed., John Wiley & Sons, Inc, 2003.
[28] R.J. Farrauto, Chem. Eng. J. 238 (2014) 172–177.
[29] T.S. Moraes, L.E.P. Borges, R. Farrauto, F.B. Noronha, Int. J. Hydrogen Energy 43 (2018) 115–126.
[30] T. Tabakova, Front. Chem. 7 (2019) 1–43.
[31] F. Velásquez, J. Espitia, O. Mendieta, S. Escobar, J. Rodríguez, J. Food Eng. 255 (2019) 32–40.
[32] O. Mendieta, G. Madrigal, L. Castro, J. Rodríguez, H. Escalante, Bioresour. Technol. 297 (2020) 122364.
[33] W.R. Jaffé, J. Food Compos. Anal. 43 (2015) 194–202.
[34] M.M. Ordoñez Díaz, Corpoica Cienc. y Tecnol. Agropecu. 18 (2017) 379.
[35] J.E. Castañeda-Suárez, A.M. González-Dumar, C.A. Usma-Rojas, N.A. Cano-Londoño, Rev. La Fac. Ciencias 6 (2017) 107–122.
[36] R. Terán Hilares, R.M. Dionízio, S. Sánchez Muñoz, C.A. Prado, R. de Sousa Júnior, S.S. da Silva, J.C. Santos, Ultrason. Sonochem. 63 (2020) 104931.
[37] L.M. López González, I. Pereda Reyes, O. Romero Romero, Waste Manag. 68 (2017) 139–145.
[38] N. Sanchez, R.Y. Ruiz, B. Cifuentes, M. Cobo, Waste Manag. 98 (2019) 1–13.

5 Conclusions and Future Work

5.1 Conclusions

A lab scale prototype of a bioethanol fuel processor unit was developed that couples the processes of (i) bioethanol reforming to produce syngas and (ii) the CO removal from the syngas produced in the reformer.

Initially, the integrated system was evaluated using powder catalysts, focusing on selecting the most suitable catalyst to remove CO from syngas in a single catalytic unit. In this first part, the following findings associated with CO removal in a single catalytic unit were found:

- ✓ A low H_2/CO ratio (<4) in actual syngas and the presence of several species from the reformer (e.g., CH_4, H_2O and CO_2) favors a complex network of reactions, making difficult the CO removal in a single catalytic unit.

- ✓ The role of active metals during CO removal was identified: Au contributes to formation of CO* intermediates, promoting CO conversion, while Cu provides reactive oxygen on the catalytic surface, favoring CO_2 yield and preventing H_2 loss. Then, a weight ratio of Au/Cu = 1 was selected to give a balance between activity and selectivity of the catalyst.

- ✓ The support also plays a key role in CO removal: high oxygen storage capacity, high surface area, strong interaction with active metals (Au and Cu), high basicity, stable and active lattice planes, and the ability to form OH^- and CO* groups are desirable characteristics for supports used in the CO removal. Consequently, an $Au_{1.0wt\%}Cu_{1.0wt\%}$ catalyst supported on polyhedra nanoparticles of CeO_2 was selected as the most promising catalyst to carry out the CO removal from a syngas, using a single catalytic unit.

Secondly, monolith reactors were evaluated, looking for to develop a compact and economic prototype. The following outcomes in the catalytic system based on monoliths were found:

- ✓ Structured catalysts are more active in both process (i.e., syngas production and CO removal) compared to their corresponding powder samples due to low pressure drops and an enhance in the mass and heat transfer in the monoliths.

- ✓ Monoliths based on a RhPt/CeO_2-SiO_2 catalyst showed no evidence of deactivation in the reforming of actual bioethanol (i.e., obtained from sugarcane press-mud) during a long stability test (120 h), ensuring the continuous production of a syngas containing mainly H_2 (> 60%), CO and CO_2. Also, the use of residual biomass, such as sugarcane press-mud, to obtain bioethanol reduces the cost of H_2 production, achieving a cost of ~ 7 USD/kg_{H2}.

- ✓ CO removal from a syngas was assessed using structured catalysts based on AuCu/CeO_2 and AuCu/CeO_2-SiO_2. Despite being less active, AuCu/CeO_2-SiO_2 is 38% cheaper than AuCu/CeO_2 and can ensure CO conversions >90%. Likewise, both structured

catalytic systems (i.e., AuCu/CeO_2 and AuCu/CeO_2-SiO_2) allowed obtaining a syngas with H_2 >65% and CO <5%, which is adequate to use in high CO-tolerant fuel cells, such as high temperature proton-exchange membrane fuel cell.

Finally, the results obtained were used as a starting point to build a scaled prototype of a fuel processor unit to produce H_2 from actual bioethanol (i.e., obtained from residual biomass). This technology is expected to be integrated into agroindustry, specifically in the non-centrifugal sugar cane sector. Therefore, this research project is a contribution to the development of unconventional technologies in Colombia and the establishment of H_2-based technologies that use domestic resources.

5.2 Future Work

Currently, the prototype is in the laboratories of Universidad de La Sabana (Chia, Colombia). Preliminary tests were carried out using inert gas (N_2) to adjust the temperature controllers, verify the operation of the pressure sensors, and select a methodology for sampling. Therefore, the next expected step is to carry out continuous and on/off cycle stability tests for long operation periods (> 200 h), using bioethanol obtained from several sources of residual biomass.

The prototype will be coupled to a high CO-tolerant H_2-FC. Currently, commercial HT-PEMFC options are being evaluated, such as those offered by Serenergy (serenergy.com). However, the future development of local H_2-FC devices should not be ruled out in order to reduce technology import costs and to have independence in equipment maintenance. Furthermore, it is expected that the coupled system (i.e., B-FPU connected to H_2-FC) will be evaluated in long stability tests (> 300 h).

It is expected that the prototype will be taken to a *Trapiche* located in Villeta (Colombia) and coupled to the *Panela* production process, to collect information on the operation of the system on site to identify opportunities for improvement, which could be necessary to develop of a more robust technology based on the prototype developed in this research.

The energy integration of the prototype could also be considered prior to the establishment of the technology. Previous works on traditional B-FPU has suggested that the outlet stream of the ethanol reformer could be used to supply energy to heat the liquid bioethanol. For this, it would be also necessary to carry out a rigorous simulation of the prototype. Consequently, apparent kinetic models obtained from experimental data for both processes (i) syngas production on a RhPt/CeO_2-SiO_2 catalyst (Table 4.2.3) and (ii) the CO removal from a syngas on AuCu/CeO_2-SiO_2 catalyst (Table 4.2.5) could be used as a starting point for energy integration in the B-FPU.

This technology seeks to reduce the negative impacts of the agroindustry on the environment and the health of the communities. Consequently, results of the developed B-FPU in this research are being used to carry out a life cycle analysis of the process, looking for to determine the effectiveness of the technology to reduce CO_2 emissions and harmful emissions in the *Panela* production in Colombia.

Finally, it was suggested in this document that removal of CO from a syngas using a single catalytic unit could be a promising strategy to reduce the cost of B-FPU. Also, the preliminary economic analysis described above was based on actual data obtained during

the building of the prototype, focusing only on the B-FPU. However, thinking about the scaling up of the technology, a detailed economic analysis should be carried out, including information on the other stages involved in the technology (e.g., obtaining and pretreatment of raw materials, fermentation process, production of electricity in the H_2-FC and adaptation of the device in the *Trapiche*) and considering also the energy integration of the process.

6 Supplementary Material

6.1 Figures

6.1.1 Figures for Chapter 2 - Section 1

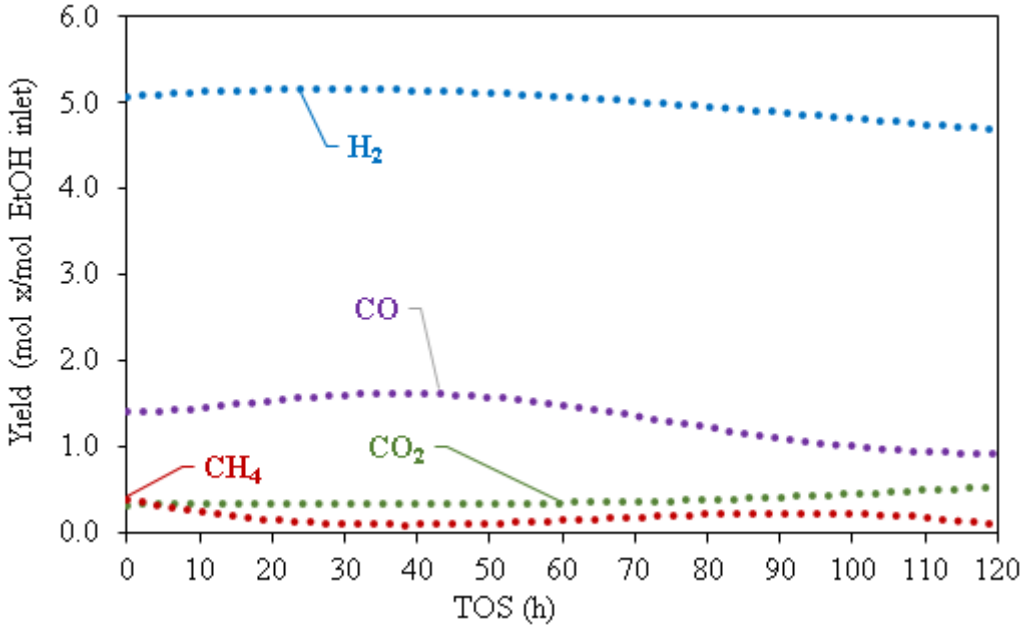

Figure SM.1. Stability during the steam reforming of ethanol over Rh-Pt/CeO_2-SiO_2 catalyst: product distribution of H_2, CO, CO_2, and CH_4 as a function of time-on-stream (TOS) on RhPt/CeO_2-SiO_2. Reaction conditions: 6.4 ± 0.2 $L*g_{cat}{}^{-1}*min^{-1}$ of SV, 50 mg of catalyst and 250 mg of inert quartz, feed was ethanol, water, and Ar with 1.8, 5.4, and 92.8 % molar, respectively.

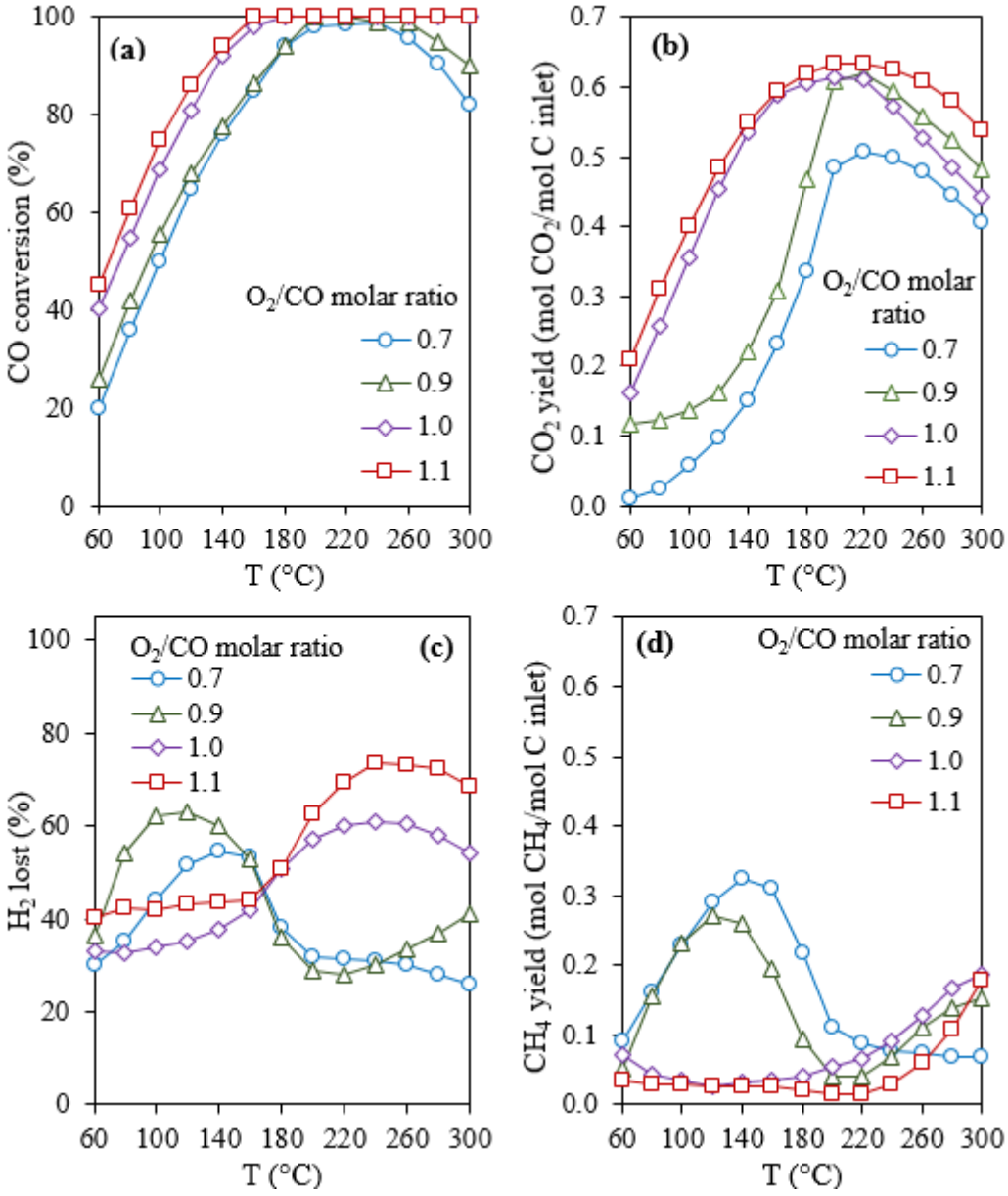

Figure SM.2. Evaluation of the effect of the inlet O_2/CO molar ratio on the CO removal: (a) CO conversion, (b) CO_2 yield, (c) H_2 conversion, and (d) CH_4 yield in the CO removal of a post-reforming stream on 1.0%Au-1.0%Cu/CeO_2 catalyst with different O_2/CO molar ratios (0.7, 0.9, 1.0, and 1.1). Reaction conditions: 8.5% H_2, 2.2% CO, 0.6% CO_2, 0.3% CH_4, 1.5% H_2O, and 86.9% Ar. A SV of 6.5 ± 0.2 $L^*g_{cat}^{-1}*min^{-1}$, 50 mg of catalyst and 250 mg of inert quartz.

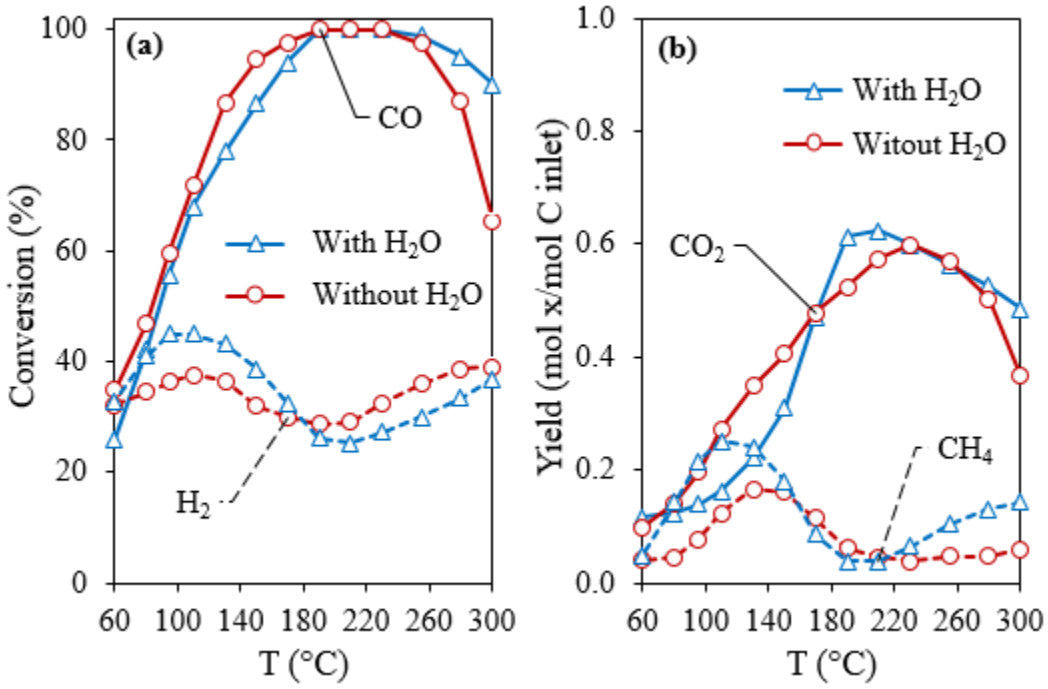

Figure SM.3. Effect of water presence on (a) CO and H_2 conversion, (b) CO_2 and CH_4 yield in the CO removal of a post-reforming stream on $Au_{1.0}Cu_{1.0}/Ce$ catalyst. Reaction conditions: A SV of 6.5 ± 0.2 $L*g_{cat}^{-1}*min^{-1}$, 50 mg of catalyst and 250 mg of inert quartz.

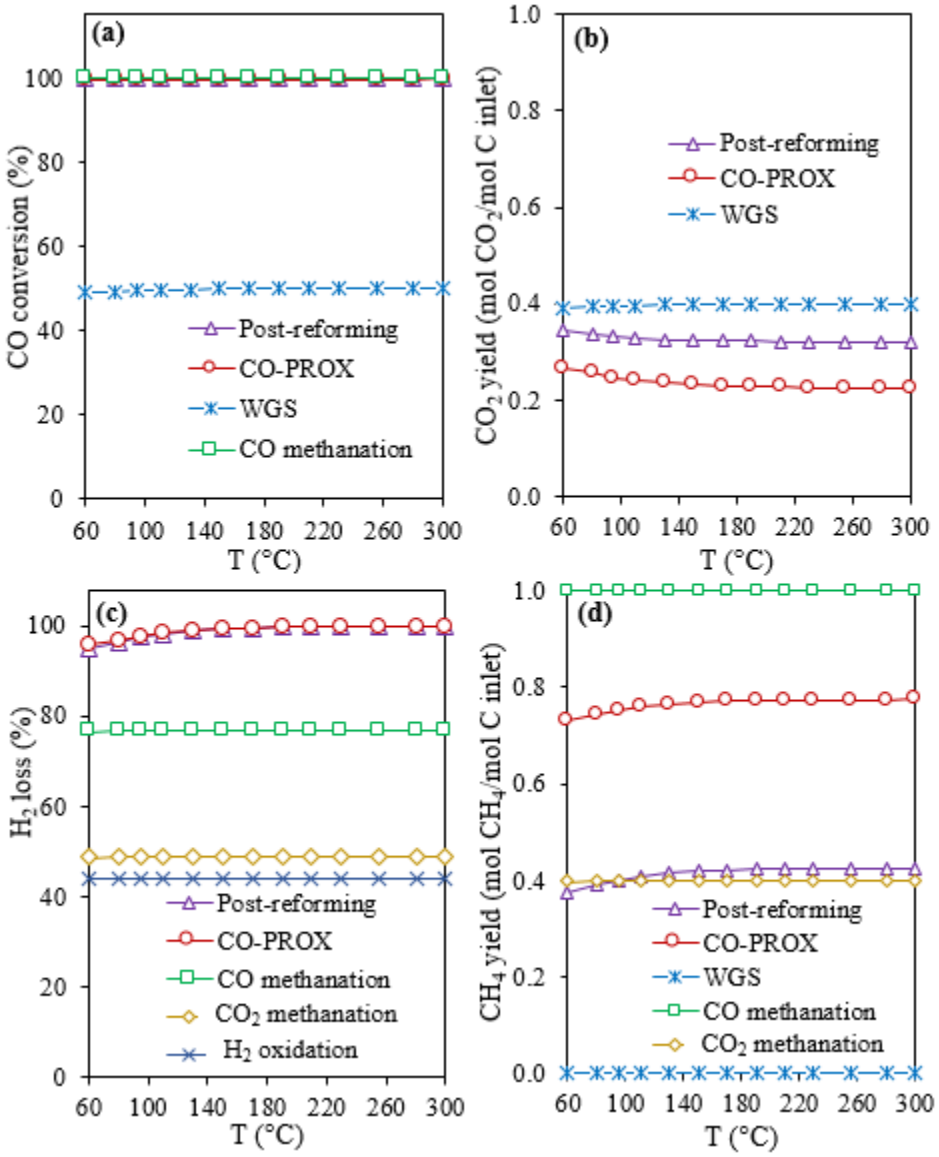

Figure SM.4. Thermodynamic equilibrium calculations for the main CO-removal reactions on (a) CO conversion, (b) CO_2 yield, (c) H_2 lost, and (d) CH_4 yield. Data were obtained using a Gibbs reactor in Aspen Plus V9.0 (Aspen Tech, Burlington, MA, USA, 2016). The inlet of reactor was the feed composition describe in Table SM.1. Thermodynamic method = NRTL-SK.

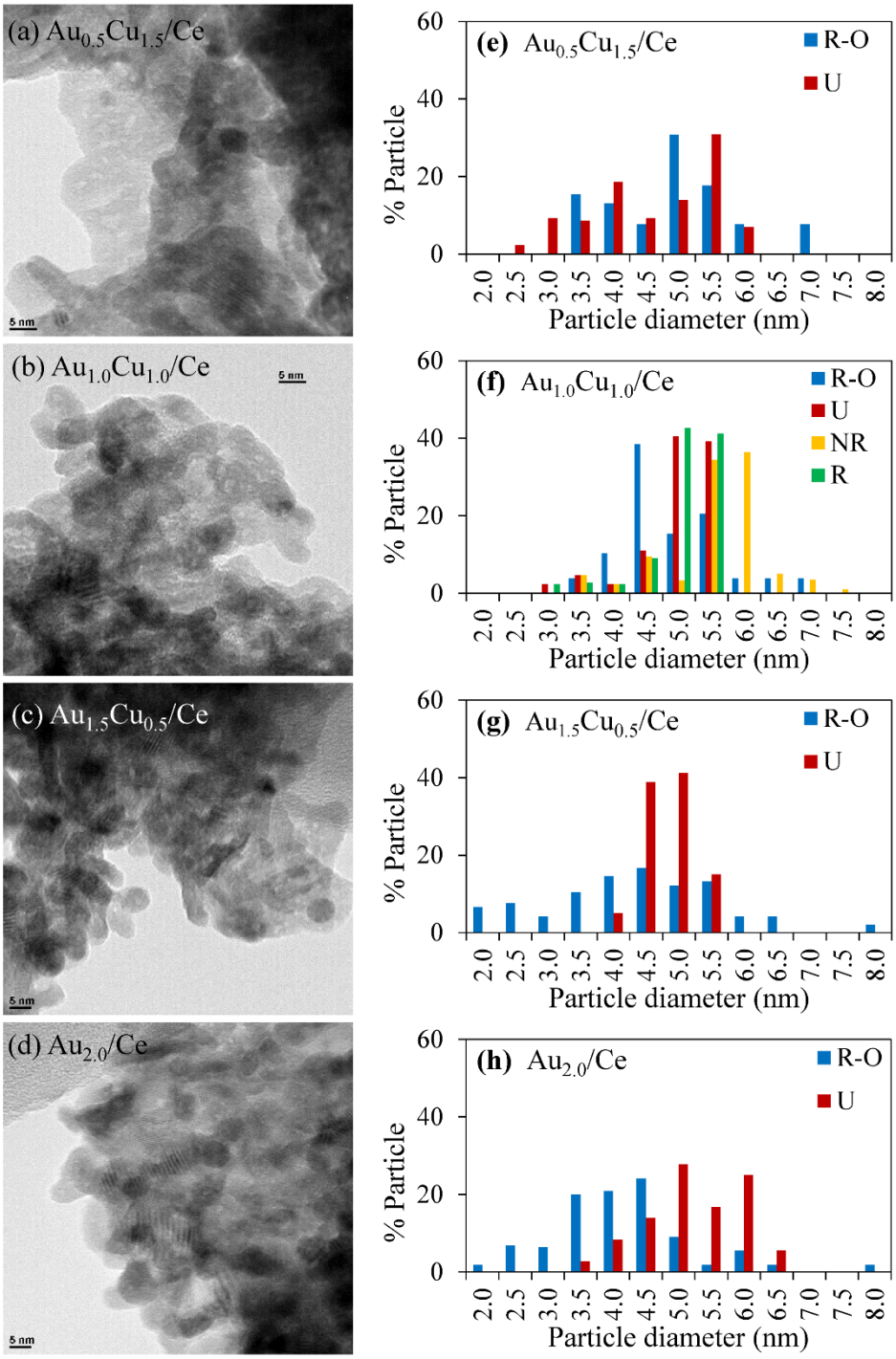

Figure SM.5. TEM images of reduced-oxidized (a) $Au_{0.5}Cu_{1.5}/Ce$, (b) $Au_{1.0}Cu_{1.0}/Ce$, (c) $Au_{1.5}Cu_{0.5}/Ce$ and (d) $Au_{2.0}/Ce$ catalysts, and (e-h) particle size distribution histograms for reduced-oxidized and used $AuCu/CeO_2$ catalysts.

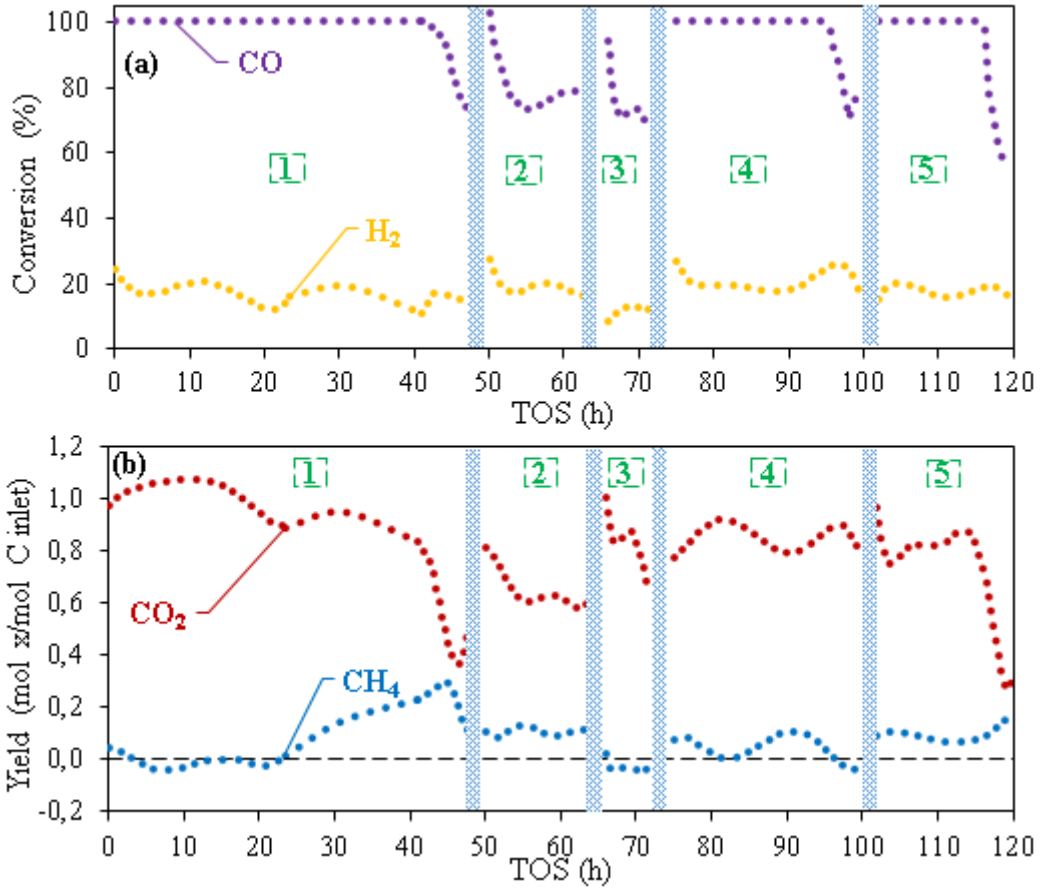

Figure SM.6. Reactivation treatments for Au-Cu/CeO_2 catalysts during the CO-removal of a post-reforming stream: (a) CO and H_2 conversion, (b) CO_2 and CH_4 yield as a function of time-of-stream, with several reactivation treatments, in the CO removal of a post-reforming stream on 1.0%Au-1.0%Cu/CeO_2 catalyst. Reaction conditions: 8.1% H_2, 2.1% CO, 0.6% CO_2, 0.3% CH_4, 1.4% H_2O, 83.1% Ar, 1.3% O_2, and 3.1% N_2. A SV of 6.5 ± 2 $L*g_{cat}^{-1}*min^{-1}$, 50 mg of catalyst and 250 mg of inert quartz. Vertical lines show reactivation treatments described in Table SM.1.

6.1.2 Figures for Chapter 2 - Section 2

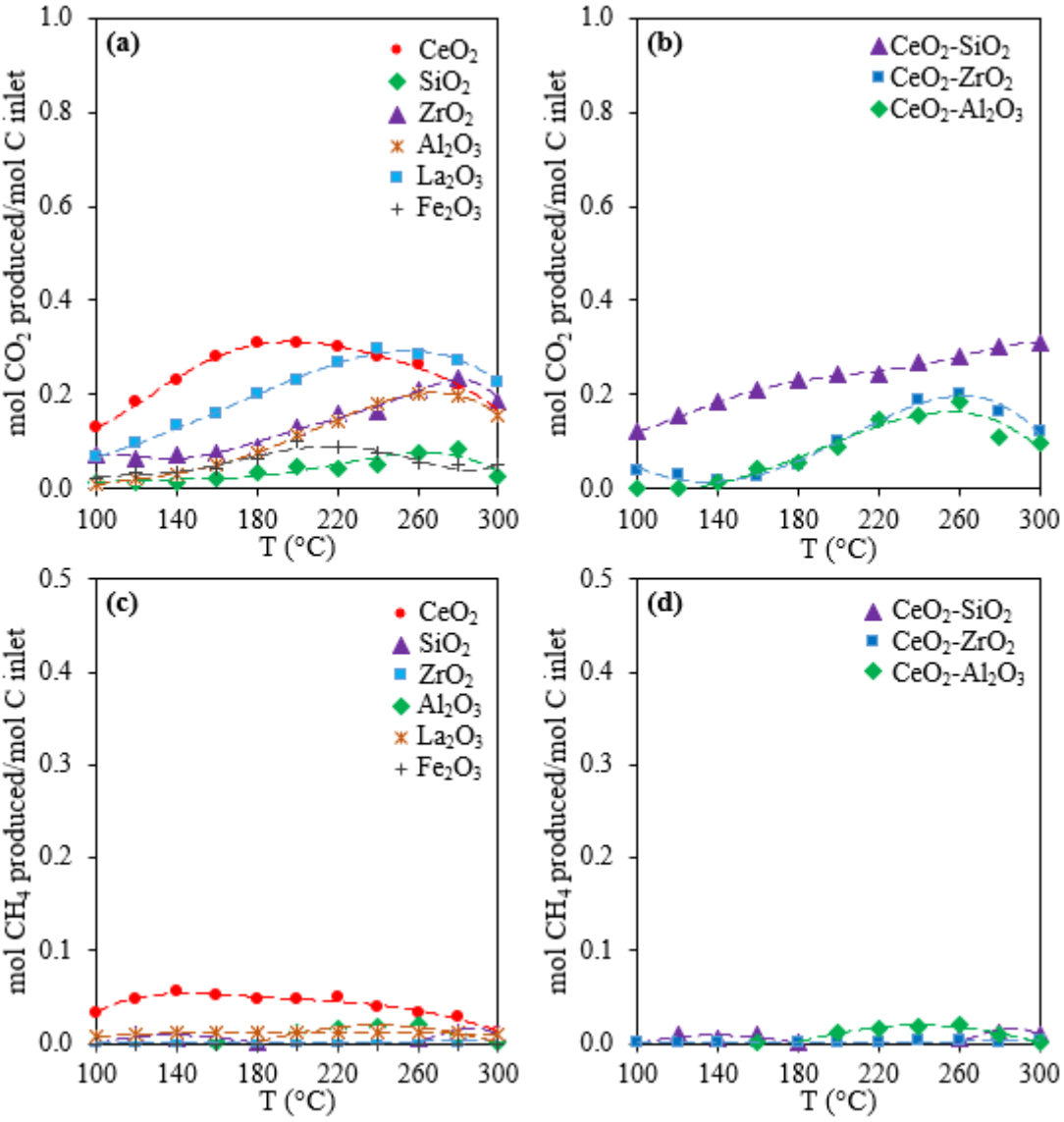

Figure SM.7. (a and b) CO_2 and CH_4 (c and d) production in the CO-Cleanup reactor with simple and dual supports. Syngas composition: 8.4% H_2, 2.2% CO, 0.6% CO_2, 0.3% CH_4, 1.6% H_2O and Ar. λ=1.8. Reaction conditions: SV=6.5 $\pm$ 0.2 Lg_{cat}-1min^{-1}; 0.050 g of catalyst and 0.250 g of inert quartz.

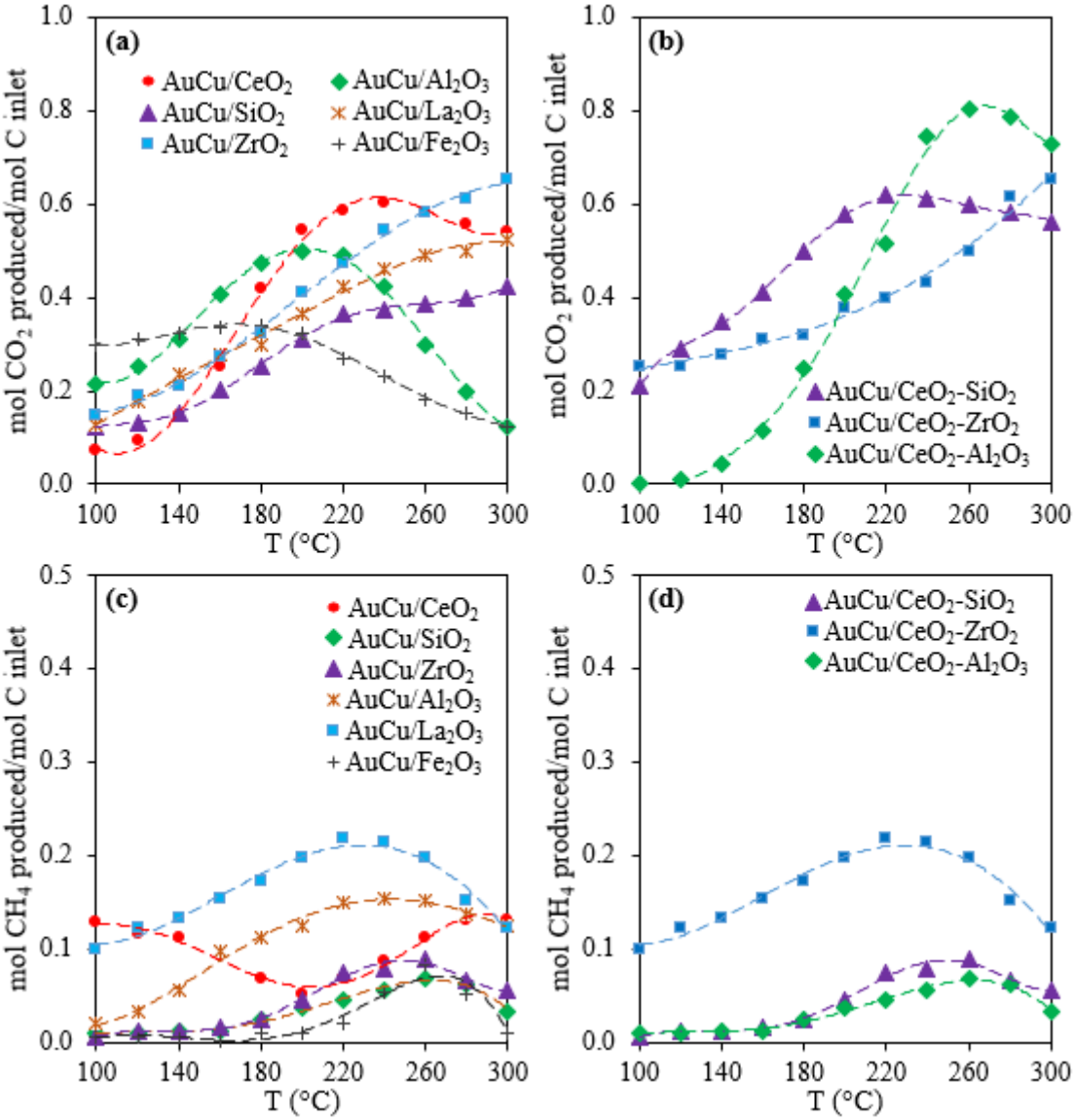

Figure SM.8. (a and b) CO_2 and CH_4 (c and d) production in the CO-Cleanup reactor with Au-Cu catalysts supported on simple and dual supports. Syngas composition: 8.4% H_2, 2.2% CO, 0.6% CO_2, 0.3% CH_4, 1.6% H_2O and Ar. λ=1.8. Reaction conditions: SV=6.5 ± 0.2 $Lg_{cat}^{-1}min^{-1}$; 0.050 g of catalyst and 0.250 g of inert quartz.

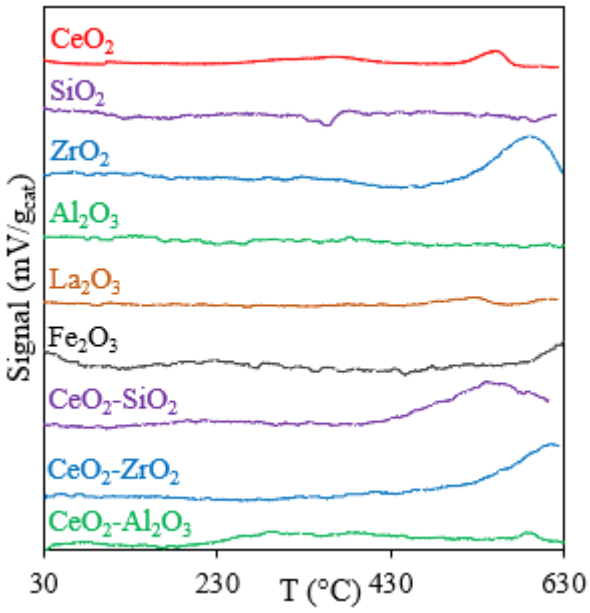

Figure SM.9. H_2-TPR profiles of bare supports evaluated in the CO-removal from an actual syngas.

6.1.3 Figures for Chapter 2 - Section 3

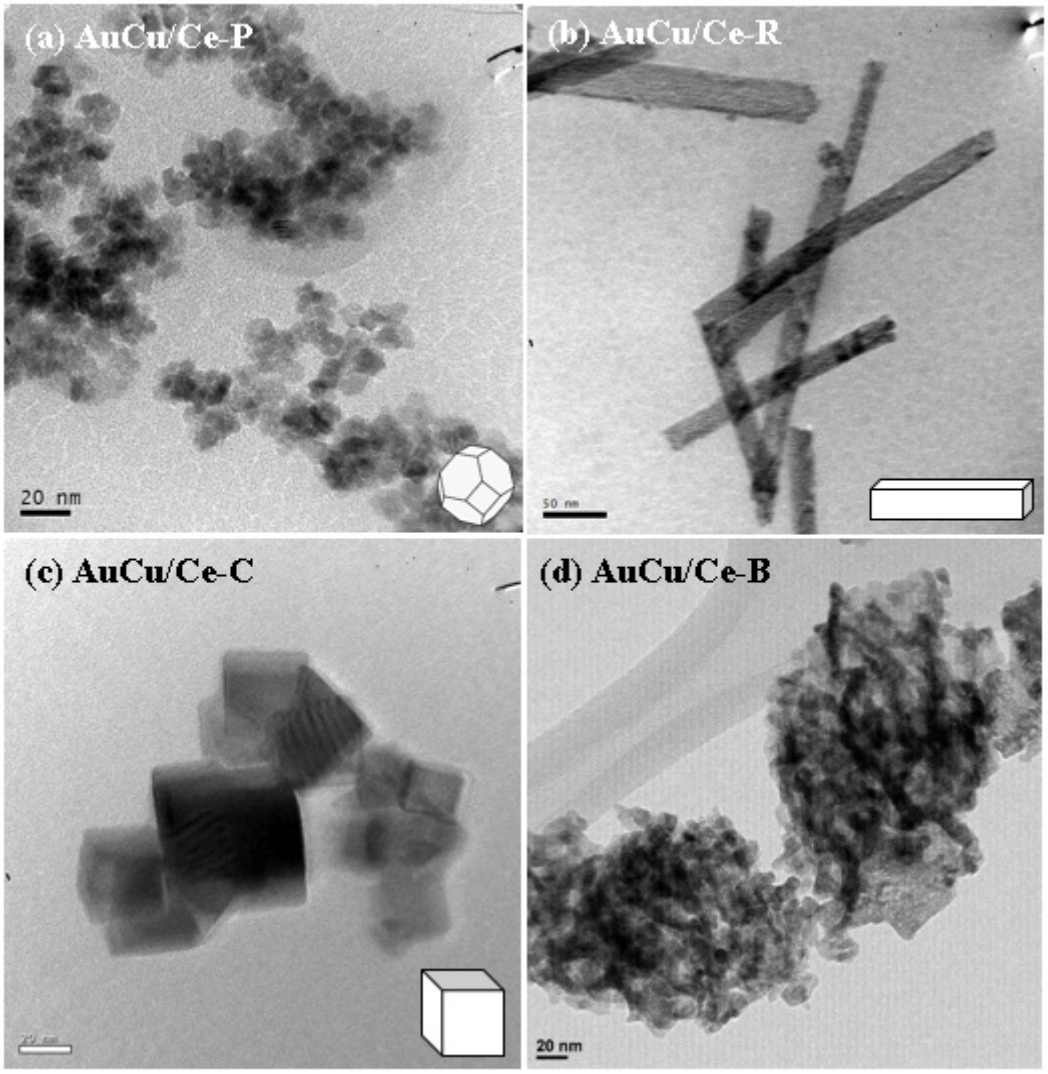

Figure SM.10. TEM micrographs of CeO_2 supports with different morphology. Suffix corresponds to the type of nano-shaped CeO_2: polyhedra (P), rods (R), cubes (C) and blank (B).

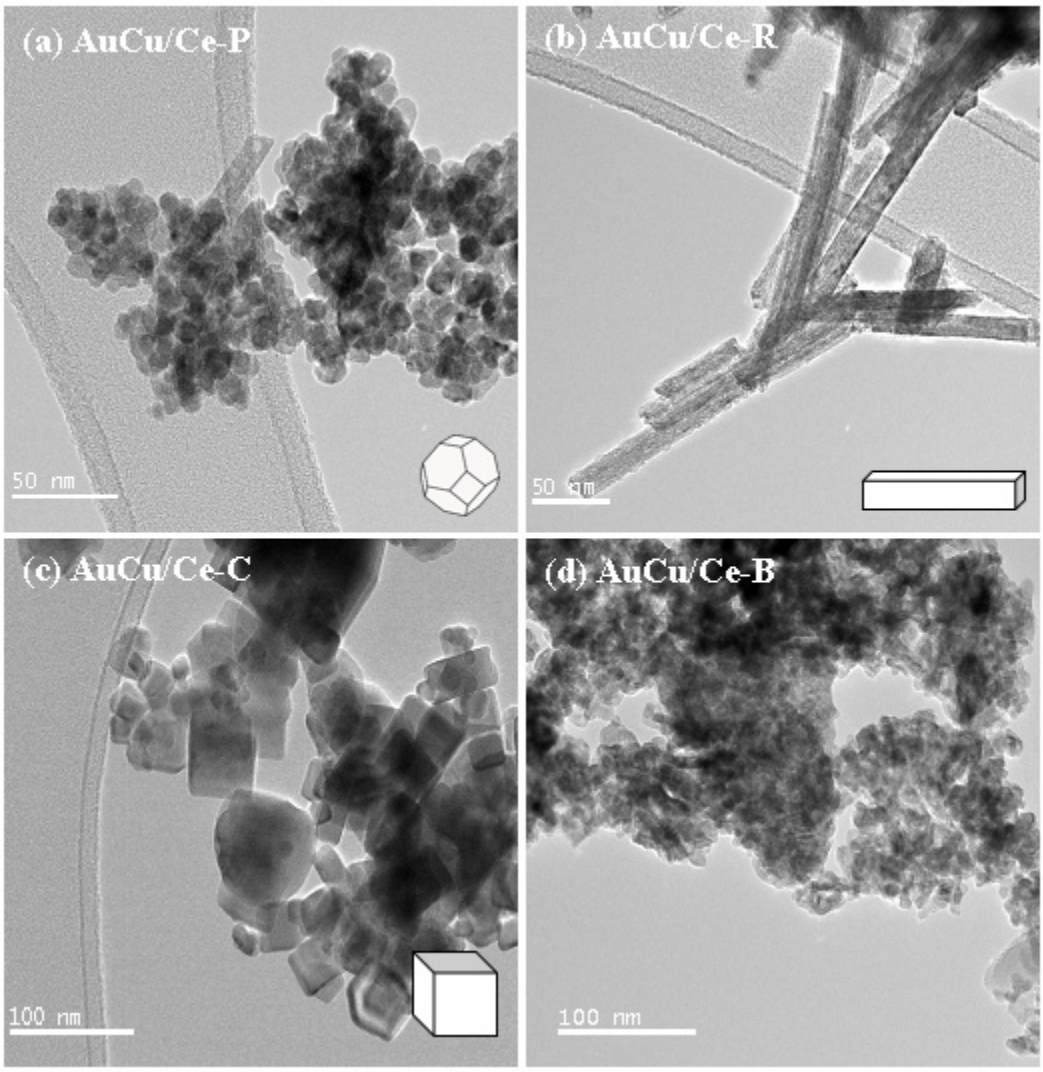

Figure SM.11. TEM micrographs of activated 1wt%Au-1wt%Cu/CeO_2 catalysts with different CeO_2 morphology. Suffix corresponds to the type of nano-shaped CeO_2: polyhedra (P), rods (R), cubes (C) and blank (B).

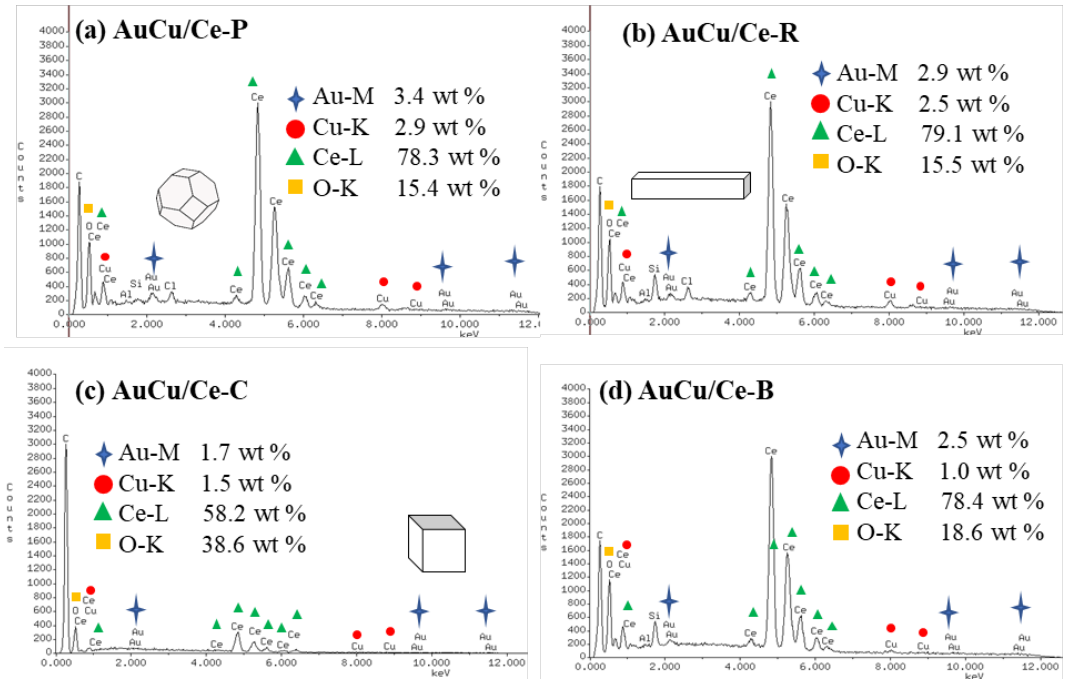

Figure SM.12. EDS spectra of activated 1wt%Au-1wt%Cu/CeO_2 catalysts with different CeO_2 morphology. Suffix corresponds to the type of nano-shaped CeO_2: polyhedra (P), rods (R), cubes (C) and blank (B).

6.1.4 Figures for Chapter 3 - Section 1

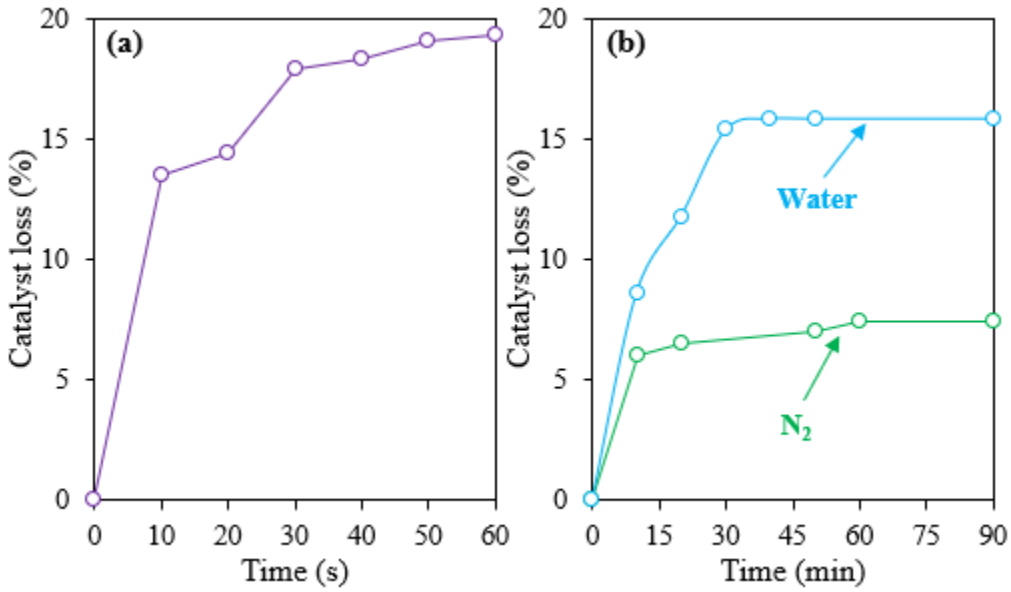

Figure SM.13. Stability of $RhPt/CeO_2$-SiO_2 coating on a monolith with a 0.12 g_{cat}/cm^3 washcoated loading evaluated by (a) ultrasonic (pulses of 10 s with amplitude of 40 %) and (b) controlled atmospheres of water (1.3 L/min) and N_2 (2 L/min).

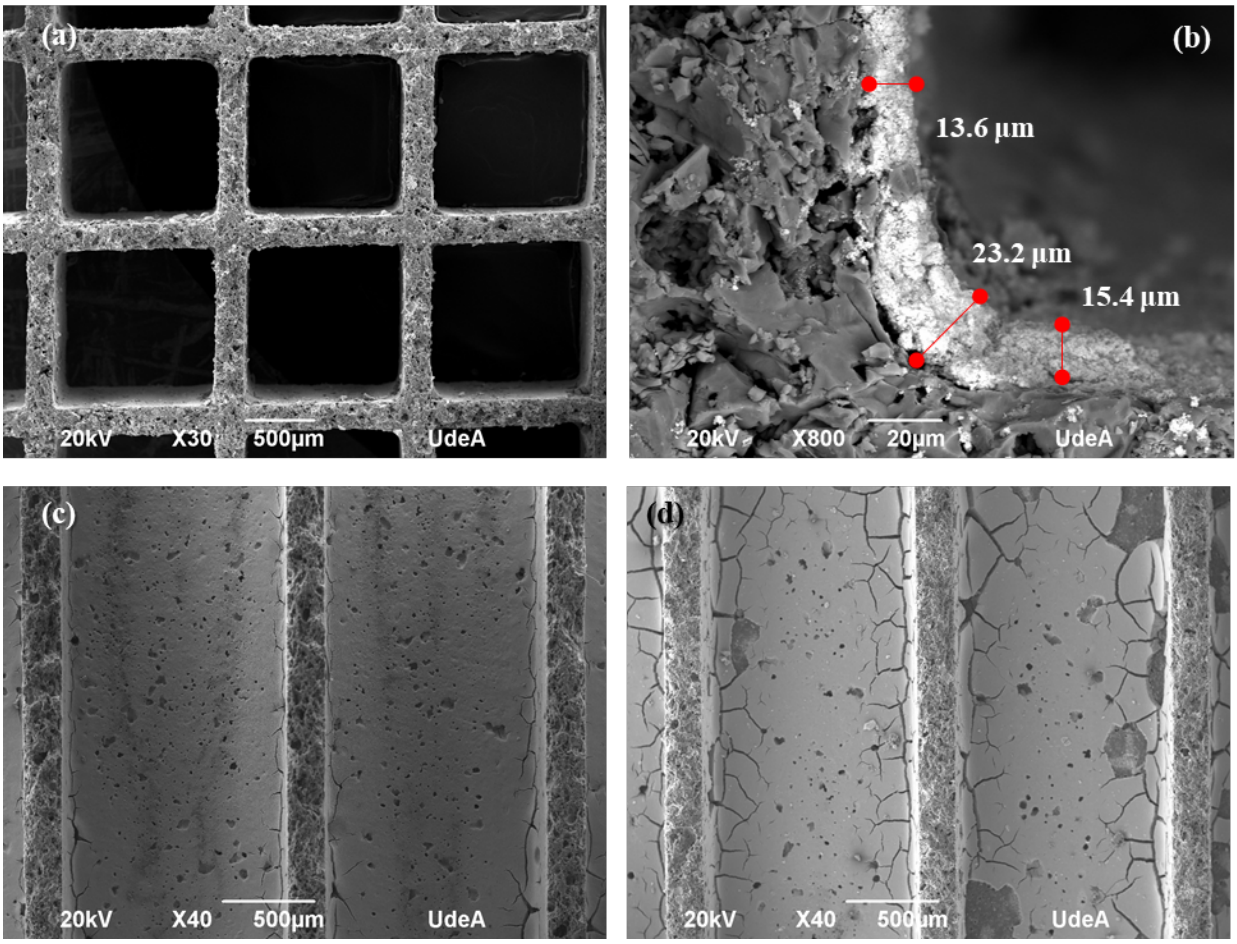

Figure SM.14. SEM micrographs for monolith with a 0.12 g_{cat}/cm^3 washcoated loading: (a) fresh monolith channels, (b) fresh monolith walls, (c) fresh wash-coating thickness and (d) spent monolith walls in stability test with synthetic bioethanol. Images were obtained in a JSM 6490LV microscope (Jeol Geo Solutions, USA). Previously, samples were coated with gold using a sputter coating machine.

6.1.5 Figures for Chapter 3 - Section 2

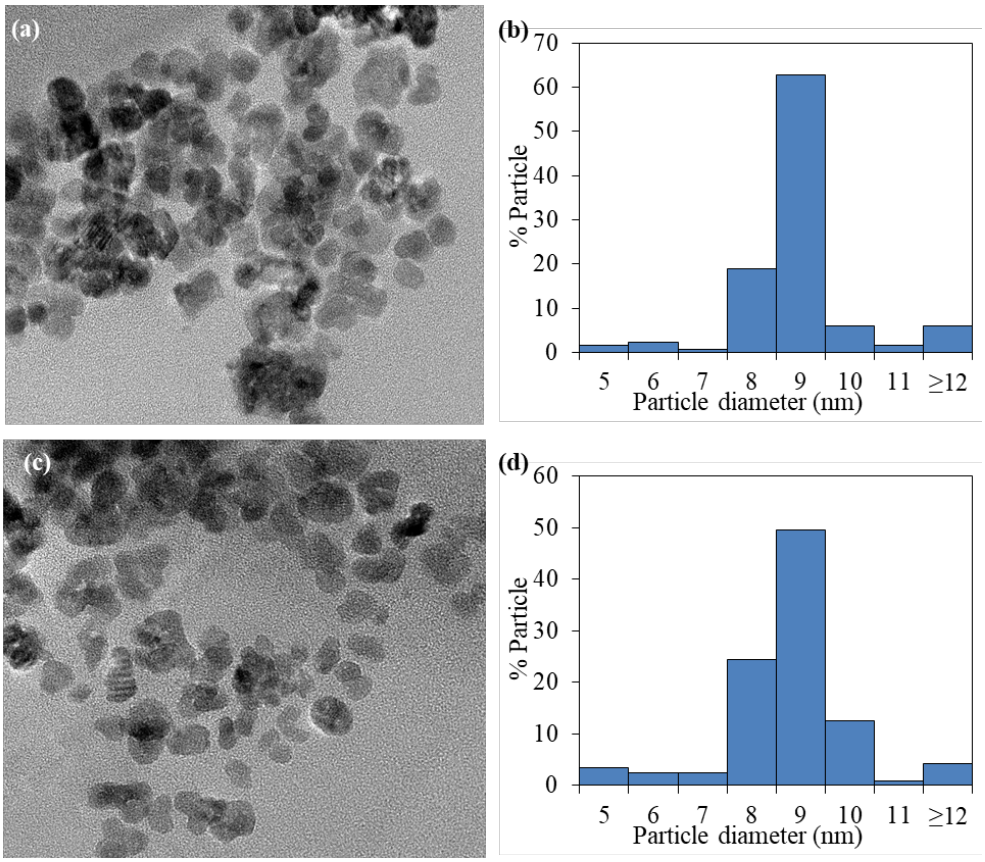

Figure SM.15. HRTEM micrographs and particle size distribution histograms for CeO_2 bare support before (a and b) and after (c and d) calcination at 500 °C for 2 h.

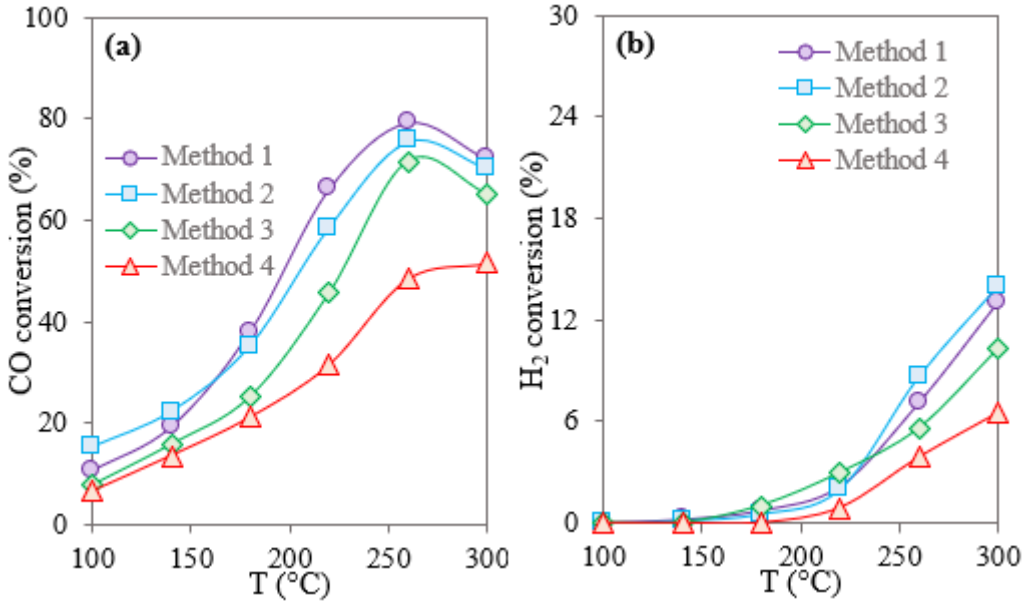

Figure SM.16. Conversion of (a) CO and (b) H_2 in the CO removal from a syngas over several catalysts of $AuCu/CeO_2$-SiO_2 (SiO_2 percent content of 50 mol% was fixed in all samples) prepared by methods described in Table S-1. Syngas feed: H_2 (19.9±0.3 mol%), CO (6.3±0.1 mol%), CO_2 (5.2±0.5 mol%), O_2 (5.6±0.3 mol%), H_2O (7.8±0.2 mol%) and N_2 (55.2±0.6 mol%). Reaction conditions: SV of 5.6 ± 0.3 L/g_{cat}*min and 0.35 g of the catalytic bed.

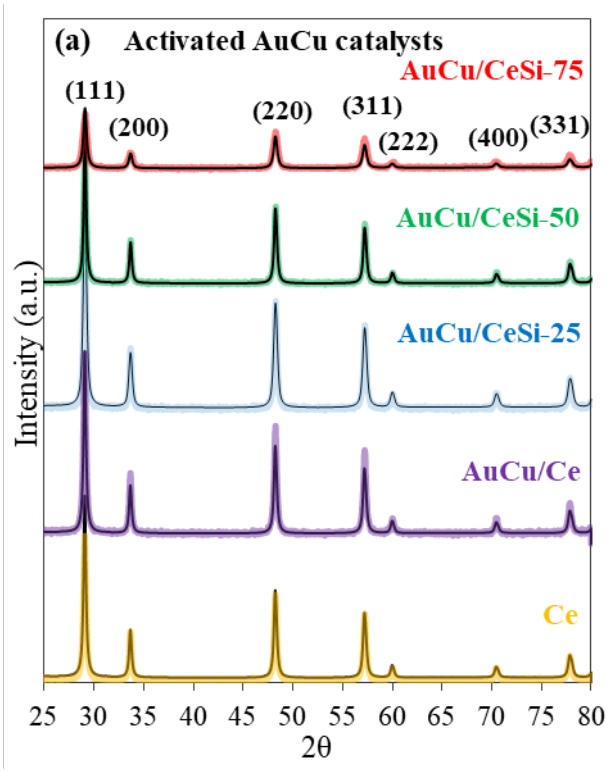

Figure SM.17. XRD profiles of CeO_2 for activated samples of AuCu catalysts. CeO_2-SiO_2 supports were labeled as CeSi-X, where X indicates the SiO2 percent content (X = 0, 25, 50 and 75 mol% of SiO_2).

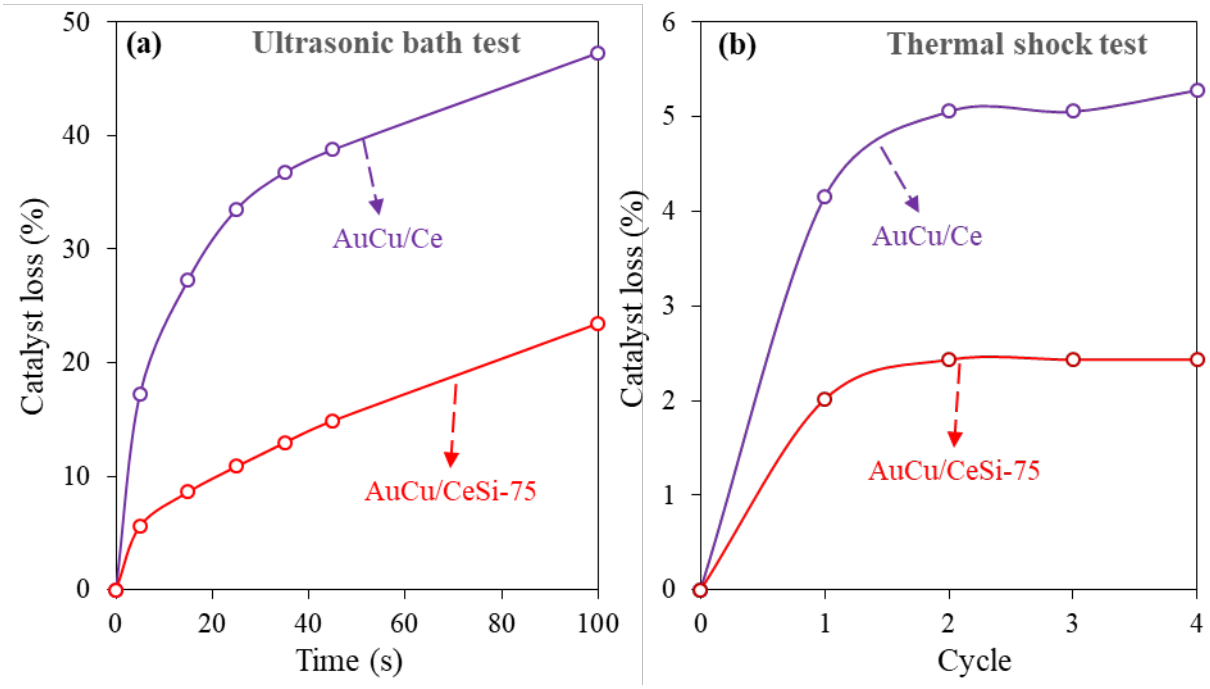

Figure SM.18. Percentage of catalyst weight loss in the stability tests of the monolith coating by (a) ultrasound and (b) thermal shock.

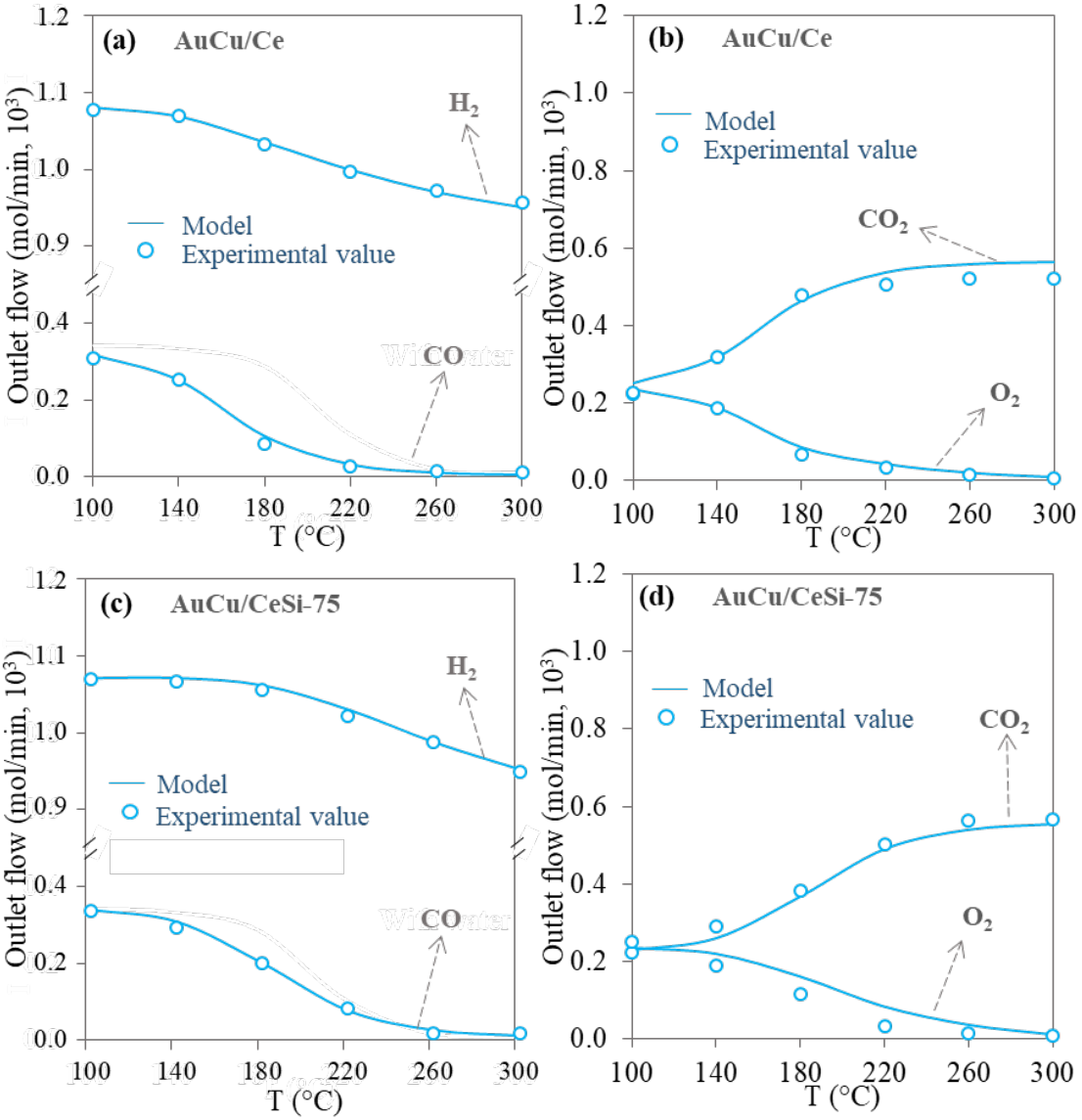

Figure SM.19. CFD-predicted and experimental values for the molar flow of CO, H_2, CO_2 and O_2 in the outlet stream of reactor monoliths washcoated with (a and b) AuCu/Ce and (c and d) AuCu/CeSi-75 catalysts. CFD model was carried out in COMSOL Multiphysics software (5.5 version).

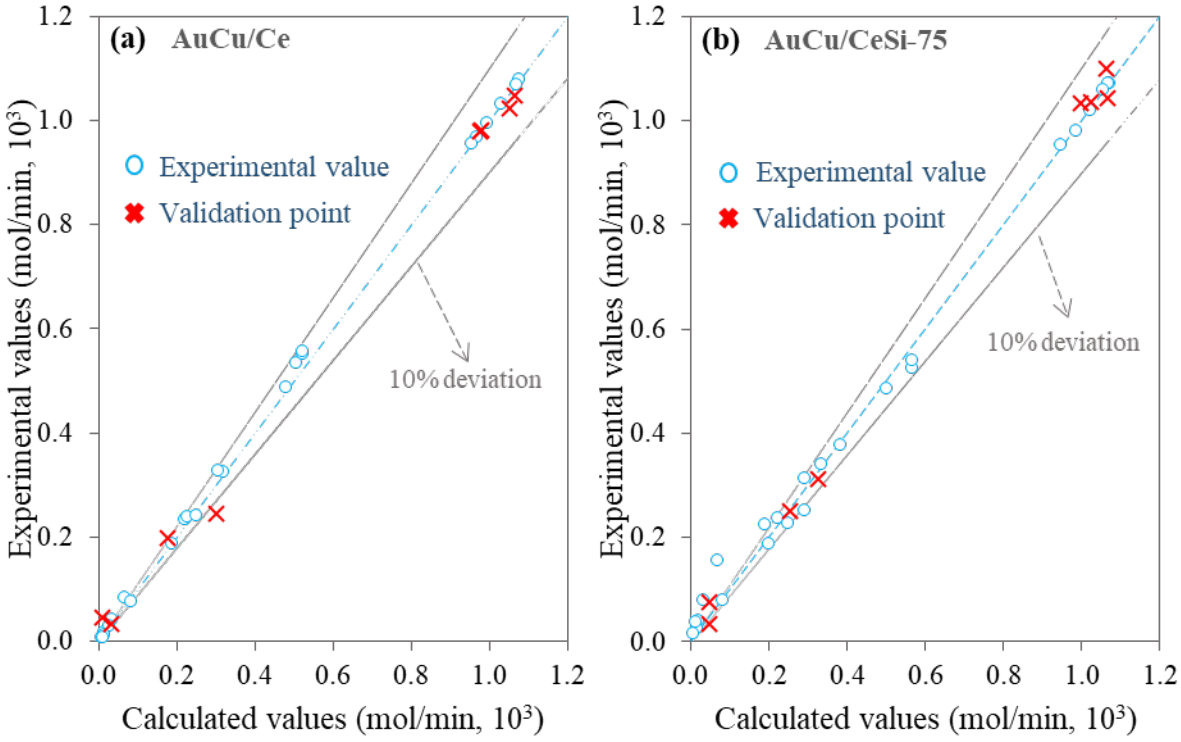

Figure SM.20. Parity plots for the reactor monoliths washcoated with (a) AuCu/Ce and (b) AuCu/CeSi-75 catalysts. CFD model was carried out in COMSOL Multiphysics software (5.5 version). Two types of experimental data are included: data used to perform the non-linear regression of the CFD model ("experimental value") and data used to confirm the effectiveness of the model to predict fluxes ("validation point").

6.1.6 Figures for Chapter 4

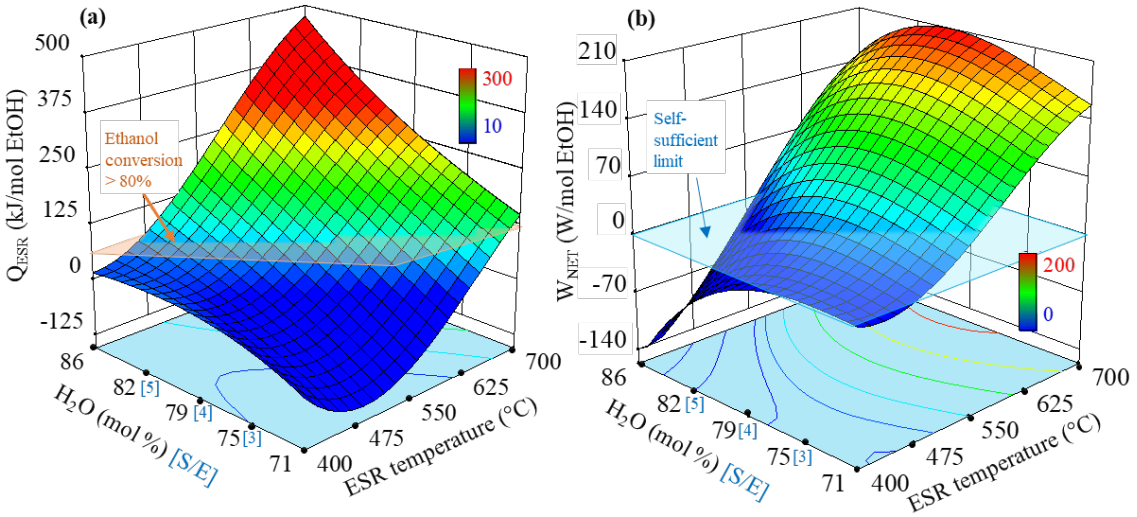

Figure SM.21. (a) Changes in enthalpy during the ESR and (b) net power production of the system presented in Figure SM.22. Response surface: Cubic model, R^2 >0.85, Adjusted R^2 >0.85 and Lack of Fit >>3 (non-significant). RhPt/CeO_2-SiO_2 catalysts were evaluated with actual bioethanol (i.e., obtained from fermentation of glucose patrons) with different S/E ratios (i.e., 3, 4, and 5). The results of catalytic tests were used to carry out an energy analysis of a B-FPU, using the methodology described in[a]. The energy balances obtained from the simulated B-FPU were used to make response surfaces in the Design Expert ® software (11 version, USA).

[a]Cifuentes, M. Figueredo, M. Cobo, Catalysts 7 (2017) 1–20

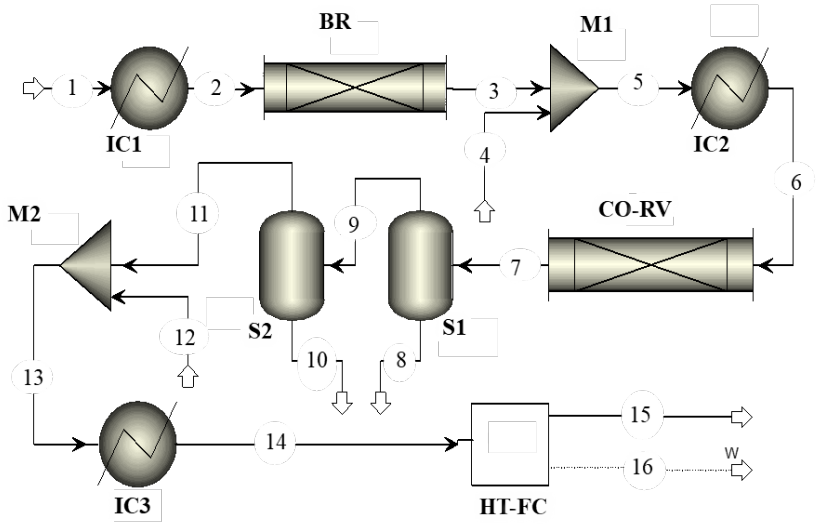

Figure SM.22. Bioethanol fuel processor unit simulated in Aspen Plus (11 version, USA). IC: heat exchanger, BR: bioethanol reformer, M: mixer, CO-RV: unit to CO removal, S: separator to remove H_2O or CO_2, HT-FC: high temperature fuel cell unit.

6.2 Tables

6.2.1 Tables for Chapter 2 - Section 1

Table SM.1. Reaction conditions to evaluate the contribution of the main reactions involved in CO removal

Reaction	Feed composition (mol %)	Catalysts amount (mg of $Au_{1.0}Cu_{1.0}/CeO_2$)	GHSV (h^{-1})
WGSR	CO (2.0), H_2O (1.0), and Ar (97.0)	50.1	63,335
CO-PROX	CO (2.0), H_2 (7.8), O_2 (1.8), N_2 (6.8), and Ar (81.6)	49.9	63,495
CO methanation	CO (2.0), H_2 (7.8), and Ar (90.2)	50.0	63,547
CO_2 methanation	CO_2 (1.0), H_2 (8.2), and Ar (90.8)	49.8	63,512
H_2 oxidation	H_2 (8.2), O_2 (1.8), N_2 (8.0), and Ar (82.0)	50.0	63,526
Post-reforming	H_2 (7.8), O_2 (1.8), N_2 (6.8), CO (2.0), CO_2 (0.5), CH_4 (0.3), and Ar (79.4)	50.1	63,498

Table SM.2. Reactivation treatment for $Au_{1.0}Cu_{1.0}/CeO_2$ catalyst.

Intervals	Conditions	TOS (h)	Carbon balance (%)
1	Catalyst treatment: spent catalyst was *in situ* reduced-oxidized under the same conditions used for catalyst activation. Post-reforming stream treatment: none	49	100 ± 9
2	Catalyst treatment: spent catalyst was *in situ* reduced with 8 mol% H_2/Ar (300 mL/min) at 300 °C for 1 h, degassed with Ar at 300 °C for 30 min, and stabilized with 10% air/Ar (300 mL/min) at 300 °C for 30 min. Post-reforming stream treatment: water was removed by condensation.	14	91 ± 4
3	Catalyst treatment: spent catalyst was *in situ* reduced with 8 mol% H_2/Ar (300 mL/min) at 300 °C for 1 h, degassed in Ar at 300 °C for 30 min, and stabilized in 10% air/Ar (300 mL/min) at 300 °C for 30 min. Post-reforming stream treatment: none	6	96 ± 5
4	Catalyst treatment: spent catalyst was reduced *in-situ* with 8 mol% H_2/Ar (300 mL/min) at 300 °C for 1 h and degassed in Ar at 300 °C for 30 min. Post-reforming stream treatment: none	28	94 ± 8
5	Catalyst treatment: spent catalyst was reduced *in situ* with 8 mol% H_2/Ar (300 mL/min) at 300 °C for 1 h and degassed in Ar at 300 °C for 30 min. Post-reforming stream treatment: none	18	90 ± 5

Table SM.3. Results of regression analysis and ANOVA for model of the experimental data for activity and yield of $AuCu/CeO_2$ catalysts in CO-removal of post-reforming stream.

Variable* /Parameter	Factors for mathematical model			
	CO conversion (%)	H_2 loss (%)	CO_2 yield (mol CO_2/mol C inlet)	CH_4 yield (mol CH_4/mol C inlet)
	-7.3.E+01	-4.3.E+01	1.8.E-01	-2.5.E-01
T	1.2.E+00	8.9.E-01	-8.1.E-03	4.5.E-03
C	6.3.E+01	2.9.E+01	9.0.E-02	6.5.E-02
T*C	3.3.E-02	-2.7.E-01	-1.5.E-03	3.4.E-04
T^2	-3.7.E-04	-2.4.E-03	1.3.E-04	-1.9.E-05
C^2	-6.7.E+01	1.1.E+02	-2.1.E-01	1.5.E-01
T^2*C	-2.7.E-03	-5.8.E-04	2.3.E-06	-1.8.E-05
T*C^2	2.3.E-01	-3.0.E-01	-4.7.E-04	3.0.E-03
T^3	-7.2.E-06	-2.5.E-06	-5.4.E-07	1.4.E-08
C^3	3.4.E+01	-1.2.E+02	3.2.E-01	-3.1.E-01
T^2*C^2	-2.3.E-04	-1.2.E-03	-1.2.E-06	-6.6.E-06
T^3*C	6.6.E-06	5.6.E-06	1.1.E-08	5.2.E-08
T*C^3	-4.2.E-02	5.9.E-01	1.5.E-04	-1.1.E-04
T^4	3.6.E-09	1.1.E-08	6.5.E-10	2.5.E-11
C^4	-6.4.E+00	2.8.E+01	-9.2.E-02	7.7.E-02
Model	Quartic	Quartic	Quartic	Quartic
F-value	234.15	23.21	79.76	22.91
Prop. F	< 0.0001	< 0.0001	< 0.0001	< 0.0001
Std. deviation	3.69	3.57	0.041	0.033
Mean	77.98	34.12	0.42	0.11
R^2	0.98	0.87	0.96	0.86
Adjusted R^2	0.98	0.83	0.94	0.82
predicted R^2	0.96	0.75	0.91	0.71
Adeq. precision	60.72	26.18	32.35	19.68
Lack of Fit	54	56	56	54

Quartic model

$$Response = F_0 + F_i \times T + F_i \times C + F_i \times T \times C + F_i \times T^2 + F_i \times C^2 + F_i \times T^2 \times C + F_i \times T \times C^2 + F_i \times T^3 + F_i \times C^3 + F_i \times T^2 \times C^2 + F_i \times T^3 \times C + F_i \times T \times C^3 + F_i \times T^4 + F_i \times C^4$$

where T = Temperature (°C), C = Au content (% wt.), and F_i are factors listed above

6.2.2 Tables for Chapter 2 - Section 2

Table SM.4. Revised papers for the selection of supports evaluated in the CO-removal.

Date	Active metals	Support I	Support II	Journal	DOI
2012	CuO	Fe_2O_3	-	Chemical Engineering Journal	10.1016/j.cej.2012.01.017
2012	Pt	Other	-	Electrochimica Acta	10.1016/j.electacta.2012.04.150
2012	-	Fe_2O_3	-	Applied Surface Science	10.1016/j.apsusc.2011.10.092
2012	-	NiO_2	-	Journal of Molecular Catalysis A: Chemical	10.1016/j.molcata.2012.05.001
2013	Ni, Co	Co_3O_4	-	Journal of Alloys and Compounds	10.1016/j.jallcom.2013.04.053
2013	CuO	TiO_2	Al_2O_3	Surface and Coatings Technology	10.1016/j.surfcoat.2012.10.031
2013	Co	Fe_2O_3	-	Chemical Engineering Journal	10.1016/j.ces.2013.02.002
2014	Co	MgO	-	Process Safety and Environmental Protection	10.1016/j.psep.2013.12.003
2014	Pt	CeO_2	-	Chemical Engineering Journal	10.1016/j.cej.2014.06.058
2014	Pd	Fe_2O_3	-	Journal of Catalysis	10.1016/j.jcat.2014.06.019
2014	Ag	Zeolite	-	Fuel	10.1016/j.fuel.2014.07.011
2014	Au	NiO_2	-	Applied Catalysis A: General	10.1016/j.apcata.2014.02.003
2014	CuO	SiO_2	CeO_2	Journal of Environmental Chemical Engineering	10.1016/j.jece.2014.03.021
2015	Co, Fe, Cr	CeO_2	-	International Journal of Hydrogen Energy	10.1016/j.ijhydene.2015.03.044
2015	-	Co_3O_4	-	Applied Catalysis A: General	10.1016/j.apcata.2014.10.024
2015	CuO	Fe_2O_3	-	Chinese Journal of Catalysis	10.1016/S1872-2067(15)60922-6

2015	Au	Zeolite	-	Catalysis Communications	10.1016/j.catcom.2015.06.018
2015	Pt	CeO_2	-	Catalysis Today	10.1016/j.cattod.2014.12.038
2015	Au, Cu	CeO_2	ZrO_2	Catalysis Today	10.1016/j.cattod.2014.08.035
2015	-	PtO_2	-	Applied Surface Science	10.1016/j.apsusc.2015.03.108
2015	CuO	CeO_2	ZrO_2	Journal of Industrial and Engineering Chemistry	10.1016/j.jiec.2015.06.038
2015	-	MnO_2	CeO_2	Applied Catalysis B: Environmental	10.1016/j.apcatb.2014.06.038
2016	Pd	Fe_2O_3	-	Journal of Environmental Chemical Engineering	10.1016/j.jece.2016.10.019
2016	-	CeO_2	ZrO_2	Applied Catalysis B: Environmental	10.1016/j.apcatb.2016.02.023
2016	Au	Zn_2SnO_4	-	Chinese Journal of Catalysis	10.1016/S1872-2067(16)62468-3
2016	-	Co_3O_4	-	Catalysis Communications	10.1016/j.catcom.2016.08.020
2016	Au	CeO_2	-	Applied Catalysis B: Environmental	10.1016/j.apcatb.2016.02.025
2016	Pd	CeO_2	-	Journal of Molecular Catalysis A: Chemical	10.1016/j.molcata.2016.08.035
2016	-	SiO_2	Al_2O_3	Journal of Molecular Graphics and Modelling	10.1016/j.jmgm.2016.08.005
2016	Ag	SiO_2	-	Catalysis Today	10.1016/j.cattod.2016.05.033
2016	-	PdO	-	Surface Science	10.1016/j.susc.2015.08.043
2016	-	Co_3O_4	-	Applied Catalysis A: General	10.1016/j.apcata.2016.03.027
2016	CuO	TiO_2	-	Catalysis Communications	10.1016/j.catcom.2016.02.001
2016	Pt	CeO_2	-	Applied Catalysis B: Environmental	10.1016/j.apcatb.2016.01.056
2016	CuO	MnO_2	-	Journal of Molecular Catalysis A: Chemical	10.1016/j.molcata.2016.08.024

2016	CuO	Peroskita	-	Applied Clay Science	10.1016/j.clay.2015.08.034
2016	Pd	ZnO	-	Catalysis Today	10.1016/j.cattod.2015.05.021
2016	-	Fe_2O_3	-	Chemical Engineering Journal	10.1016/j.cej.2016.04.136
2016	Au	TiO_2	-	Catalysis Today	10.1016/j.cattod.2015.09.040
2016	Au	Fe_2O_3	CeO_2	Catalysis Today	10.1016/j.cattod.2016.05.059
2016	-	Co_3O_4	-	Materials Letters	10.1016/j.matlet.2016.06.108
2016	-	Co_3O_4	-	Chinese Journal of Catalysis	10.1016/S1872-2067(15)60969-X
2016	Au	TiO_2	-	Applied Surface Science	10.1016/j.apsusc.2016.01.285
2016	-	Fe_2O_3	-	Journal of Molecular Catalysis A: Chemical	10.1016/j.molcata.2016.01.003
2016	Au	Other	-	Journal of Colloid and Interface Science	10.1016/j.jcis.2016.06.072
2016	Au	$LaPO_4$	-	Journal of the Taiwan Institute of Chemical Engineers	10.1016/j.jtice.2016.01.016
2016	Pt	Al_2O_3	-	International Journal of Hydrogen Energy	10.1016/j.ijhydene.2016.08.170
2016	Pt	Other	-	Surface Science	10.1016/j.susc.2015.08.024
2017	CuO	Nb_2O_5	-	Catalysis Communications	10.1016/j.catcom.2017.04.008
2017	Zn, Pt	CeO_2	-	Applied Catalysis B: Environmental	10.1016/j.apcatb.2017.04.044
2017	Pt, Fe	Fe_2O_3	Co_3O_4	Chinese Journal of Catalysis	10.1016/S1872-2067(17)62838-9
2017	CuO	MnO_2	CeO_2	Catalysis Communications	10.1016/j.catcom.2017.05.016
2017	Pt	MnO_2	-	Journal of Electroanalytical Chemistry	10.1016/j.jelechem.2016.09.031
2017	Au	$LaPO_4$	-	Chinese Journal of Chemical Engineering	10.1016/j.cjche.2017.08.008
2017	Fe, Mn	CeO_2	-	Catalysis Today	10.1016/j.cattod.2016.11.046
2017	Mn	Co_3O_4	-	Solid State Sciences	10.1016/j.solidstatesciences.2017.07.
2017	Mn	Co_3O_4	-	Fuel	10.1016/j.fuel.2017.04.140
2017	Au	CeO_2	-	Applied Surface Science	10.1016/j.apsusc.2017.04.158

2017	-	MgO	-	Applied Catalysis B: Environmental	10.1016/j.apcatb.2016.11.043
2017	CuO	CeO_2	Zeolite	Microporous and Mesoporous Materials	10.1016/j.micromeso.2017.02.016
2017	-	Zeolite	-	Applied Catalysis B: Environmental	10.1016/j.apcatb.2017.06.083
2017	Co	ZnO	-	Ceramics International	10.1016/j.ceramint.2017.06.157
2017	Pd	TiO_2	SnO_2	Applied Catalysis B: Environmental	10.1016/j.apcatb.2017.02.017
2017	Pd	Fe_2O_3	-	Fuel Processing Technology	10.1016/j.fuproc.2017.02.037
2017	CuO	CeO_2	-	Journal of Power Sources	10.1016/j.jpowsour.2017.01.127
2017	Mn	CeO_2	-	Applied Catalysis B: Environmental	10.1016/j.apcatb.2017.03.049
2017	Co	Co_3O_4	-	Chemical Physics Letters	10.1016/j.cplett.2017.02.085
2017	Au	TiO_2	-	Catalysis Today	10.1016/j.cattod.2016.05.056
2017	CuO	CeO_2	-	International Journal of Hydrogen Energy	10.1016/j.ijhydene.2017.02.088
2017	CuO	CeO_2	-	Journal of Rare Earths	10.1016/j.jre.2017.05.015
2017	Pd	Al_2O_3	-	Applied Catalysis B: Environmental	10.1016/j.apcatb.2017.02.038
2017	Pt	TiO_2	-	Molecular Catalysis	10.1016/j.mcat.2017.01.014
2017	-	CeO_2	Other	Catalysis Today	10.1016/j.cattod.2017.06.017
2017	-	Al_2O_3	SnO_2	Applied Surface Science	10.1016/j.apsusc.2017.01.058
2017	Ag	Zeolite	-	Fuel	10.1016/j.fuel.2016.10.037
2017	Au	TiO_2	-	Applied Surface Science	10.1016/j.apsusc.2016.10.076
2017	-	Carbon	-	Molecular Catalysis	10.1016/j.molcata.2016.12.007
2017	Ag	SiO_2	-	Microporous and Mesoporous Materials	10.1016/j.micromeso.2017.01.016

2017	Pd, Rh	Al_2O_3	-	Catalysis Today	10.1016/j.cattod.2016.10.010
2017	Au, Cu	SiO_2	-	Catalysis Today	10.1016/j.cattod.2016.08.003
2017	Pd	CeO_2	MnO	Applied Catalysis B: Environmental	10.1016/j.apcatb.2017.01.020
2017	-	CeO_2	-	Catalysis Today	10.1016/j.cattod.2016.04.016
2017	Pd	Co_3O_4	-	Applied Catalysis A: General	10.1016/j.apcata.2016.12.021
2017	Pt	CeO_2	-	Applied Catalysis A: General	10.1016/j.apcata.2017.08.012
2017	Mn	Co_3O_4	-	Solid State Sciences	10.1016/j.solidstatesciences.2017.07.
2017	Ni	ZrO_2	-	Applied Catalysis A: General	10.1016/j.apcata.2017.02.001
2018	-	SiO_2	Co_3O_4	Microporous and Mesoporous Materials	10.1016/j.micromeso.2017.07.016
2018	Pt	Fe_2O_3	-	Applied Catalysis A: General	10.1016/j.apcata.2018.09.014
2018	Pd	SiO_2	Al_2O_3	Applied Catalysis B: Environmental	10.1016/j.apcatb.2018.06.059
2018	Cu	CeO_2	-	Catalysis Today	10.1016/j.cattod.2018.10.037
2018	Cu -Ni	CeO_2	Al_2O_3	International Journal of Hydrogen Energy	10.1016/j.ijhydene.2018.12.127
2018	Ru	TiO_2	ZrO_2	International Journal of Hydrogen Energy	10.1016/j.ijhydene.2018.10.061
2018	Ni	ZrO_2	-	International Journal of Hydrogen Energy	10.1016/j.ijhydene.2018.06.173
2018	-	ZrO_2	-	Applied Catalysis B: Environmental	10.1016/j.apcatb.2018.03.001
2018	Ni	ZrO_2	-	Applied Catalysis B: Environmental	10.1016/j.apcatb.2018.06.045
2019	Au	TiO_2	-	International Journal of Hydrogen Energy	10.1016/j.ijhydene.2018.11.050
2019	Cu	Co_3O_4	-	Molecular Catalysis	10.1016/j.mcat.2019.01.020
2019	-	Other	-	Applied Catalysis B: Environmental	10.1016/j.apcatb.2018.12.022
2019	Pt	Zeolite	-	Applied Catalysis A: General	10.1016/j.apcata.2018.12.034
2019	Ni	ZrO_2	-	Applied Catalysis B: Environmental	10.1016/j.apcatb.2018.11.024

Table SM.5. Surface area, OSC, OSCC and weight loss of Au–Cu catalysts supported on single and dual supports.

Support	BET surface area (m^2/g_{cat})		OSC in fresh samples at 300 °C (μmol O_2/g_{cat})	OSCC in fresh samples at 300 °C (μmol O_2/g_{cat})	Weight loss (%)	
	Fresh	Used			Fresh	Used
CeO_2	52.4	55.4	61	135	1.1	0.6
SiO_2	466.5	410.6	41	49	1.4	1.1
ZrO_2	51.6	44.9	55	99	1.6	0.6
Al_2O_3	96	68.6	36	55	1.7	0.2
La_2O_3	14.1	15.3	21	68	5.5	2.1
Fe_2O_3	38.1	36.7	5	16	0.7	0.8
CeO_2-SiO_2	163.2	155.2	54	105	-2.7	1.8
CeO_2-ZrO_2	44.3	40.5	46	110	0.2	2.0
CeO_2-Al_2O_3	72.7	69.1	41	120	2.0	1.0

6.2.3 Tables for Chapter 2 - Section 3

Table SM.6. Carbon balance for activity tests.

Temperature (°C)	Carbon balances (%)			
	AuCu/Ce-P	AuCu/Ce-R	AuCu/Ce-C	AuCu/Ce-B
300	91	92	98	96
280	92	91	97	92
260	90	91	98	93
240	87	90	97	91
220	85	86	95	82
200	87	87	92	81
180	87	86	94	84
160	89	85	90	83
140	91	92	96	89
120	93	90	97	90
100	92	90	96	92

Table SM.7. Actual loading and surface abundance of Au and Cu on $AuCu/CeO_2$ catalysts.

Catalysts[1]	Actual loading (wt%) in fresh samples[2]		Surface element content (wt%)[3]	
	Au	Cu	Au	Cu
AuCu/Ce-P	1.14	0.82	1.3	4.8
AuCu/Ce-R	0.86	0.91	2.1	5.2
AuCu/Ce-C	0.77	0.89	2.6	5.8
AuCu/Ce-B	0.83	0.92	1.1	6.1

[1]Suffix corresponds to the kind of CeO_2 nano-shaped: polyhedra (P), rods (R), cubes (C) and blank (B). [2]Measured by AAS. [3]Measured by XPS.

Table SM.8. Carbon deposition and crystal size of $AuCu/CeO_2$ catalysts.

Catalyst[1]	Sample	Weight loss (%)[2]				Ceria lattice parameter (Å)[3]
		Total	ΔT1	ΔT2	ΔT3	
AuCu/Ce-P	U	2.4	1.4	0.2	0.8	5.41933
	S	2.5	1.6	0.6	0.3	5.41880
AuCu/Ce-R	U	2.9	2.0	0.5	0.4	5.41941
	S	3.1	2.4	0.6	0.1	5.41942
AuCu/Ce-C	U	2.2	1.4	0.6	0.2	5.41846
	S	2.6	1.6	0.2	0.8	5.41991
AuCu/Ce-B	U	1.9	1.3	0.3	0.3	5.41962
	S	2.9	1.8	0.4	0.7	5.41974

[1]Suffix corresponds to the type of nano-shaped CeO_2: polyhedra (P), rods (R), cubes (C) and blank (B). U: used sample; and S: stability sample. [2]Weight loss measured by TGA. ΔT1: 80 – 250 °C, ΔT2: 250 to 600 °C, and ΔT3: 600 to 1000 °C. [3]Measured by XRD.

6.2.4 Tables for Chapter 3 - Section 2

Table SM.9. Methods evaluated for the synthesis of AuCu catalysts supported on a dual metal oxide of CeO_2-SiO_2.

Synthesis method	Description [a,b]
1	✓ Polycrystalline CeO_2 nanoparticles were obtained by the hydrothermal method as described in [1]. ✓ Dual support was obtained adding nanoparticles of CeO_2 in a slurry of SiO_2 (Merck, Germany). The mixing was dried at 80 °C for 12 h, carefully crushed in a mortar and calcined at 500 °C for 2 h. ✓ 1 wt% Au and 1 wt% Cu were impregnated on the CeO_2-SiO_2 support by deposition-precipitation and incipient wetness impregnation methods, respectively, using the procedure described in [2].
2	✓ Dual support was obtained from aqueous solutions of Ce ($Ce(NO_3)_3{\cdot}6H_2O$, Sigma Aldrich, USA) and SiO_2 (Merck, Germany) [3]. The solution was dried at 80 °C for 24 h and calcined at 500 °C in a muffle for 4 h. ✓ 1 wt% Au and 1 wt% Cu were impregnated in the CeO_2-SiO_2 support by deposition-precipitation and incipient wetness impregnation methods, respectively, using the procedure described in [2].
3	✓ Polycrystalline CeO_2 nanoparticles were obtained by the hydrothermal method as described in [1]. Subsequently, 1 wt% Au and 1 wt% Cu were impregnated on the CeO_2 support by deposition-precipitation and incipient wetness impregnation methods, respectively, using the procedure described in [2]. Then, AuCu/CeO_2 catalyst was obtained. ✓ 1 wt% Au and 1 wt% Cu were impregnated in the SiO_2 (Merck, Germany) support by deposition-precipitation and incipient wetness impregnation methods, respectively, using the procedure described in [2]. Then, AuCu/SiO_2 catalyst was obtained. ✓ The required amount of both samples (i.e., AuCu/CeO_2 and AuCu/SiO_2) were carefully crushed and mixed in a mortar.

4	✓ SiO_2 was included during the preparation of polycrystalline CeO_2 particles[1]. Briefly, a 0.3 M NaOH solution was mixed with $Ce(NO_3)_3{\cdot}6H_2O$ (Sigma Aldrich, USA), under continuous stirring for 1 h at 500 rpm. Then, the required amount of SiO_2 (Merck, Germany) was added into the mixing. The slurry obtained was heated in an airtight container for 24 h at 100. The precipitate was neutralized with water and calcined at 500 °C for 2 h. ✓ 1 wt% Au and 1 wt% Cu were impregnated on the CeO_2-SiO_2 support by deposition-precipitation and incipient wetness impregnation methods, respectively, using the procedure described in [2].

[a] Molar ratio of Ce:Si of 1:1 was ensured in all samples.
[b] All catalysts of AuCu were calcined at 500 °C for 4 h and sifted using a 140-mesh sieve. Before reaction, catalyst samples were activated by a reduction at 300 °C with 8% H_2/Ar stream for 1 h, followed by a purge with pure Ar stream for 30 min and stabilization in 10% air/Ar stream for 30 min.

[1] D.G. Araiza, A. Gómez-Cortés, G. Díaz. Catal. Today. 282 (2017) 185–194.
[2] B. Cifuentes, F. Bustamante, J.A. Conesa, L.F. Córdoba, M. Cobo. Int. J. Hydrogen Energy. 43 (2018) 17216–17229.
[3] B. Cifuentes, F. Bustamante, M. Cobo. Catalysts. 9 (2019) 852–877.

Table SM.10. Assumptions for the CFD model in COMSOL Multiphysics software [a] [b] [c] [d]

Assumption	Description
1	Steady state conditions
2	Ideal gas behavior
3	Newtonian flow (i.e., viscosity is independent of stress)
4	Inertial term on the Navier Stokes equation is neglected (i.e., low Re number, inertial terms would be unimportant relative to the viscous terms)
5	Reactions take place only at the surface of the catalyst (i.e., external and internal mass transfer limitations are neglected)
6	Conductive heat transfer within the catalyst layer is same to that of the cordierite
7	The temperature of the external wall of the monolith was fixed as a boundary condition (i.e., temperature of external wall is equal to the temperature of the furnace)

[a] B. Cifuentes, R. Torres, J. Llorca. Int. J. Hydrogen Energy. (2019) In Press 10.1016/j.ijhydene.2019.11.034.

[b] I. Uriz, G. Arzamendi, E. López, J. Llorca, L.M. Gandía. Chem. Eng. J. 167 (2011) 603–609.

[c] M. Wang, X. Lan, Z. Li. Int. J. Heat Mass Transf. 51 (2008) 3630–3641.

[d] A.A. Rostami, A.S. Mujumdar, N. Saniei. Und Stoffuebertragung. 38 (2002) 359–367.

Table SM.11. Cost of precursors and yield for the synthesis of AuCu catalysts.

Substance	Price (USD/g) [b]	
	Catalog [c]	Colombia [d]
NaOH	0.02	0.07
$Ce(NO_3)_3 \cdot 6H_2O$	0.74	4.21
SiO_2	0.13	0.71
$HAuCl_4 \cdot 3H_2O$	152	181
$Cu(NO_3)_2 \cdot 3H_2O$	0.14	0.57
Cordierite monolith	0.30	0.50
Efficiency of production [a]		
Obtaining CeO_2 nanoparticles		0.45
Obtaining CeO_2-SiO_2 support		0.90
Obtaining AuCu/CeO_2-SiO_2 catalysts		0.80

[a] Efficiency includes loss during mixing, calcination, filtration and sieving processes; [b] Currency exchange rate at January 2020 was used (i.e., USD = 3288 COP and USD = 0.9 EUR); c Values correspond to catalog of Sigma Aldrich (www.sigmaaldrich.com), Merck (www.merckmillipore.com) and Alfa Aesar (www.alfa.com) on February 2020; d Price in Colombia include taxes and delivery costs.

Table SM.12. Kinetic parameters for CO removal from syngas over AuCu/Ce and AuCu/CeSi-75 catalysts obtained in COMSOL Multiphysics software.

Reaction	AuCu/Ce		AuCu/CeSi-75	
	E_a (kJ/mol)	A (pre-exponential factor)	E_a (kJ/mol)	A (pre-exponential factor)
$CO + \frac{1}{2}O_3 \rightarrow CO_3$	20	$1.6 \cdot 10^{-3}$ ($m^4/mol^* s^* g_{cat}$)	30	$2.2 \cdot 10^{-2}$ ($m^4/mol^* s^* g_{cat}$)
$CO + H_2O \rightleftharpoons CO_2 + H_2$	63	$7.3 \cdot 10^{3}$ ($mol/m^* s^* g_{cat}$)	65	$5.42 \cdot 10^{3}$ ($mol/m^* s^* g_{cat}$)
$H_2 + \frac{1}{2}\ O_2 \rightarrow H_2O$	43	1.3 ($mol/m^* s^* g_{cat}$)	55	1.2 ($mol/m^* s^* g_{cat}$)